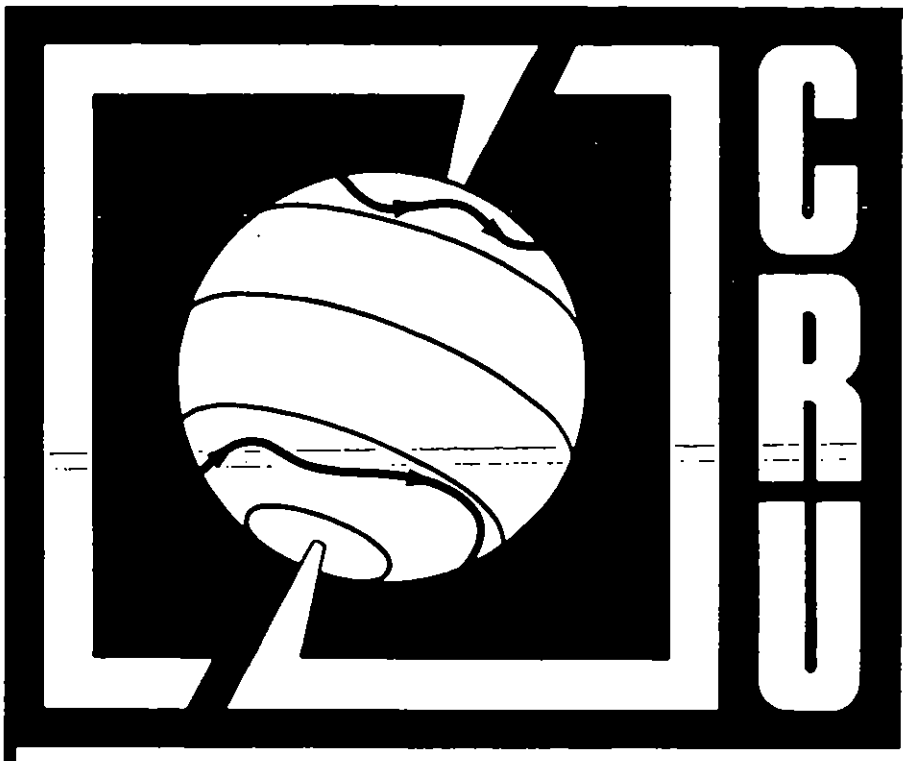

CLIMATIC CHANGE SCENARIOS FOR THE UK

Final Report to the Institute of Hydrology

Under Contract F/60/C1/21

June 1990

CLIMATIC RESEARCH UNIT

School of Environmental Sciences

University of East Anglia

Norwich, NR4 7TJ

England

CLIMATIC CHANGE SCENARIOS FOR THE UK

Final Report to the Institute of Hydrology

Under Contract F/60/C1/21

June 1990

EXECUTIVE SUMMARY

When considering scenarios of future climates due to increases in greenhouse gas concentrations, most studies only address the problem of temperature and precipitation. Here we produce and discuss scenarios of climate change for the British Isles for a wide range of other climate variables. The parameters considered are mean wind speeds, maximum gust speeds, daily weather types, the number of gales, incoming solar radiation and evaporation.

The scenarios are developed using two techniques: first, the output from general circulation models; second, variations in past climates, particularly during past warm periods. Finally, we consider problems arising from the use of spatial analogues (regions where present climate is similar to that predicted for the future in Britain).

The report is arranged in two distinct parts. In Part 1, we discuss possible changes in the wind field due to the greenhouse effect. If we consider only the direct grid-point output from GCMs (using the UKMO model), then a small increase in annual wind speeds is suggested over central and northern Scotland, and a slight decrease over the remainder of the country, with the largest changes occurring in spring. By linking GCM results to a boundary layer flow model, we created fine-resolution scenarios for three test regions. These take into account the effects of orography, exposure and roughness length on wind speeds. We find that the largest changes in near-surface wind speeds occur in the autumn season, between +5% and +8%. The greatest effect is seen in the more exposed parts of the test regions.

The sensitivity of gust speeds to a change in the mean hourly wind speed was also analysed, taking Dungeness as the example. It was found that, for the most realistic forcing of mean winds ($+0.5ms^{-1}$), the expected maximum gust in 100 years would have a speed of $31ms^{-1}$, around $8ms^{-1}$ higher than the present-day value. Whereas we would expect four occurrences in 100 years of gust speeds greater than $20ms^{-1}$ on the basis of current conditions, this figure rises to 15 for the realistic forcing scenario.

Part 2 examines possible impacts arising from the greenhouse effect on daily weather patterns, gale frequency, radiation and evaporation over the British Isles. Daily weather type and gale frequency scenarios were constructed by comparison of warm and cold periods from the instrumental record. The warm periods demonstrated a relative increase in anticyclonicity in spring and summer, and a relative decrease in northerliness in summer and autumn. The frequency of gales in the winter season increases in the warm periods, at the expense of the frequency of autumn gales. Although no overall increase in annual frequency was observed, the most recent warm period (1970-89) has seen a higher frequency of very severe gales.

Radiation and evaporation scenarios were constructed using the direct grid-point output from GCMs. The models suggest increases in incoming radiation in summer and, to a lesser extent, in spring. Changes in the other seasons would be small. Overall the changes would be of the order of $10wm^{-2}$, or an increase of about 4%. Evaporation should increase in all seasons except winter, with the greatest changes found over Scotland and northern England.

TABLE OF CONTENTS (PART 1)

TABLE OF CONTENTS (PART 2)

FIGURES (PART 1)

FIGURES (PART 2)

TABLES (PART 1)

TABLES (PART 2)

PART 1

SCENARIOS OF MEAN WIND SPEEDS AND MAXIMUM GUST SPEEDS IN A HIGH GREENHOUSE GAS WORLD

J.P. Palutikof and X. Guo

1. INTRODUCTION

The impacts on climate of the greenhouse effect will not be limited simply to a global warming. All elements of the climate system will be affected, and the changes will vary substantially from region to region. This section of the report examines the possible effects of greenhouse gas induced warming on wind speeds over the U.K. In particular, we have concentrated on the construction of scenarios for the upland regions of the country. In these areas, a substantial change in wind speeds has implications not only for the natural ecosystem, but also for the economic development of the forestry and wind energy resource. We have taken three approaches to the problem:

1. The output from General Circulation Models (GCMs) is used to examine the effects on mean wind speeds over the U.K. as a whole at the annual and seasonal level. The grid-point output from the GCM control and perturbed runs are compared, and the results interpolated over the U.K. in order to construct the scenario.

2. The 'broad-brush' approach described above takes little or no account of the factors which cause the near-surface wind to differ substantially from the wind above the boundary layer: topography, surface roughness, proximity to a coastal discontinuity etc. In order to derive scenarios of the near-surface wind field we have linked the vector mean wind output from GCMs to a boundary-layer model to examine in detail changes in the wind regime over certain upland areas of the U.K.

3. The sensitivity of gust speeds to a change in the mean wind speed is examined by statistical analysis. It is assumed that both the mean speed and the gust speed distribution can be described by the 2-parameter Weibull distribution. We impose changes in the mean speed of $+0.5ms^{-1}$, $+1.0ms^{-1}$ and $+1.5ms^{-1}$, and examine the effect on the gust speed. Maximum annual gust speed time series are reconstructed for a duration of 100 years. For the development of the methodology we take as our example Dungeness.

Each of these approaches to the problem of constructing regional scenarios of changes in the wind field as a result of the greenhouse effect is discussed in a separate section below.

2. COARSE RESOLUTION WIND SCENARIOS

The grid-point wind speed output from GCMs can be used directly for the construction of scenarios of changes in the wind field over the U.K. linked to the greenhouse effect. For the scenario construction we have used data from the U.K. Meteorological Office GCM (UKMO), fully described by Wilson and Mitchell (1987). This model has a horizontal resolution of 5^0 by 7.5^0, and 11 levels in the vertical, as shown in Fig. 1.1. Grid-point output from this model includes values for the mean monthly surface wind speed. We have used this output to investigate greenhouse-gas related changes in the broad-scale wind field over the U.K. Annual and seasonal mean wind speeds were calculated from the twelve monthly values.

The left-hand side of Fig. 1.2 shows a contoured map of the annual mean wind speed from the $1xCO_2$ UKMO run, for the area around the British Isles. The annual mean is computed from the grid-point output for the twelve months of the year. To assess the performance of the model, we can compare this with present-day wind speeds from observational data. In GCMs, the topographic height within a grid box is constant, and each grid box is specified as being either land or ocean. Therefore we cannot compare the GCM $1xCO_2$ results directly with near-surface observations of wind, since these are influenced by such factors as the orography of the anemometer environment, the surface roughness, and the proximity to a coastal discontinuity. Instead, we have used the Moore model of on- and off-shore winds, based on 900mb wind speeds for the period 1961-70 (Moore, 1982; Barthelmie et al., 1990).

The Moore model extrapolates downwards from the 900mb level to 60m above the ground by assuming a logarithmic wind speed profile in the boundary layer. The wind speeds are modelled on a 10km by 10km grid. Over land, no account is taken of orography. Roughness lengths are not taken into account explicitly, although the formulation of the model over land and over sea is different. A down-wind disturbance due to the coastal discontinuity is introduced. The model

results have been validated using data from ocean weather ships, gas and oil platforms, and from tall masts over land. The 'flat-land' and offshore annual mean wind speeds computed by the Moore model from 900mb observations, and shown on the right-hand side of Fig. 1.2, provide a benchmark of present-day conditions against which the performance of the UKMO control run can be evaluated. Although the Moore wind speeds are computed for 60m above the surface, whereas the UKMO wind speeds are for surface winds, the relative variations are still comparable. The formulation of the Moore model is such that the wind speeds cannot easily be extrapolated beyond the area shown in Fig. 1.2.

In the UKMO model wind speeds are at a minimum of less than $4.5ms^{-1}$ over southeast England. They increase across the country from south to north, to a maximum of $5.4\text{-}5.6ms^{-1}$ over northern Scotland, and towards the southwest to a maximum of $4.7\text{-}4.9ms^{-1}$ over Cornwall. It should be recalled, however, that these patterns are derived from values at only a few grid points, and therefore to some extent are a function of the characteristics of the contouring package used. The Moore model shows minimum wind speeds over south-east England, inland from the coast ($5.5\text{-}6.0ms^{-1}$). Wind speeds increase towards the coast, and across the country towards the west and northwest., reaching $8.5\text{-}9.0ms^{-1}$ in some parts of northern Scotland. We may assume that the UKMO wind speeds apply to the standard 10m height, and that they are related to the 60m winds by a power law profile with an exponent of 0.16. On this basis, the UKMO wind speeds match the Moore model values in the southeast of the country well. In the high wind-speed regions of northern Scotland the UKMO model underestimates the Moore model wind speeds by around $1.5ms^{-1}$. Overall, therefore, the match is reasonably good and the UKMO geographical pattern over the land is realistic, although the wind speeds over the sea to the west of Scotland appear low relative to those over the sea between Scotland and Scandinavia.

Fig. 1.3 shows the results from the $2xCO_2$ equilibrium response run for annual mean wind speeds, side-by-side with the $2xCO_2\text{-}1xCO_2$ differences. The

annual mean for both the perturbed and the control run has been calculated from the grid-point output for each of the twelve months of the year. It can be seen that a small increase over central and northern Scotland is predicted for a $2xCO_2$ world, and a small decrease (not exceeding $0.3ms^{-1}$) for the remainder of the country.

The $1xCO_2$ model results for each season are shown in Fig. 1.4. These maps are computed from the monthly grid-point output of the UKMO GCM, as follows: DJF for winter, MAM for spring, JJA for summer, SON for autumn. Wind speeds are highest in winter and lowest in summer. The only season in which the spatial pattern deviates markedly from that demonstrated by the annual scenario (Fig. 1.2) is summer. The UKMO model suggests that in this season the south of England lies in a region of lower wind speeds between maxima $>5.2ms^{-1}$ over the Bay of Biscay and the North Sea. In this season the large-scale atmospheric circulation is generally weak and indeterminate. We would expect GCMs to perform less well in this season than at times of the year when the circulation patterns are strong and clear-cut. Moreover, the GCM scenarios have less relevance to actual surface conditions, since these are dominated by local thermal circulations, which cannot be modelled by coarse resolution GCMs.

Figs. 1.5-1.8 show the greenhouse-effect wind field scenarios for the four seasons. The left-hand side of each figure shows the spatial pattern contoured from the $2xCO_2$ equilibrium results. The right-hand side shows the $2xCO_2$-$1xCO_2$ differences. It is obvious from these maps that the spatial patterns of wind speeds in the perturbed run are broadly the same as those in the control run. The only differences lie in the intensity of the pattern (whether the isolines move closer together or further apart) and the position of the isolines (determining whether a particular location is subject to higher or lower wind speeds).

When we examine the $2xCO_2$-$1xCO_2$ differences shown on the right-hand side of Figs. 1.5-1.8, it is clear that the largest changes over the U.K. occur in the spring season. These range from an increase of $0.1\text{-}0.2ms^{-1}$ over western Scotland,

to a decrease of more than $0.2ms^{-1}$ in southern Ireland and southwest Britain. In spring, summer and winter an increase in wind speeds is shown over the northern part of the country, counterbalanced by a decrease in the south. In autumn the scenario suggests that wind speeds will decrease slightly over the whole of the British Isles.

These scenarios, based directly on the coarse resolution output from the UKMO GCM, indicate only a small change in wind speeds over the U.K. in a $2xCO_2$ world. However, as already noted, they have little relevance for conditions on the ground. This is not only because the underlying wind data are taken from only a few grid points, but also because the parametrization of the lower surface of the boundary layer (orography, surface roughness etc.) is too coarse to produce results applicable to a particular place. For this reason, we have linked the coarse-resolution GCM output to a fine resolution boundary-layer model in order to derive site-specific scenarios. This procedure, and the results, are described in the next section.

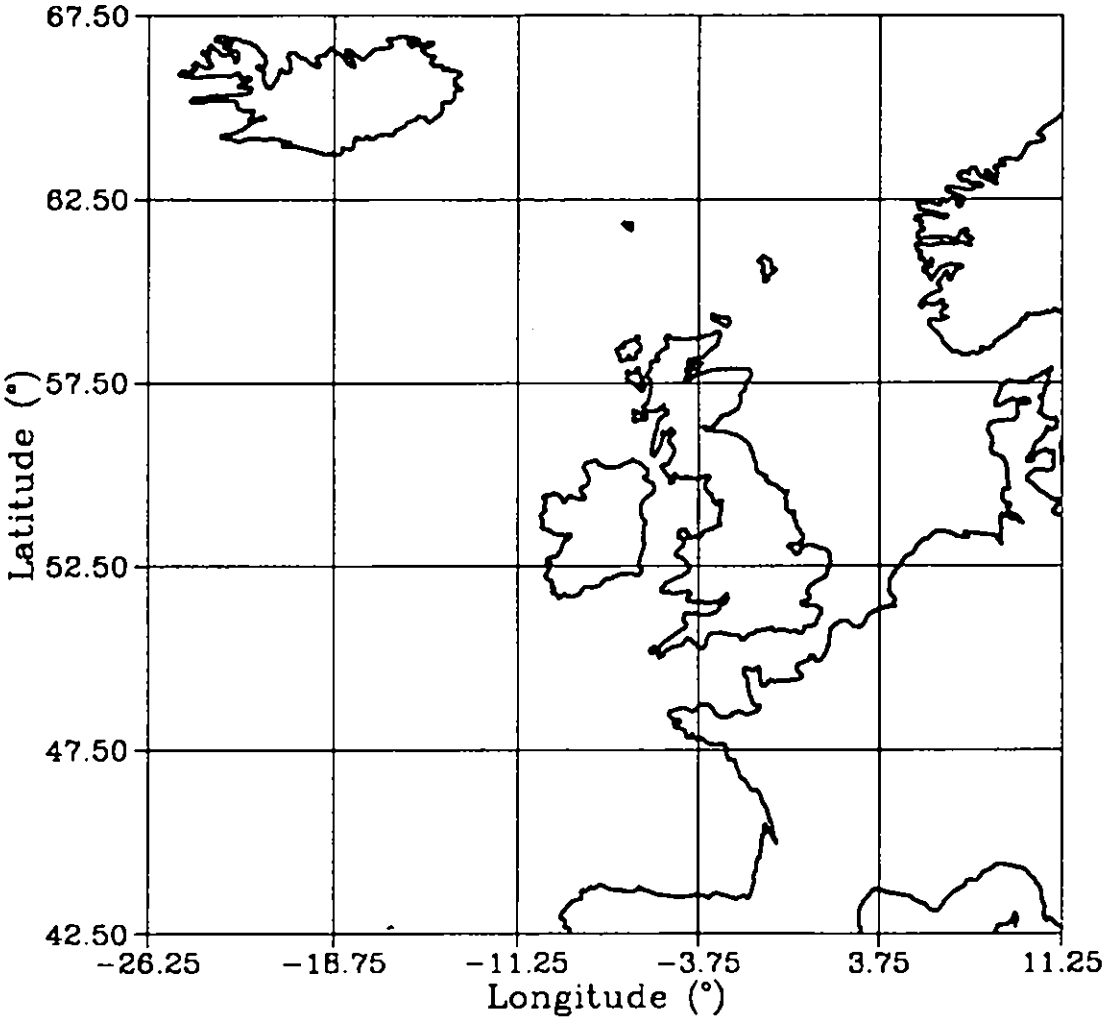

Fig. 1.1 Horizontal grid position of the UKMO GCM.

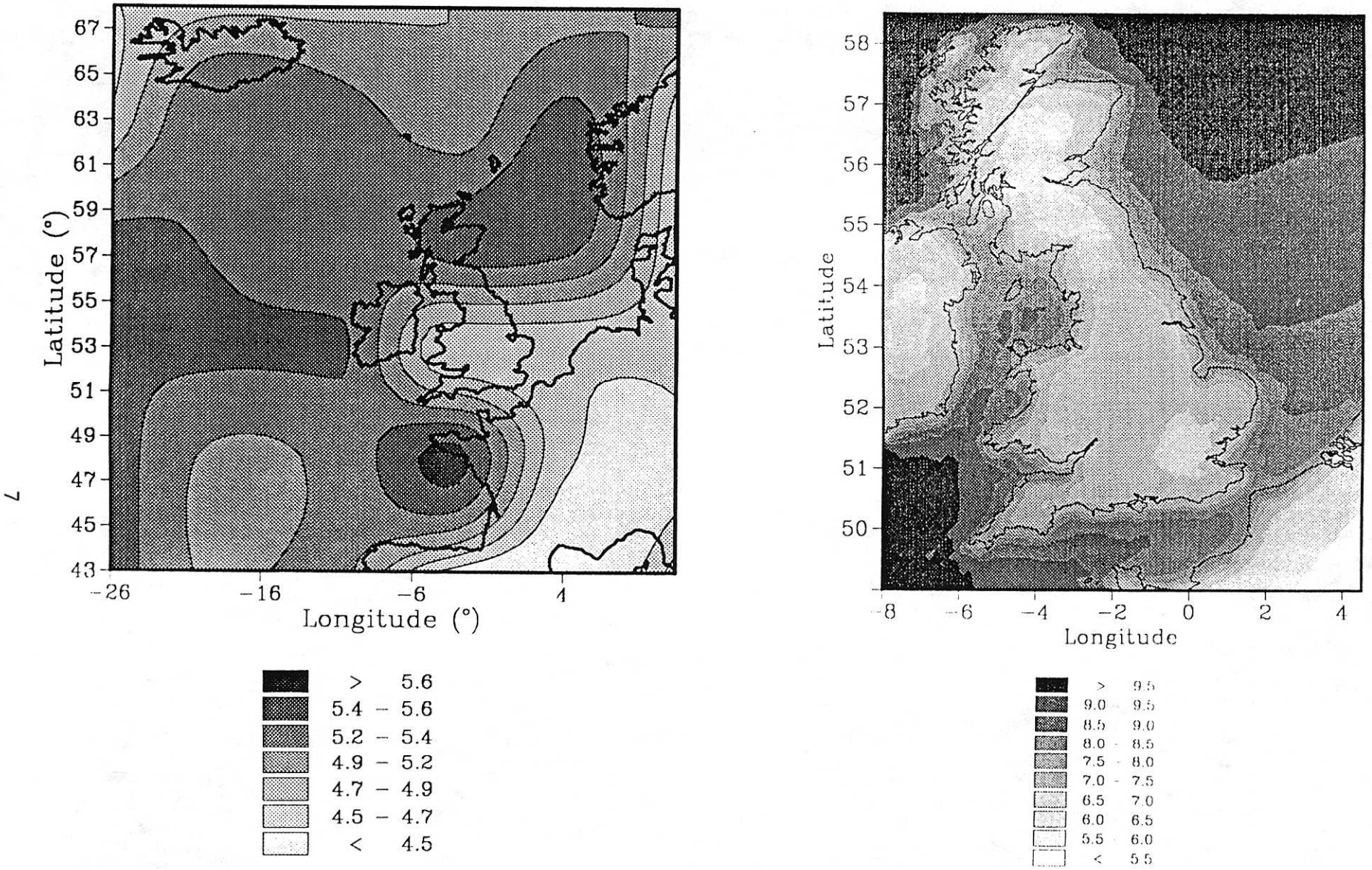

Fig. 1.2 Modelled present-day annual mean wind speeds over the British Isles (ms^{-1}). Left-hand side shows the results from the UKMO $1xCO_2$ simulation. Right-hand side shows the results from the Moore model (Moore, 1982).

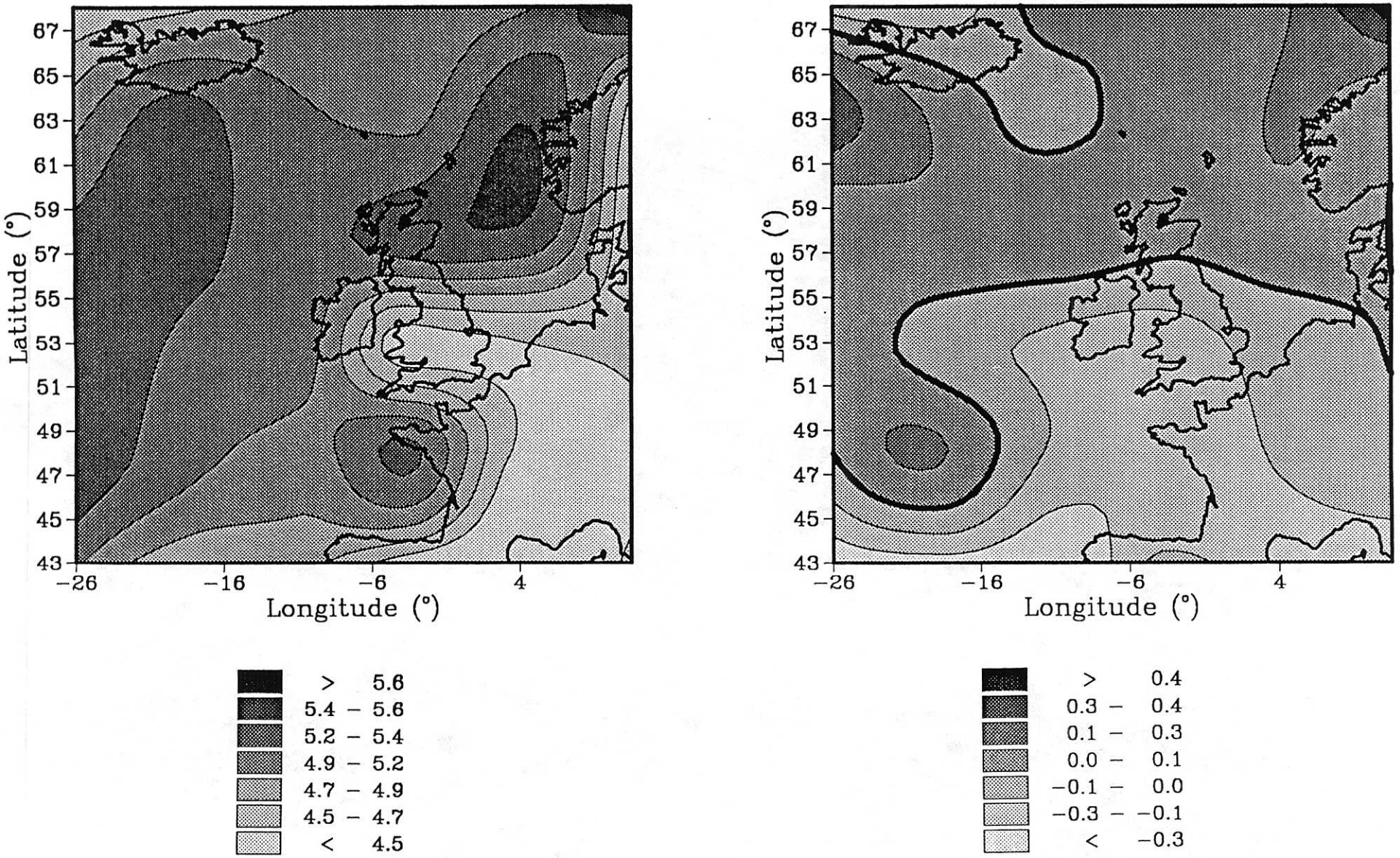

Fig. 1.3 UKMO model annual mean wind speeds for the British Isles (ms^{-1}). Left-hand side shows results for the $2xCO_2$ model simulation. Right-hand side shows the $2xCO_2$-$1xCO_2$ difference.

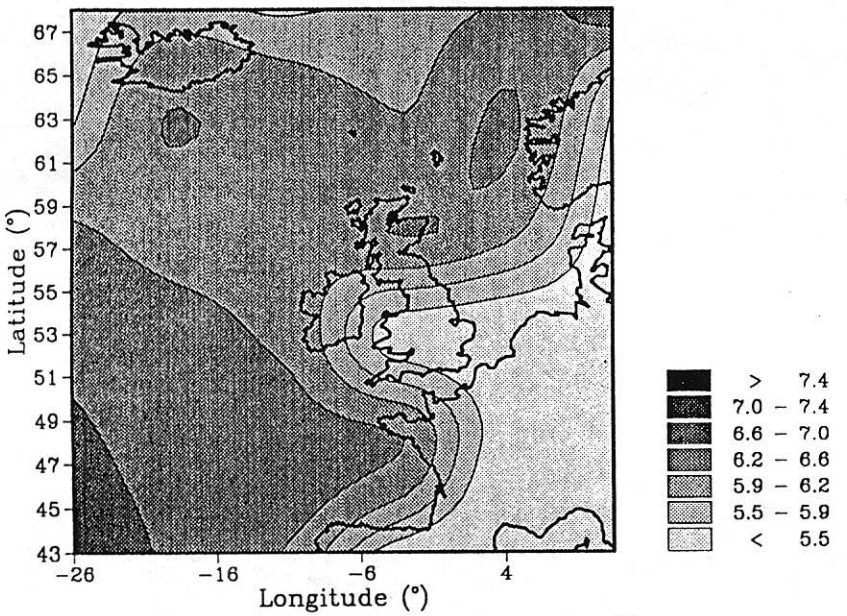

UKMO $1xCO_2$ winter mean wind speed (ms^{-1})

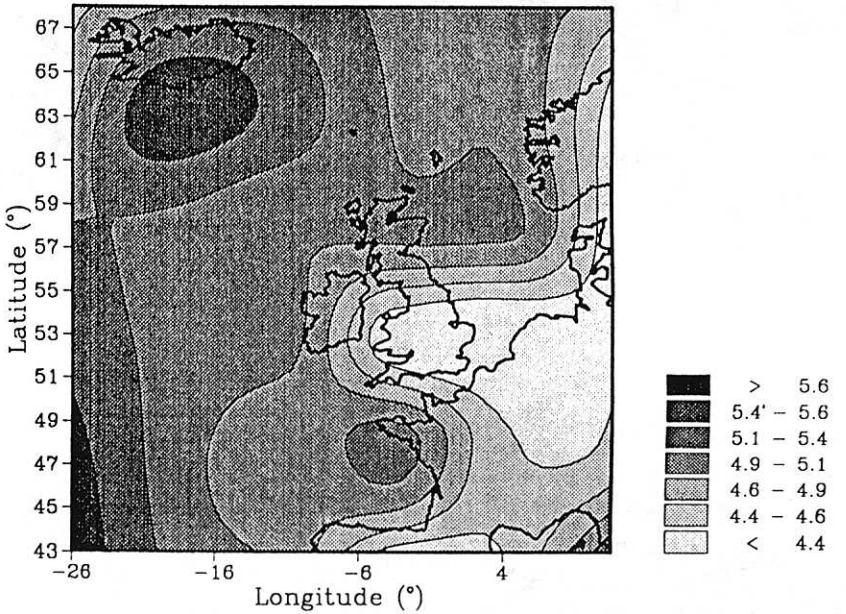

UKMO $1xCO_2$ spring mean wind speed (ms^{-1})

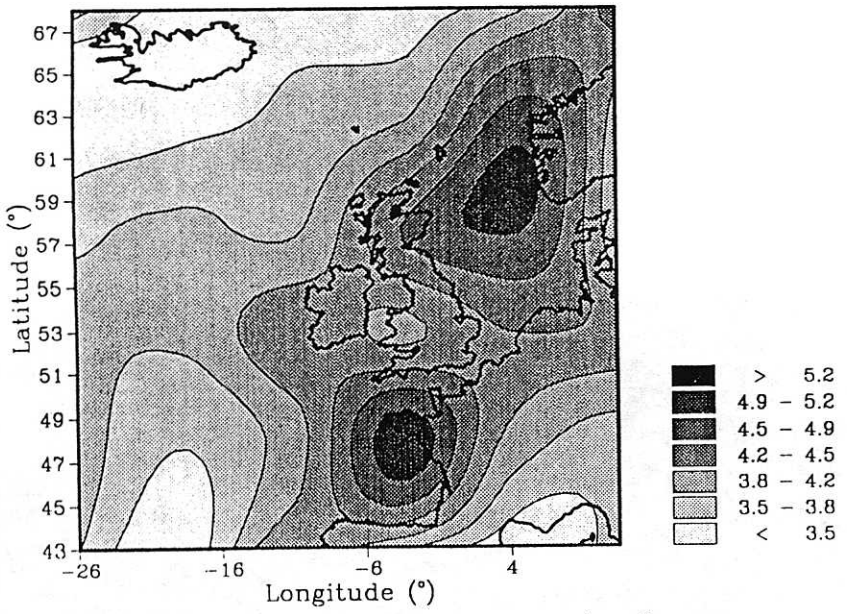

UKMO $1xCO_2$ summer mean wind speed (ms^{-1})

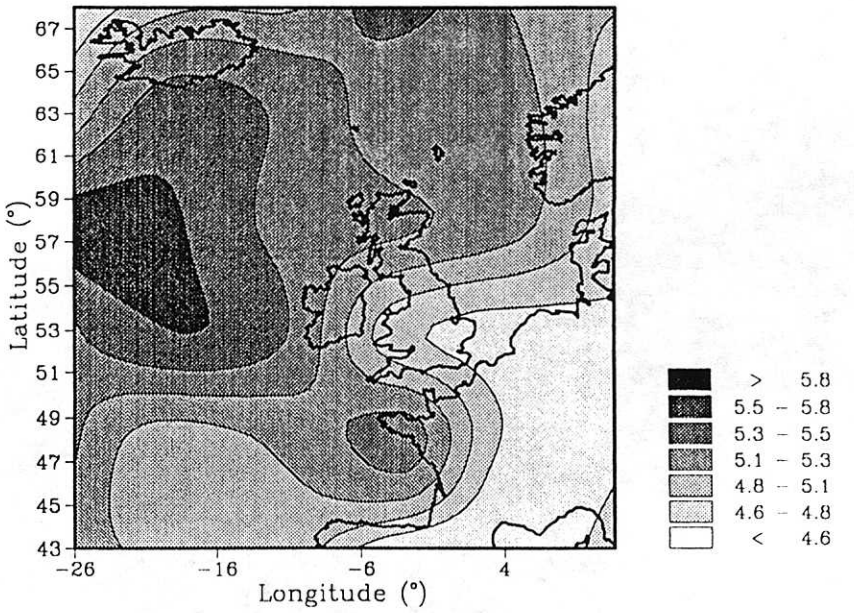

UKMO $1xCO_2$ autumn mean wind speed (ms^{-1})

Fig. 1.4 UKMO $1xCO_2$ seasonal model simulations (ms^{-1}).

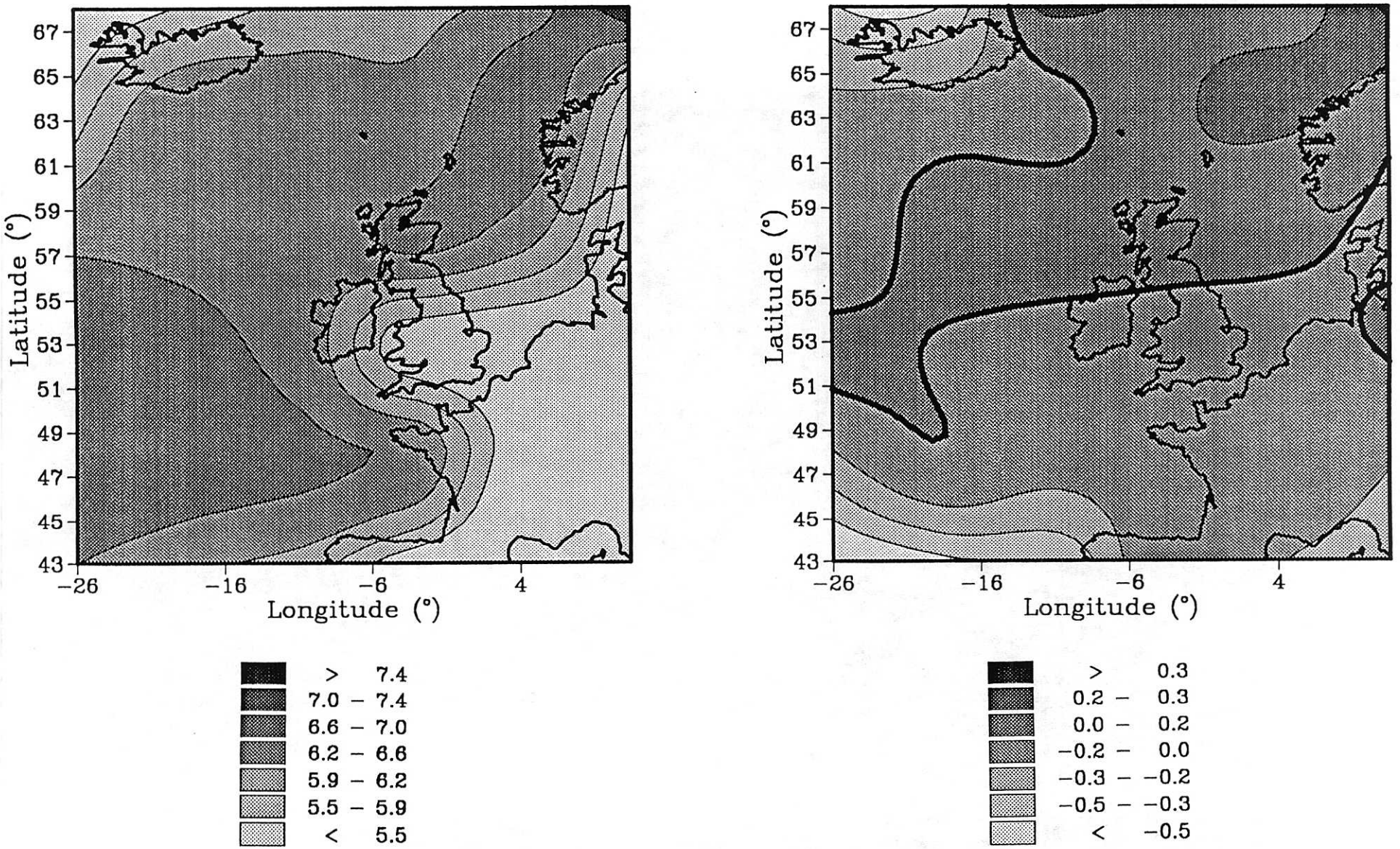

Fig. 1.5 UKMO model winter mean wind speeds for the British Isles (ms^{-1}). Left-hand side shows results for the $2xCO_2$ model simulation. Right-hand side shows the $2xCO_2$-$1xCO_2$ differences.

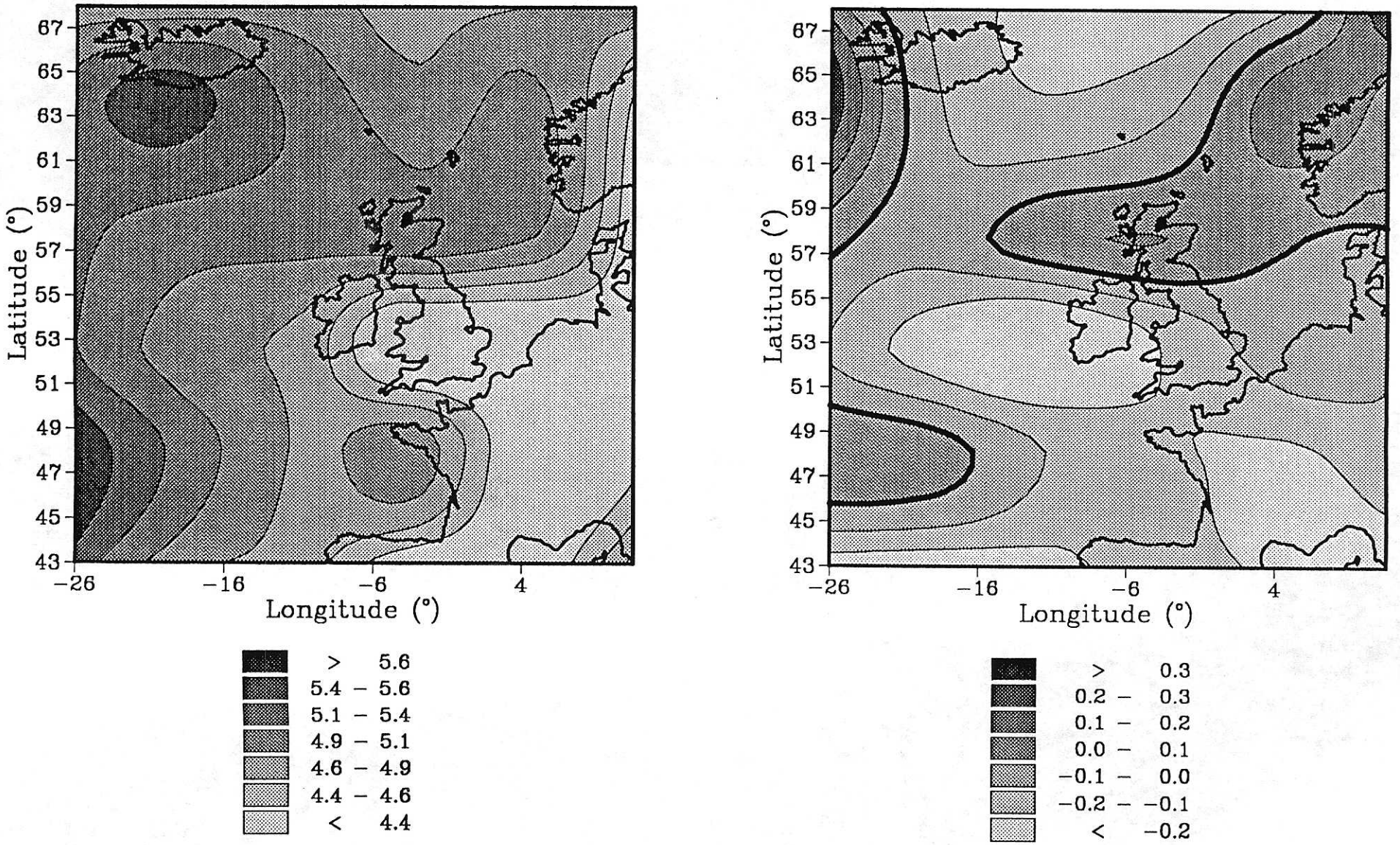

Fig. 1.6 UKMO model spring mean wind speeds for the British Isles (ms^{-1}). Left-hand side shows results for the $2xCO_2$ model simulation. Right-hand side shows the $2xCO_2$-$1xCO_2$ differences.

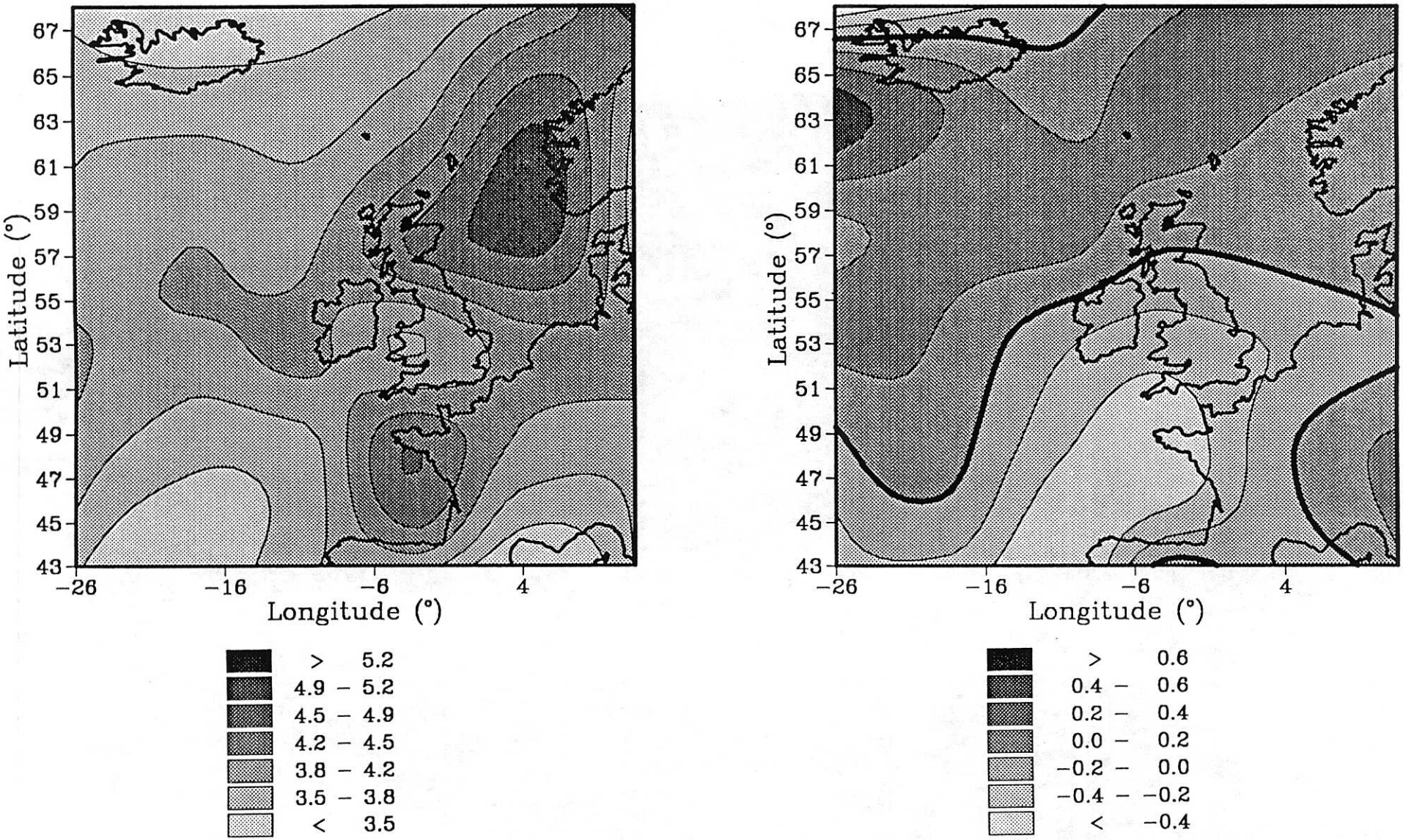

Fig. 1.7 UKMO model summer mean wind speeds for the British Isles (ms^{-1}). Left-hand side shows results for the $2xCO_2$ model simulation. Right-hand side shows the $2xCO_2$-$1xCO_2$ differences.

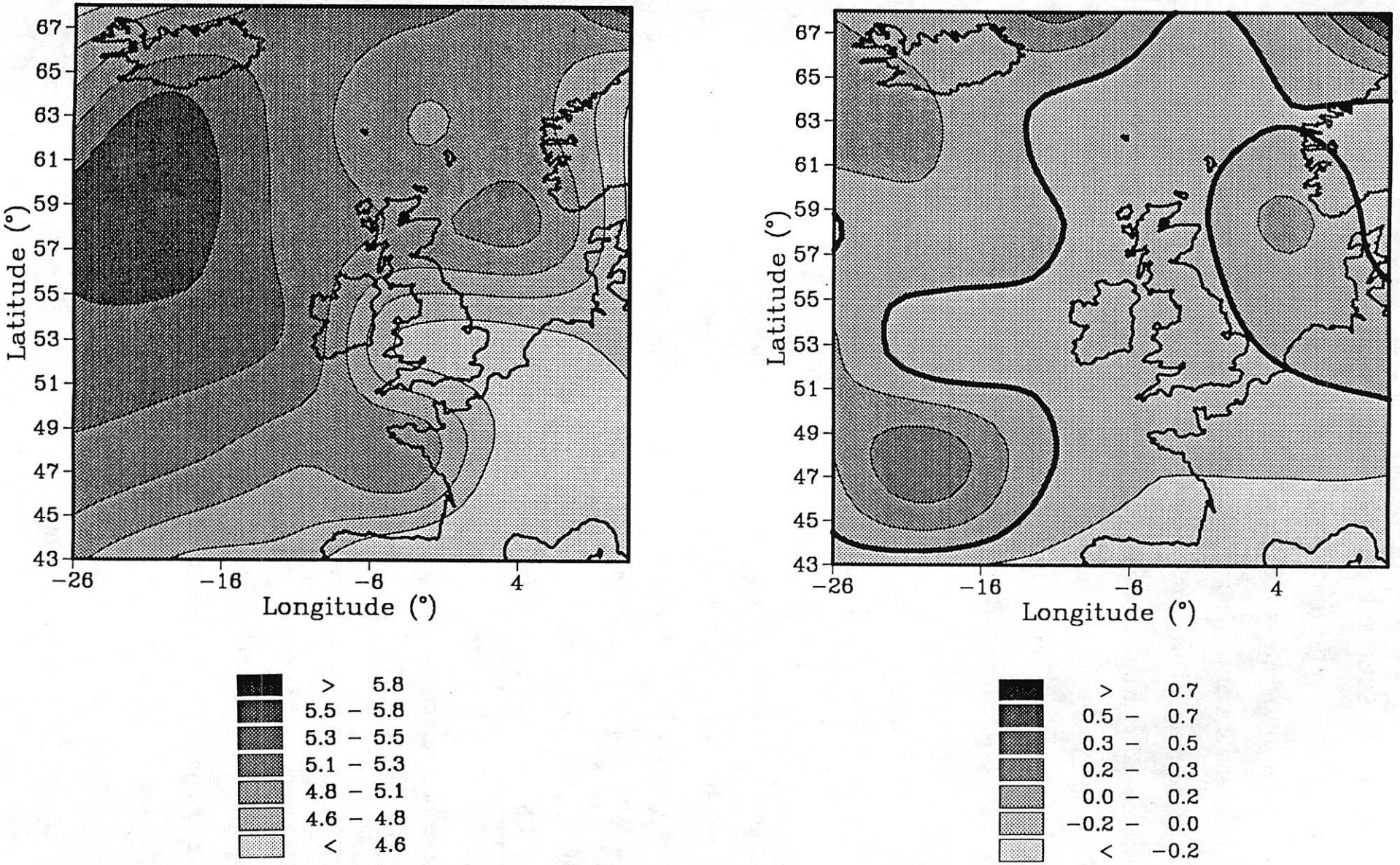

Fig. 1.8 UKMO model autumn mean wind speeds for the British Isles (ms^{-1}). Left-hand side shows results for the $2xCO_2$ model simulation. Right-hand side shows the $2xCO_2$-$1xCO_2$ differences.

3. REGIONAL SCENARIOS OF THE WIND FIELD IN A HIGH-CO_2 WORLD

In this section of the report we concentrate on the construction of regional scenarios in upland areas of Britain. There are two reasons for this. First, the implications of a large change in wind speeds appear potentially more damaging for upland areas, where much of the economy is based on the exploitation of resources affected by the wind, such as forestry. Second, the development of a methodology for scenario construction in upland areas is a more complex problem than it is in lowland areas with little or no orography.

Regional scenarios of changes in the wind field due to the greenhouse effect cannot be constructed directly from GCM output. To take the case of the UKMO model, which is typical, the British Isles are completely boxed by twelve grid points. Two grid points are at latitude/longitude positions overlying the British Isles (see Fig. 1.1). If this situation is contrasted with the pronounced spatial variability of wind speed, it is apparent that the grid point output from GCMs can only be taken as the first step in regional scenario construction. An interface must be found between the coarse resolution model output and the fine resolution required for a regional prediction. Numerical models of the boundary layer provide such an interface.

3.1 Characteristics of the boundary layer model CONFORM

Wind flow over areas of level terrain is relatively simple to model and good levels of accuracy are achieved using methods such as that developed by Petersen et al. (1981). The same cannot be said for areas of complex terrain. In such regions, wind speeds are highly variable: on hilltops they will approach the free-stream value, whereas in confined valleys they may bear little relation to the large-scale circulation but instead be governed almost entirely by local, largely thermal, influences. At the same time, the data network for upland regions is often inadequate, as shown in Table 1.1. The combination of these two circumstances, along with the need for wind speed predictions for pollution monitoring and in the forestry and wind energy industries, has lead to a

substantial research initiative on the development of boundary layer models to predict wind speeds.

Boundary layer models range in sophistication from mass consistent models, which simply attempt to make the wind flow over the terrain non-divergent, to those with full dynamics. A review of wind models over complex terrain has been carried out by Physick (1988). With increasing complexity there is of course a computing penalty, and model choice is generally constrained by considerations such as the computing power available and the spatial resolution required. In this study we have used a simple ideal flow model, CONFORM, based on the conformal mapping technique in complex analysis. This model is fully described by Guo and Palutikof (1990), and has been shown to give good results in modelling the present-day wind field.

CONFORM makes three assumptions about the characteristics of the wind flow. It assumes, first, that the streamlines of the real flow coincide with the streamlines of the ideal flow and, second, that the air density is constant with depth close to the ground. Thus the real flow speed-up factors can be assumed to be the same as those for the ideal flow. Finally, by assuming neutral stability the model application can be extended from two-dimensional to three-dimensional flow. The terrain is treated as a number of parallel sections oriented along the wind direction. Each section can be treated as a two-dimensional problem, with no transfer of air between the sections. In common with many boundary layer models, thermal flows, such as anabatic and katabatic winds, are neglected. Further, the terrain gradients must be low enough that flow separation does not occur.

Table 1.1 Altitude of anemometer sites in the U.K.

Anemometer altitude	Number	Percent
Below 100m	106	74.6
100-200m	24	16.9
Above 200m	12	8.5
Total	142	100.0

In order to apply the model, the first step is to digitize the terrain. CONFORM handles topography in the form of terrain heights at the intersections of a two-dimensional grid. The model extends the real terrain grid to some distance from the test region until the topography is flat and equal in height to the minimum terrain height in the test region itself. This method of handling the terrain is similar to that used in the MS3DJH model (Walmsley et al., 1986). The model is run once for each wind direction and the topographic grid is rotated prior to each run in order to bring it into line with the direction of the wind flow. It is assumed that the vertical wind speed profile in the constant height region is logarithmic. As the air moves over the two-dimensional terrain 'slices' the speed-up factors are calculated. Observational data from one or more anemometer sites in the test region is then used to transform these speed-up factors into a prediction of the real wind speed at each of the grid intersections. These predictions can be contoured to produce a wind-speed map of the whole test region.

In this discussion we have not considered the influence of roughness length on wind speed. In order to incorporate this effect into the model, it would be necessary to produce a roughness length map of the test region. In fact, it has been shown (Guo, 1989) that wind speeds at the heights above ground considered here (10m or above) are relatively insensitive to surface roughness changes. For this reason, and in view of the work entailed in making any other assumption, the effects of variable surface roughness length across the region have been neglected.

3.2 Construction of greenhouse scenarios from CONFORM

In order to apply GCM results to numerical modelling of the boundary layer, information on both wind speed and wind direction is required. This information is contained in the vector mean winds. The Climatic Research Unit has GCM vector mean wind grid-point output for the Goddard Institute of Space Studies (GISS) GCM and the Geophysical Fluid Dynamics Laboratory (GFDL) GCM. The

GISS GCM (Hansen et. al., 1984) has a horizontal grid resolution of 7.83° latitude by 10° longitude whereas the GFDL model (Manabe, personal communication) has a resolution of 4.45° latitude by 7.5° longitude.

The difference between the vector mean wind for the GCM perturbed run and the control run was calculated for each grid point around the British Isles. Then, the $2xCO_2$-$1xCO_2$ difference for the test region was calculated by interpolation from the GCM grid-point values. This difference was assumed to represent the change due to the greenhouse effect over the constant-height region of CONFORM.

In order to develop scenarios of wind speeds in a high greenhouse gas world, it is necessary to have a baseline estimate of wind speeds and directions in the constant height region on which to impose the vector mean wind difference. This is obtained from the observational data available for the test region. Suppose there are two anemometer sites in the test region, both well exposed and not subject to topographic channeling or thermal wind circulations. By averaging their wind direction observations, we can obtain a wind rose of the frequency of wind directions for the constant-height region. Ten-degree bins were used in this study for the construction of this wind rose. A mean speed can then be assigned to each ten-degree bin, by subtracting the speed-up factors from the observed wind speeds as appropriate, and calculating a mean.

The $2xCO_2$-$1xCO_2$ vector mean wind difference for the constant-height region was then added to the mean wind speed of each ten-degree bin of the present-day wind rose. Although the new wind speeds may not lie along the centre point of the ten-degree bins, the mean speed and directional frequency for each bin can be calculated from those vector winds which lie within the bin boundaries. Using this new data set for the constant-height region, CONFORM is run to obtain the greenhouse gas perturbation at each grid-point in the test area. This procedure was followed to obtain scenarios both for the year as a whole and for each season.

3.3 The test regions

In applying the method outlined above, a major constraint is the effort required to digitize the terrain data. For this Report, three areas were considered for which the digitization had already been performed. There is no doubt that the increasing availability of digitized terrain data bases will lead to major advances in boundary layer modelling. The three test regions are all located in upland areas of the British Isles.

The first region is a 10kmx10km area of the Northern Pennines, encompassing the two anemometer sites of Great Dun Fell (GDF) and Moor House. The area is shown in Fig. 1.9. Data are available for the two sites for the year 1971. The GDF anemometer is located on the summit of a hill on the western edge of the Pennines, overlooking the Eden valley to the west. The anemometer is sited 10m above the ground. The Moor House anemometer is some 5km to the east of GDF, on an eastwards facing slope. The instrument was at 13m above the ground. The siting characteristics of the anemometers are given in Table 1.2. A west-east topographic profile through the two sites is also shown in Fig. 1.9.

The second test region (shown in Fig. 1.10) is in Devon, and was originally selected to test model performance on a larger spatial scale. It is a well-networked area of relatively complex terrain, where the topographic gradients are unlikely to cause flow separation. There are five anemometer sites (see Table 1.2) in the region, and we have wind speed and direction data for the year 1985.

The third test region is the main island of Shetland, shown in Fig. 1.11. We have data for three sites, Susetter Hill, Scroo Hill and Lerwick, described in Table 1.2. The terrain is relatively steep in this location, so that the possibility of flow separation arises.

Differing scales and contour intervals in figs 1.9 - 11 confuse.

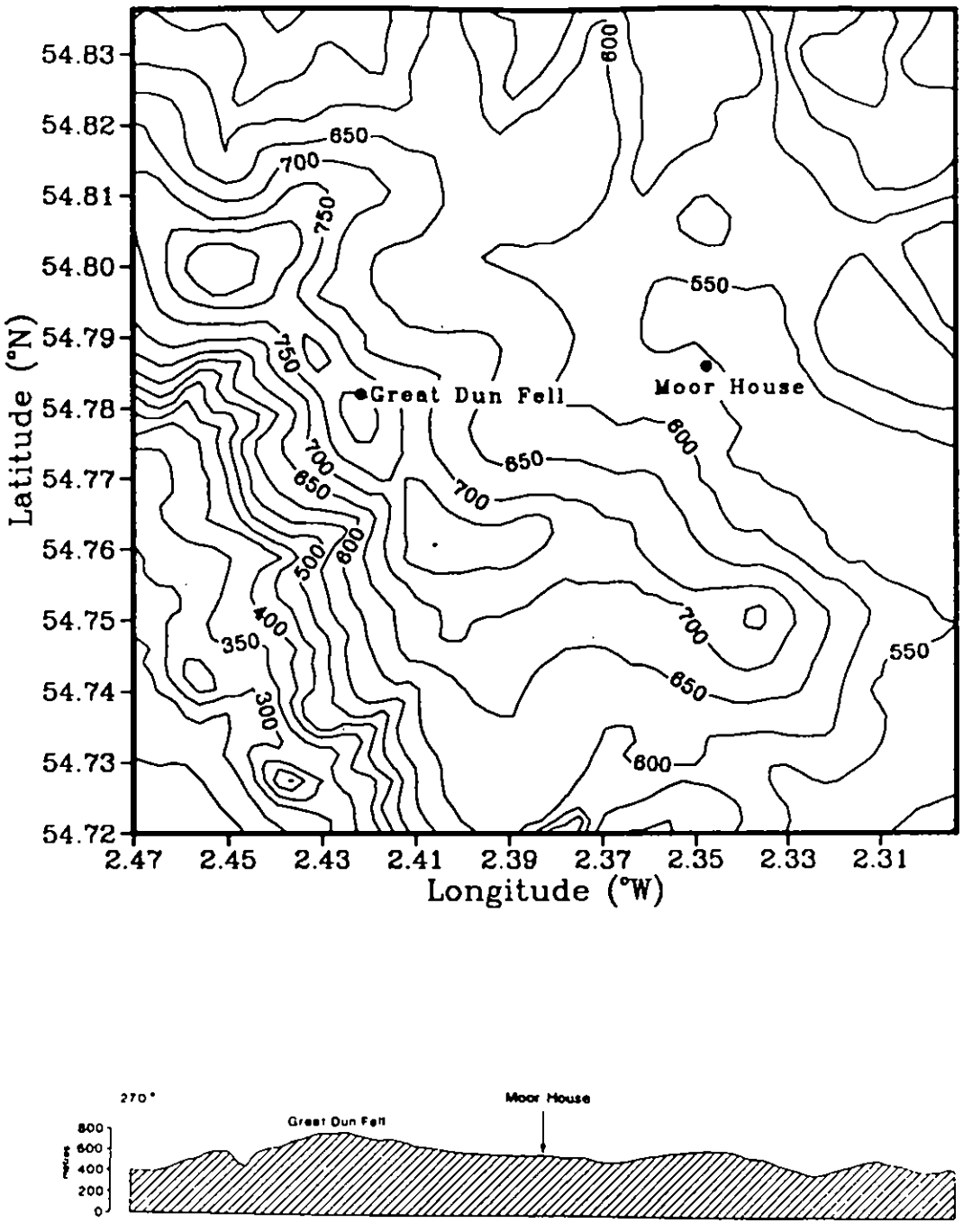

Fig. 1.9 The Northern Pennines test region, with a topographic profile W-E through the two anemometer sites.

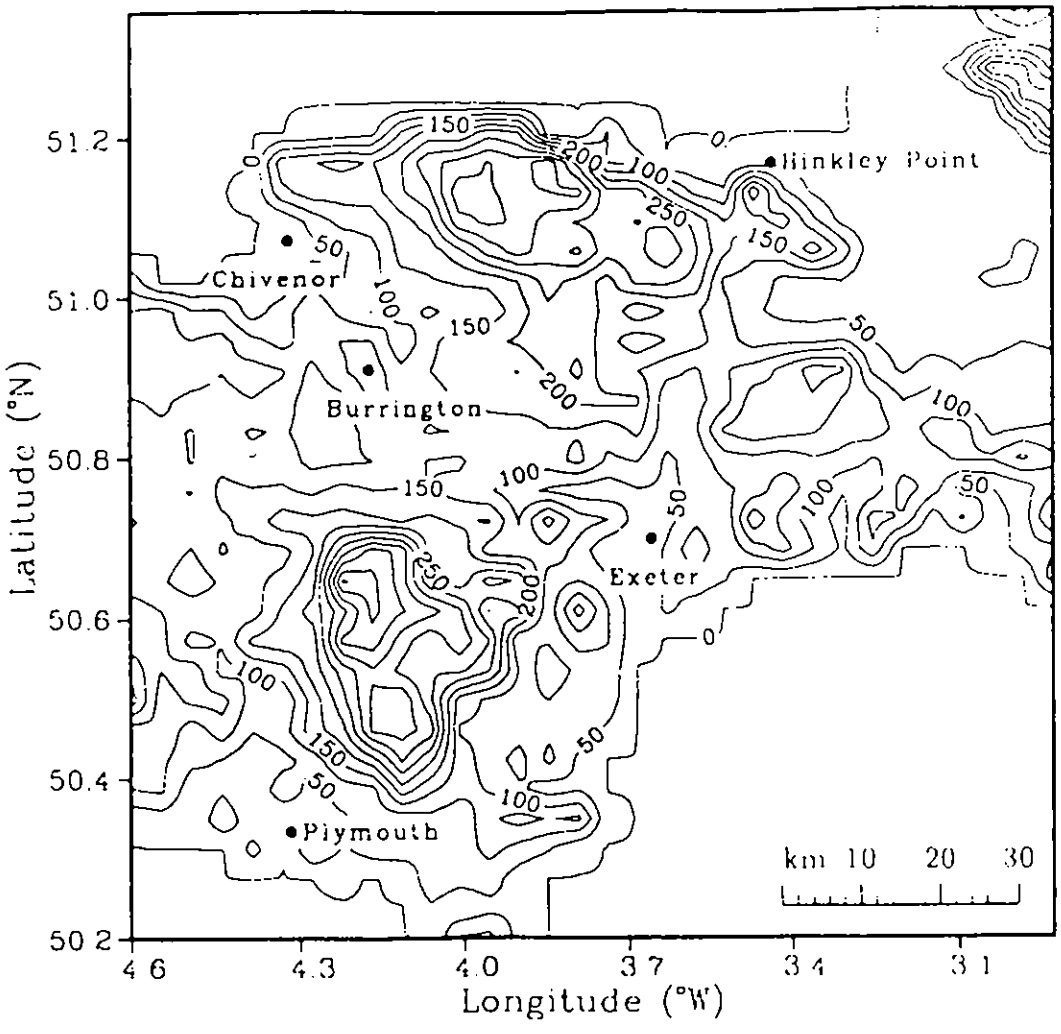

Fig. 1.10 The Devon test region.

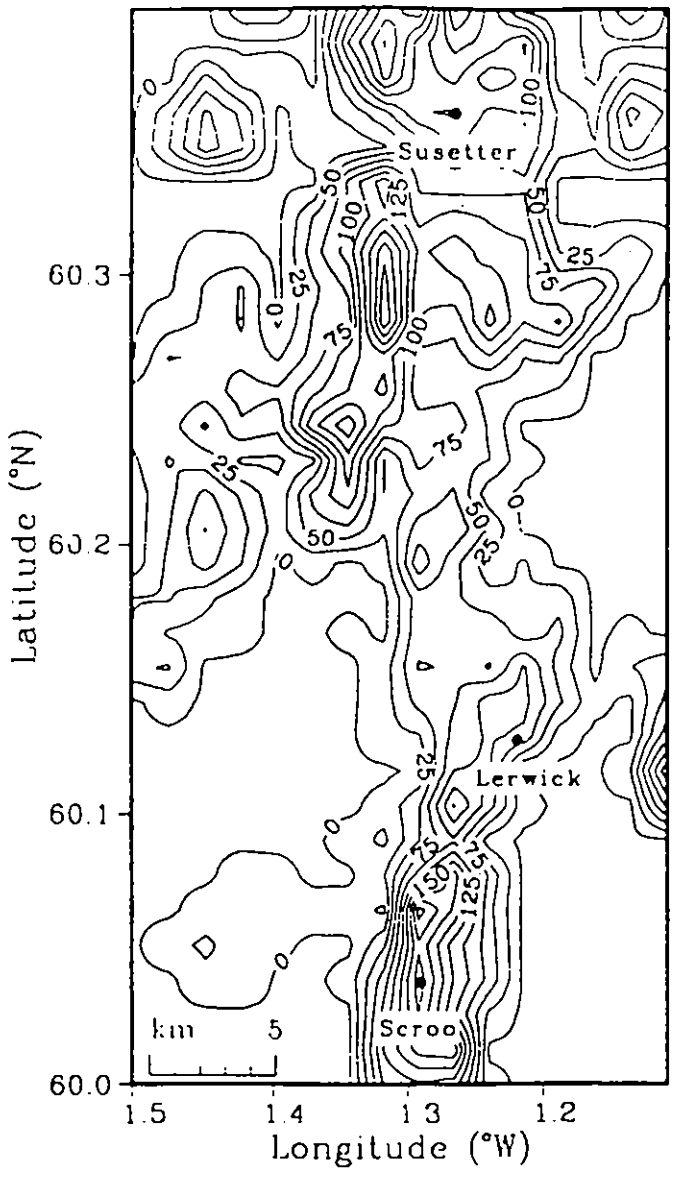

Fig. 1.11 The Shetland Main Island test region.

3.4 Wind speed scenarios for the three test regions in a high CO_2 world

CONFORM has been used to model the wind field in each of the three test regions. Initialization of the model in each case was performed from the available observational data. The observational data were also employed to construct present-day wind roses of wind speed by direction, and the frequency of occurrence of winds in each of the ten-degree directional bins. These wind roses were then perturbed by applying the vector mean wind differences ($2xCO_2$-$1xCO_2$) from GCM ouput. Finally, CONFORM was run using the perturbed wind roses to obtain scenarios of the wind field in a high greenhouse gas world.

The underlying forcing mechanism for the scenario construction is the vector mean wind grid-point output for $1xCO_2$ and $2xCO_2$ from the GISS and GFDL GCMs. This is shown in Figs. 1.12-1.41, along with the $2xCO_2$-$1xCO_2$ vector mean differences, calculated in CRU. The arrows shown in these diagrams originate at the grid-point they refer to, and contain information about the wind speed (the length of the arrow) and the direction (the orientation of the arrow). We can

Table 1.2 Site characteristics of test region anemometers

Station	Height (m)		OS Grid Reference
	AMSL	AGL	
Northern Pennines			
Great Dun Fell	847	10	(35) 710322
Moor House	595	13	(35) 759326
Devon			
Exeter	43	12	(30) 001933
Burrington	210	10	(21) 606168
Chivenor	15	10	(21) 495347
Plymouth	64	13	(20) 492529
Hinkley Point	30	10	(31) 167452
Shetland			
Lerwick	85	10	(411) 453397
Scroo Hill	248	10	(411) 406298
Susetter Hill	175	10	(411) 417648

AMSL - above mean sea level
AGL - above ground level

compare the model results for the control run with known present-day conditions in order to obtain some idea of model performance.

Fig. 1.12 shows the annual $1xCO_2$ vector mean winds for the GFDL GCM (calculated from the annual values). There is a prevailing westerly flow over the whole of the British Isles, which accords well with reality, although we might have expected a more southwesterly component. The strong southerly component over Iceland suggests that the Iceland low pressure system is, in the GCM, displaced towards the northeast from its true position. The performance of the GISS model is less encouraging (see Fig. 1.15). The prevailing flow to the north and west of the British Isles is from the north, turning towards the north-west over the land surface itself. However, the north-west component is weak, and may be the result of resolving two strong but opposed wind flows.

At the seasonal level, the GFDL model output continues to compare well with reality. In the winter control run (Fig. 18) the prevailing wind flow is from the southwest, whereas in spring and autumn (Figs. 1.24 and 1.36) it is from the SSW and west respectively. In summer, the model flow is predominantly northerly. However, as already noted, in this season the large-scale atmospheric circulation is weak and ill-defined. It is therefore hardly surprising that the GCM fails to model the summer wind flow accurately. In the GISS GCM winter control run results (Fig. 1.21), the vector mean wind across the British Isles is from the southwest but this forms only a small part of a chaotic pattern over the total region shown in the figure. In the other seasons the mean flow is either from the north (spring, Fig. 1.27, and summer, Fig. 1.33) or indeterminate (autumn, Fig. 1.39).

From the above discussion, more credibility can be placed on the GFDL model results, whereas the GISS GCM appears to model the present-day wind field less accurately. Test region scenarios are presented for both models in this report, although in the discussion we have concentrated on the GFDL results.

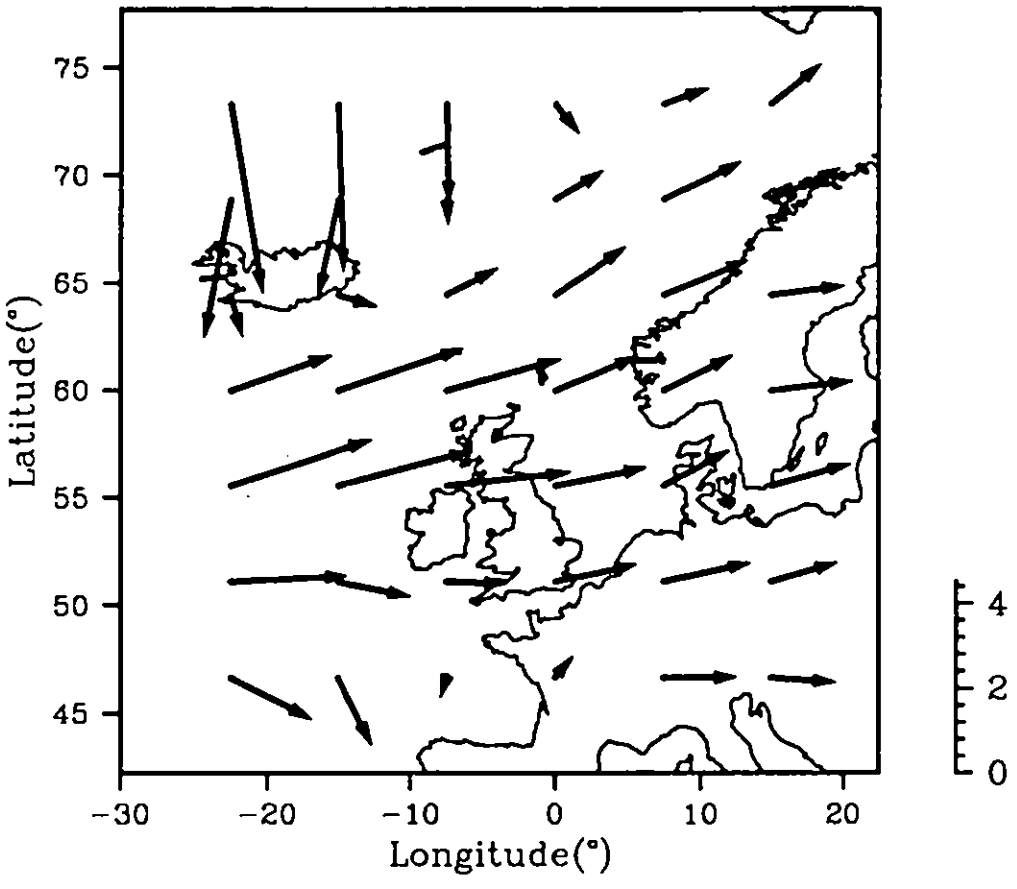

GFDL annual $1xCO_2$ vector mean wind speed (ms^{-1})

Fig. 1.12

Compact diagrams

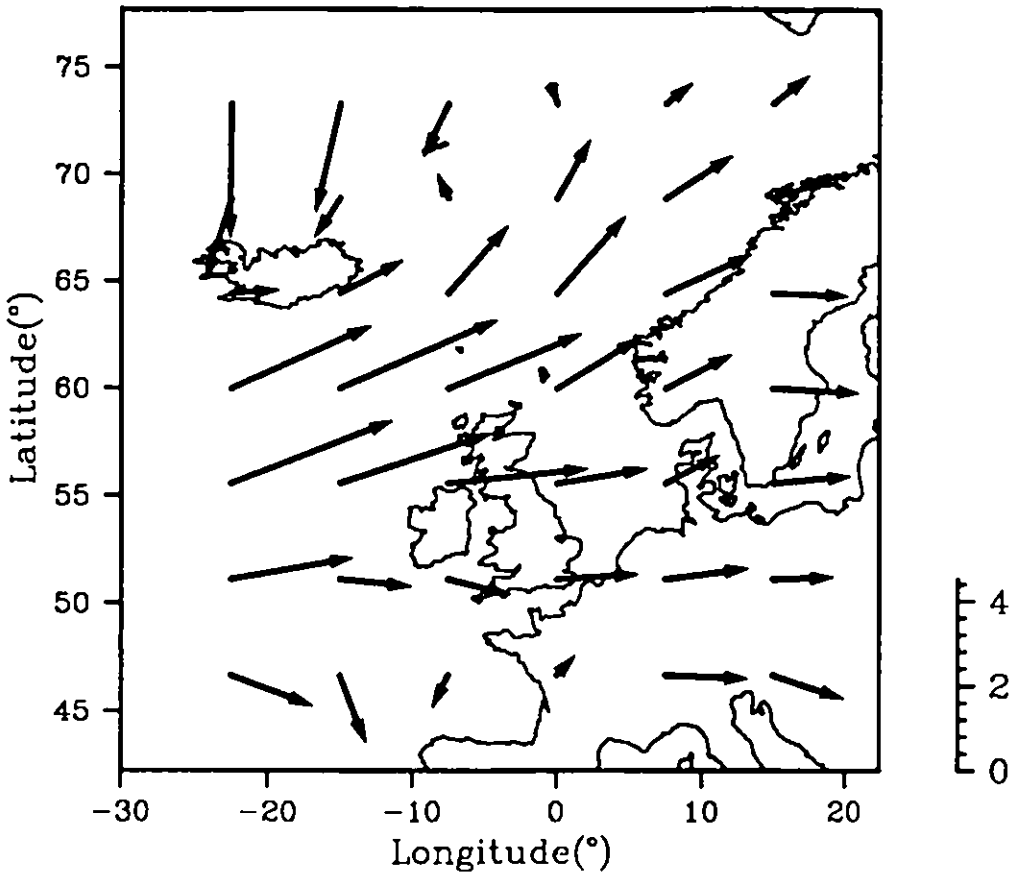

GFDL annual $2xCO_2$ vector mean wind speed (ms^{-1})

Fig. 1.13

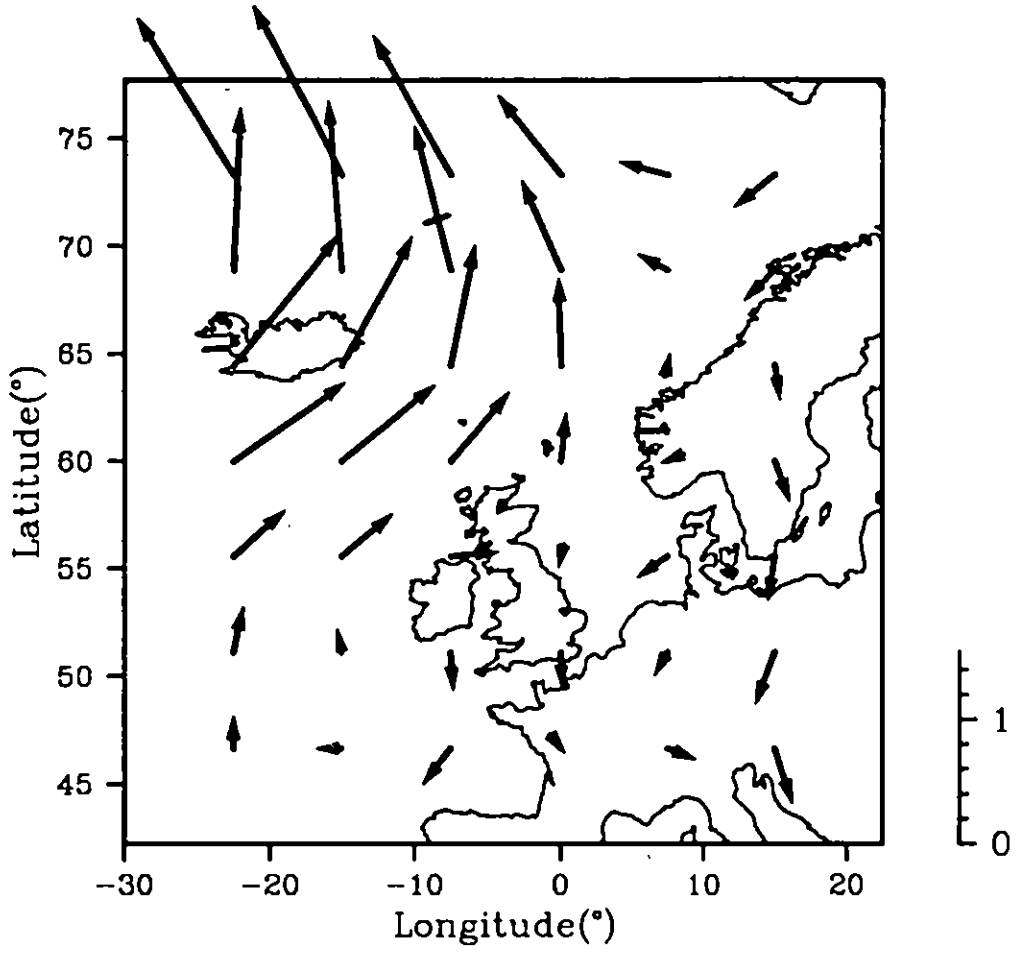

GFDL annual $2xCO_2-1xCO_2$ vector mean wind speed (ms^{-1})

Fig. 1.14

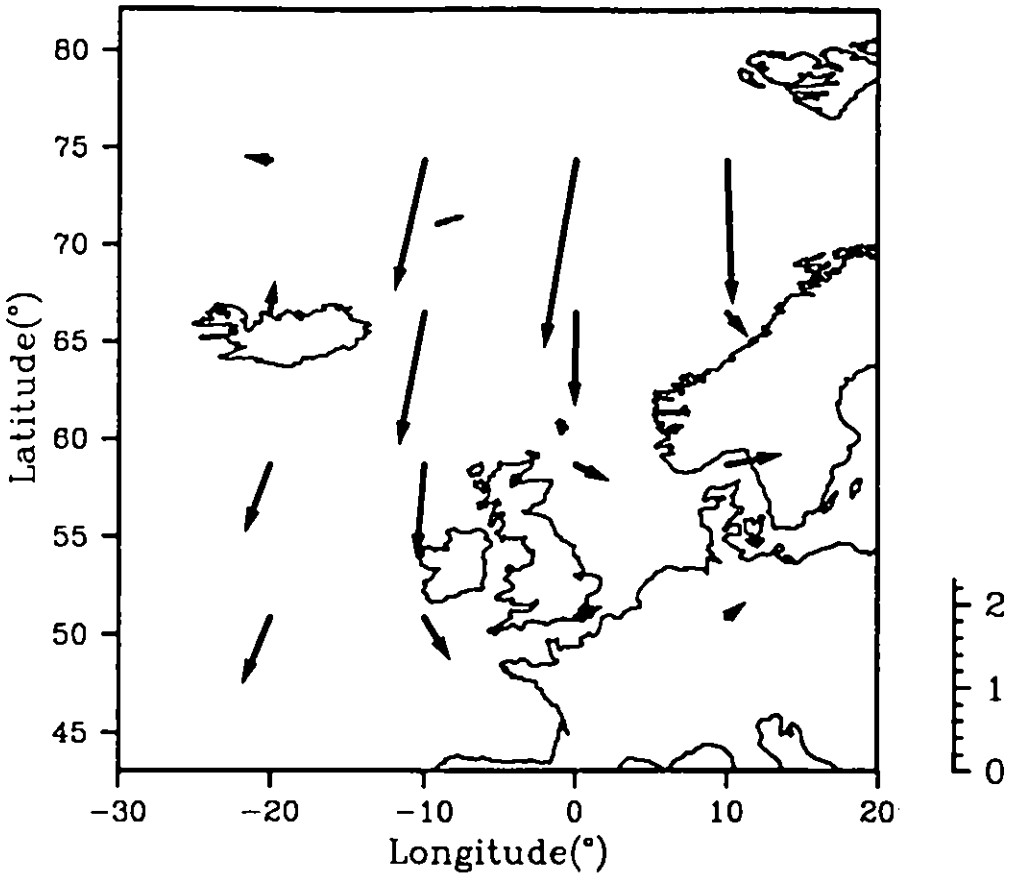

GISS annual $1xCO_2$ vector mean wind speed (ms^{-1})

Fig. 1.15

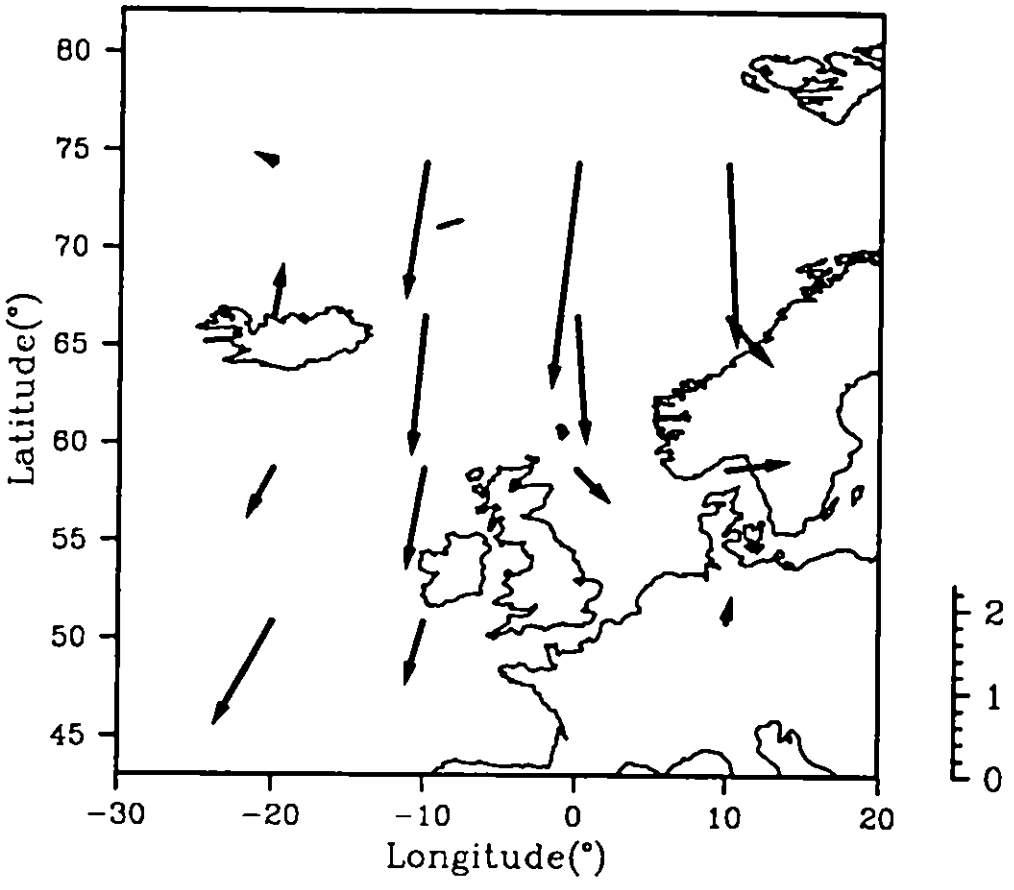

GISS annual $2xCO_2$ vector mean wind speed (ms^{-1})

Fig. 1.16

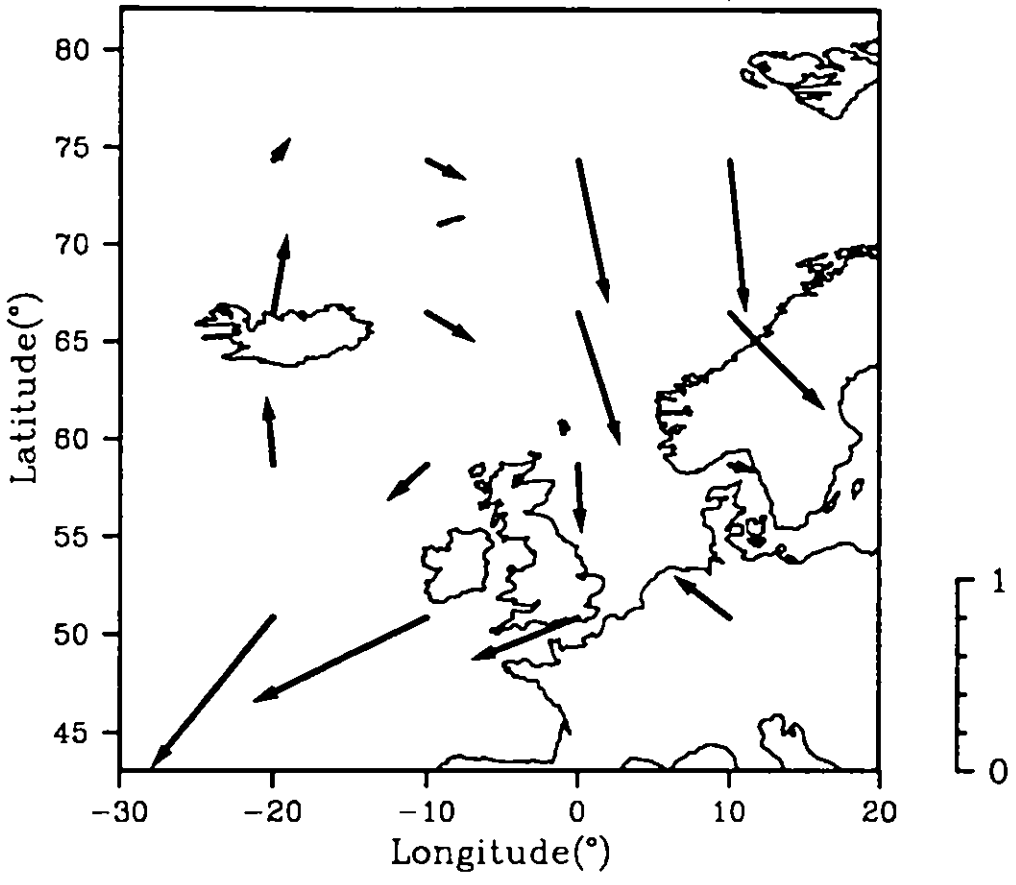

GISS annual $2xCO_2-1xCO_2$ vector mean wind speed (ms^{-1})

Fig. 1.17

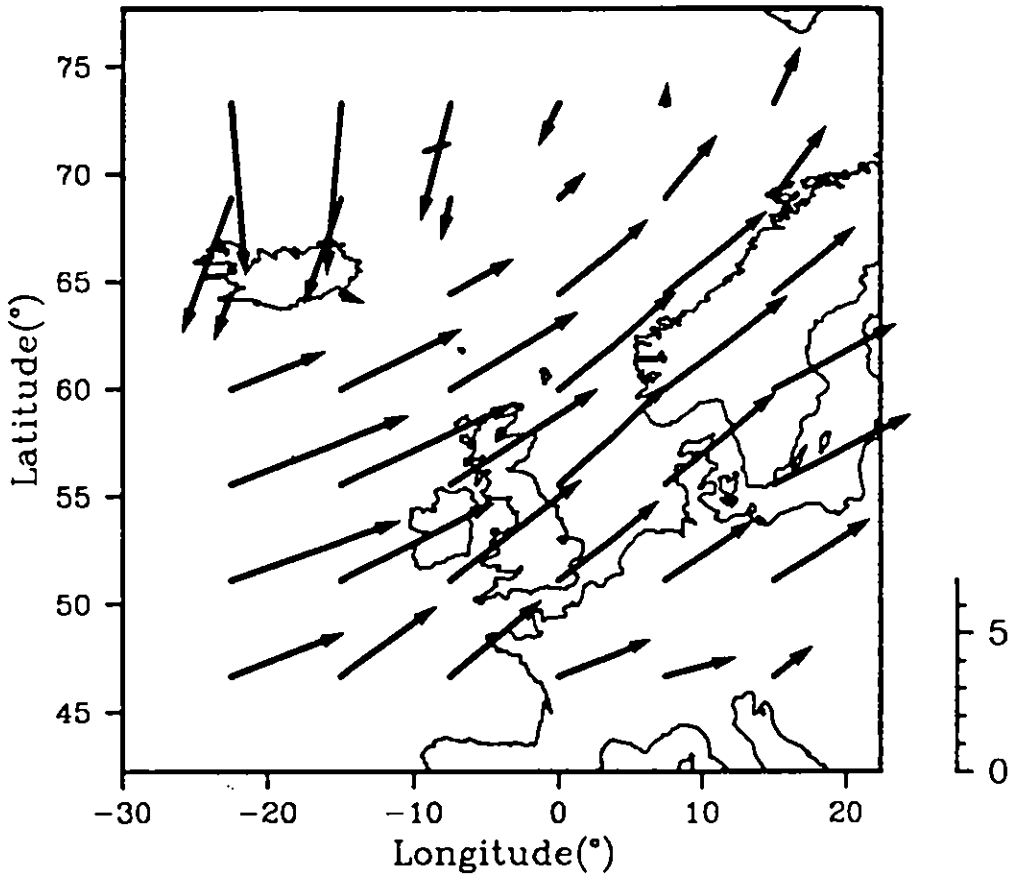

GFDL winter $1xCO_2$ vector mean wind speed (ms^{-1})

Fig. 1.18

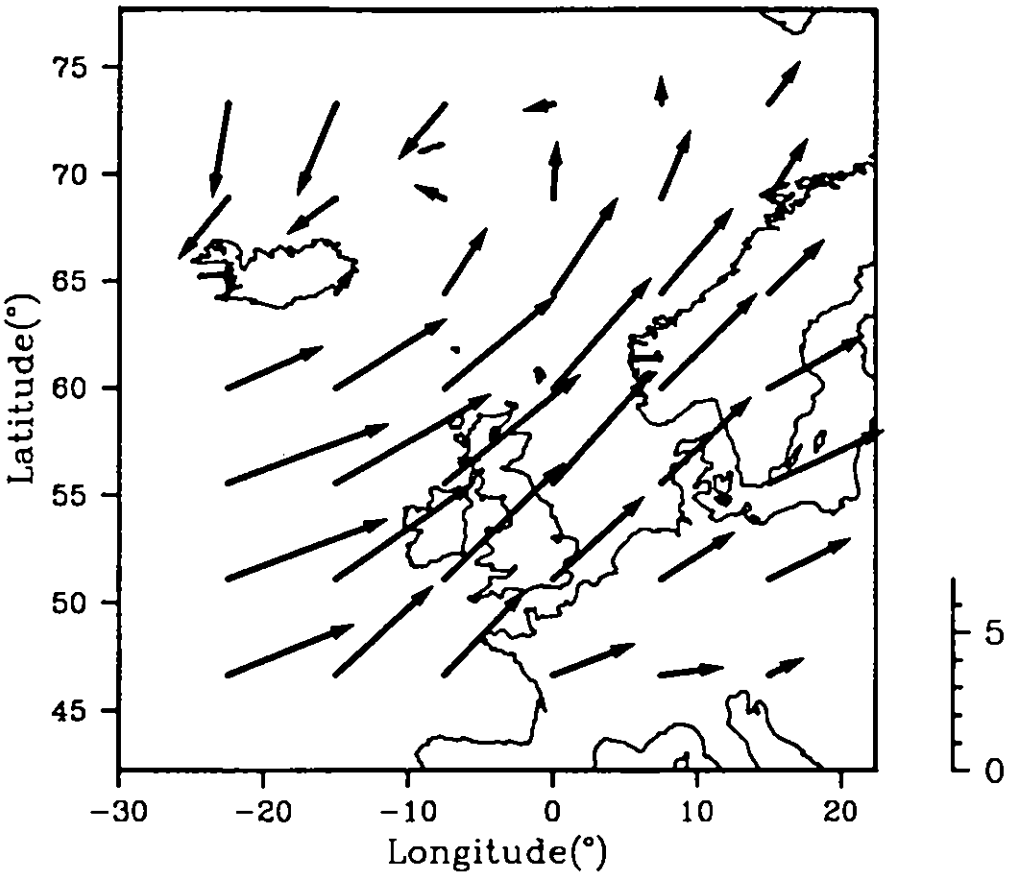

GFDL winter $2xCO_2$ vector mean wind speed (ms^{-1})

Fig. 1.19

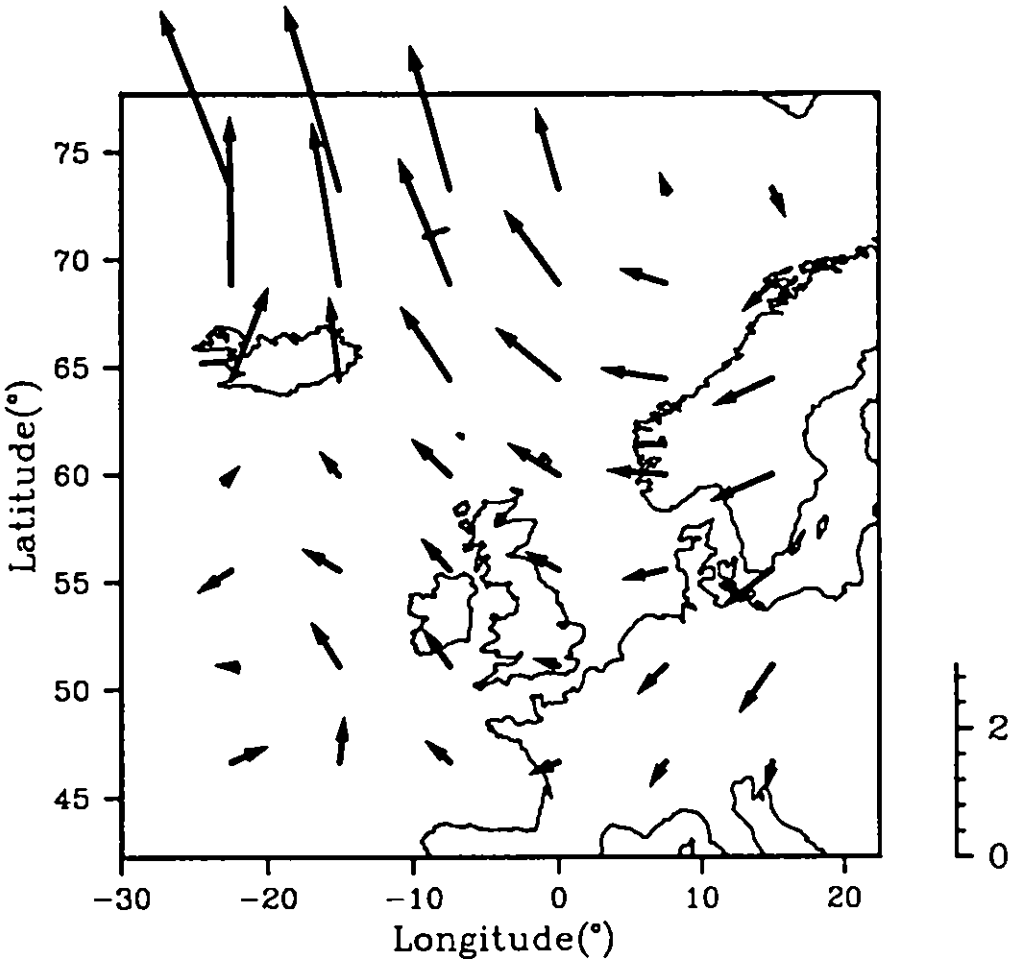

GFDL winter $2xCO_2-1xCO_2$ vector mean wind speed (ms^{-1})

Fig. 1.20

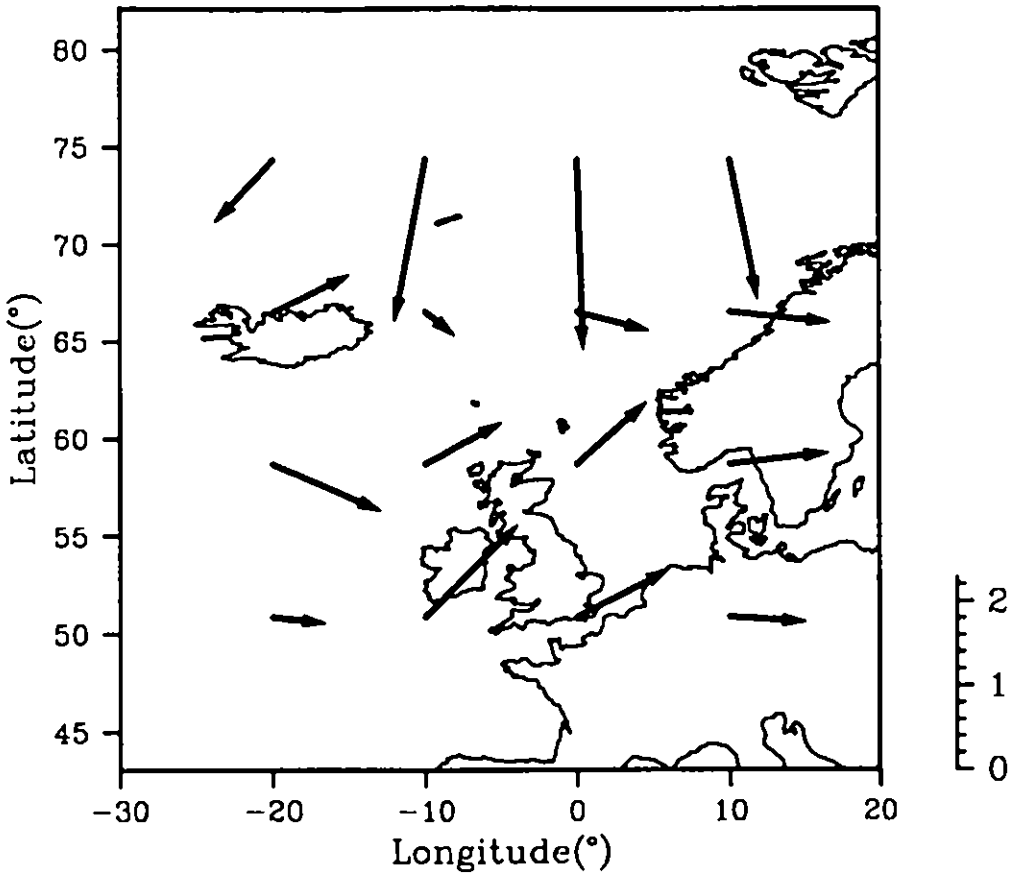

GISS winter 1xCO_2 vector mean wind speed (ms^{-1})

Fig. 1.21

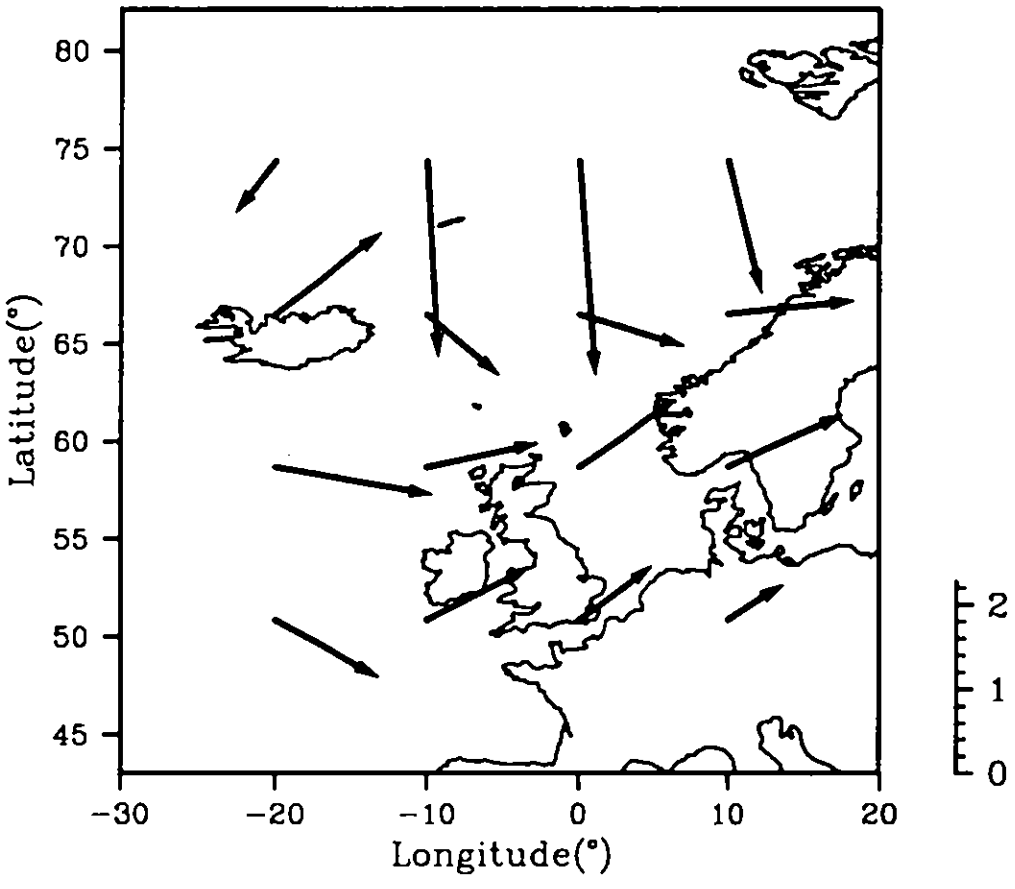

GISS winter $2xCO_2$ vector mean wind speed (ms^{-1})

Fig. 1.22

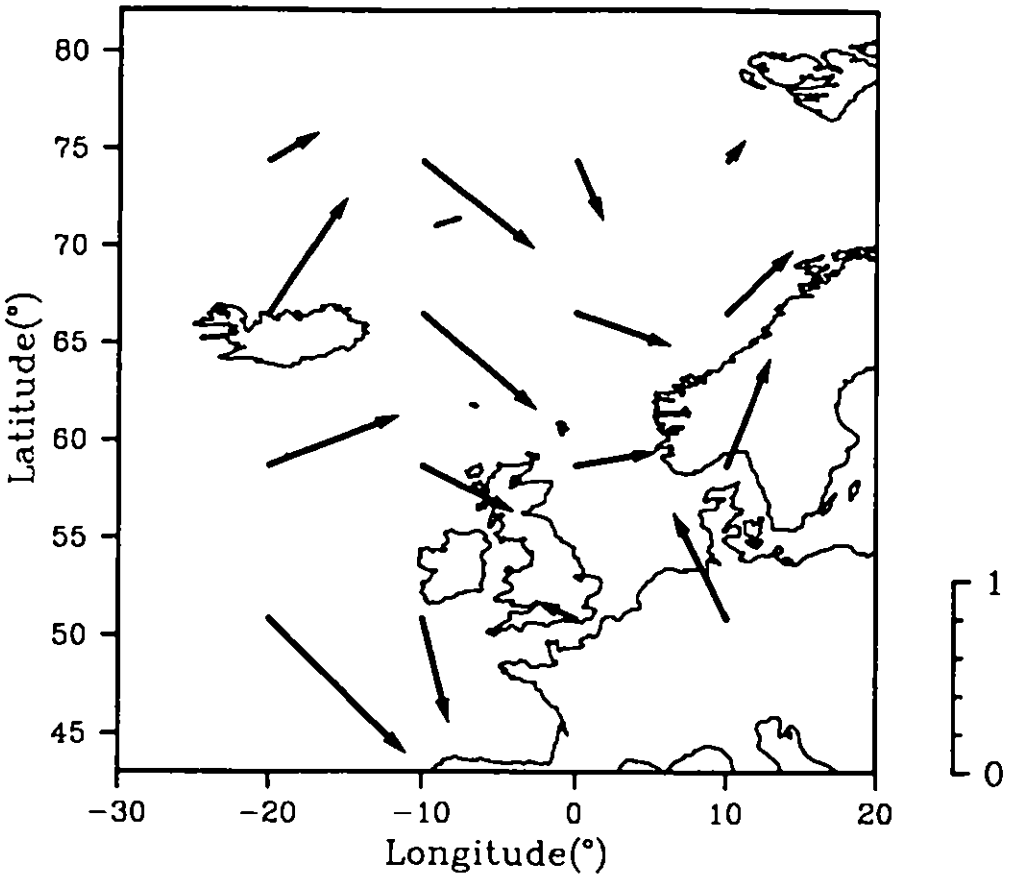

GISS winter $2xCO_2 - 1xCO_2$ vector mean wind speed (ms^{-1})

Fig. 1.23

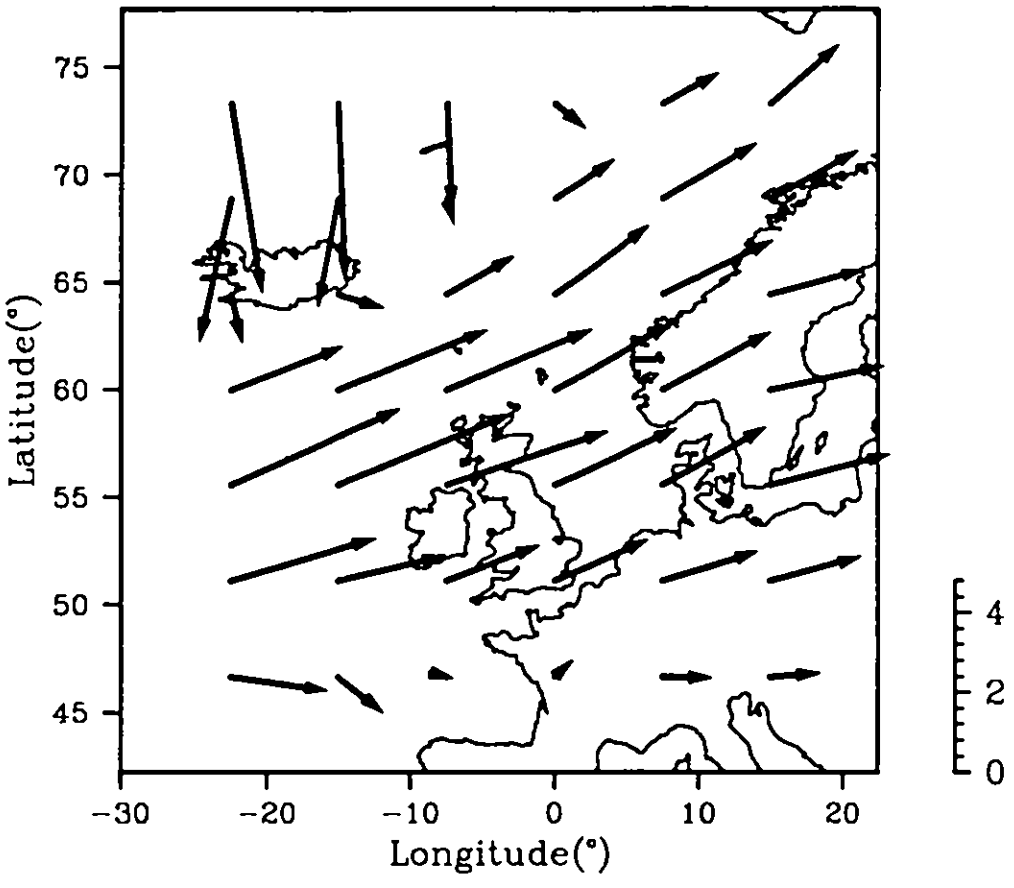

GFDL spring 1xCO_2 vector mean wind speed (ms^{-1})

Fig. 1.24

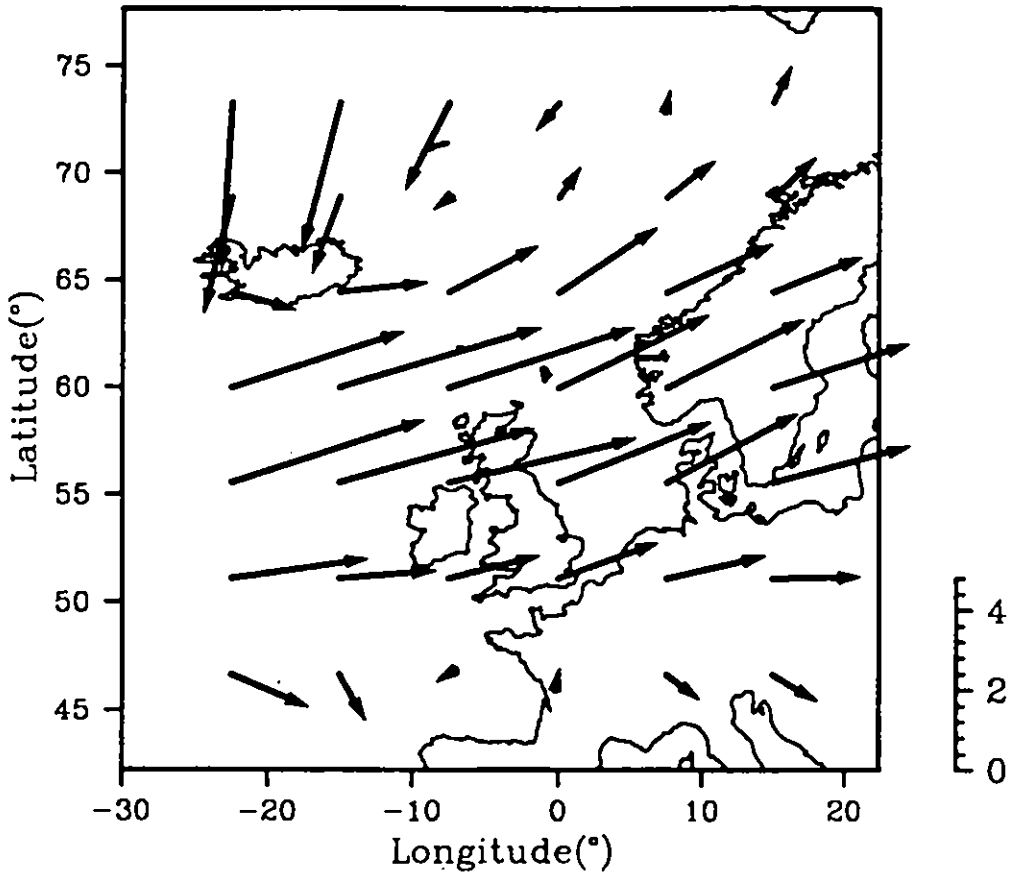

GFDL spring $2xCO_2$ vector mean wind speed (ms^{-1})

Fig. 1.25

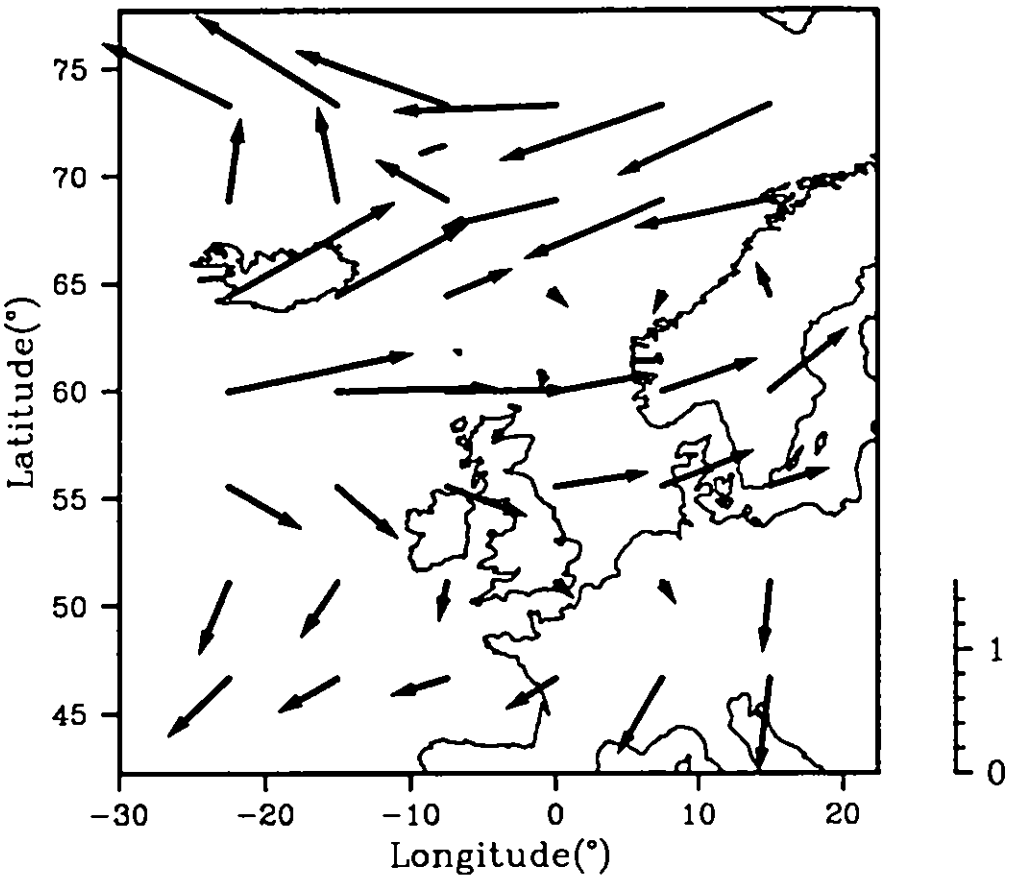

GFDL spring $2xCO_2-1xCO_2$ vector mean wind speed (ms^{-1})

Fig. 1.26

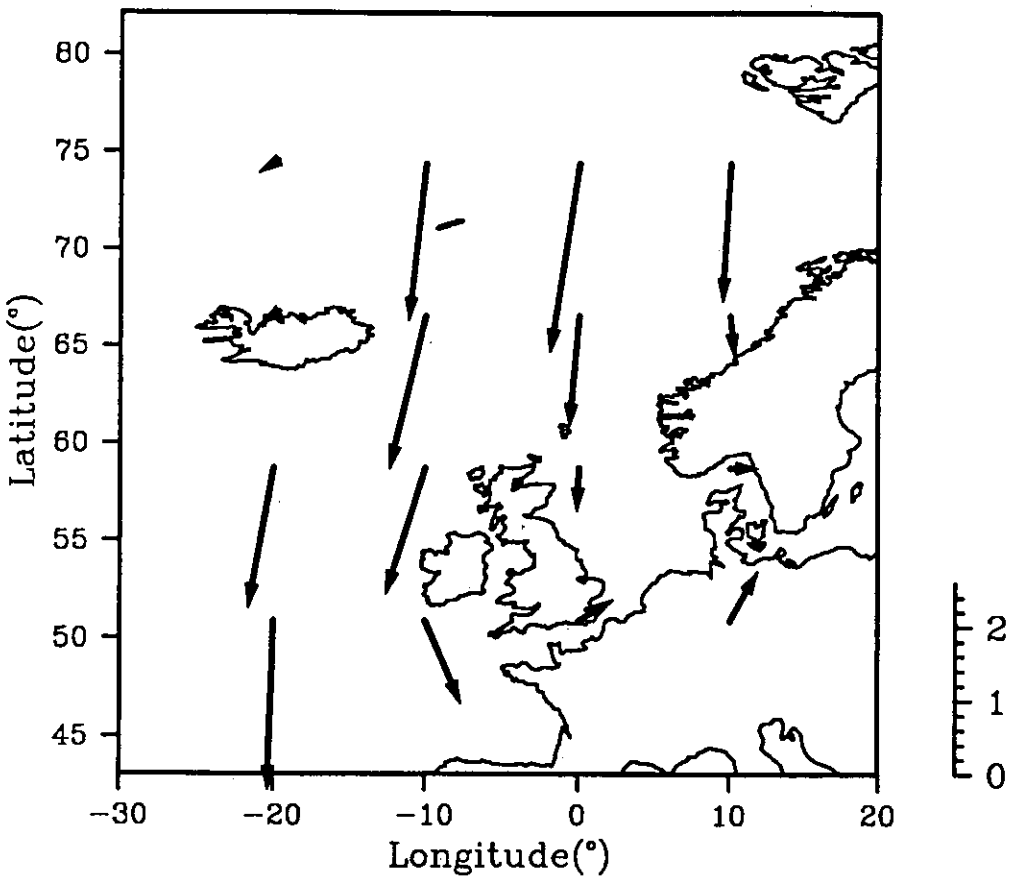

GISS spring 1xCO_2 vector mean wind speed (ms^{-1})

Fig. 1.27

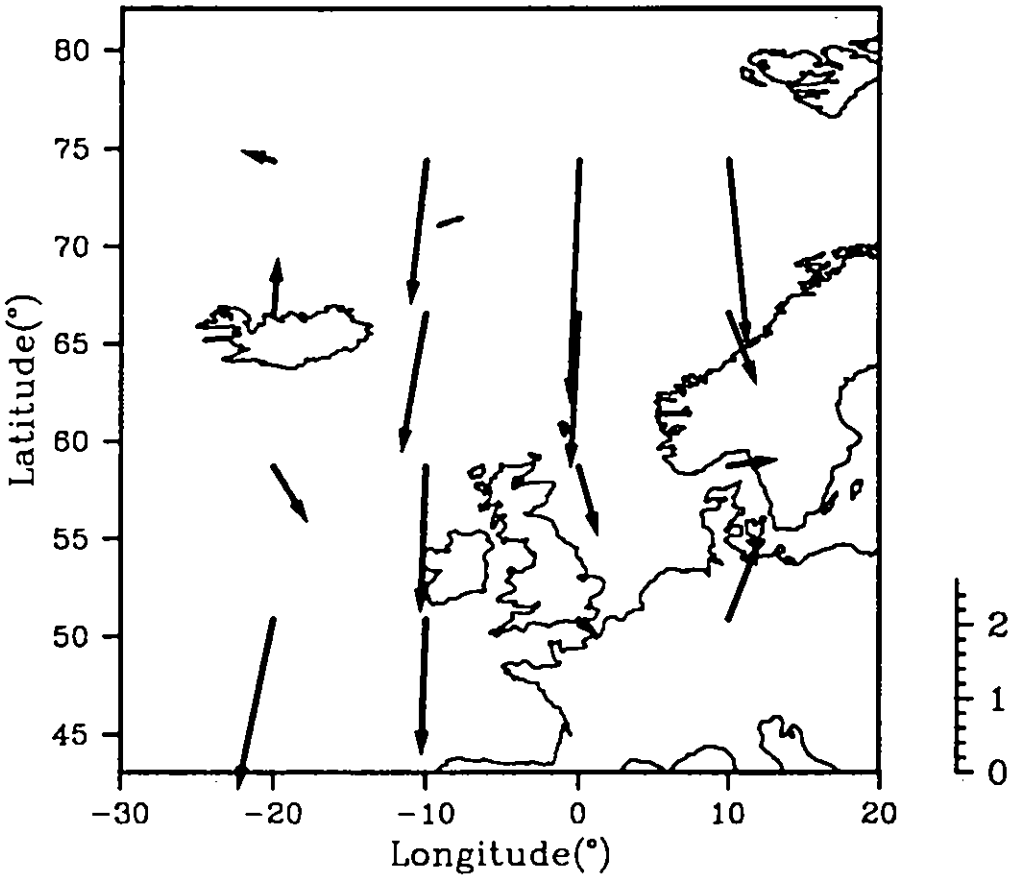

GISS spring $2xCO_2$ vector mean wind speed (ms^{-1})

Fig. 1.28

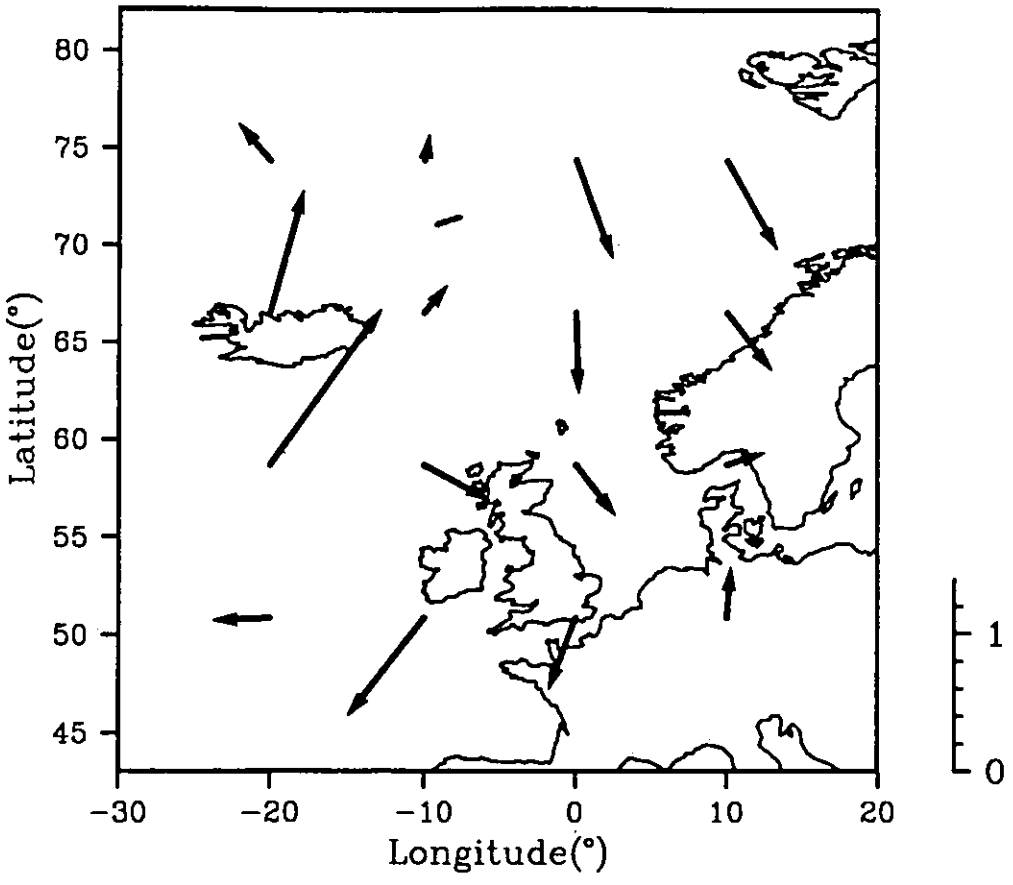

GISS spring $2xCO_2-1xCO_2$ vector mean wind speed (ms^{-1})

Fig. 1.29

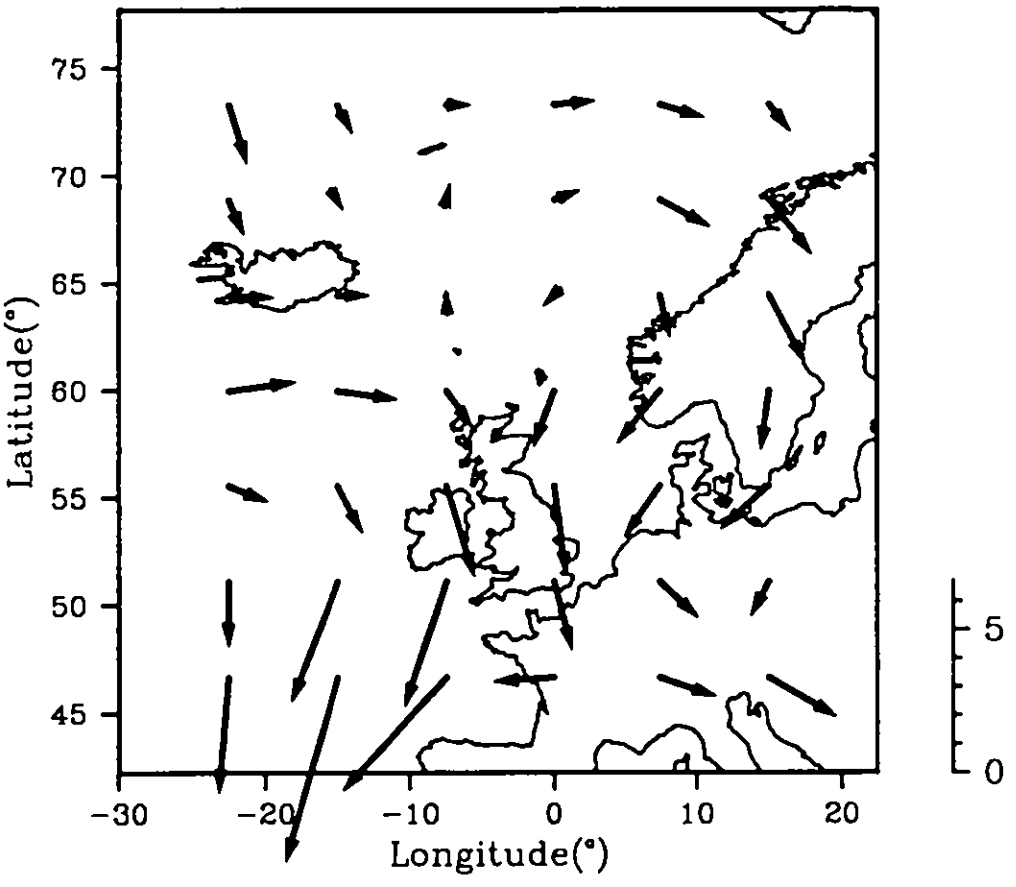

GFDL summer 1xCO_2 vector mean wind speed (ms^{-1})

Fig. 1.30

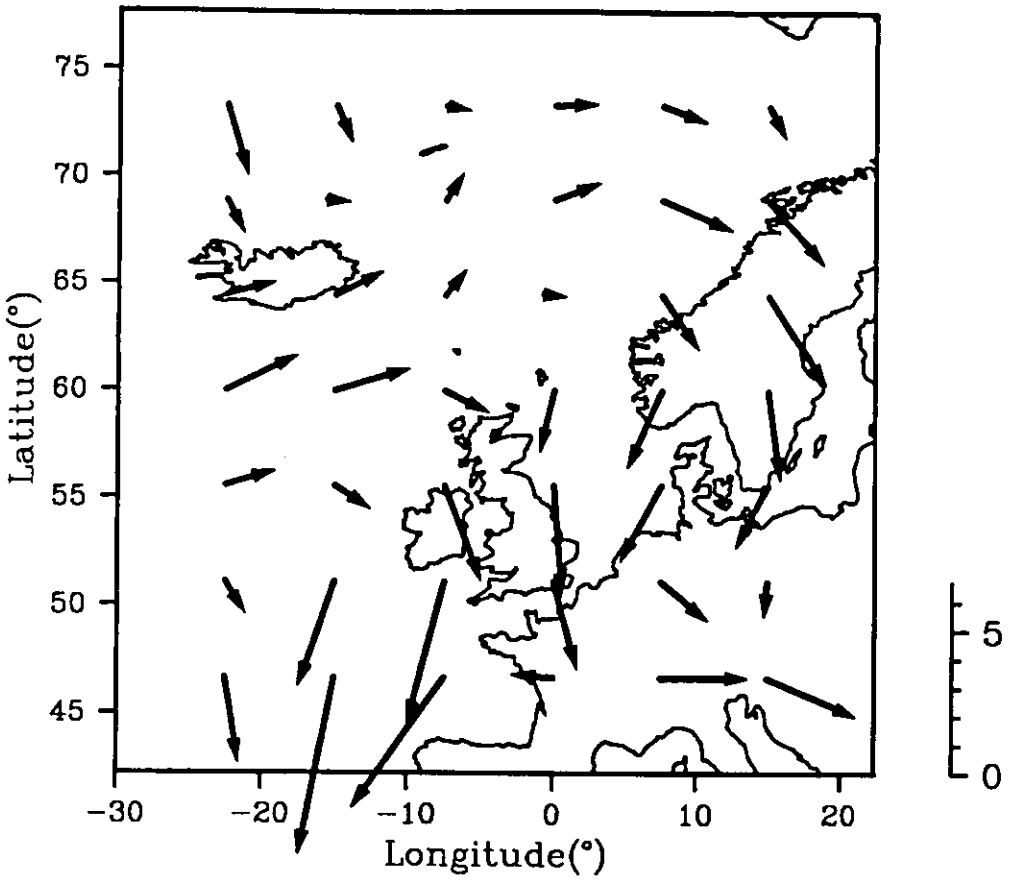

GFDL summer $2xCO_2$ vector mean wind speed (ms^{-1})

Fig. 1.31

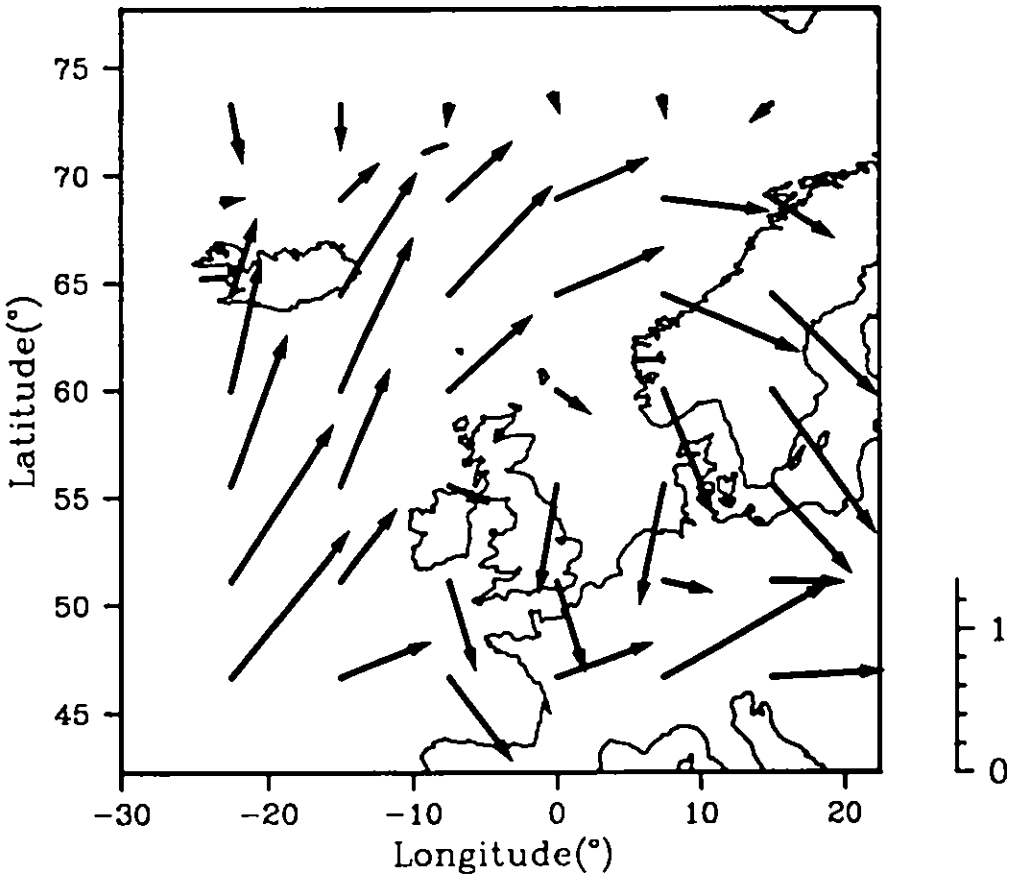

GFDL summer $2xCO_2-1xCO_2$ vector mean wind speed (ms^{-1})

Fig. 1.32

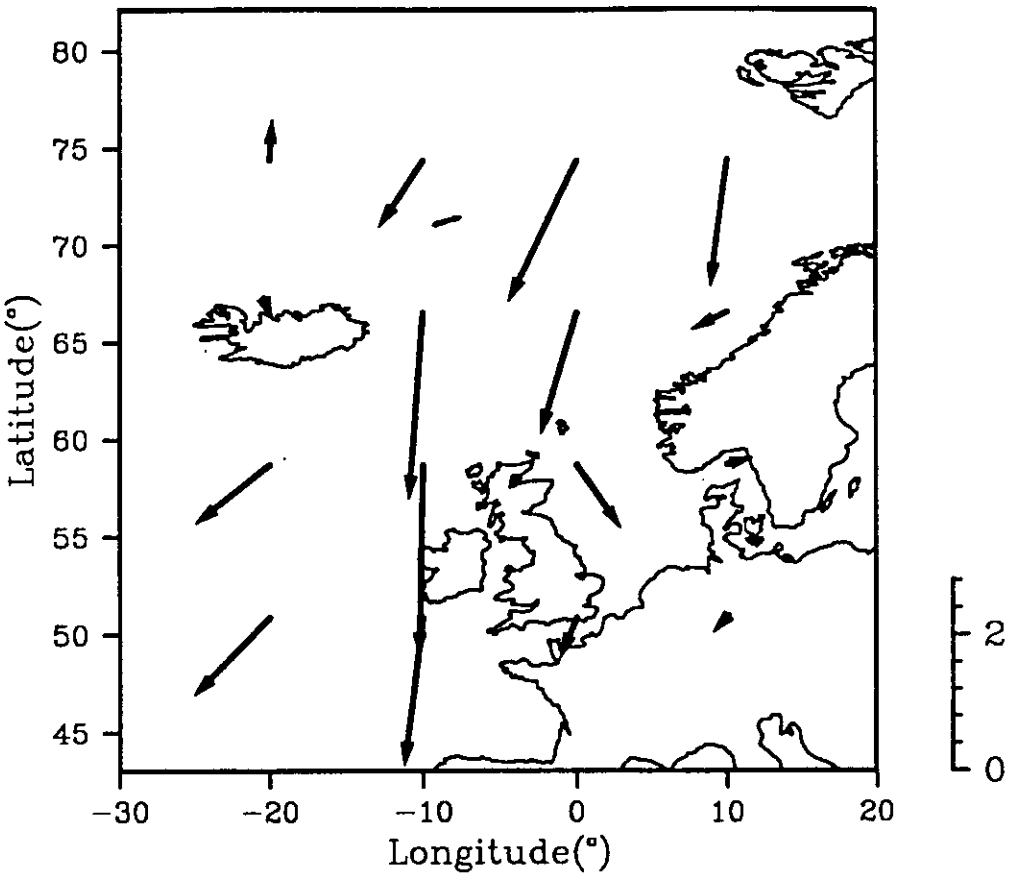

GISS summer 1xCO_2 vector mean wind speed (ms^{-1})

Fig. 1.33

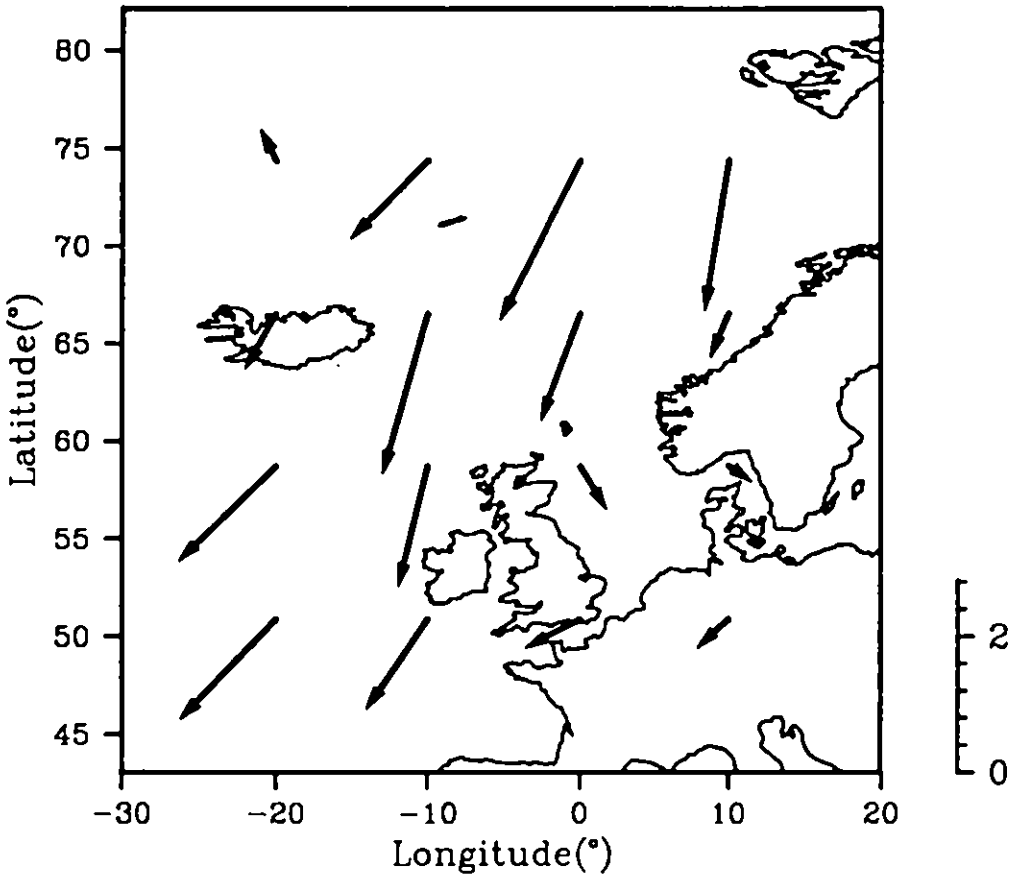

GISS summer $2xCO_2$ vector mean wind speed (ms^{-1})

Fig. 1.34

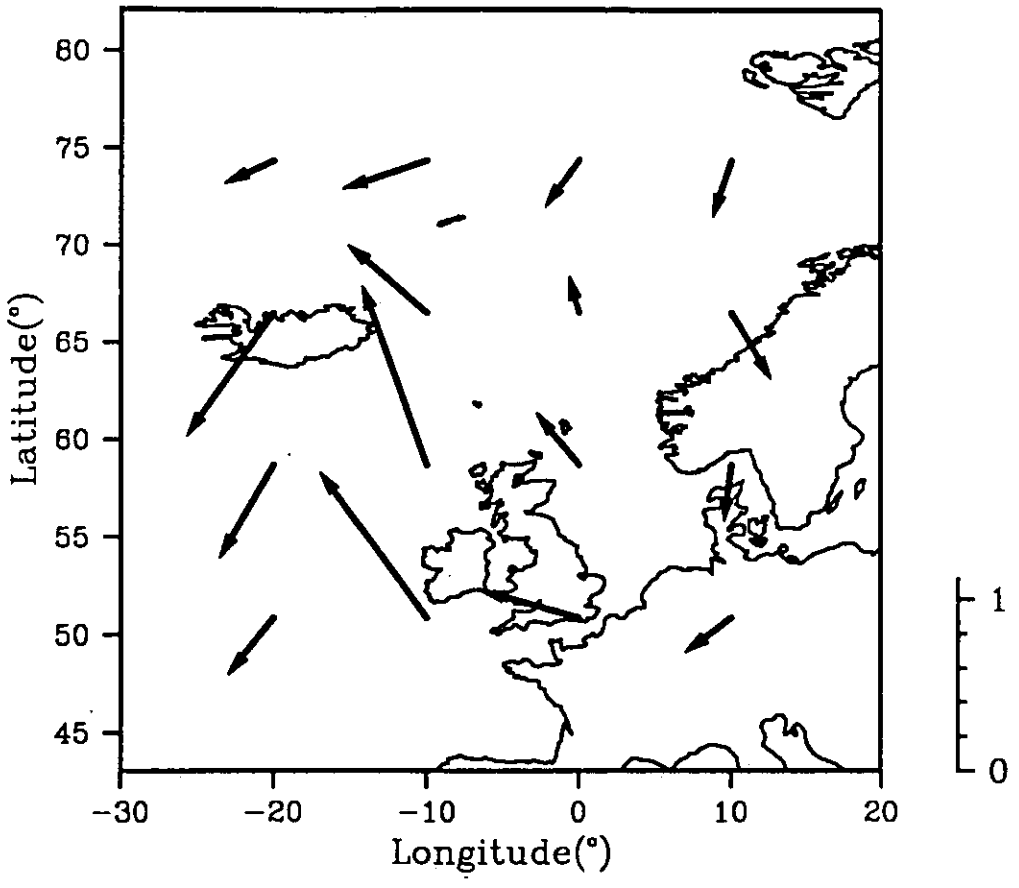

GISS summer $2xCO_2-1xCO_2$ vector mean wind speed (ms^{-1})

Fig. 1.35

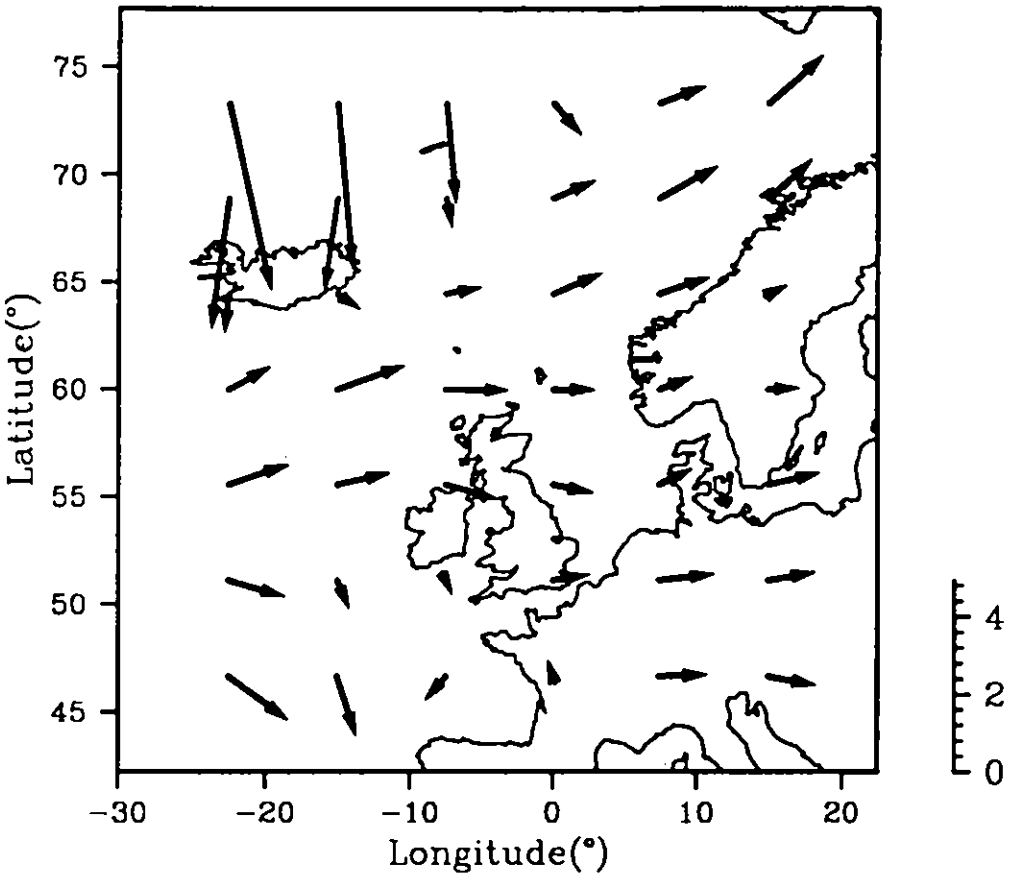

GFDL autumn 1xCO_2 vector mean wind speed (ms^{-1})

Fig. 1.36

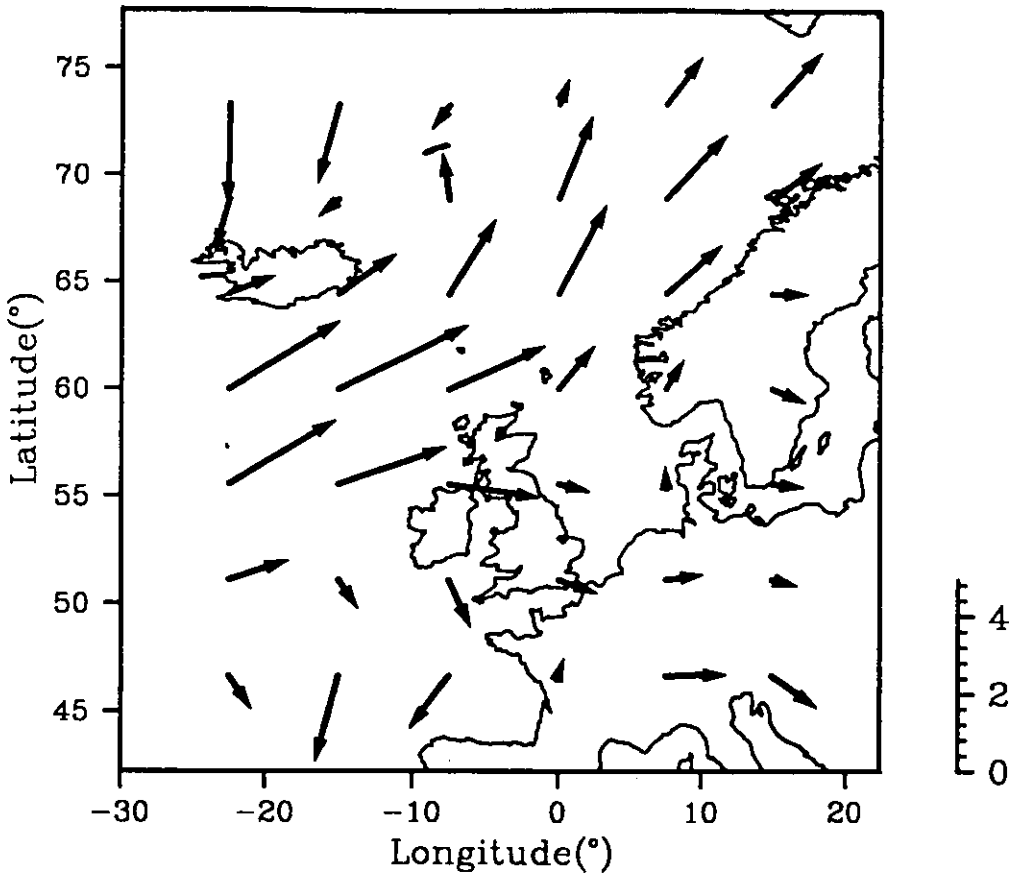

GFDL autumn $2xCO_2$ vector mean wind speed (ms^{-1})

Fig. 1.37

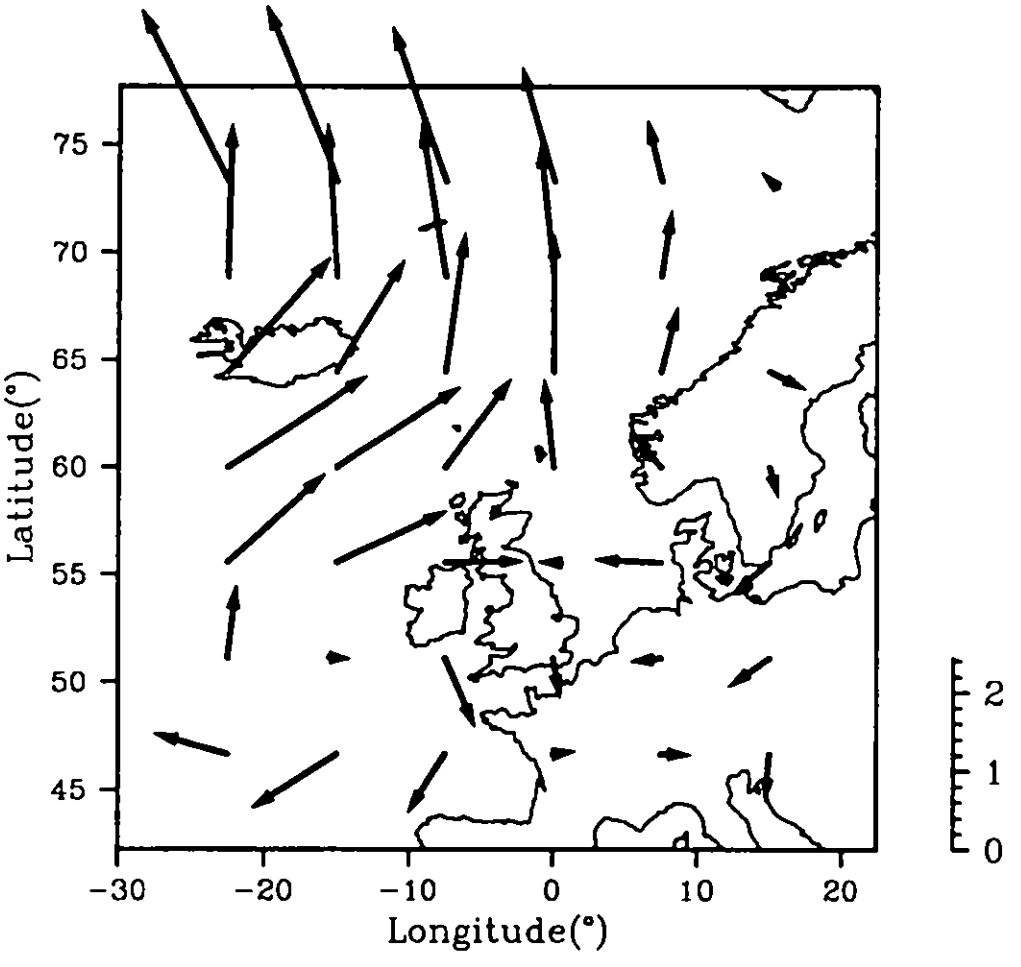

GFDL autumn $2xCO_2-1xCO_2$ vector mean wind speed (ms^{-1})

Fig. 1.38

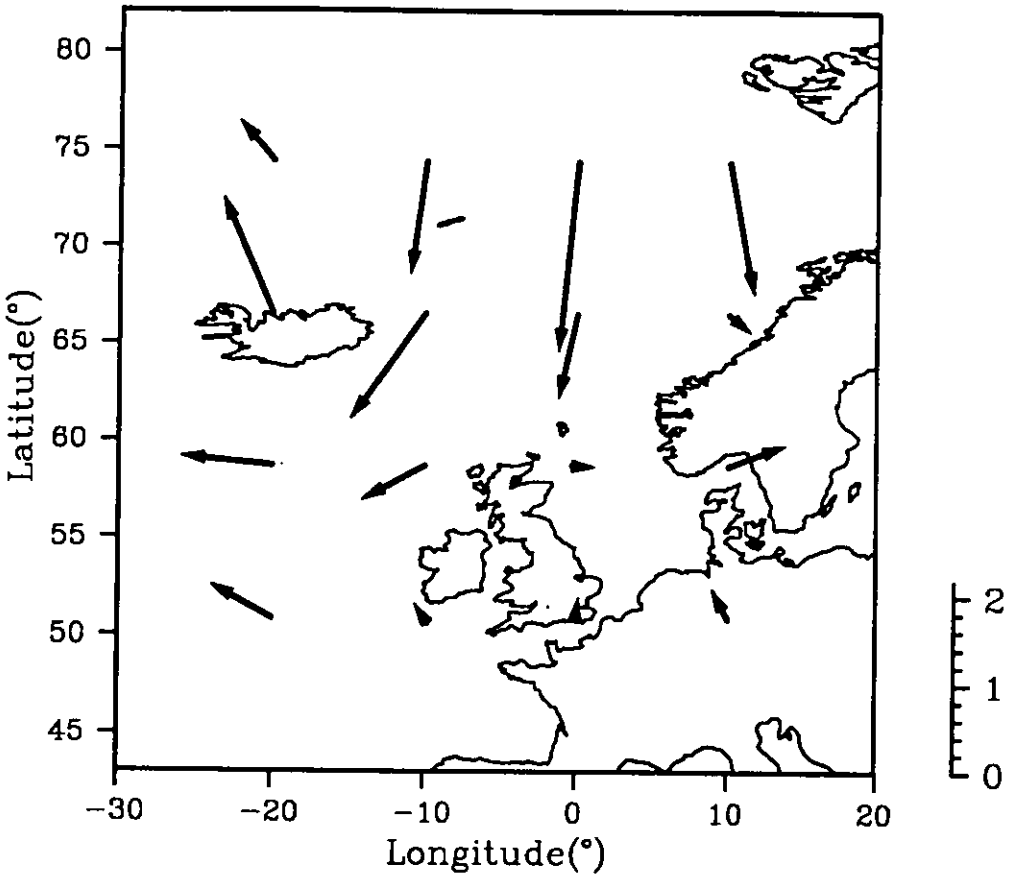

GISS autumn 1xCO_2 vector mean wind speed (ms^{-1})

Fig. 1.39

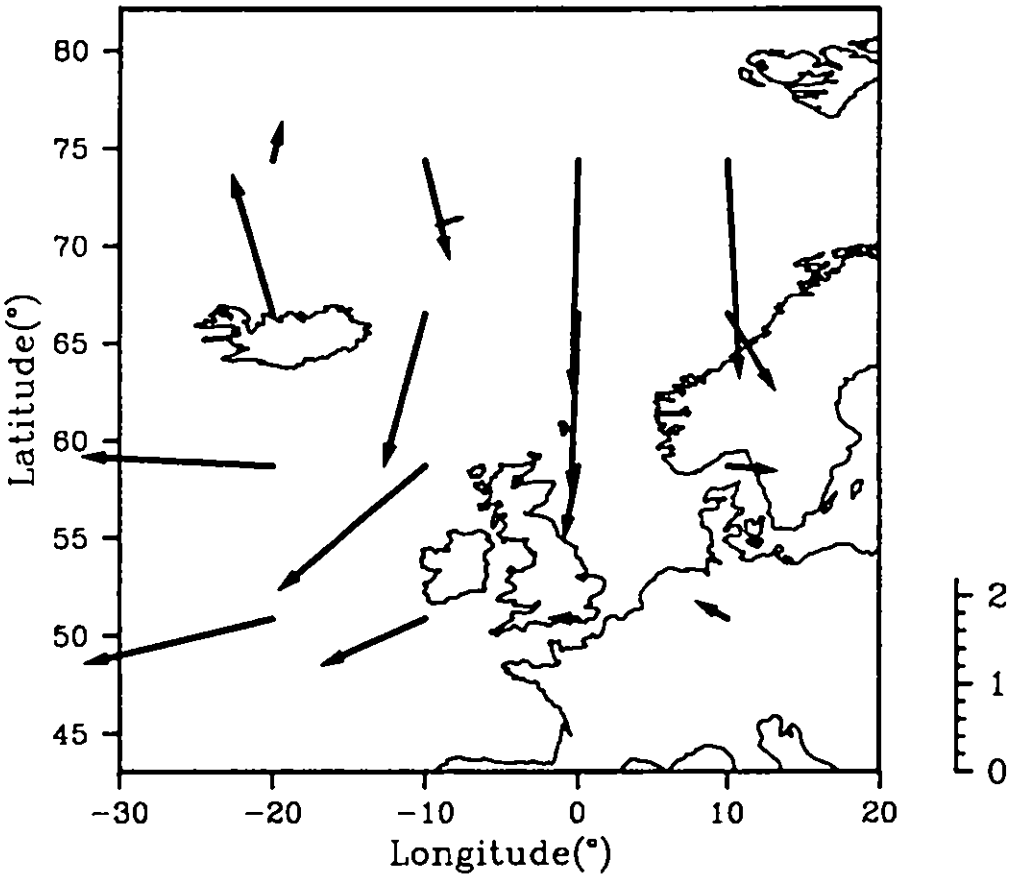

GISS autumn $2xCO_2$ vector mean wind speed (ms^{-1})

Fig. 1.40

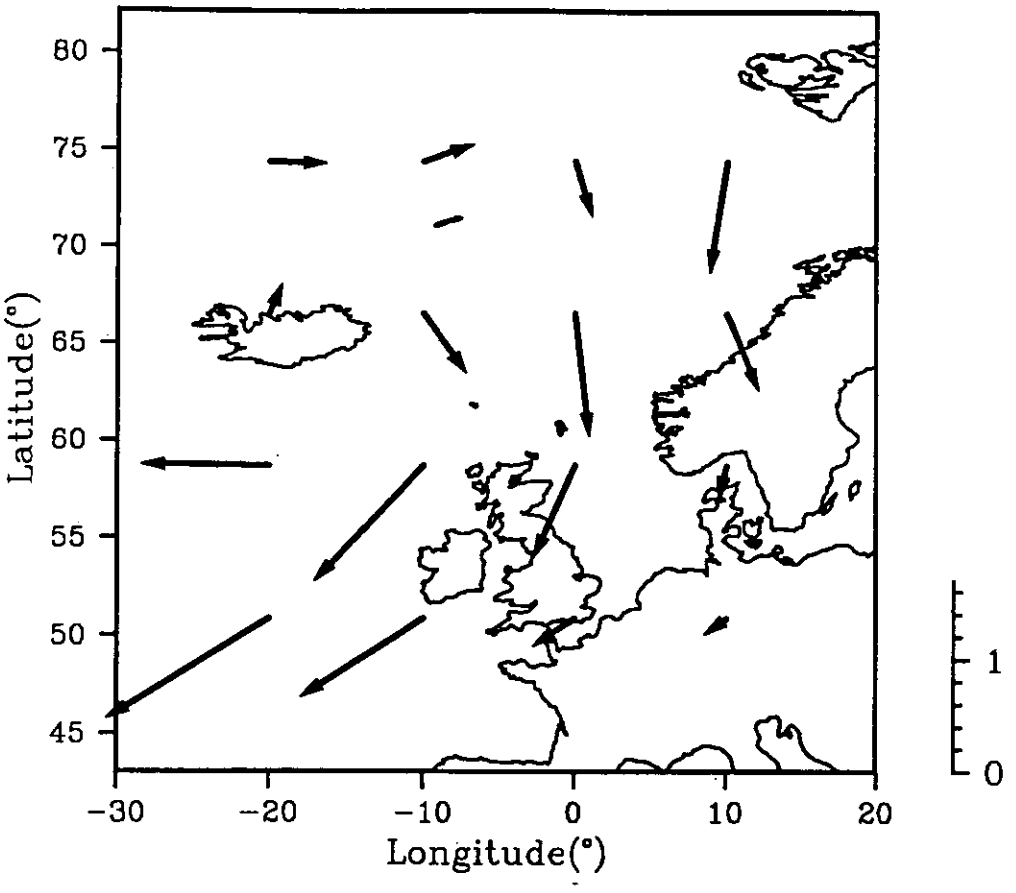

GISS autumn $2xCO_2-1xCO_2$ vector mean wind speed (ms^{-1})

Fig. 1.41

Sometimes too many adjectives, sometimes too few

3.4.1 The Northern Pennines

The map of present-day variations in annual mean wind speed over this test region, as modelled by CONFORM, is shown in Fig. 1.42. The model was initialized with 1971 data from Great Dun Fell and Moor House. The grid resolution was 200m by 200m. Clearly the initial state will affect the ultimate prediction of wind speed changes in a high-CO_2 world. It is therefore important that 1971 should be a 'typical' year in the context of long-term conditions. Fig. 1.43 shows the annual mean wind speeds at Great Dun Fell and Moor House for the period 1971-79. It can be seen that, whereas at Great Dun Fell the 1971 mean was slightly below the nine year average, at Moor House the year was slightly windier than normal. Therefore, the modelled present-day wind field for this test region, based on 1971 data, should be representative. In Fig. 1.42, wind speeds are clearly related to relative altitude (see Fig. 1.9), ranging from less than 7ms^{-1} in the low-lying southwest section of the map, to over 11ms^{-1} on the highest summit. Presumably this is because CONFORM recognises that GDF and MTH are exposed sites subject to overspeeding. How would they have coped if more data had been available?

It should be noted that in all the contour maps presented here the upper and lower categories are no wider than the intermediate categories. Thus, in Fig. 1.42, the intermediate categories are 0.9ms^{-1} wide. The wind speed in those areas shaded in the highest wind speed category will therefore not exceed 12.3ms^{-1}, and the wind speed in those areas shaded in the lowest category will not be less than 6.1ms^{-1}.

Seasonal patterns are shown in Fig. 1.44. Wind speeds in autumn and winter are substantially higher than those in spring and summer, but the spatial patterns are broadly the same throughout the year.

The results of imposing the 2xCO_2 perturbation from the GFDL GCM on the present-day wind field are displayed in Figs. 1.45-1.49 for the year as a whole and for each season. The left-hand side of each figure shows the 2xCO_2 wind field and the right-hand side shows the 2xCO_2-1xCO_2 difference. The annual differences are small, indicating a slight increase in wind speeds of not more than 0.3ms^{-1}

anywhere in the test region. The trend in winter is for a slight reduction in wind speeds, whereas the other three seasons generally show windier conditions. The greatest change is in autumn, when an increase of between 0.5ms^{-1} and 1.0ms^{-1} is indicated. As shown by Fig. 1.50, this represents an increase of between 5% and 9%. The highest actual changes are found over hill tops and just below the summits on slopes facing the prevailing wind. Highest percentage changes are concentrated in the same areas.

The GISS model results (Fig. 1.51-1.55) are almost the exact opposite of the GFDL GCM results. A slight decrease in annual wind speeds in a high-CO_2 world is suggested. This reduction is present in all seasons except winter, when a small increase occurs. The greatest change is found in autumn: a fall of up to 0.6ms^{-1} in the mean wind speed over the highest summits of the test region.

3.4.2 The Devon test region

Present-day wind speed patterns modelled by CONFORM for this region (based on 1985 data) are shown in Figs. 1.56-1.57. The grid resolution of the model in this case was 1km by 1km. Wind speeds in this area are considerably lower than those recorded in the Northern Pennines. In order to assess the representativeness of 1985 in the context of the long-term picture, we have examined annual mean wind speeds for the 1975-1985 period for Exeter (Fig. 1.58).

The changes due to a CO_2 forcing, as indicated by the GFDL GCM, are shown in Figs. 1.59-1.63. Over the year as a whole, a small increase in wind speeds is suggested, generally less than 0.1ms^{-1}. This increase is present in all four seasons of the year. The greatest absolute changes are seen in winter and spring, achieving over 0.2ms^{-1} in some parts of the test region.

The GISS model results (Figs. 1.64-1.68) indicate a small negative change at the annual level in a high greenhouse gas world over the Devon test region. A slight decrease in wind speeds in the winter and summer seasons is balanced by a slight increase in spring and autumn. The greatest change is manifest in the

summer, when a substantial area of the test region is predicted to experience a decrease in wind speeds of around $0.2ms^{-1}$.

3.4.3. Shetland Main Island

The Shetland test region was modelled by CONFORM using a 350mx350m grid. The period for which data were available for construction of the present-day wind field (Fig. 1.69-1.70) was May to December 1986. In Fig. 1.70, therefore, spring is represented only by data from May, and winter by data from December. Annual wind speeds in Shetland are of the same order as those observed in the Northern Pennines test region. In Fig. 1.70, highest wind speeds are shown in the winter (December only) and autumn seasons. The low values in spring are probably due to the fact that the windiest months of this season (March and April) are missing in this analysis. The annual mean wind speeds for the period 1957-86 for Lerwick, one of the three anemometer sites in the test region, are shown in Fig. 1.71. The annual mean wind speed in 1986 was slightly above the long-term mean.

The $2xCO_2$-$1xCO_2$ changes in the wind field, and the $2xCO_2$ wind speeds, are shown for the GFDL GCM in Figs. 1.72-76. In these scenarios, the spring season changes are calculated by comparing GCM ouput for May with the May observed data, and the winter changes calculated by comparing December GCM output with December observations. The changes at the annual level are quite small, less than $+0.3ms^{-1}$. However, lower wind speeds are indicated in winter (up to $-0.3ms^{-1}$) and summer (up to $-0.2ms^{-1}$). A small positive change is suggested in spring, over most of the test region less than $0.2ms^{-1}$. The greatest change is found in autumn: at least $+0.4ms^{-1}$ everywhere in the test region, rising to almost $+1.0ms^{-1}$ in places. The autumn changes are expressed as a percentage change in Fig. 1.77, which shows increases of between 4% and 8% across the test region.

Figs. 1.78-1.82 show the GISS GCM-based results for $2xCO_2$ and $2xCO_2$-$1xCO_2$. The annual changes are very small. A positive change of up to $0.2ms^{-1}$ in

offset by lower wind speeds in the other three seasons, up to a maximum of between -0.2ms^{-1} and -0.3ms^{-1}.

3.5 Conclusions

We have used the vector mean wind speed output from the GFDL and GISS GCMs with the boundary-layer model CONFORM to construct regional scenarios of the change in the wind field due to the greenhouse effect. Three test regions have been investigated: the Northern Pennines, Devon and the Main Island of Shetland.

The results from the two GCMs are not always consistent with regard to the sign of the change. When we compare the vector mean wind field for the 1xCO_2 simulation with present-day conditions, the GFDL model results are clearly superior to those produced by the GISS GCM.

For the Northern Pennines, the GFDL GCM and CONFORM indicate an increase in wind speeds due to the greenhouse effect in all seasons except winter. The greatest increases are seen in the autumn, between +0.3ms^{-1} and +0.7ms^{-1}. When expressed as a percentage, this represents a 5-8% increase, with the greatest change experienced over hill tops and just below the summits on slopes facing the prevailing wind. Changes of a similar sign and magnitude are indicated for Shetland, except in summer when wind speeds show a slight drop. The greatest increase is again in the autumn, of between 4% and 8%. Little change is indicated for the Devon test region.

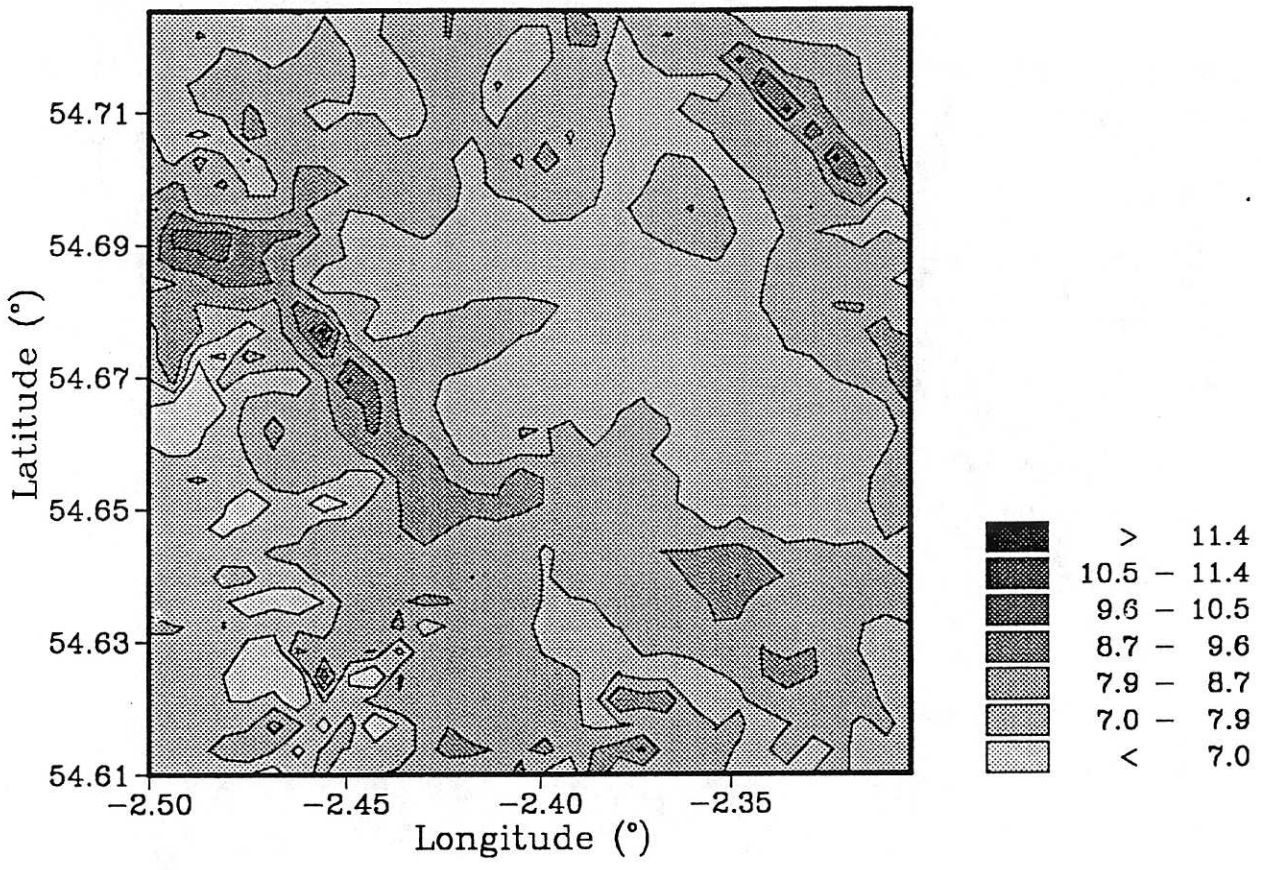

Fig. 1.42 Present-day annual mean wind speeds (ms^{-1}) in the Northern pennines, as modelled by CONFORM.

Should be plotted as a histogram!

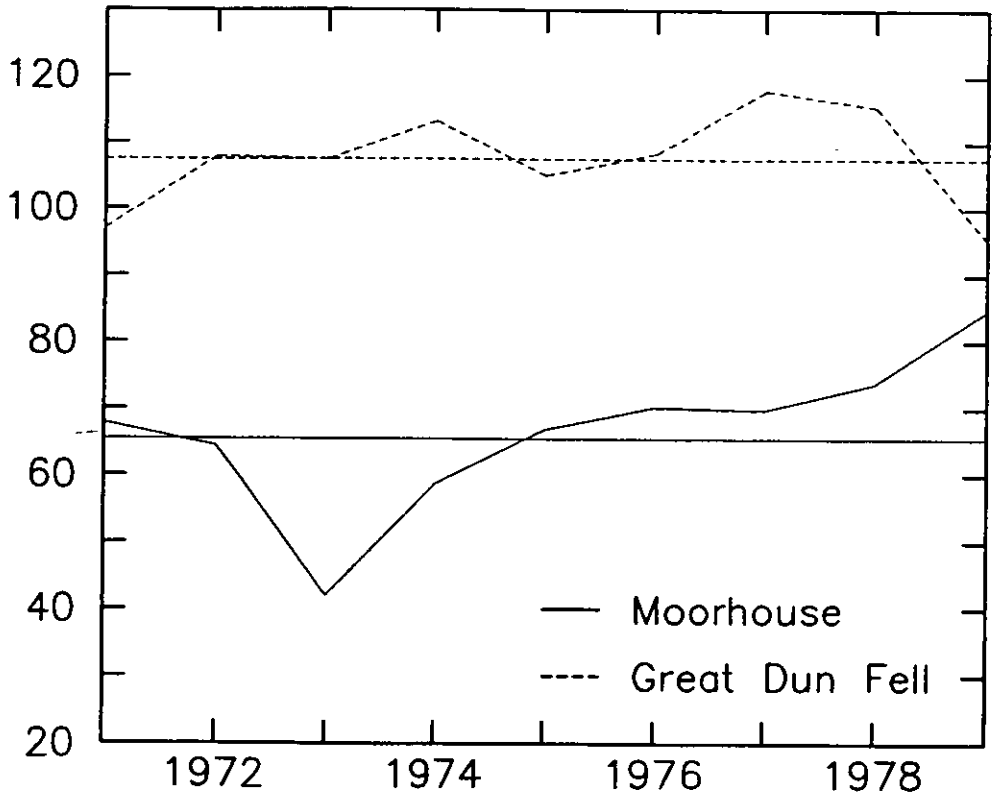

Fig. 1.43 Annual mean wind speeds (tenths ms^{-1}) at Great Dun Fell and Moor House, 1971-79.

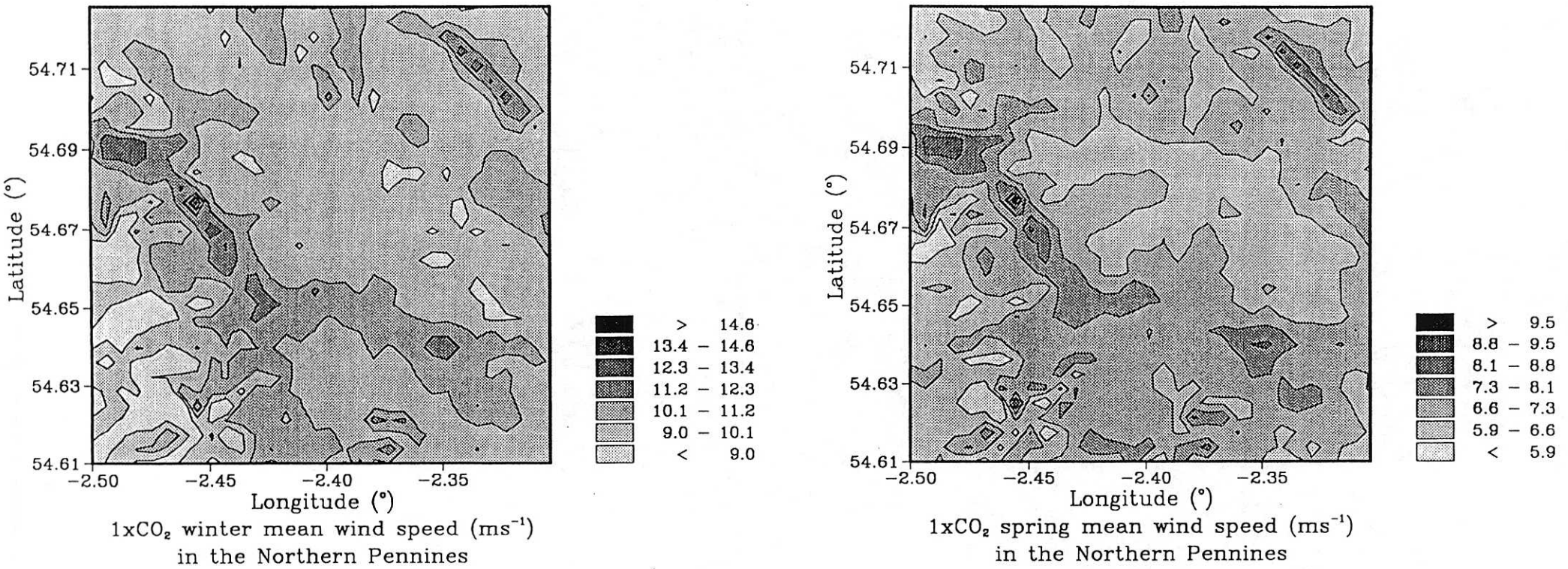

Fig. 1.44 Present-day seasonal mean wind speeds (ms^{-1}) in the Northern Pennines, as modelled by CONFORM.

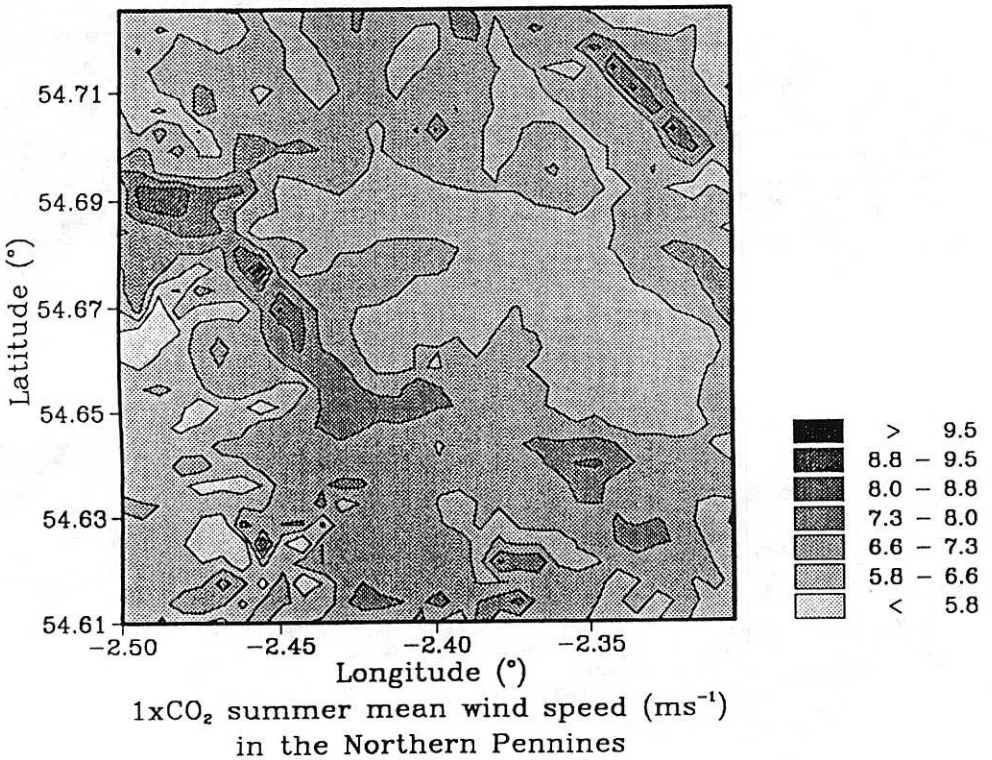

$1xCO_2$ summer mean wind speed (ms^{-1})
in the Northern Pennines

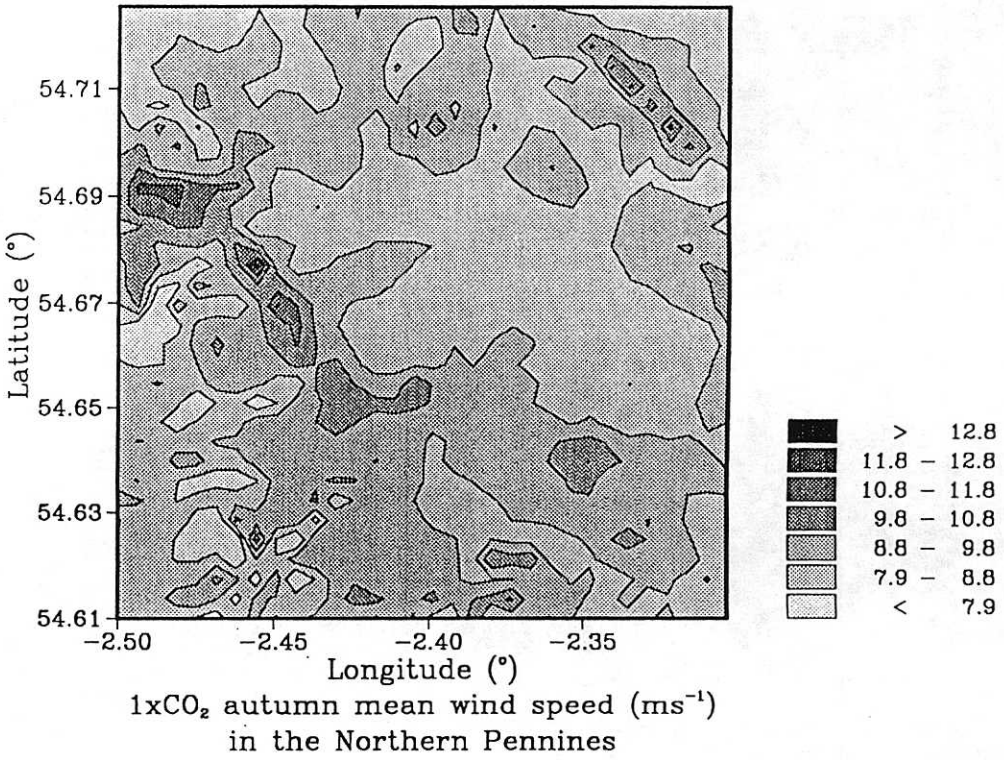

$1xCO_2$ autumn mean wind speed (ms^{-1})
in the Northern Pennines

Fig. 1.44 cont.

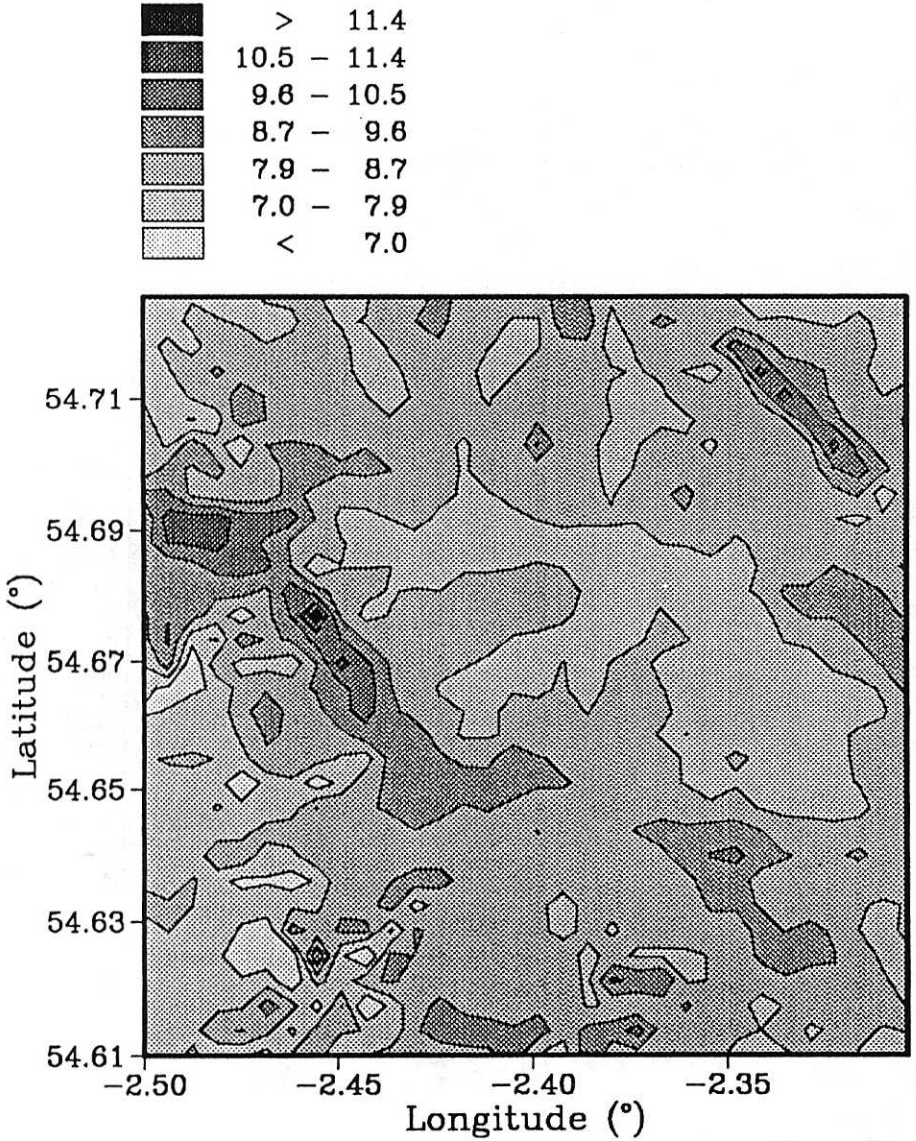

$2xCO_2$ annual mean wind speed (ms^{-1})
in the Northern Pennines for GFDL

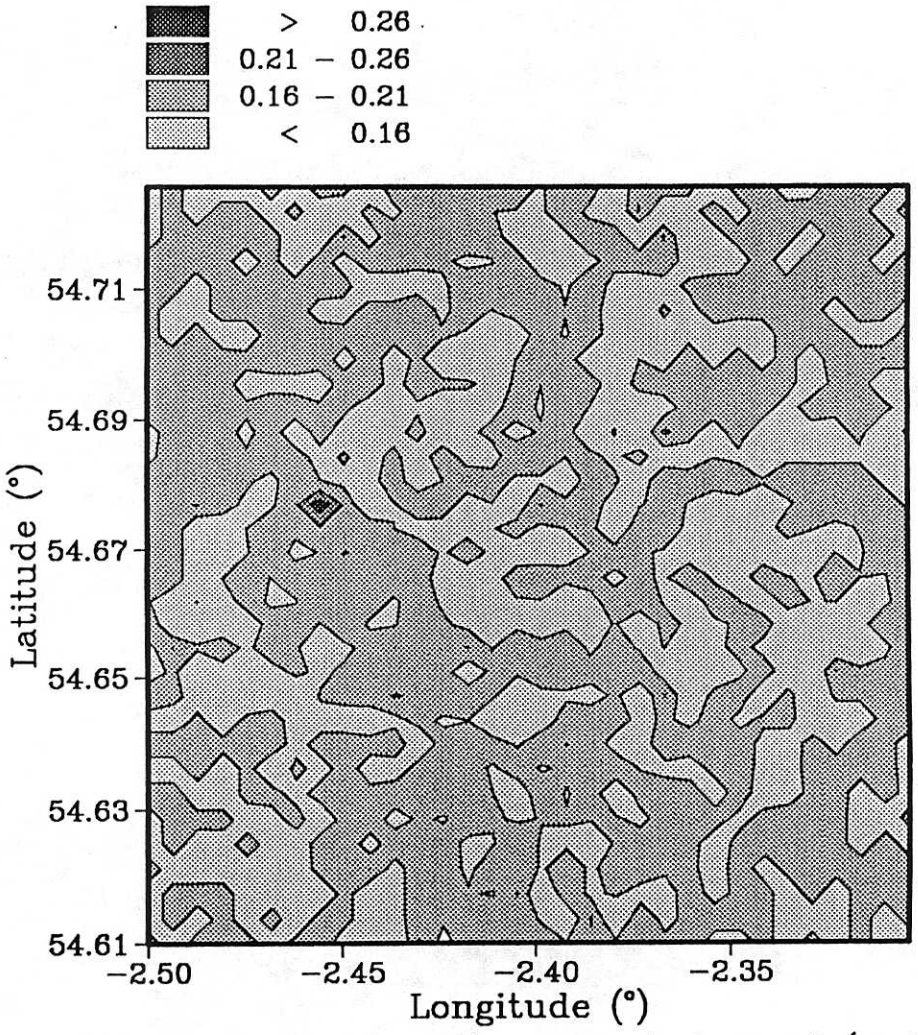

$2xCO_2 - 1xCO_2$ annual mean wind speed (ms^{-1})
in the Northern Pennines for GFDL

Fig. 1.45

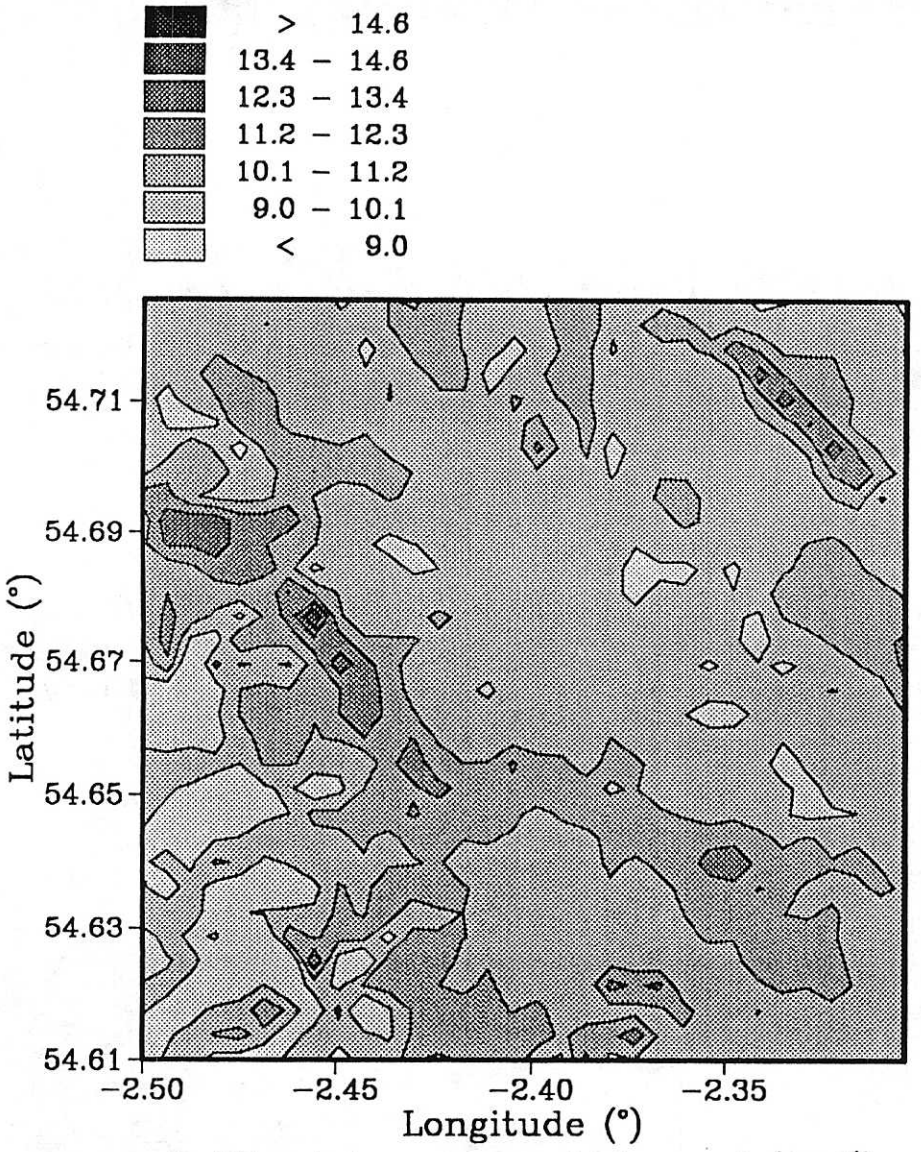

$2xCO_2$ winter mean wind speed (ms^{-1}) in the Northern Pennines for GFDL

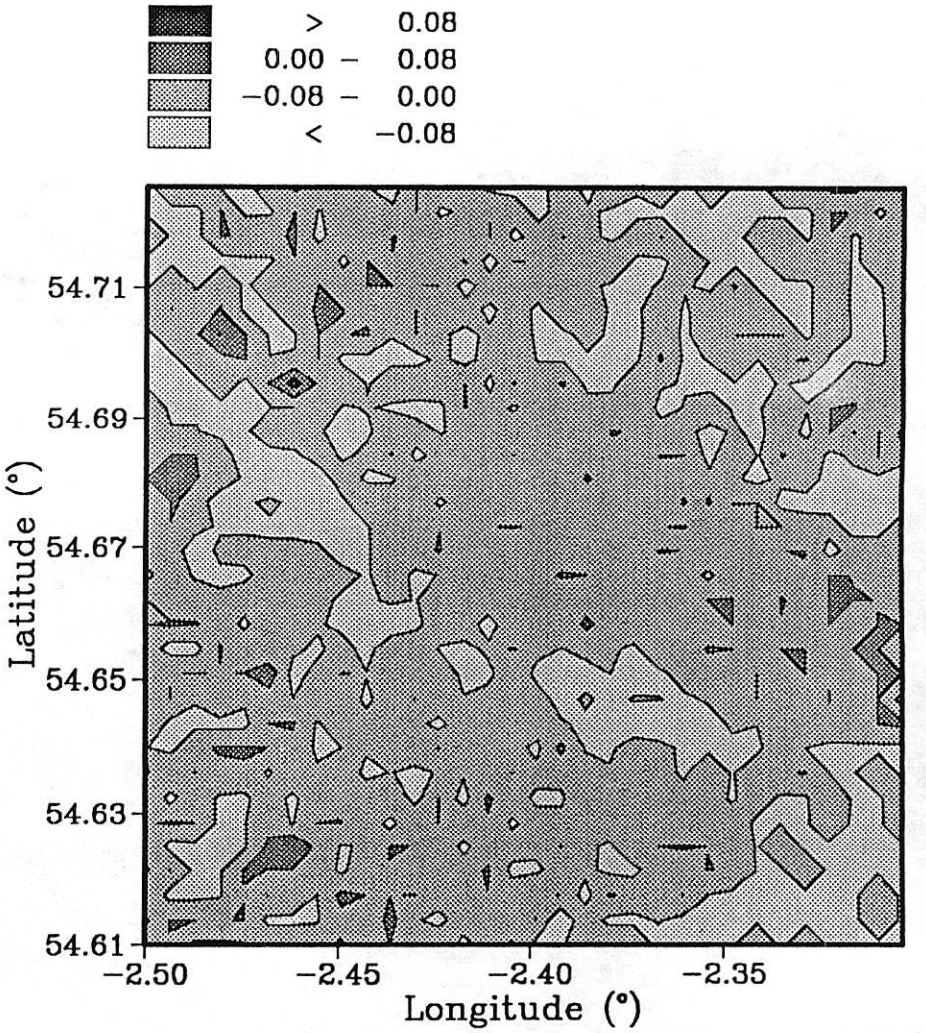

$2xCO_2 - 1xCO_2$ winter mean wind speed (ms^{-1}) in the Northern Pennines for GFDL

Fig. 1.46

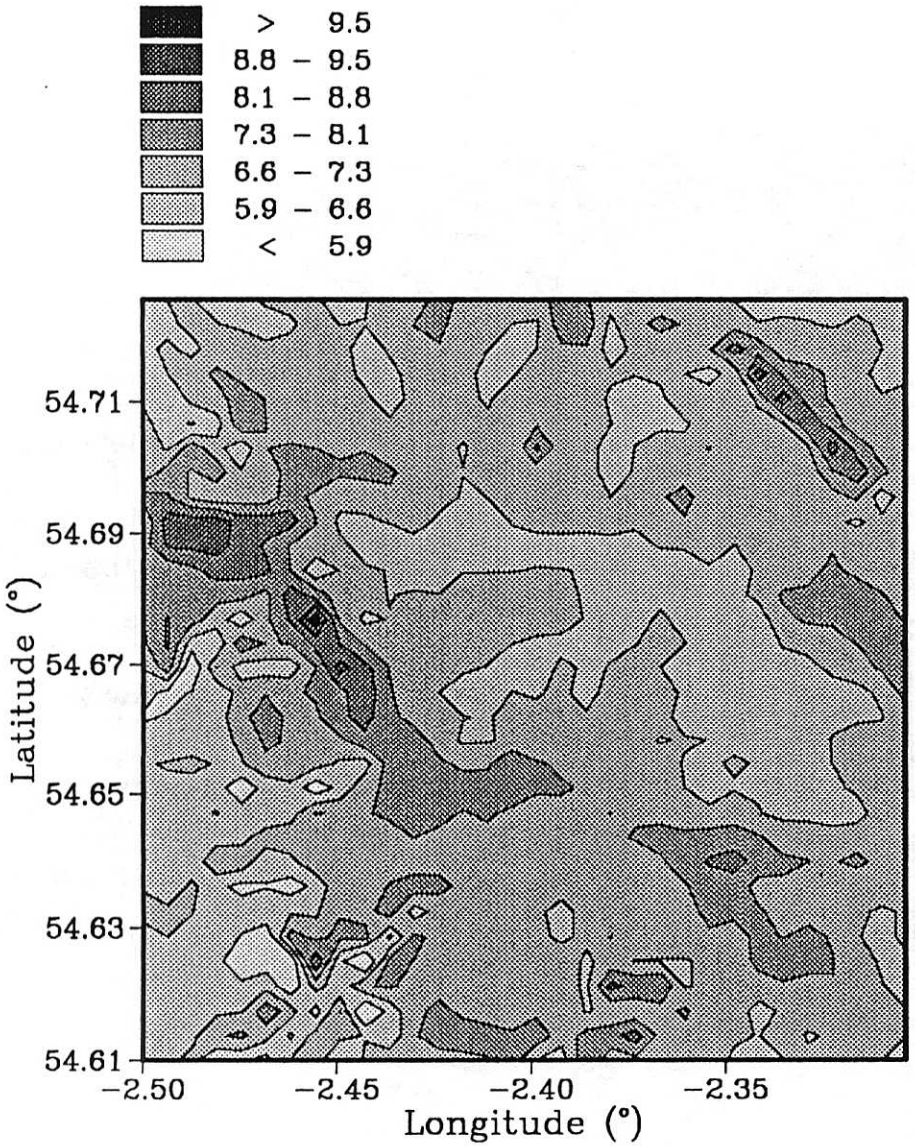

$2xCO_2$ spring mean wind speed (ms^{-1}) in the Northern Pennines for GFDL

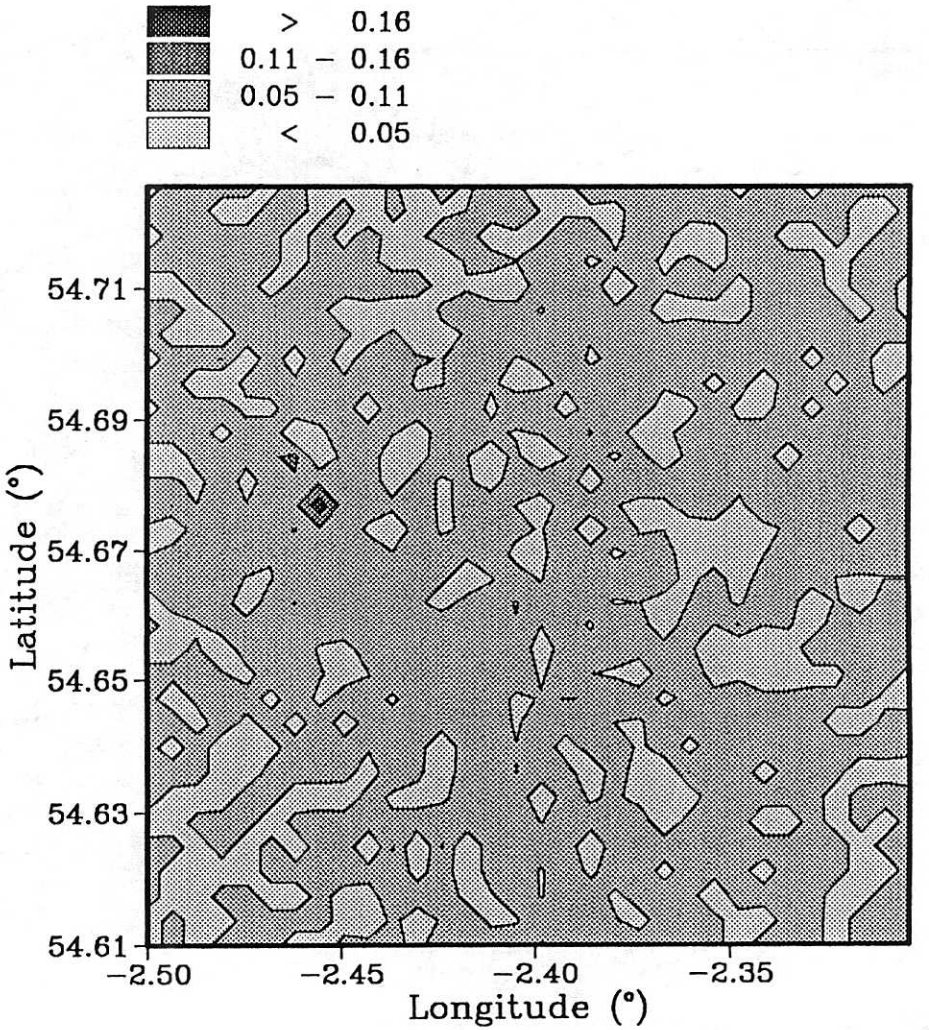

$2xCO_2 - 1xCO_2$ spring mean wind speed (ms^{-1}) in the Northern Pennines for GFDL

Fig. 1.47

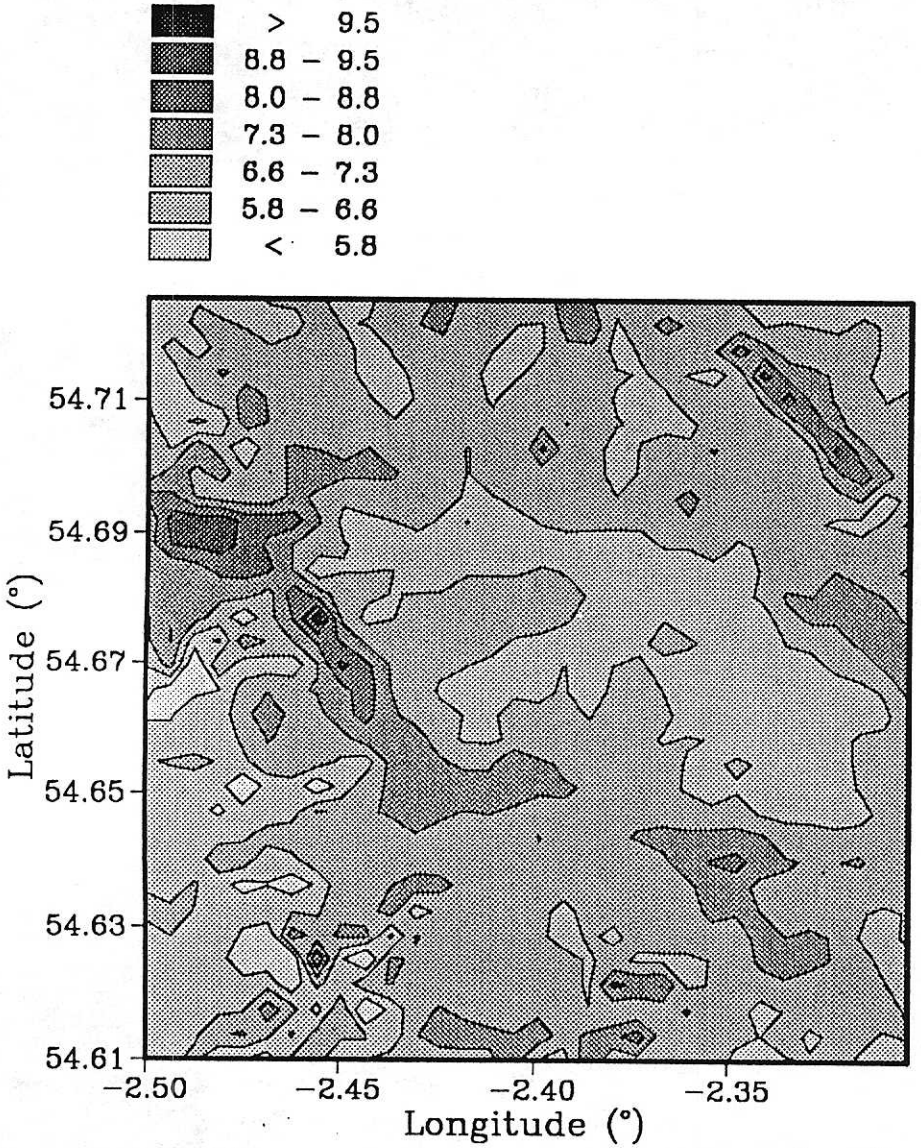

$2xCO_2$ summer mean wind speed (ms^{-1}) in the Northern Pennines for GFDL

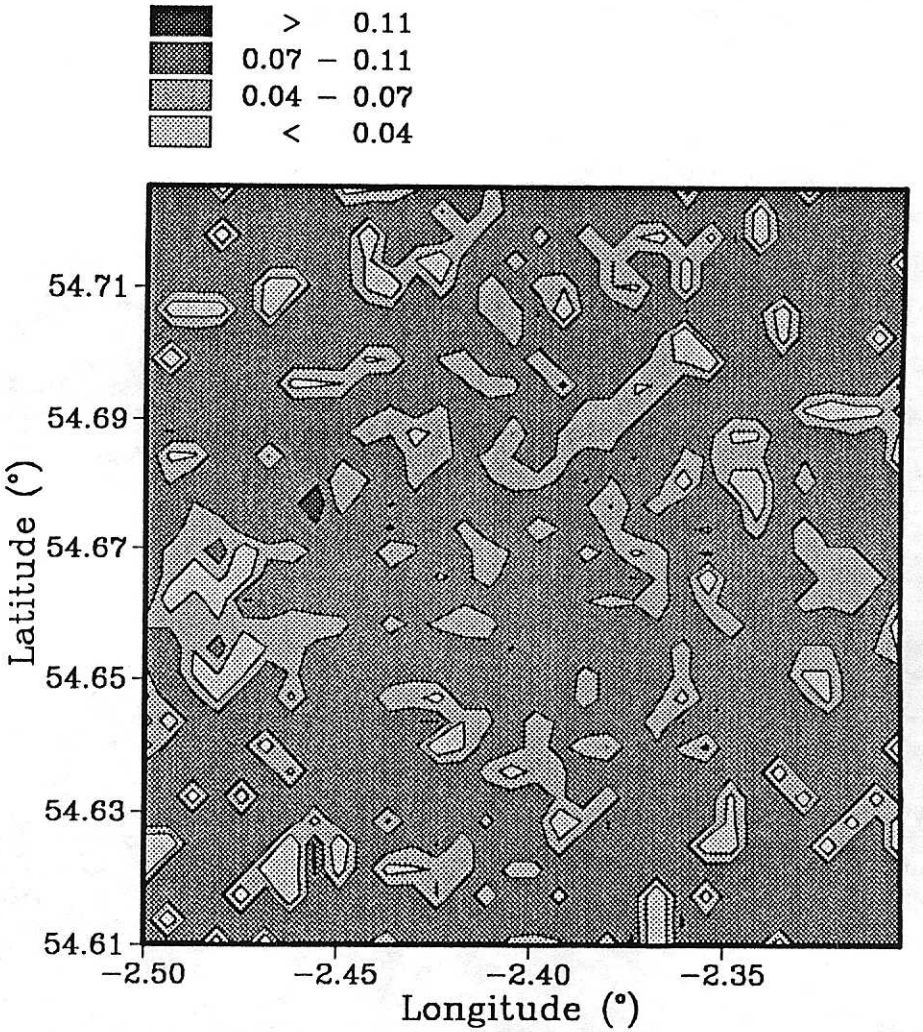

$2xCO_2 - 1xCO_2$ summer mean wind speed (ms^{-1}) in the Northern Pennines for GFDL

Fig. 1.48

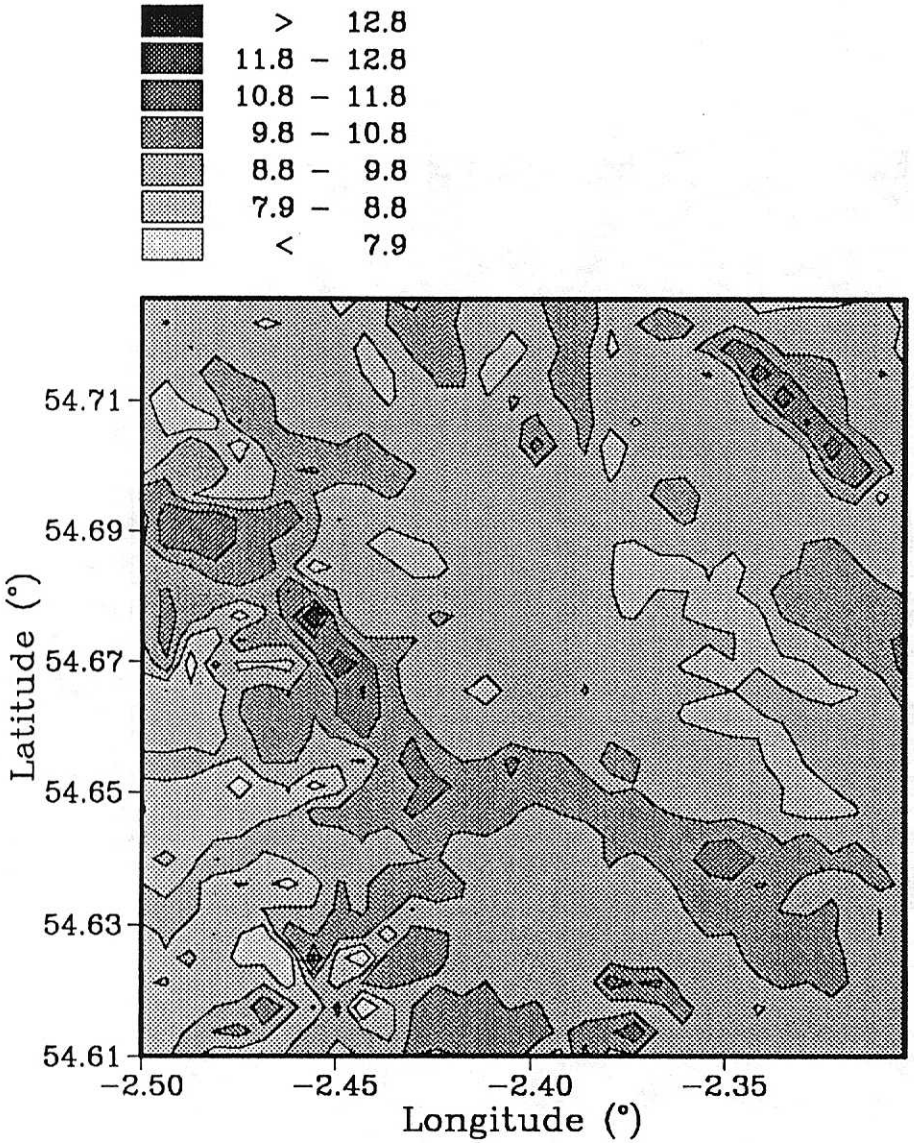

$2xCO_2$ autumn mean wind speed (ms^{-1}) in the Northern Pennines for GFDL

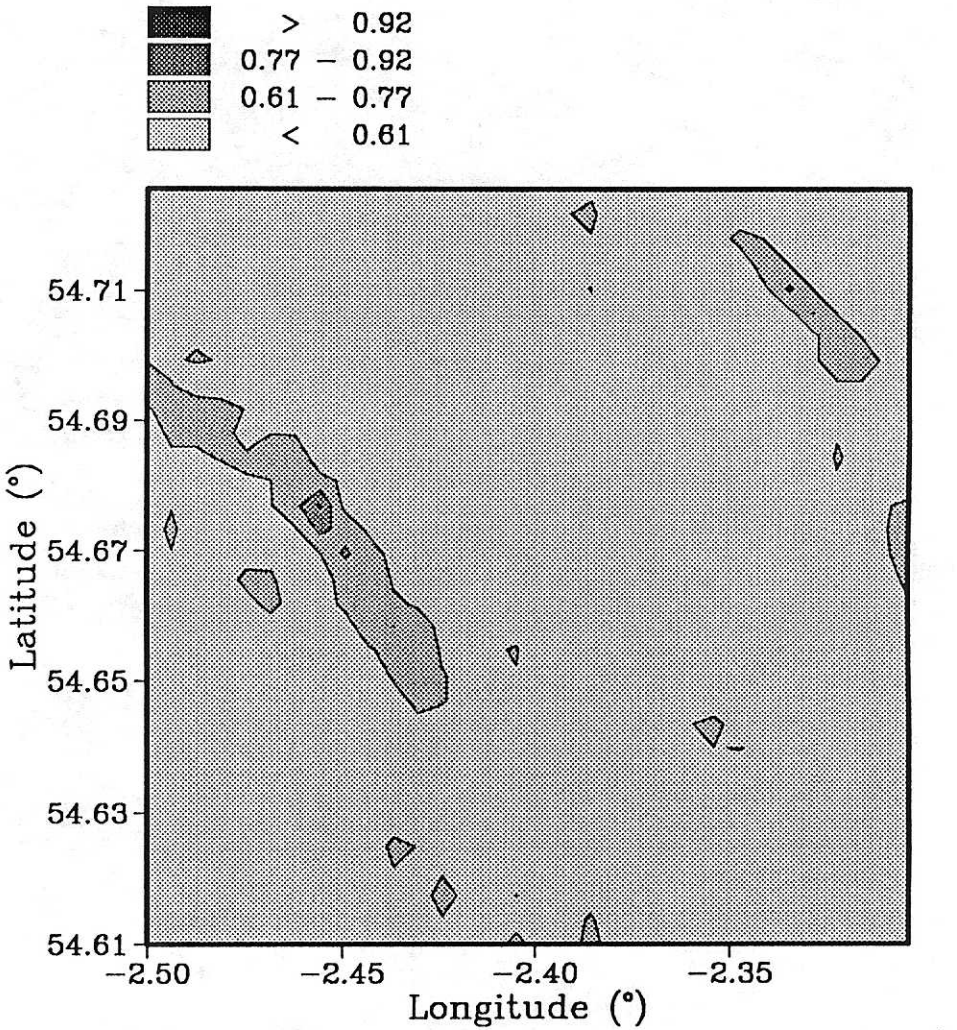

$2xCO_2 - 1xCO_2$ autumn mean wind speed (ms^{-1}) in the Northern Pennines for GFDL

Fig. 1.49

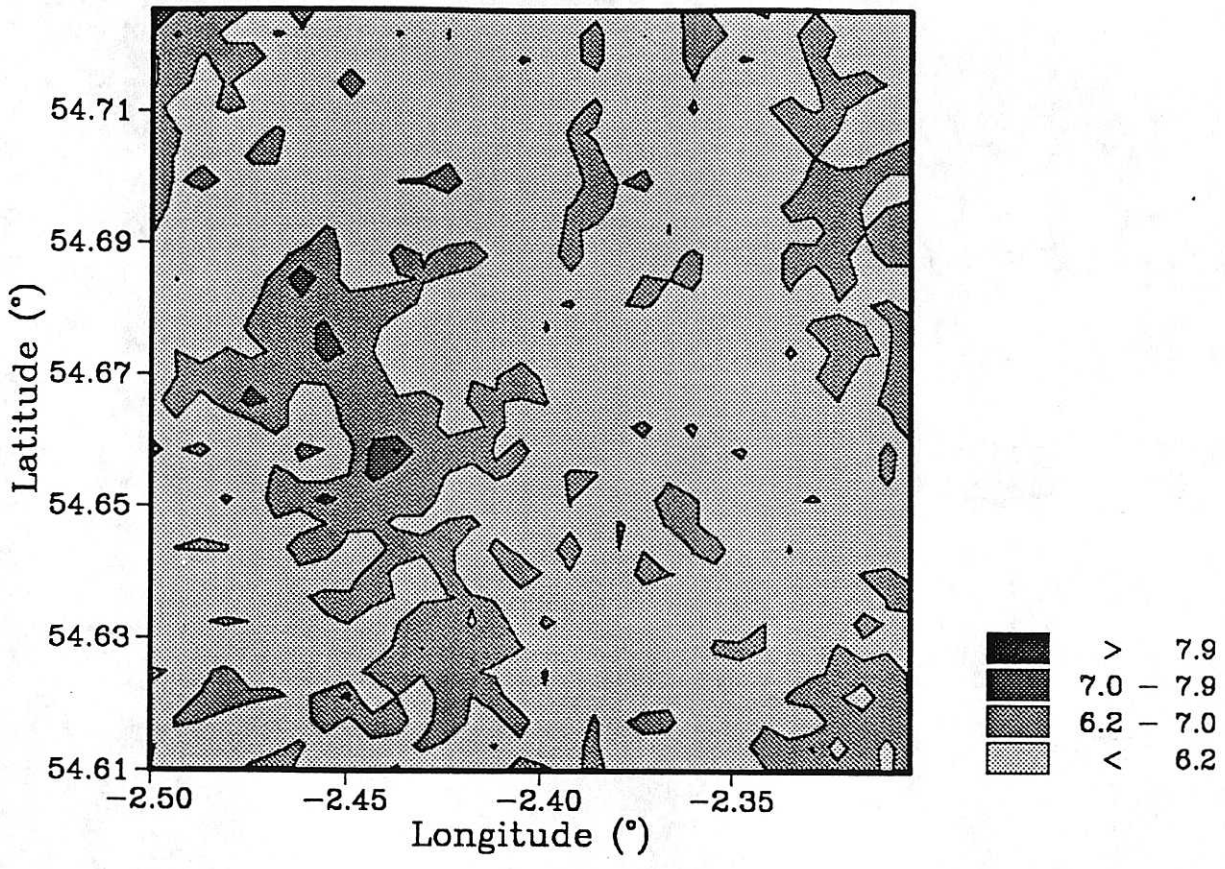

Fig. 1.50 $2xCO_2$-$1xCO_2$ percentage difference in autumn mean wind speed over the Northern Pennines test region, as modelled by the GFDL GCM and CONFORM.

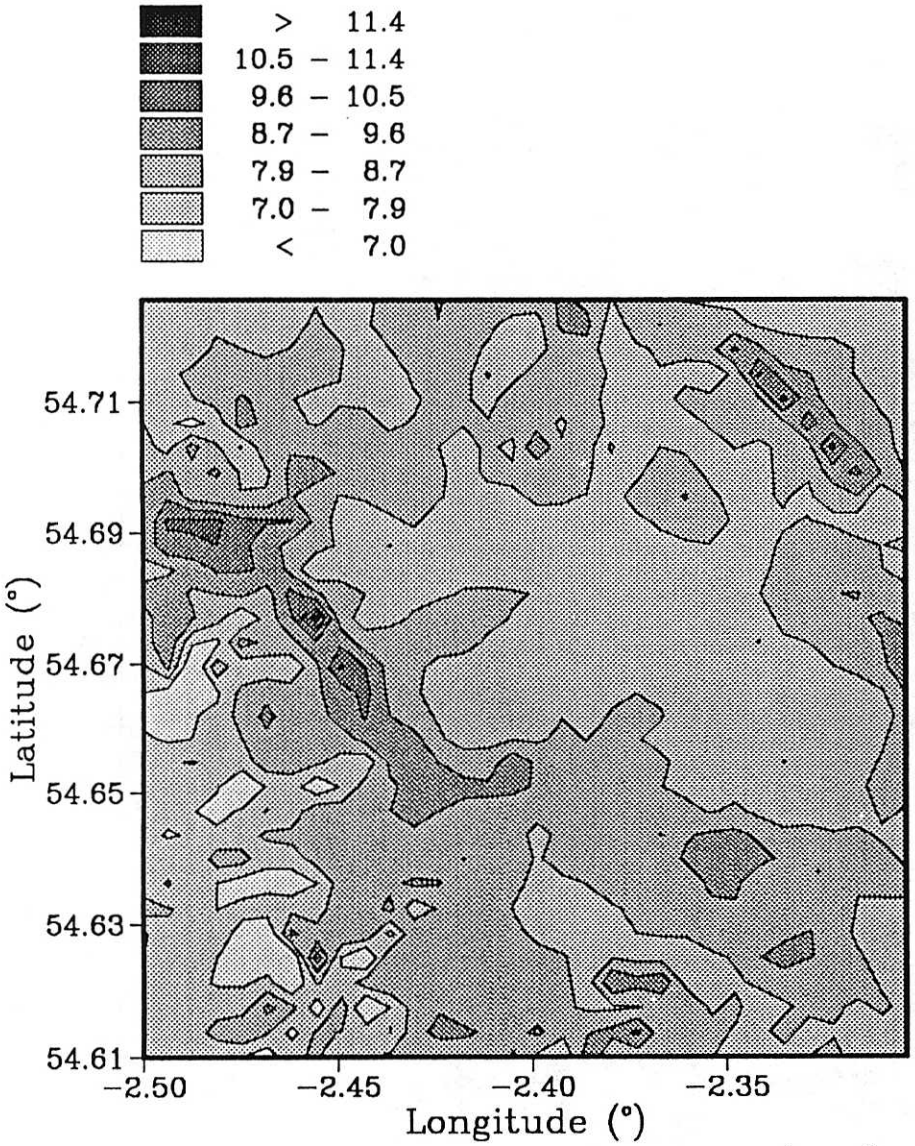

$2xCO_2$ annual mean wind speed (ms^{-1}) in the Northern Pennines for GISS

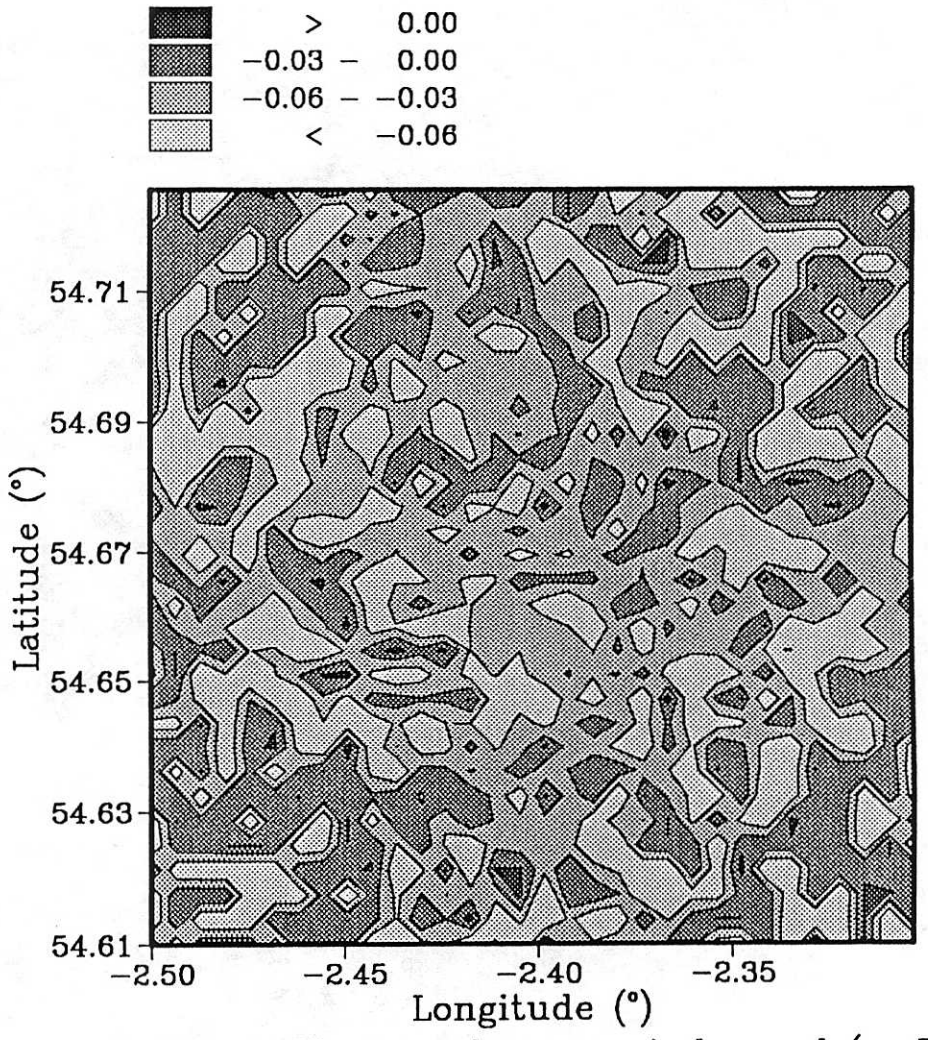

$2xCO_2 - 1xCO_2$ annual mean wind speed (ms^{-1}) in the Northern Pennines for GISS

Fig. 1.51

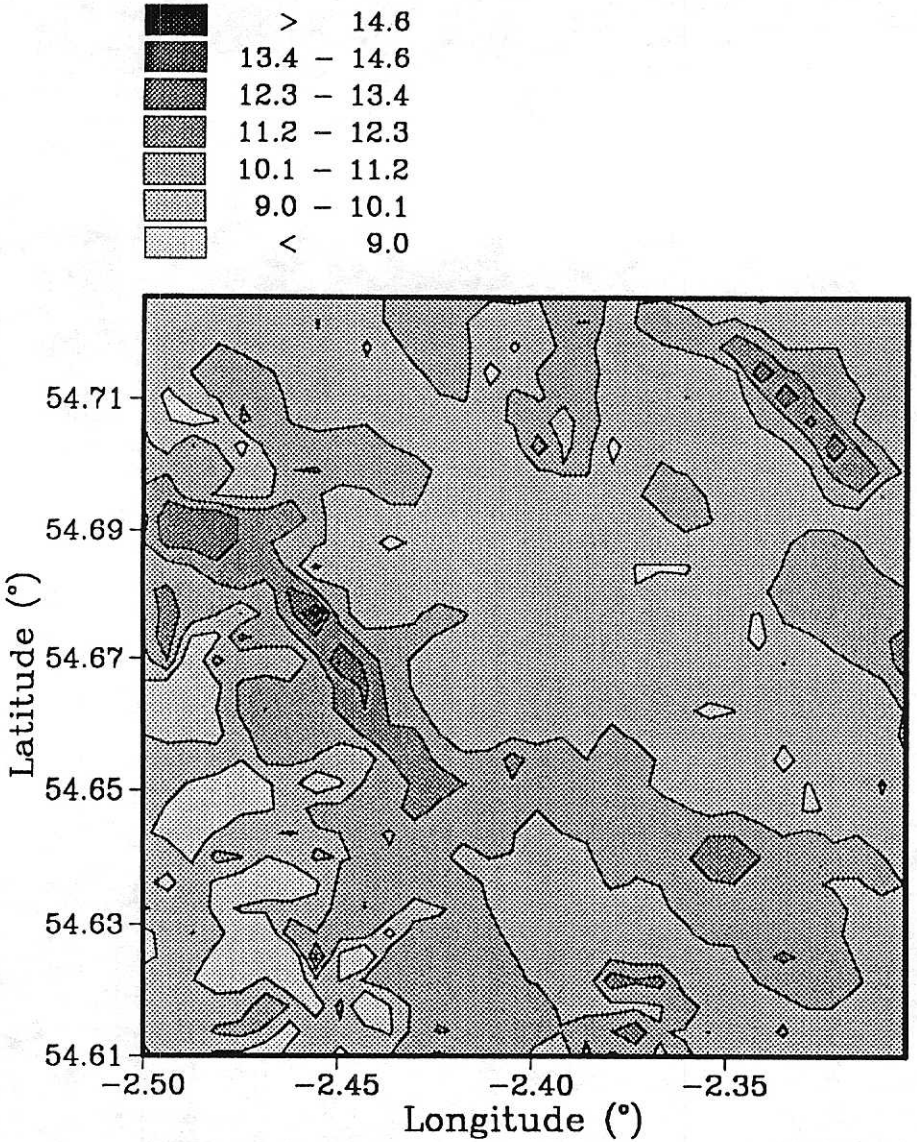

$2xCO_2$ winter mean wind speed (ms^{-1}) in the Northern Pennines for GISS

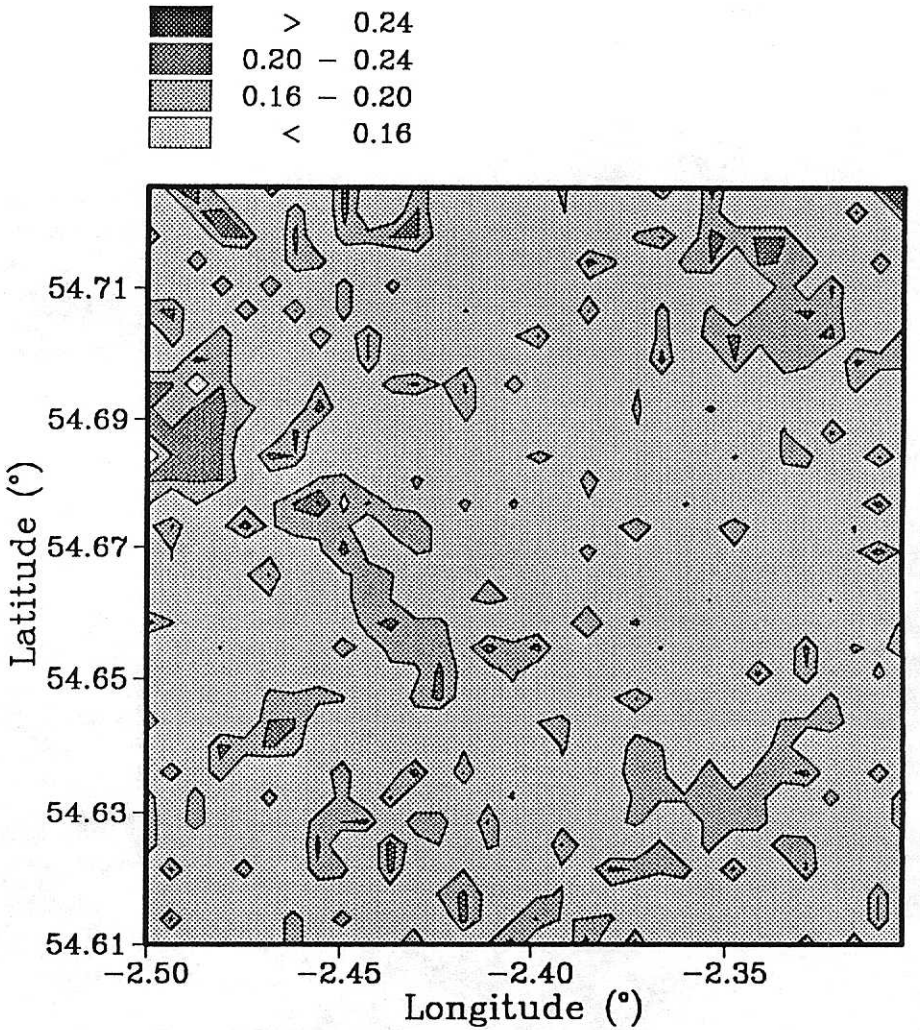

$2xCO_2 - 1xCO_2$ winter mean wind speed (ms^{-1}) in the Northern Pennines for GISS

Fig. 1.52

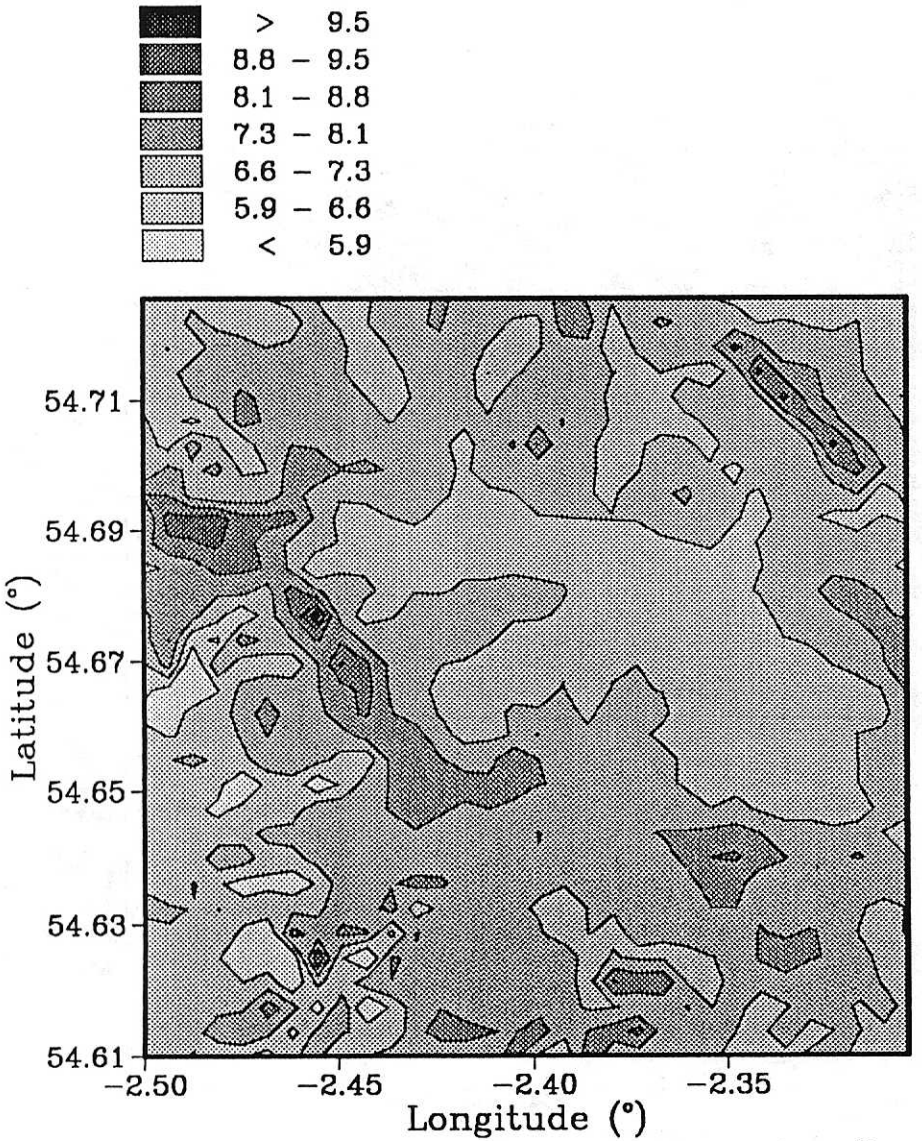

$2xCO_2$ spring mean wind speed (ms^{-1}) in the Northern Pennines for GISS

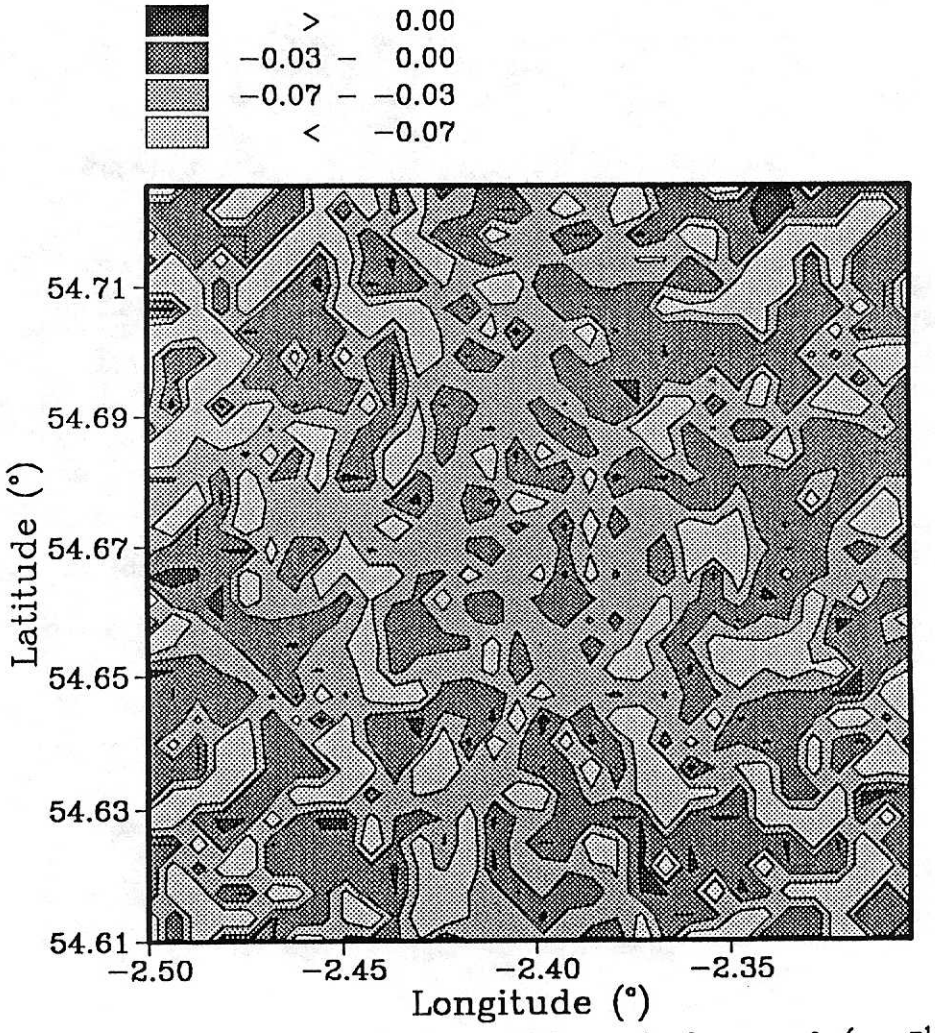

$2xCO_2 - 1xCO_2$ spring mean wind speed (ms^{-1}) in the Northern Pennines for GISS

Fig. 1.53

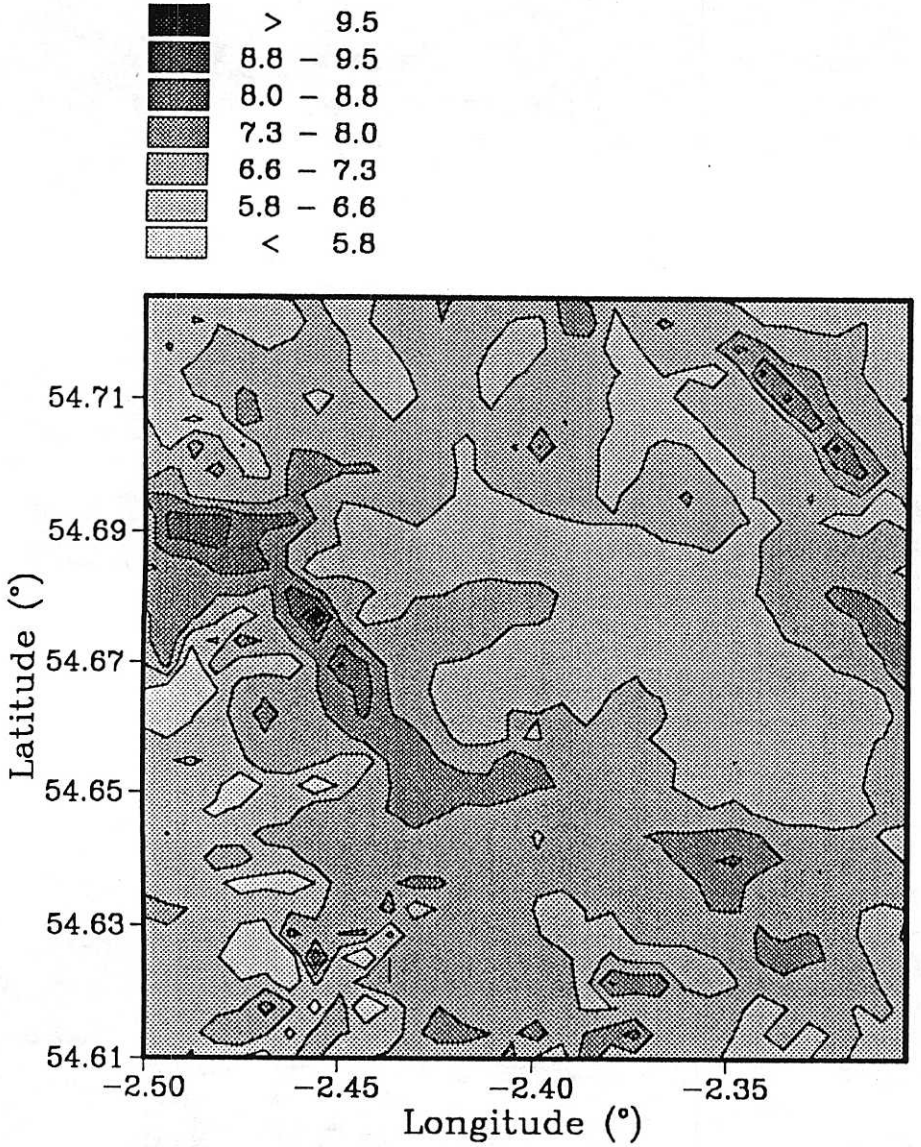

$2xCO_2$ summer mean wind speed (ms^{-1}) in the Northern Pennines for GISS

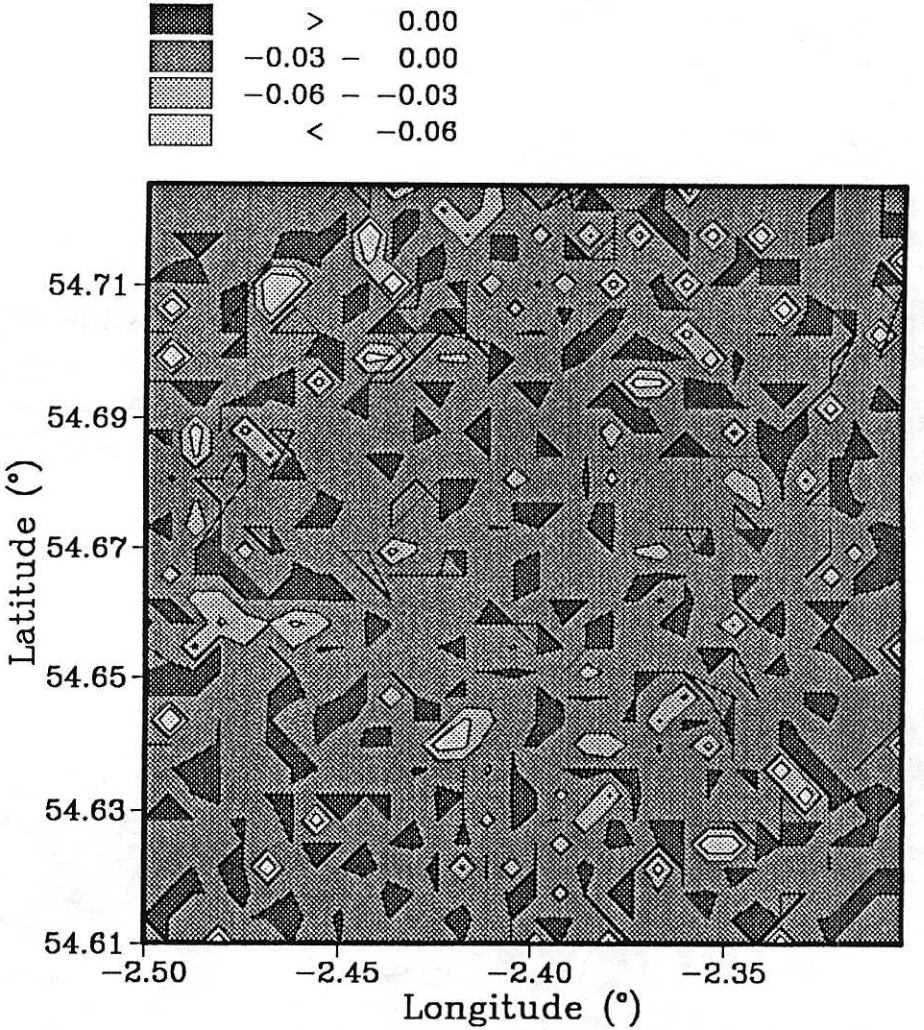

$2xCO_2 - 1xCO_2$ summer mean wind speed (ms^{-1}) in the Northern Pennines for GISS

Fig. 1.54

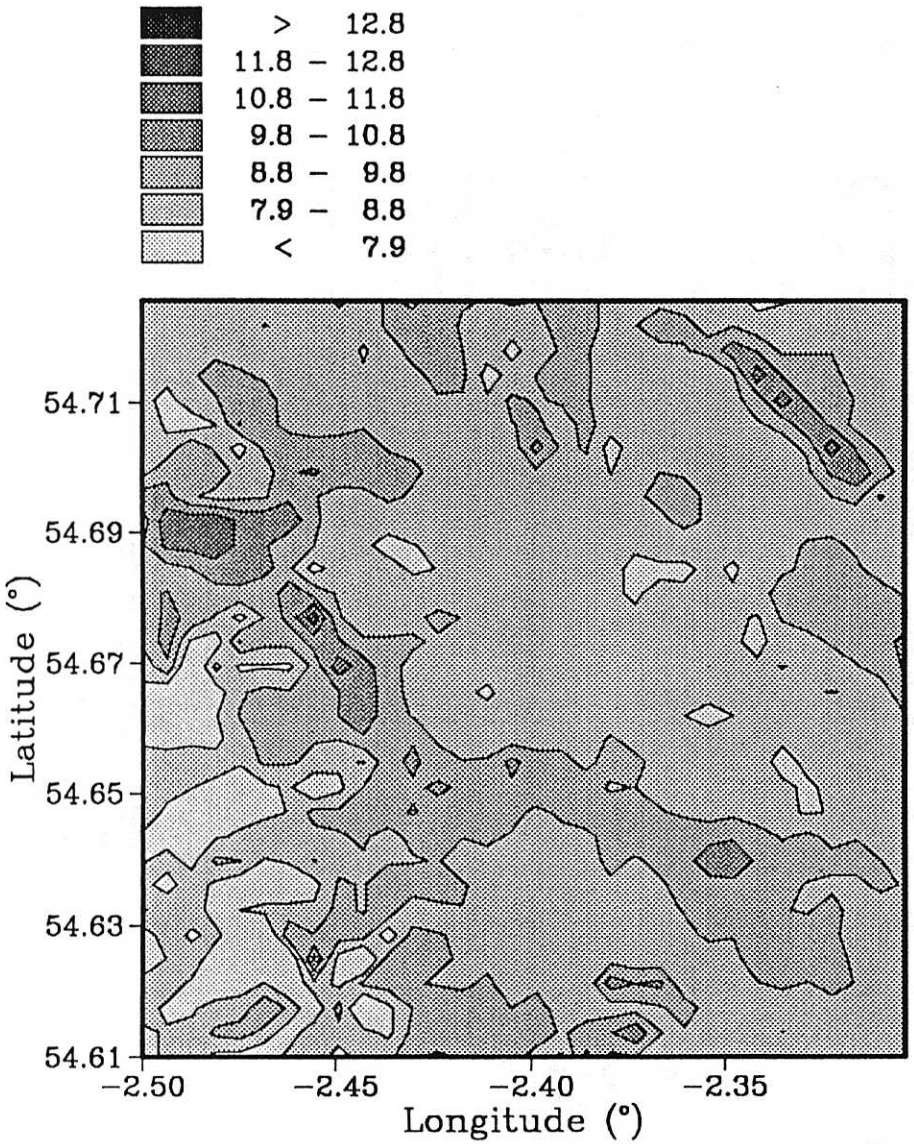

$2xCO_2$ autumn mean wind speed (ms^{-1}) in the Northern Pennines for GISS

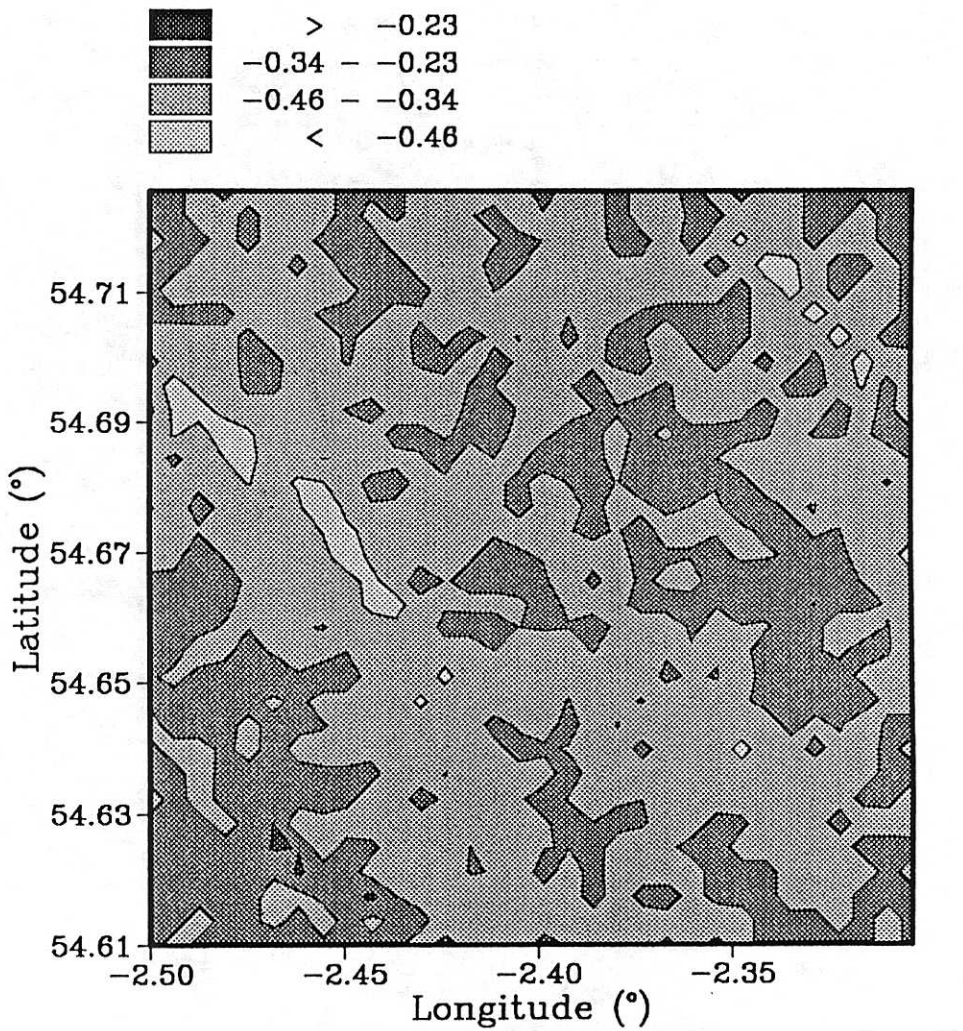

$2xCO_2 - 1xCO_2$ autumn mean wind speed (ms^{-1}) in the Northern Pennines for GISS

Fig. 1.55

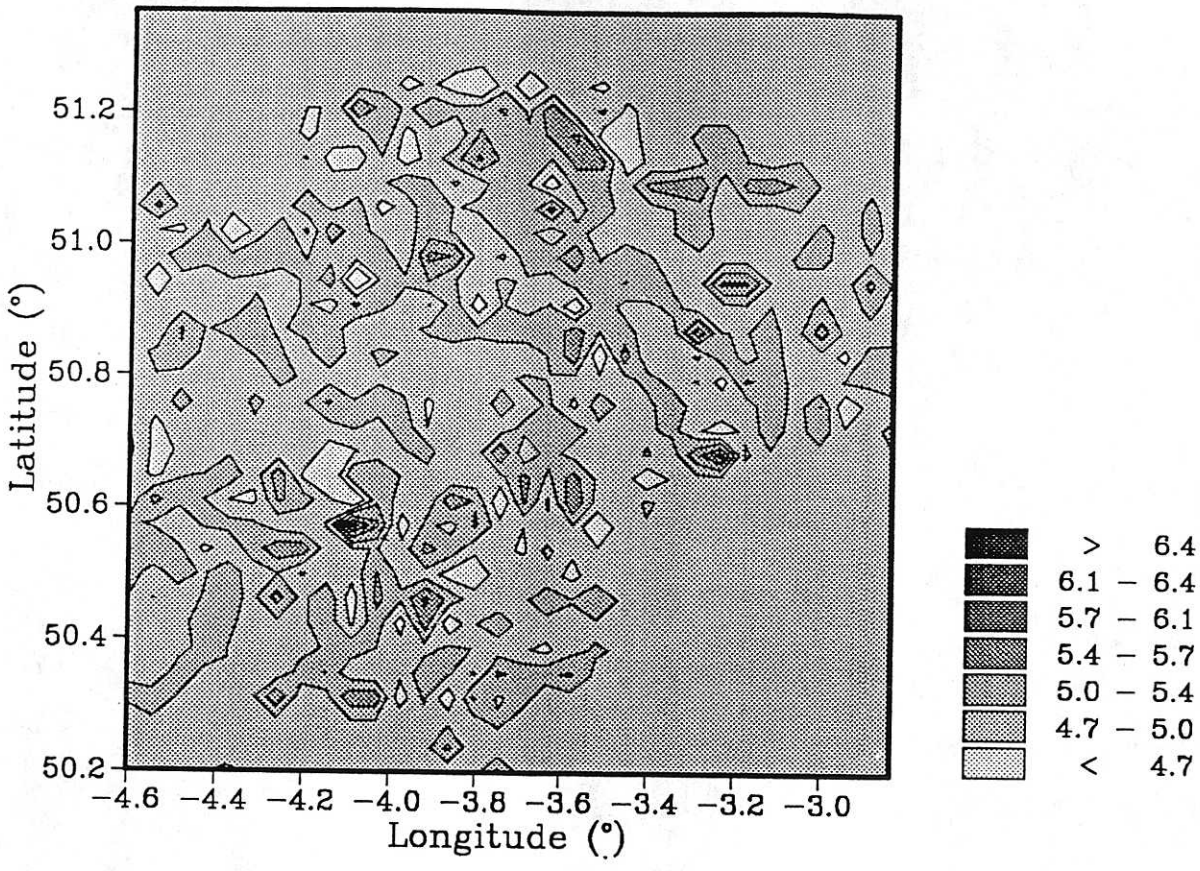

Fig. 1.56 Present-day annual mean wind speeds (ms^{-1}) in the Devon test region, as modelled by CONFORM.

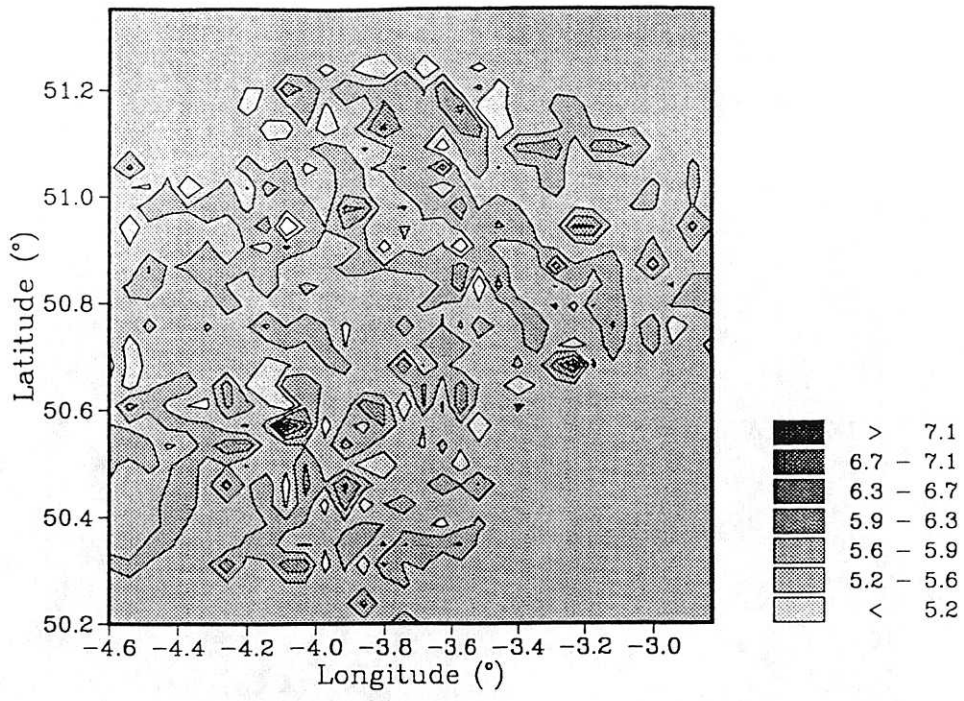

$1xCO_2$ winter mean wind speed (ms^{-1}) in Devon

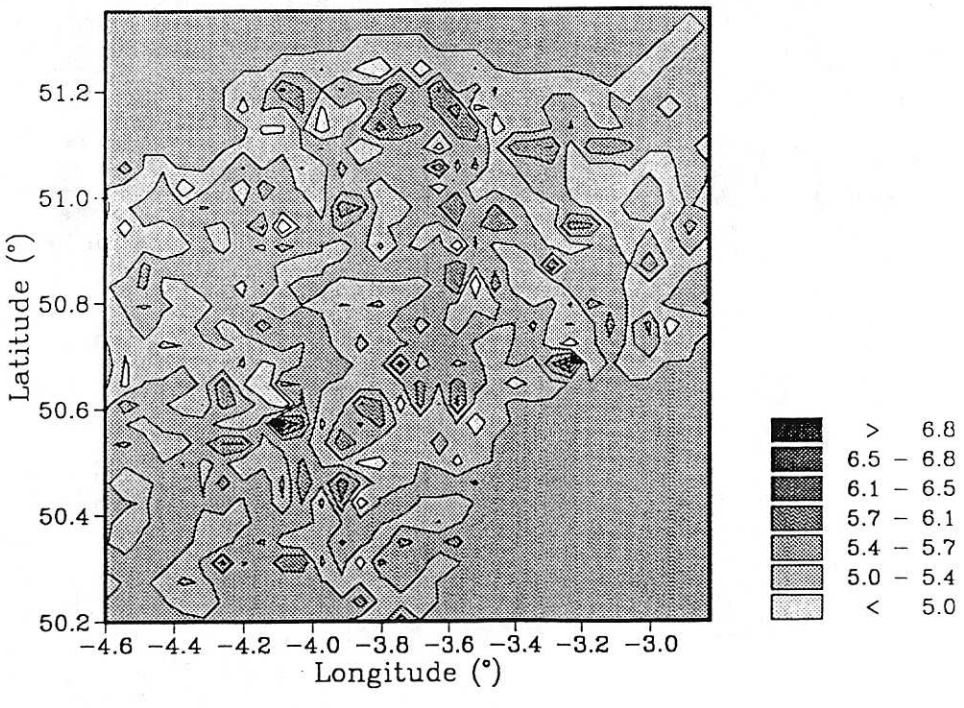

$1xCO_2$ spring mean wind speed (ms^{-1}) in Devon

Fig. 1.57 Present-day seasonal mean wind speeds (ms^{-1}) in the Devon test region, as modelled by CONFORM.

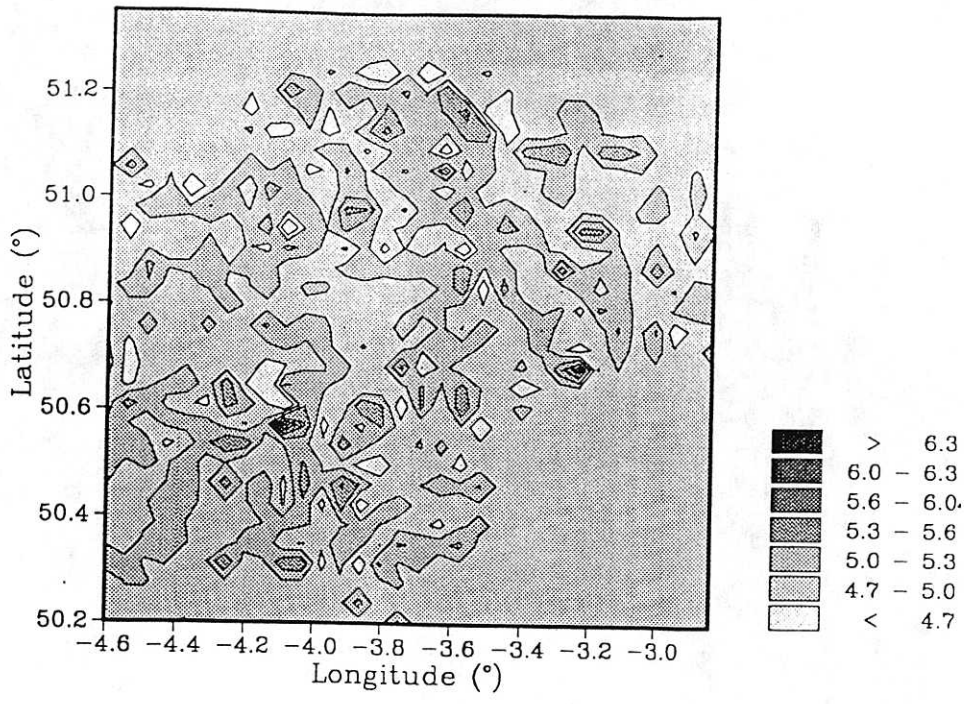

$1xCO_2$ summer mean wind speed (ms^{-1}) in Devon

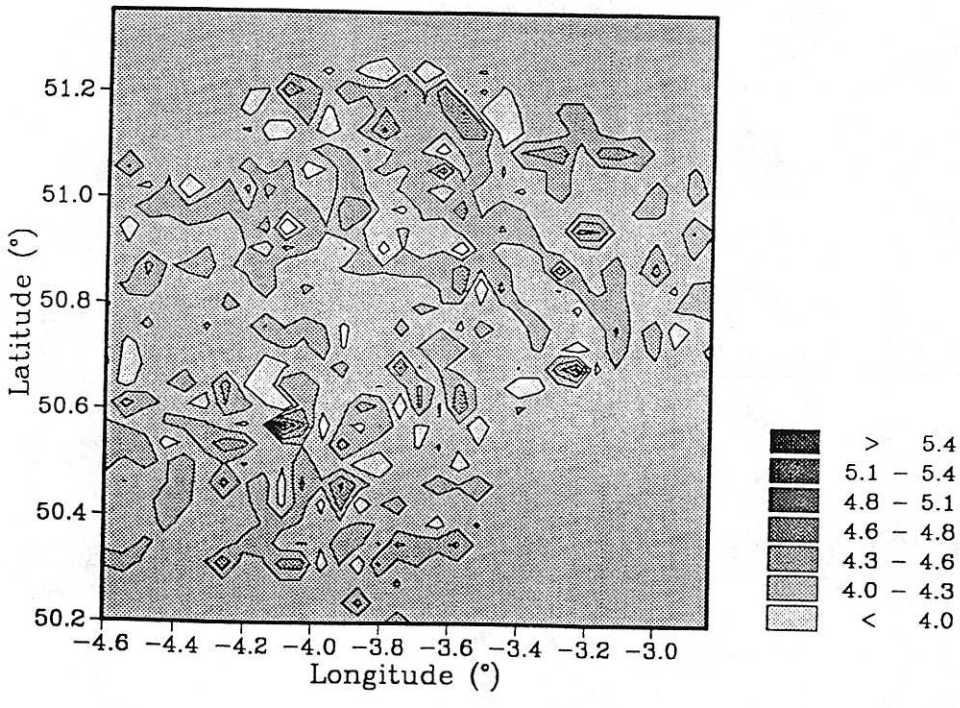

$1xCO_2$ autumn mean wind speed (ms^{-1}) in Devon

Fig. 1.57 cont.

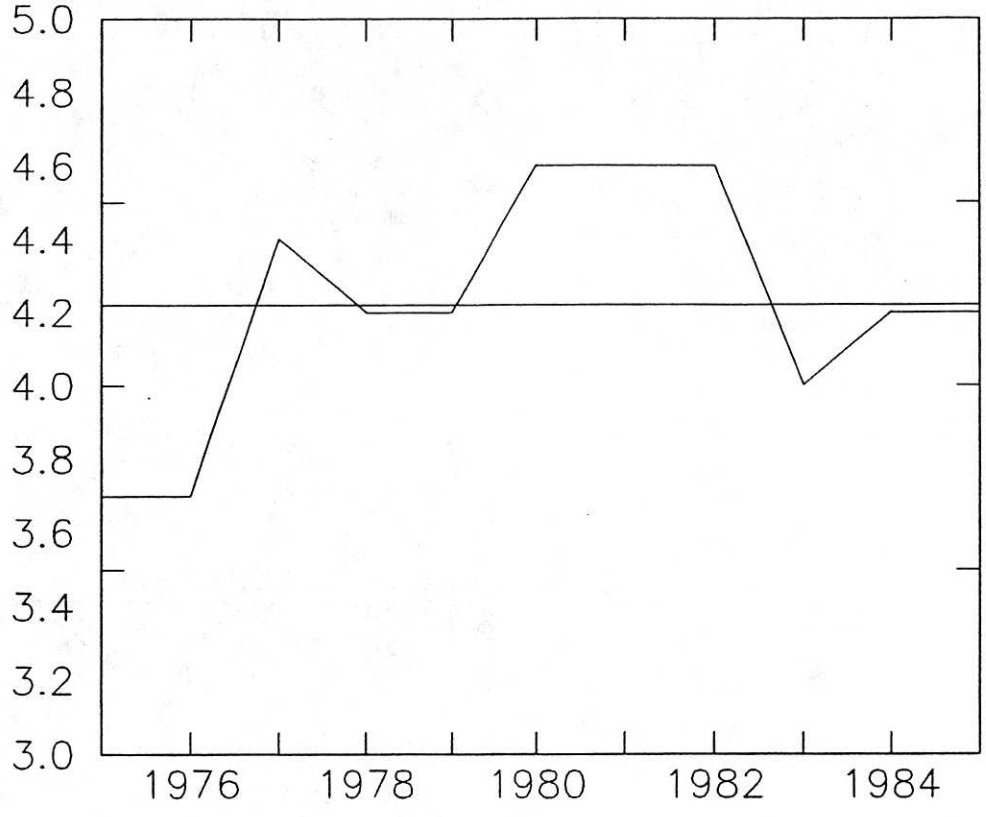

Fig. 1.58 Annual mean wind speeds (ms^{-1}) at Exeter, 1975-85.

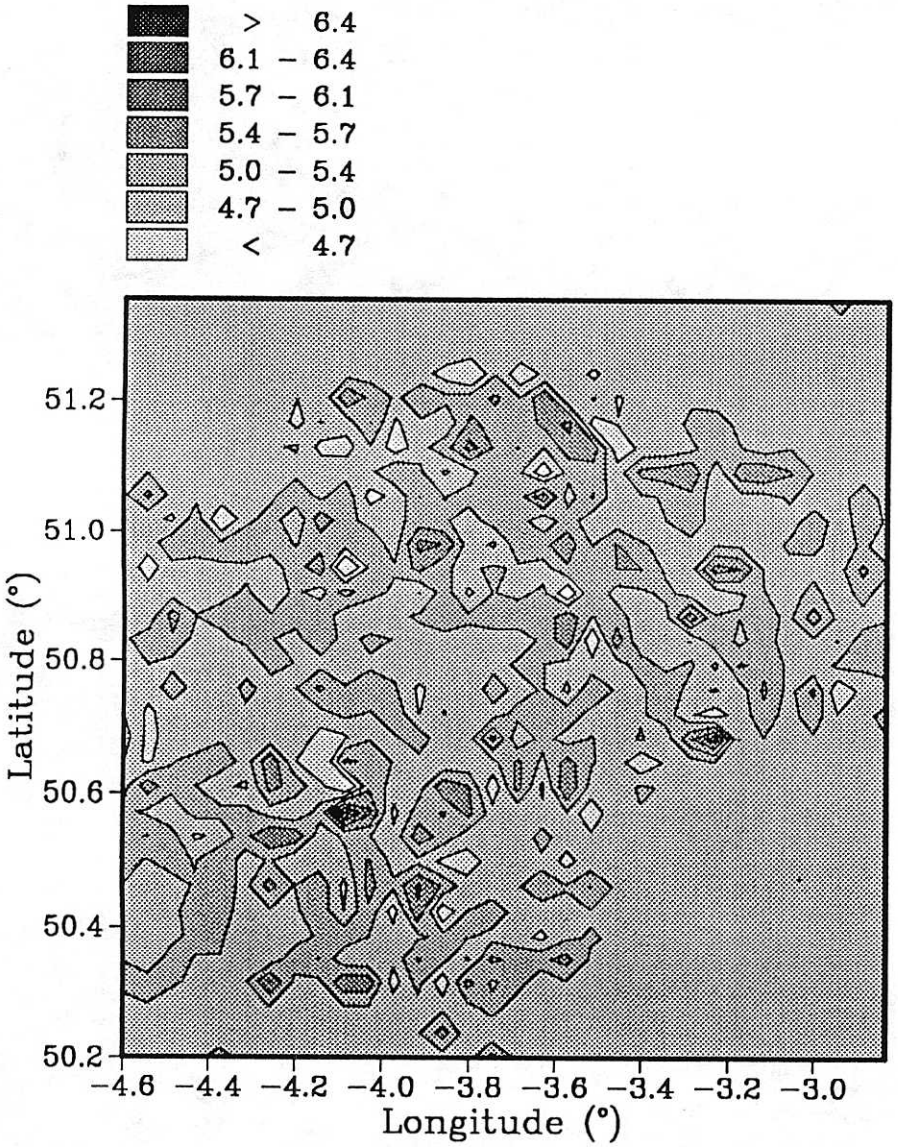

$2xCO_2$ annual mean wind speed (ms^{-1}) in Devon for GFDL

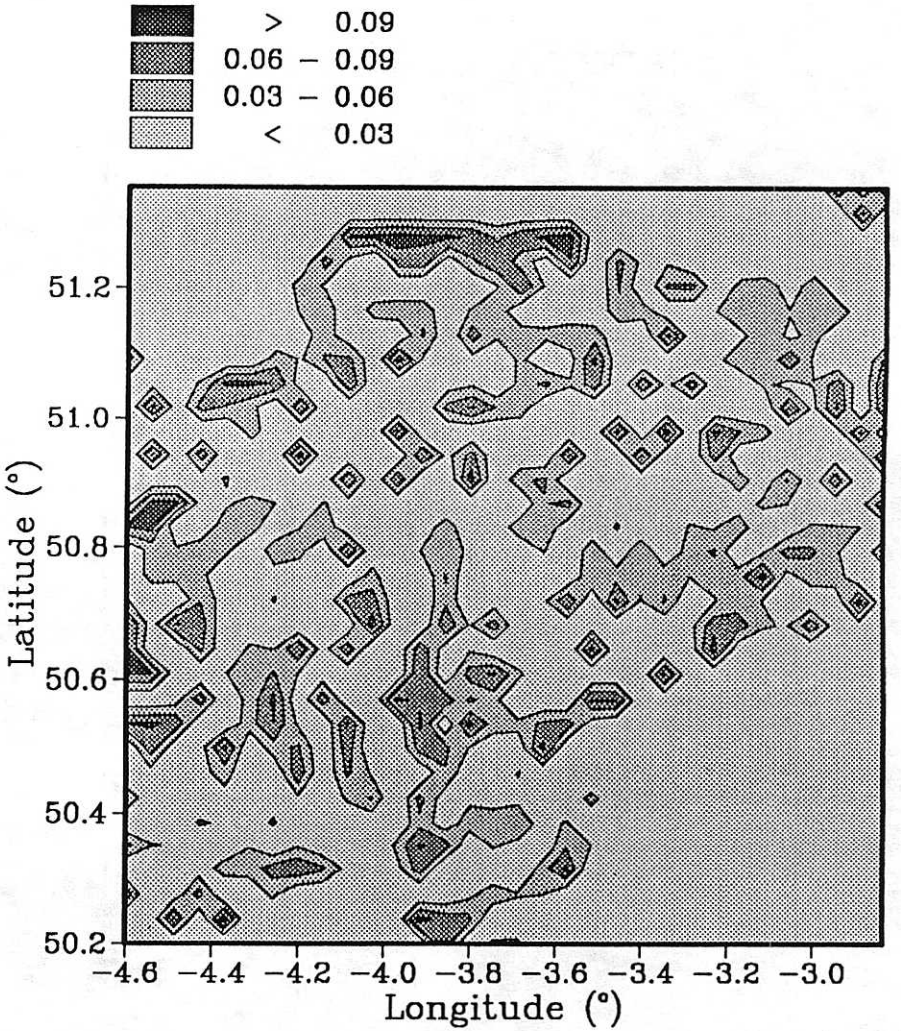

$2xCO_2 - 1xCO_2$ annual mean wind speed (ms^{-1}) in Devon for GFDL

Fig. 1.59

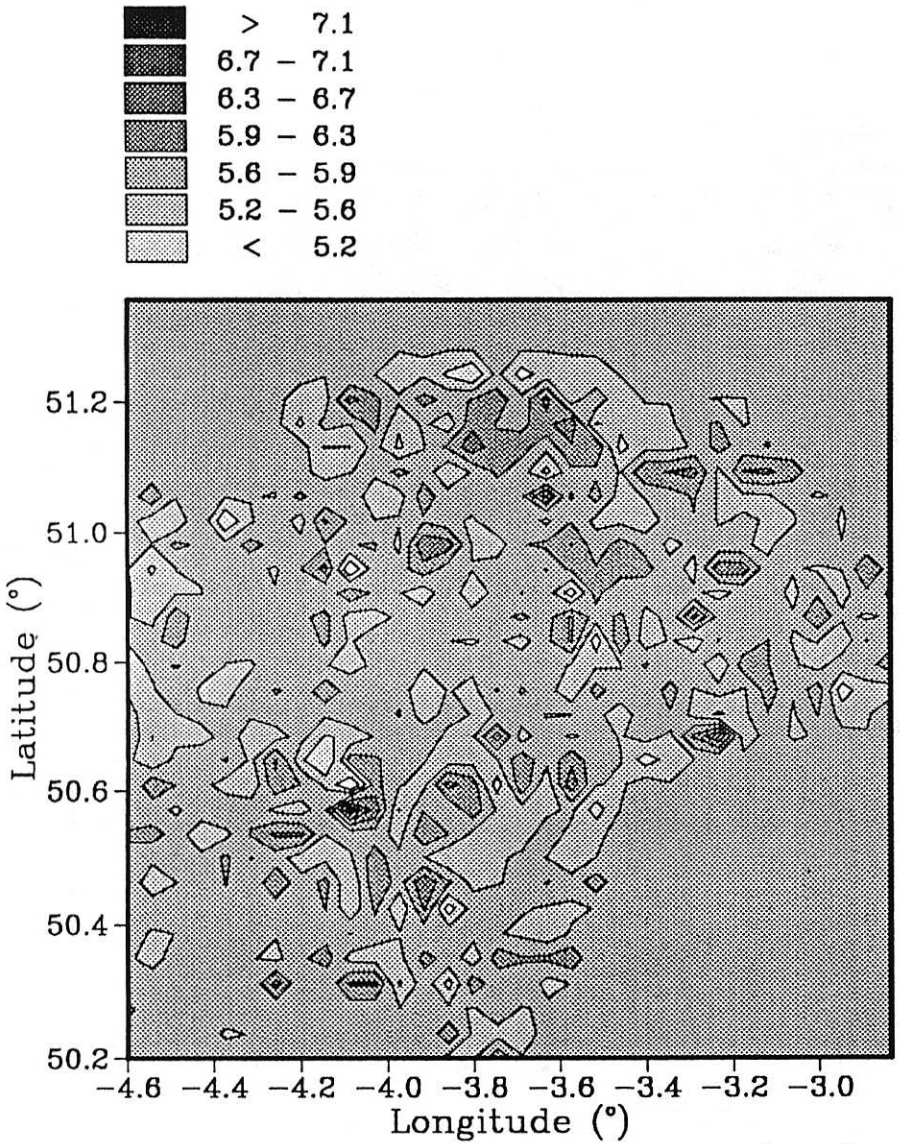

$2xCO_2$ winter mean wind speed (ms^{-1})
in Devon for GFDL

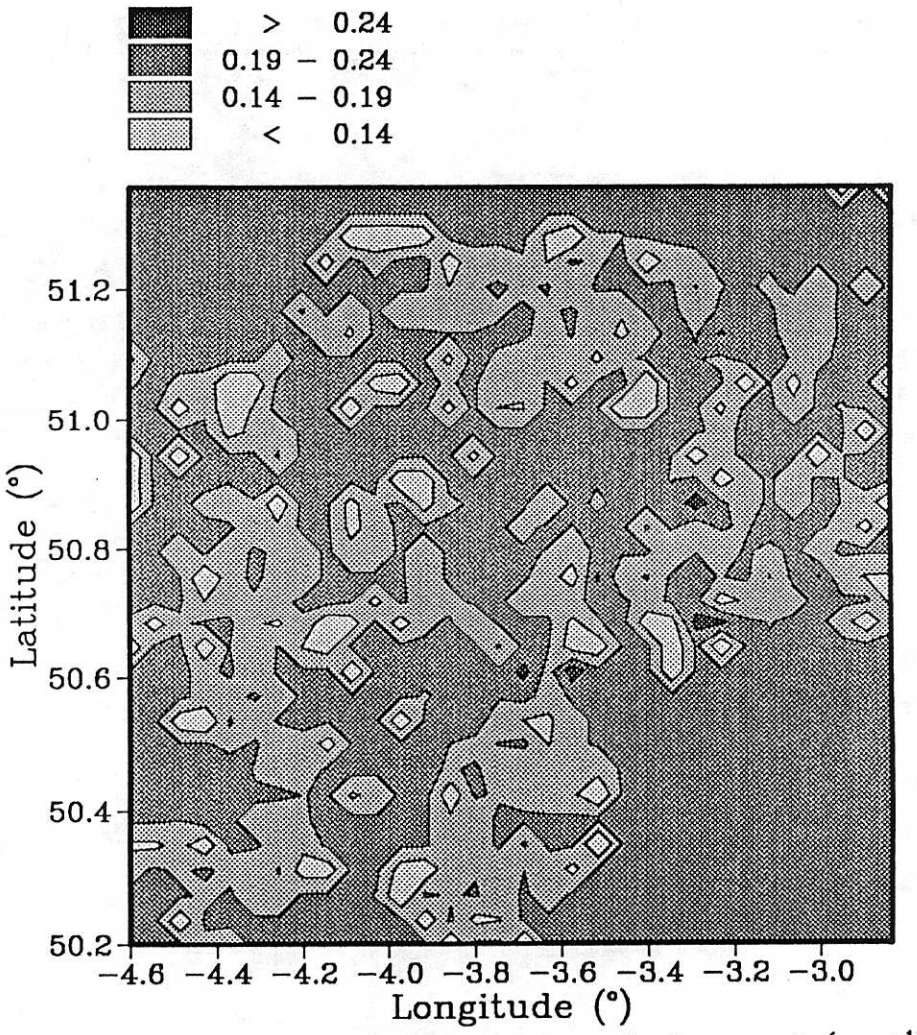

$2xCO_2 - 1xCO_2$ winter mean wind speed (ms^{-1})
in Devon for GFDL

Fig. 1.60

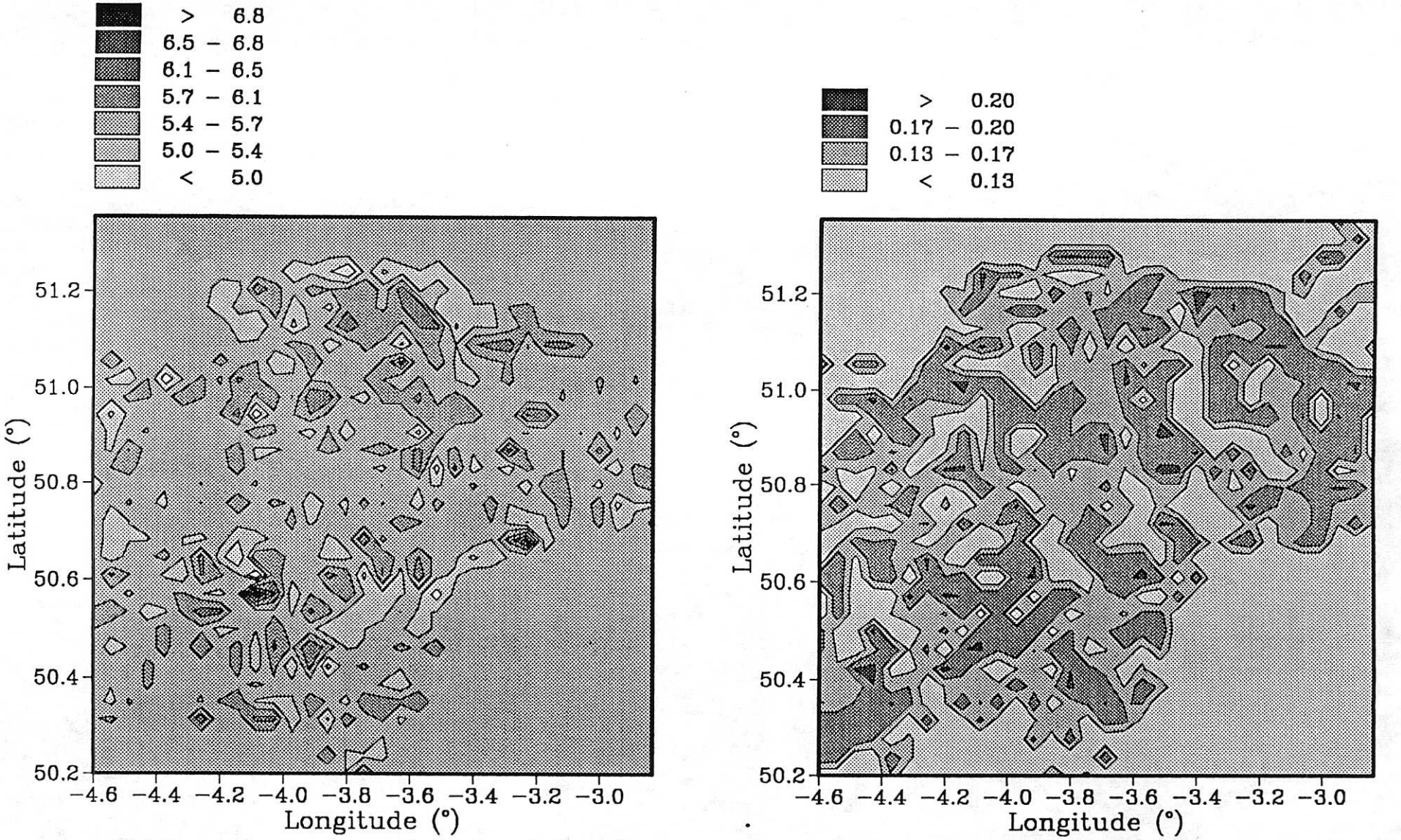
> 6.8
6.5 – 6.8
6.1 – 6.5
5.7 – 6.1
5.4 – 5.7
5.0 – 5.4
< 5.0
Latitude (°)
51.2
51.0
50.8
50.6
50.4
50.2
−4.6 −4.4 −4.2 −4.0 −3.8 −3.6 −3.4 −3.2 −3.0
Longitude (°)
2xCO₂ spring mean wind speed (ms⁻¹)
in Devon for GFDL
> 0.20
0.17 – 0.20
0.13 – 0.17
< 0.13
Latitude (°)
51.2
51.0
50.8
50.6
50.4
50.2
−4.6 −4.4 −4.2 −4.0 −3.8 −3.6 −3.4 −3.2 −3.0
Longitude (°)
2xCO₂−1xCO₂ spring mean wind speed (ms⁻¹)
in Devon for GFDL

Fig. 1.61

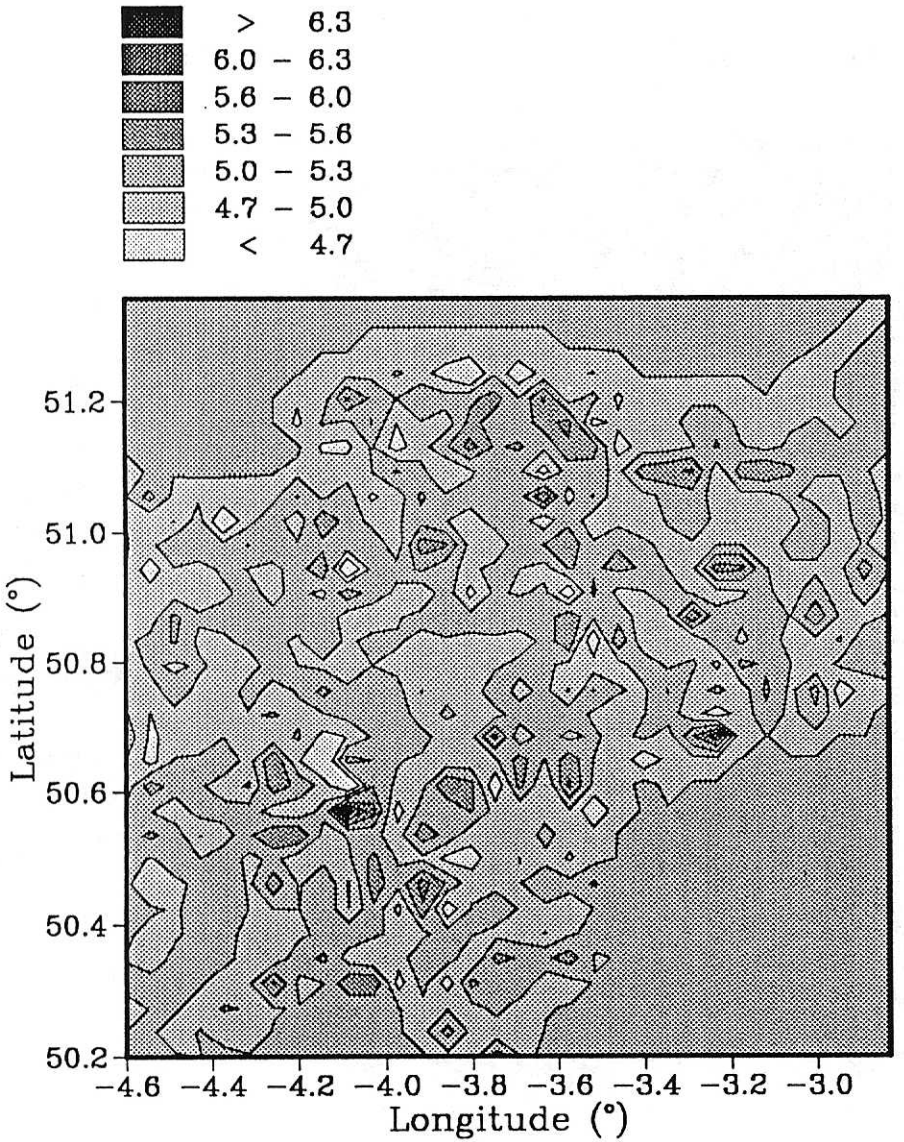

$2xCO_2$ summer mean wind speed (ms^{-1}) in Devon for GFDL

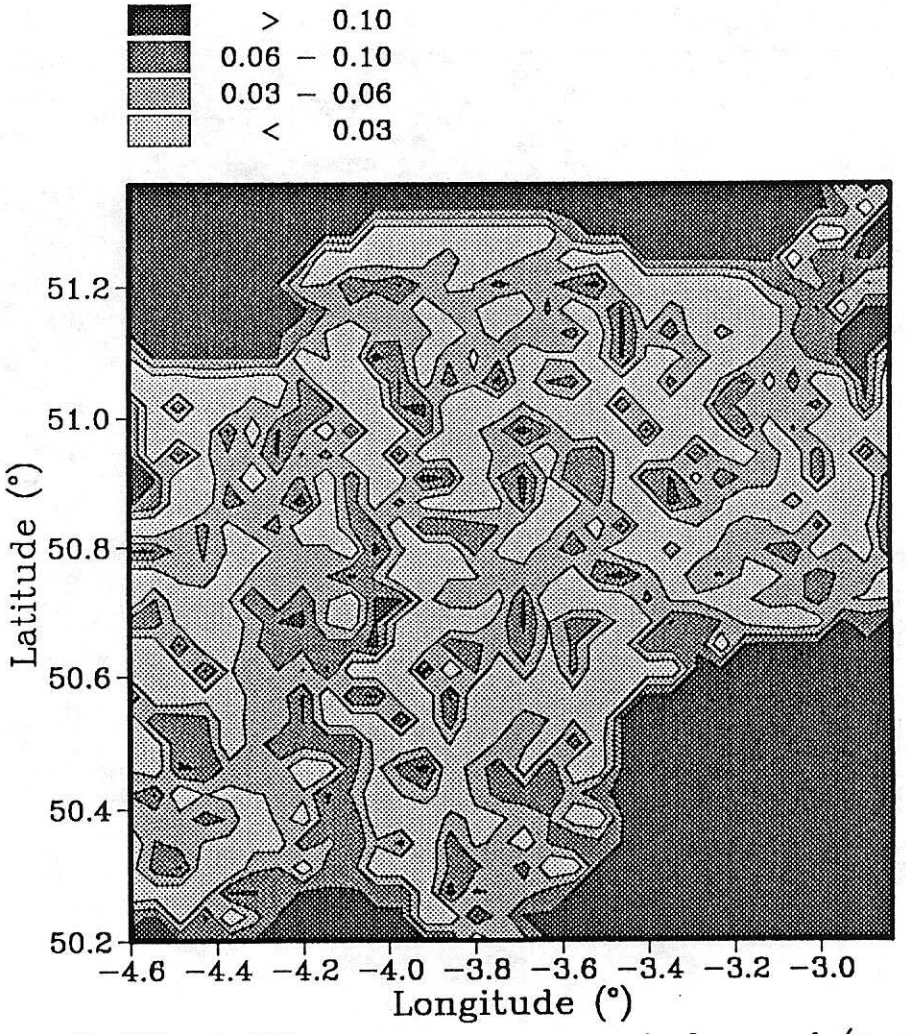

$2xCO_2 - 1xCO_2$ summer mean wind speed (ms^{-1}) in Devon for GFDL

Fig. 1.62

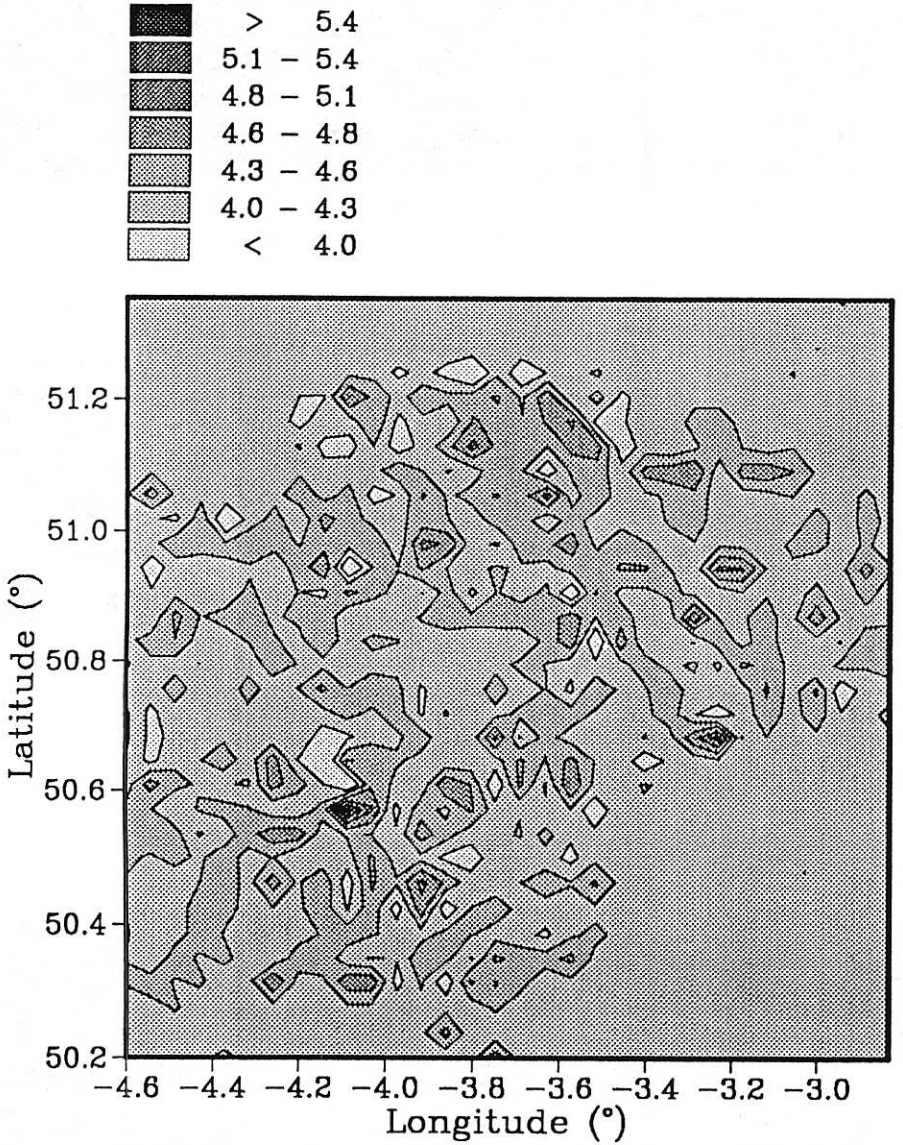

$2xCO_2$ autumn mean wind speed (ms^{-1}) in Devon for GFDL

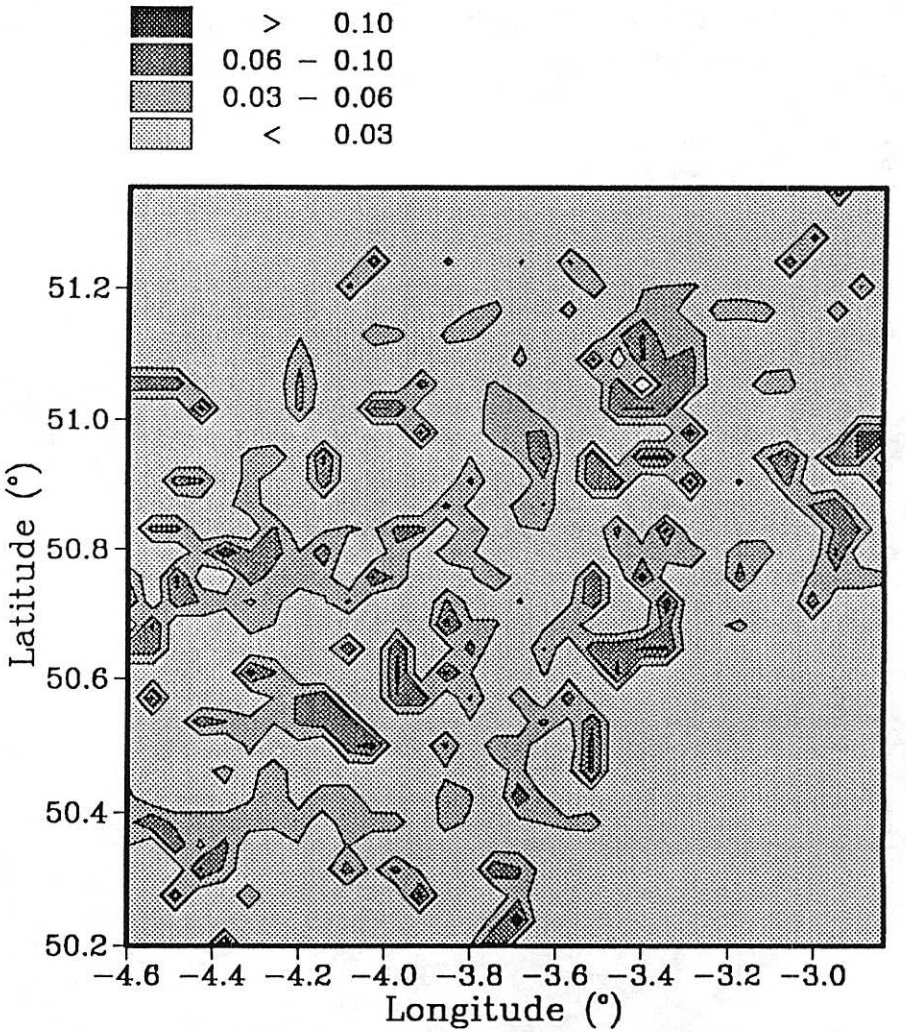

$2xCO_2 - 1xCO_2$ autumn mean wind speed (ms^{-1}) in Devon for GFDL

Fig. 1.63

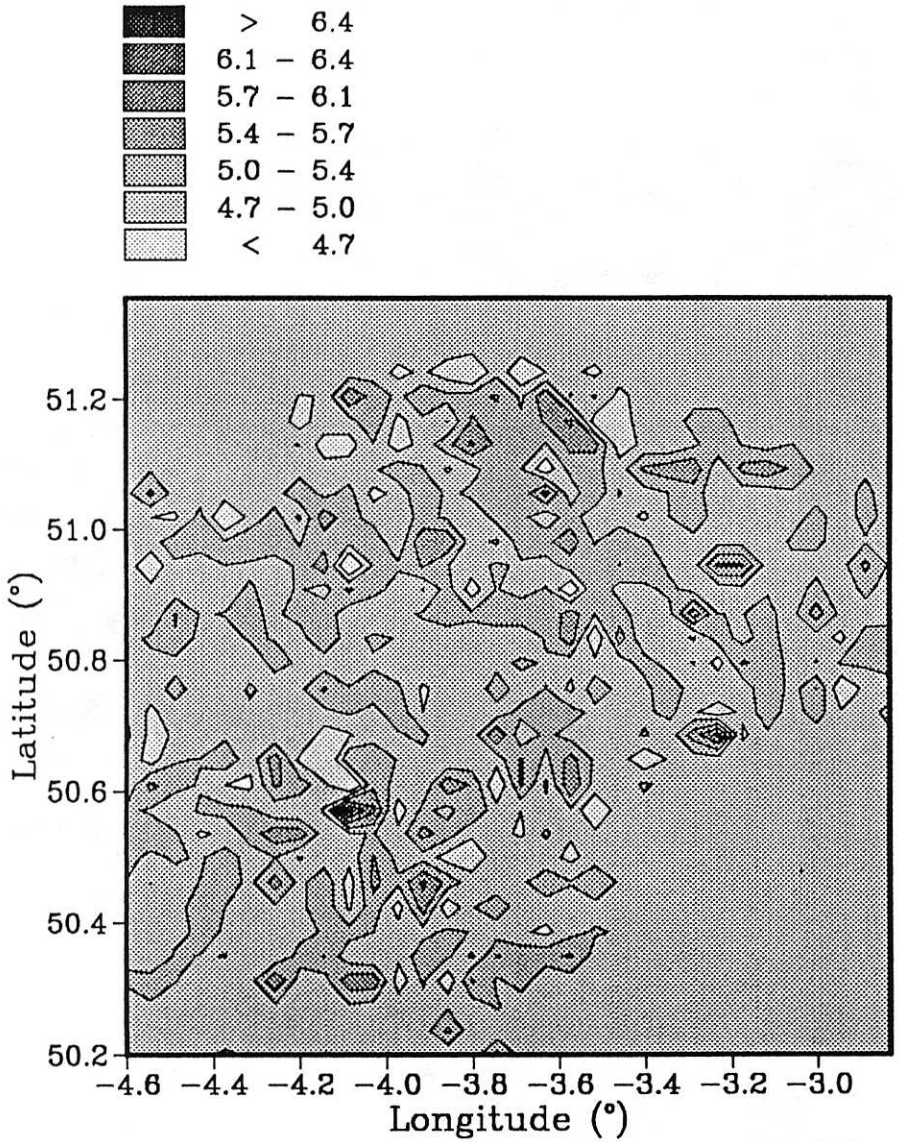

$2xCO_2$ annual mean wind speed (ms^{-1})
in Devon for GISS

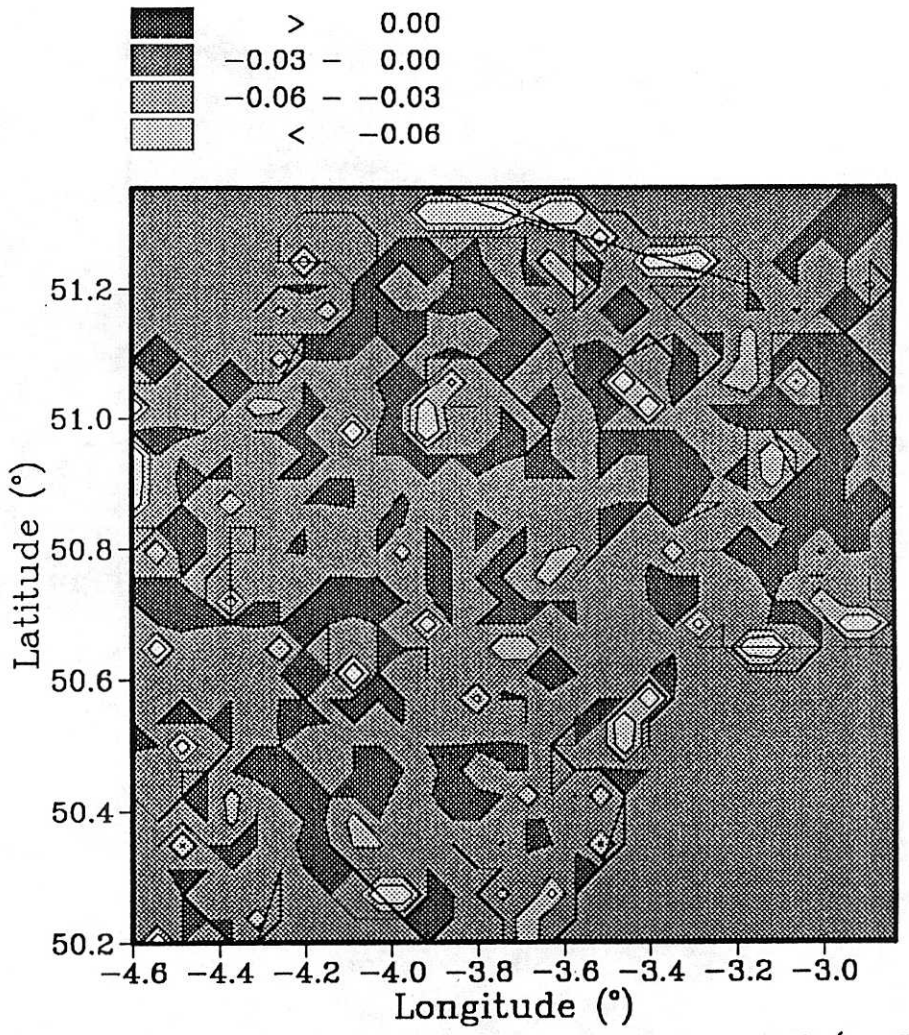

$2xCO_2 - 1xCO_2$ annual mean wind speed (ms^{-1})
in Devon for GISS

Fig. 1.64

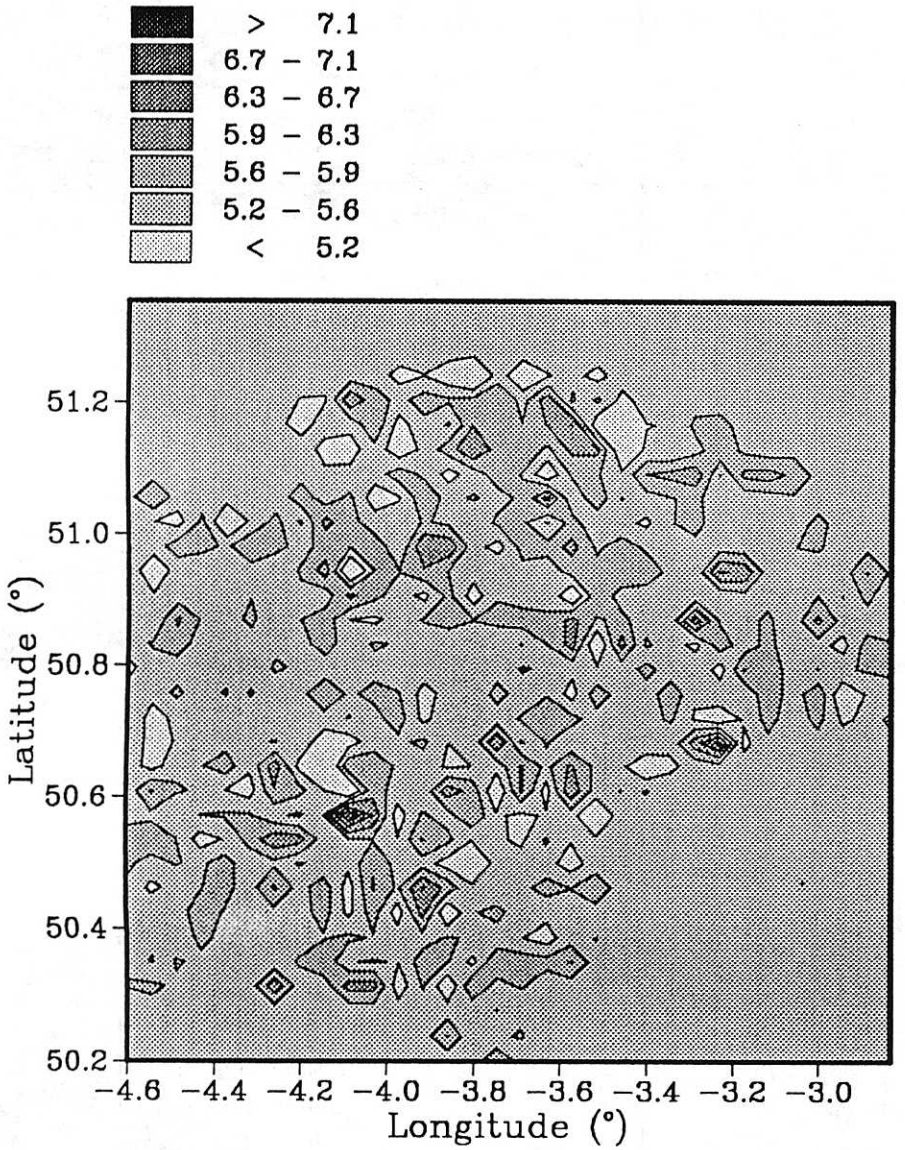

$2xCO_2$ winter mean wind speed (ms^{-1}) in Devon for GISS

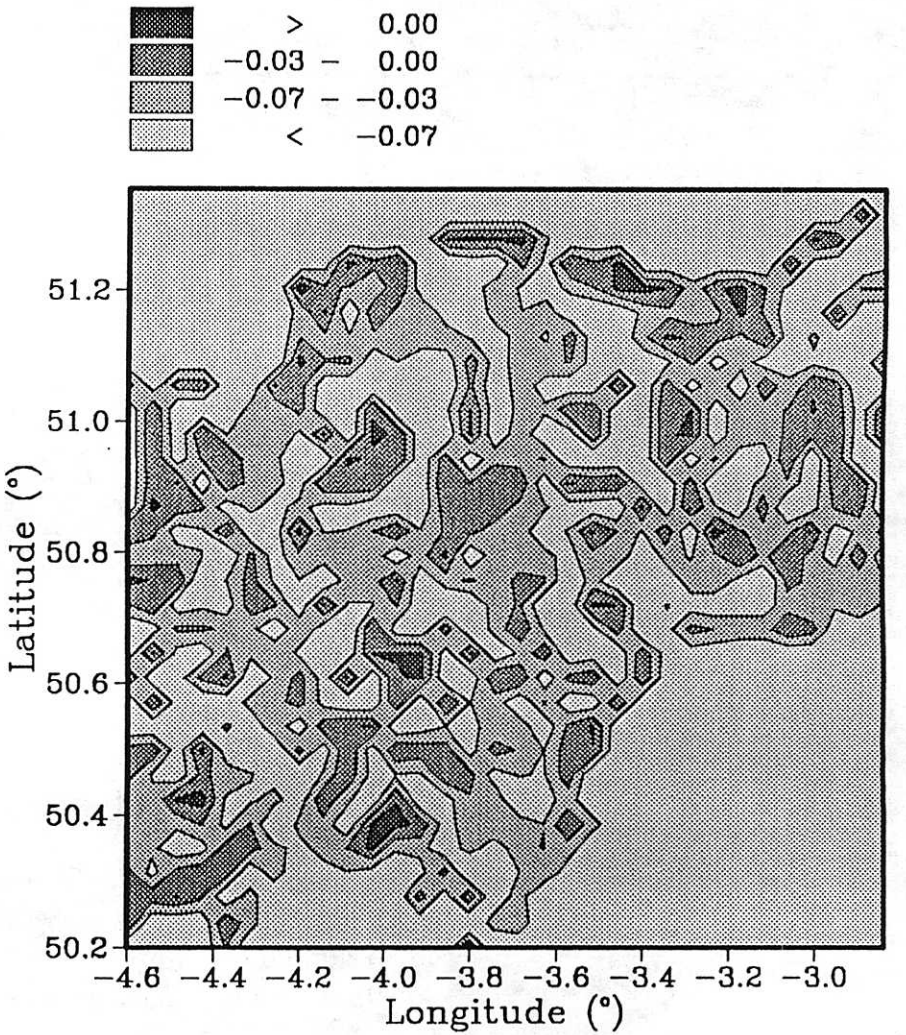

$2xCO_2 - 1xCO_2$ winter mean wind speed (ms^{-1}) in Devon for GISS

Fig. 1.65

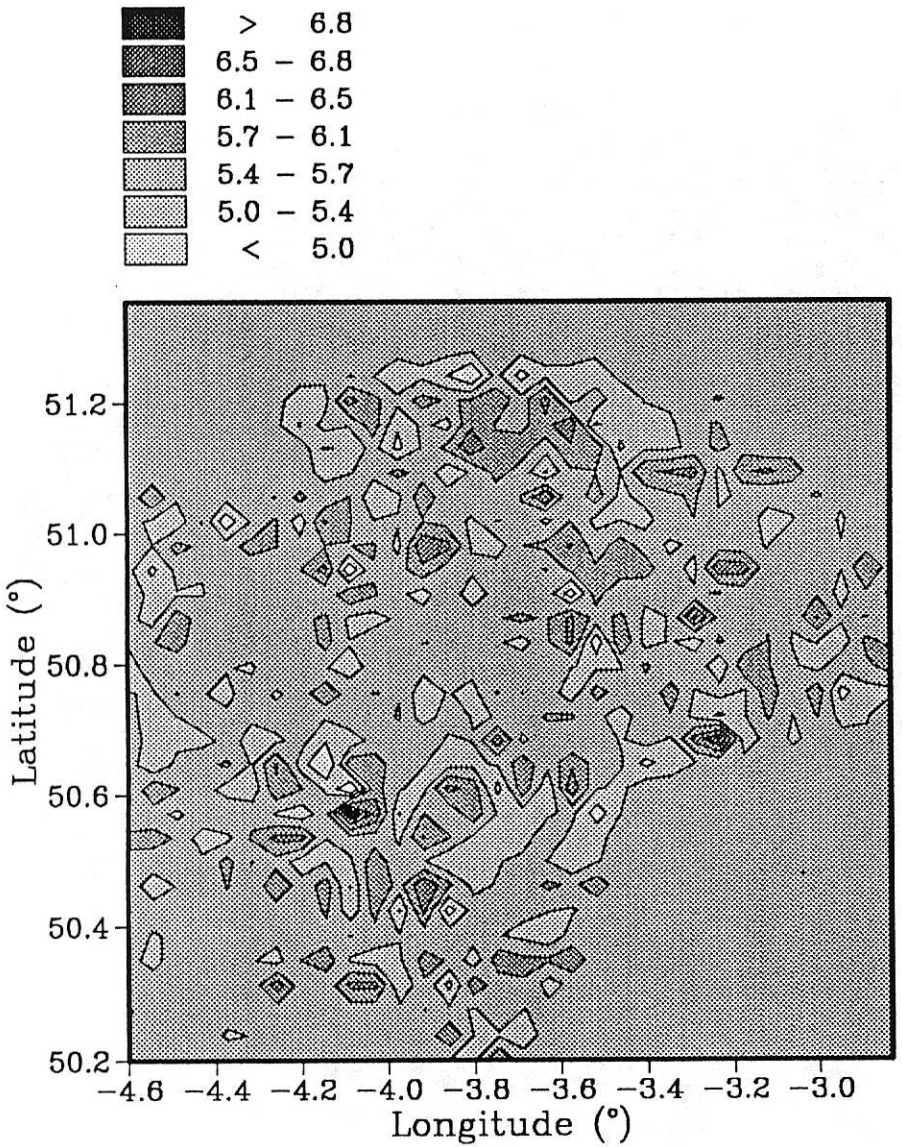

$2xCO_2$ spring mean wind speed (ms^{-1})
in Devon for GISS

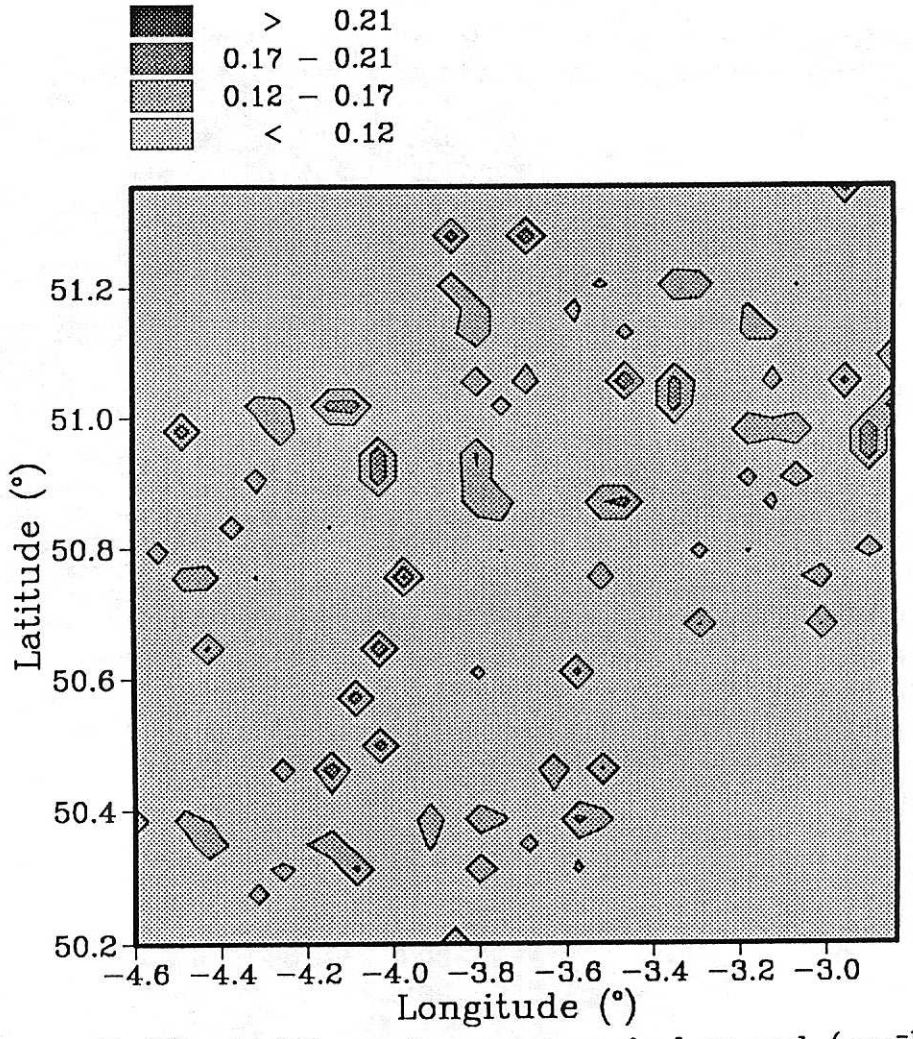

$2xCO_2 - 1xCO_2$ spring mean wind speed (ms^{-1})
in Devon for GISS

Fig. 1.66

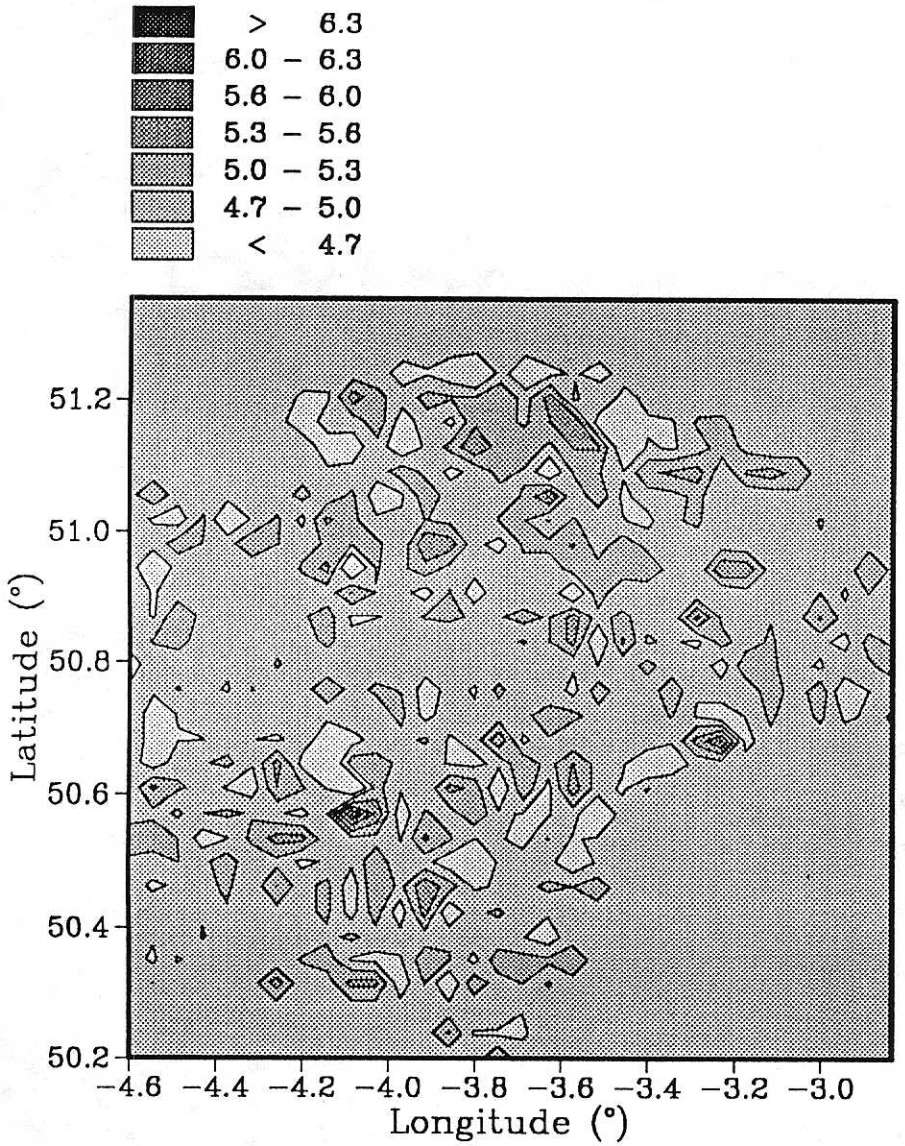

$2xCO_2$ summer mean wind speed (ms^{-1})
in Devon for GISS

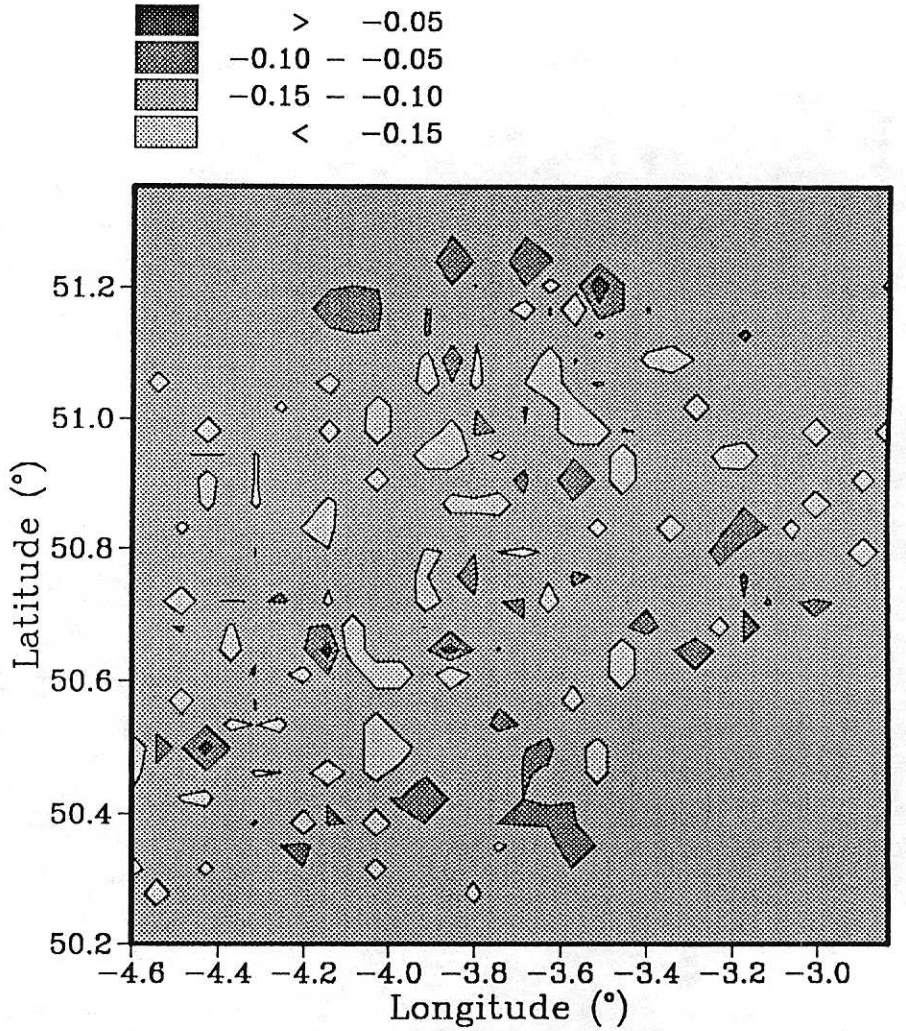

$2xCO_2 - 1xCO_2$ summer mean wind speed (ms^{-1})
in Devon for GISS

Fig. 1.67

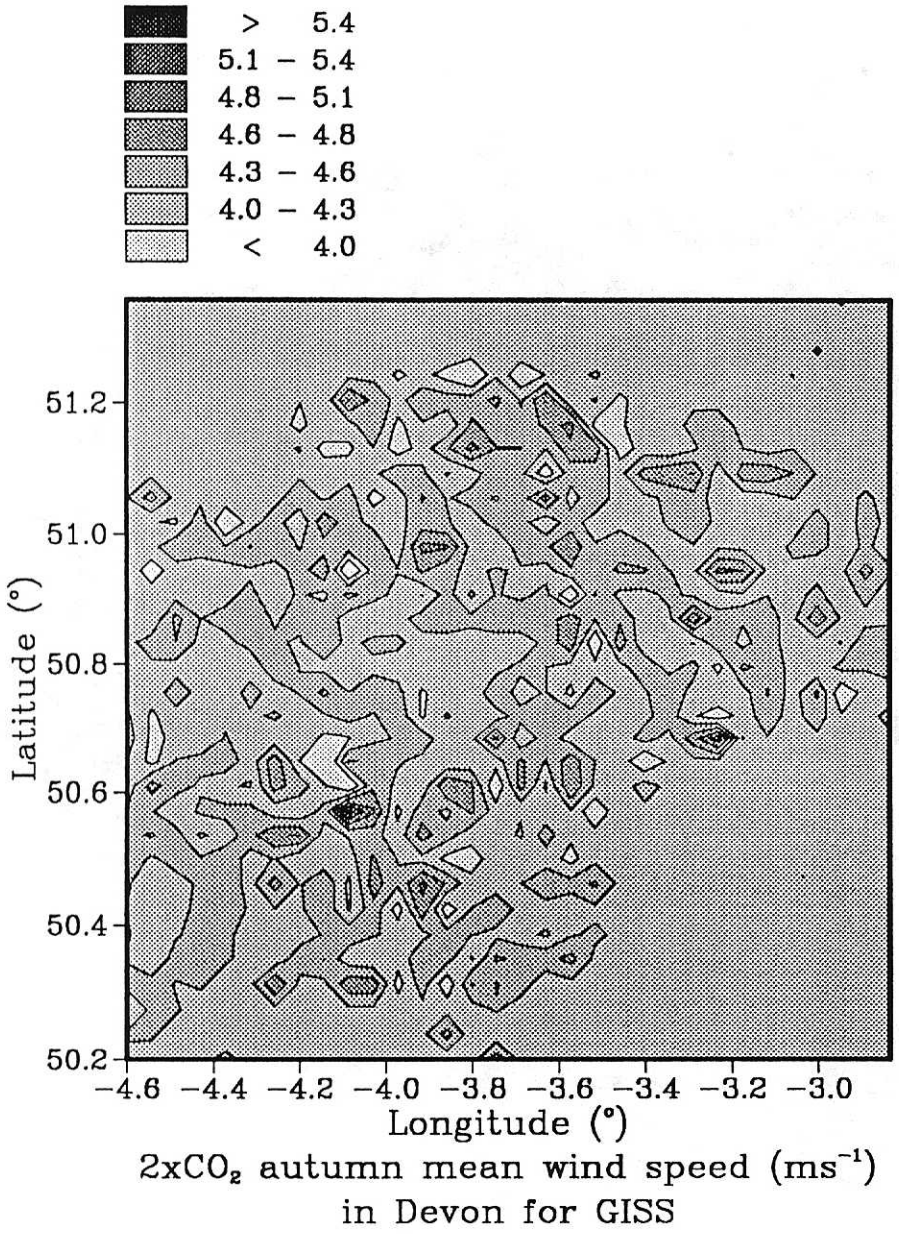

$2xCO_2$ autumn mean wind speed (ms^{-1}) in Devon for GISS

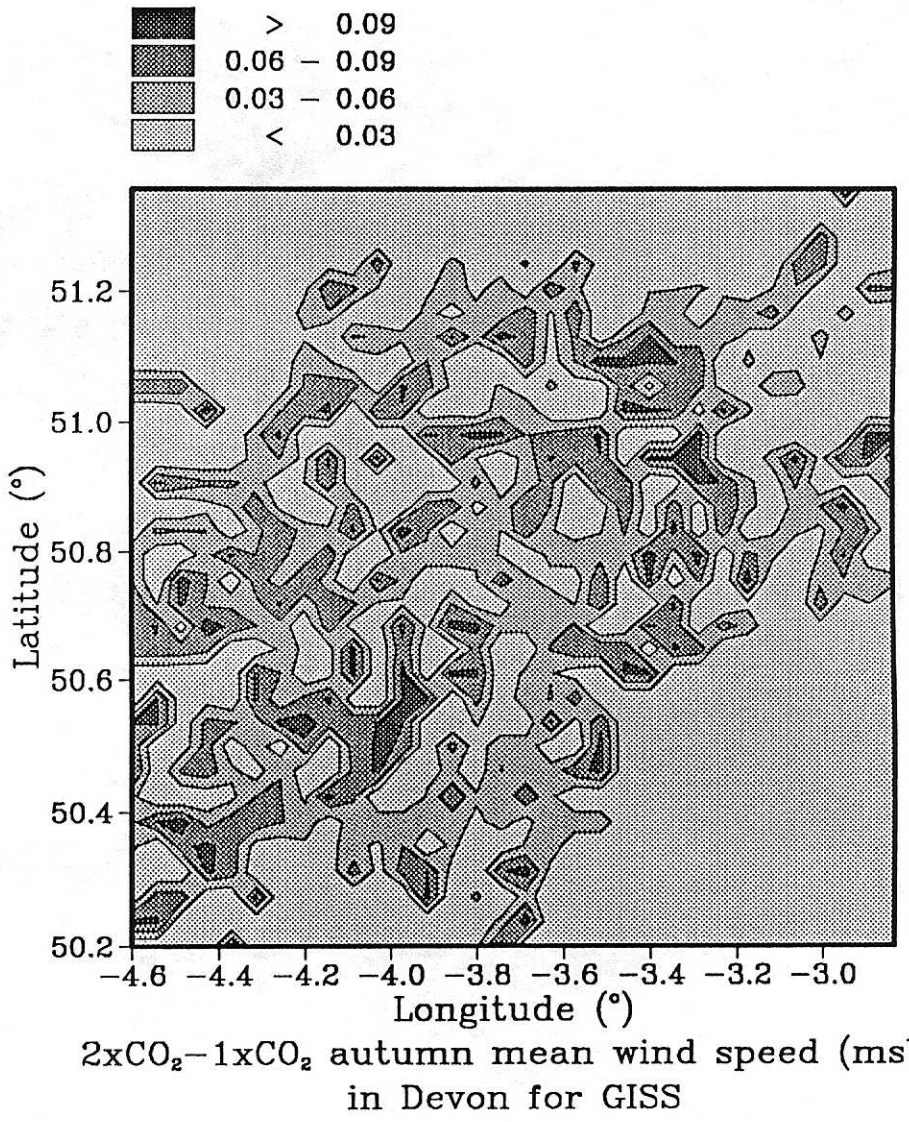

$2xCO_2 - 1xCO_2$ autumn mean wind speed (ms^{-1}) in Devon for GISS

Fig. 1.68

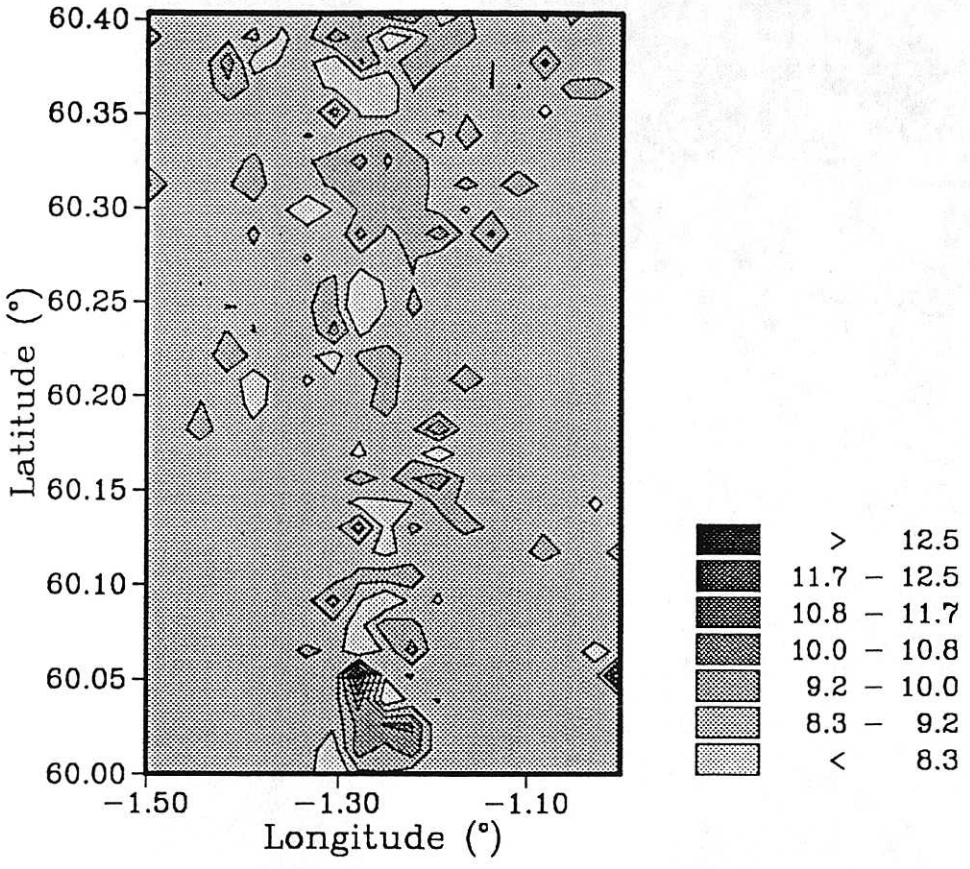

Fig. 1.69 Present-day annual mean wind speeds (ms^{-1}) in the Shetland Main Island test region, as modelled by CONFORM.

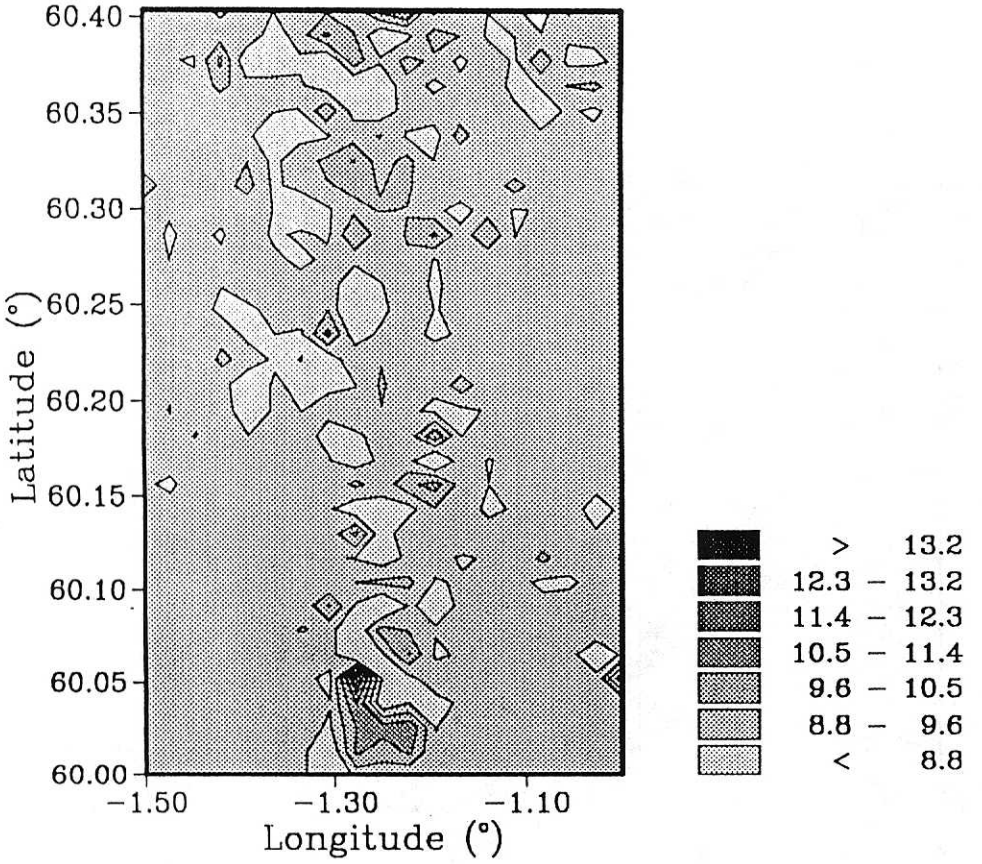

$1xCO_2$ winter mean wind speed (ms^{-1})

in Shetland

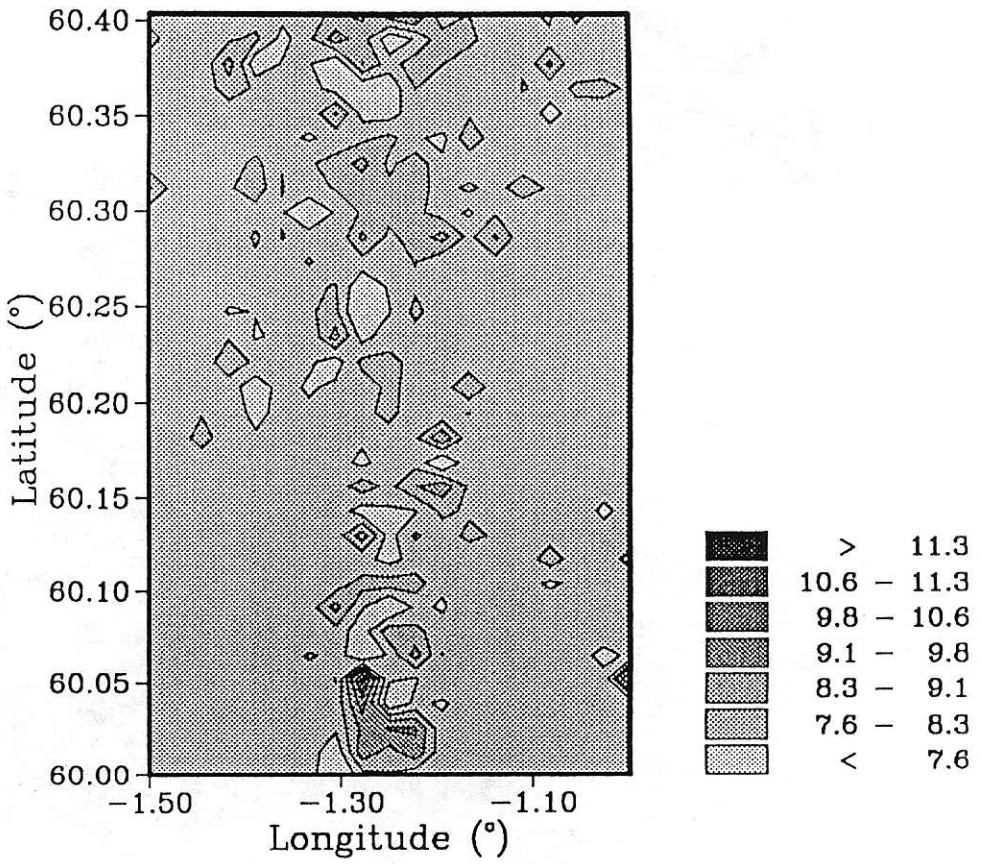

$1xCO_2$ spring mean wind speed (ms^{-1})

in Shetland

Fig. 1.70 Present-day seasonal mean wind speeds (ms^{-1}) in Shetland Main Island, as modelled by CONFORM.

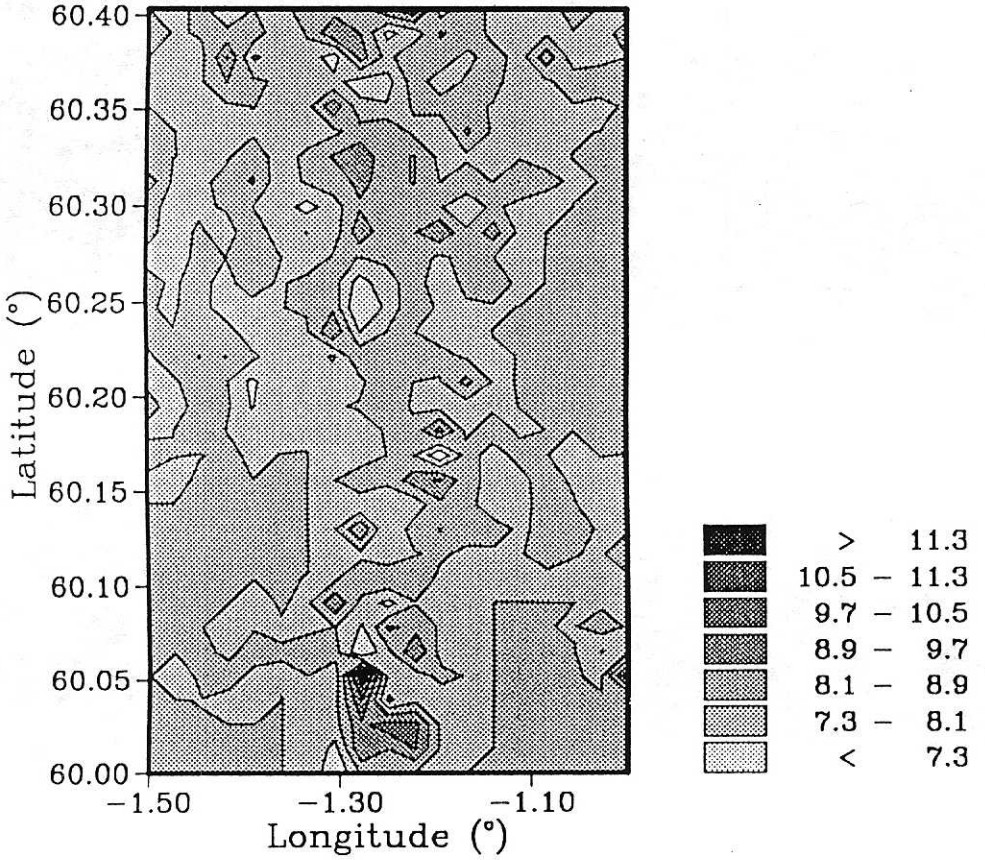

$1xCO_2$ summer mean wind speed (ms^{-1})

in Shetland

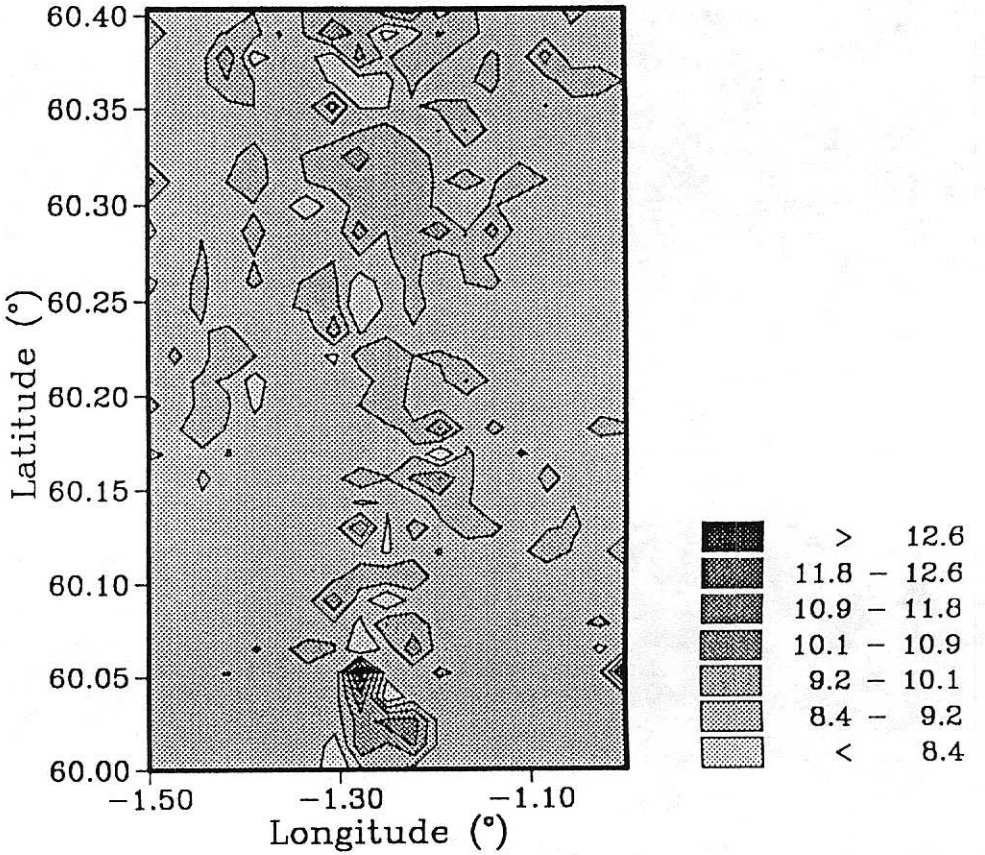

$1xCO_2$ autumn mean wind speed (ms^{-1})

in Shetland

Fig. 1.70 cont.

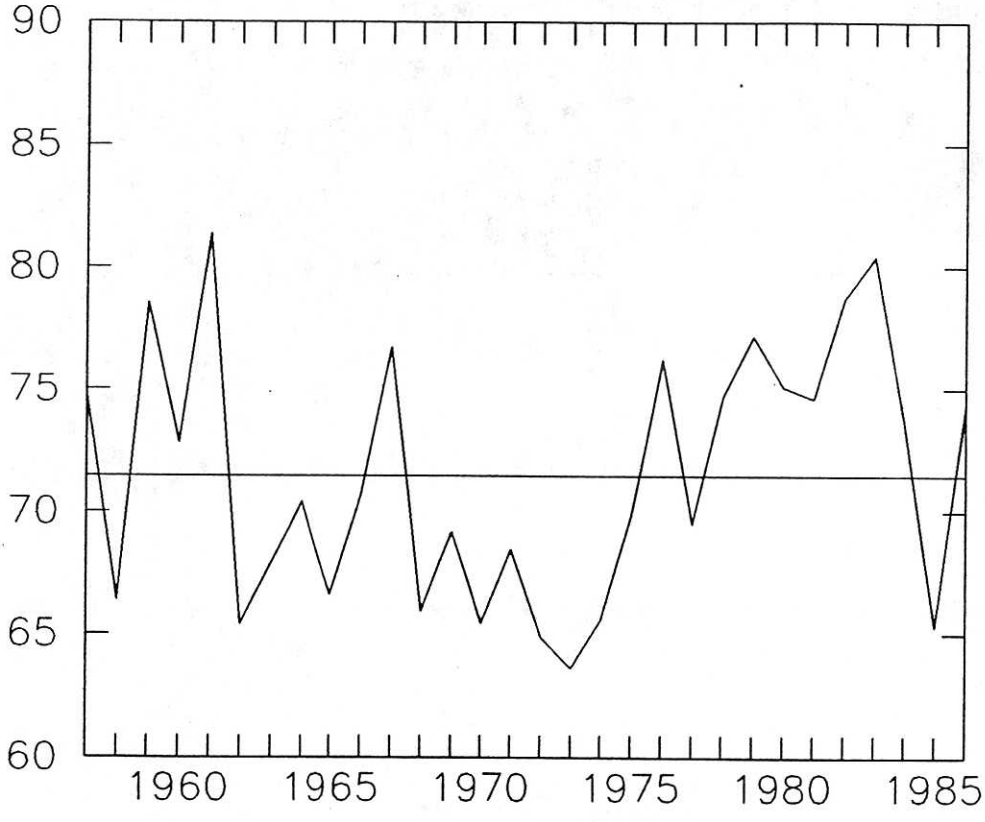

Fig. 1.71 Annual mean wind speeds (tenths ms^{-1}) at Lerwick, 1957-86.

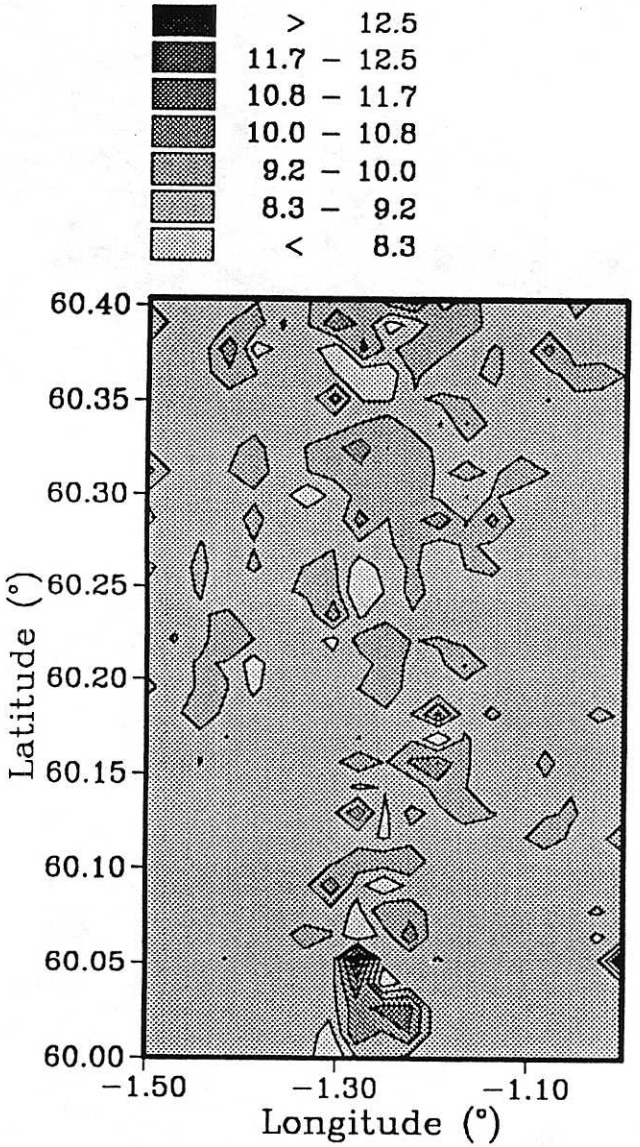

$2xCO_2$ annual mean wind speed (ms^{-1}) in Shetland for GFDL

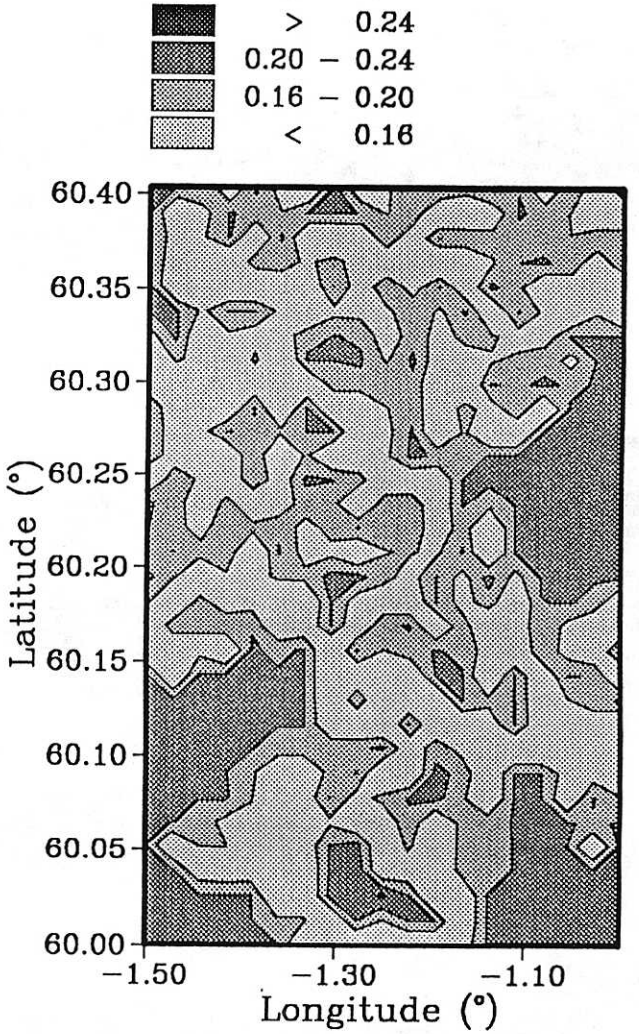

$2xCO_2 - 1xCO_2$ annual mean wind speed (ms^{-1}) in Shetland for GFDL

Fig. 1.72

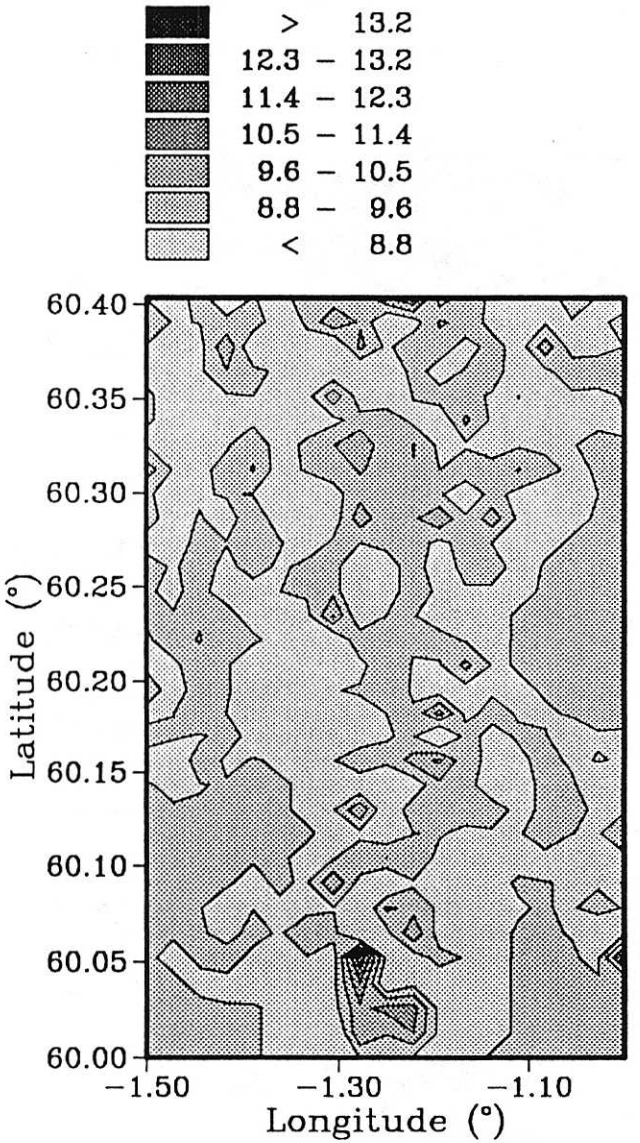

$2xCO_2$ winter mean wind speed (ms^{-1}) in Shetland for GFDL

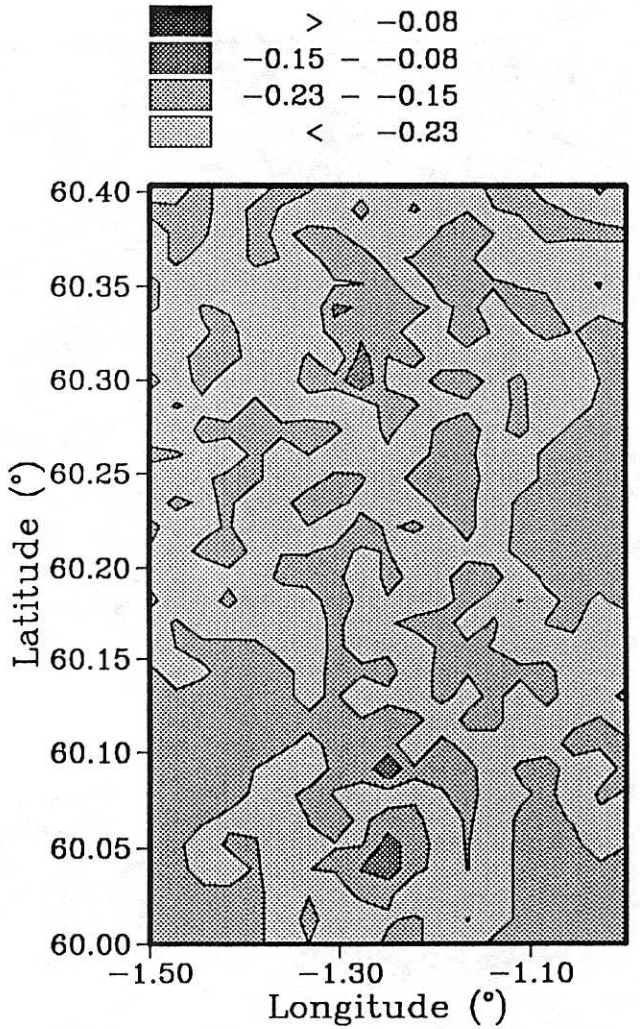

$2xCO_2 - 1xCO_2$ winter mean wind speed (ms^{-1}) in Shetland for GFDL

Fig. 1.73

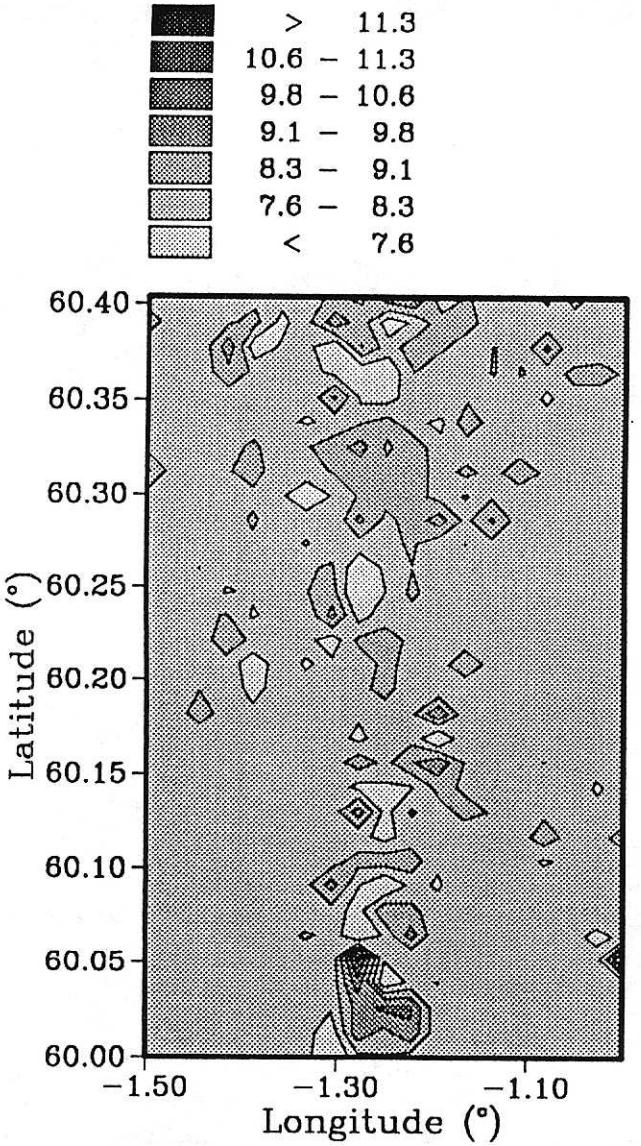

$2xCO_2$ spring mean wind speed (ms^{-1}) in Shetland for GFDL

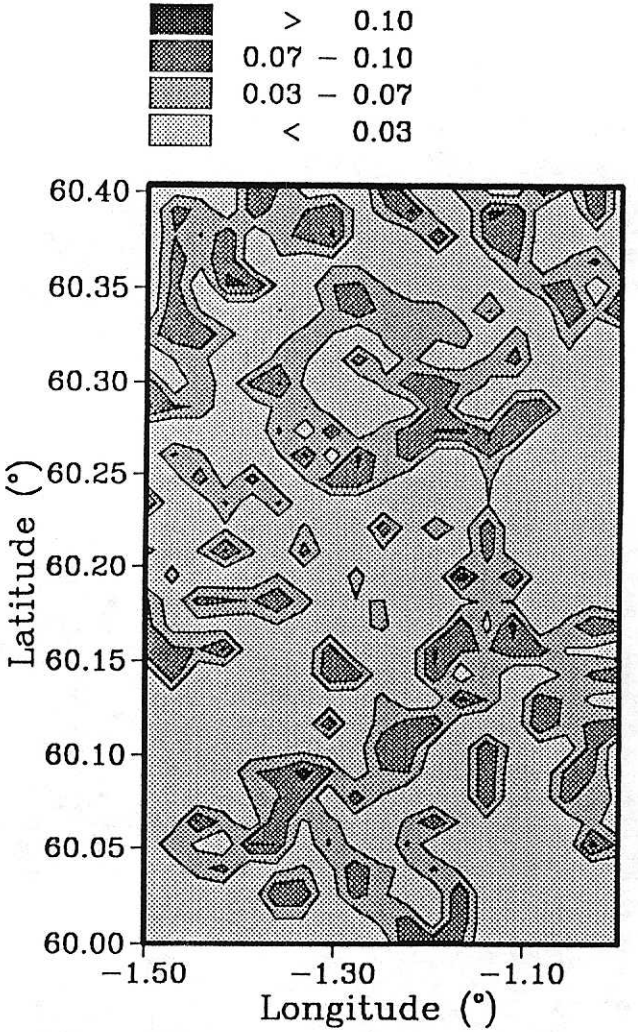

$2xCO_2 - 1xCO_2$ spring mean wind speed (ms^{-1}) in Shetland for GFDL

Fig. 1.74

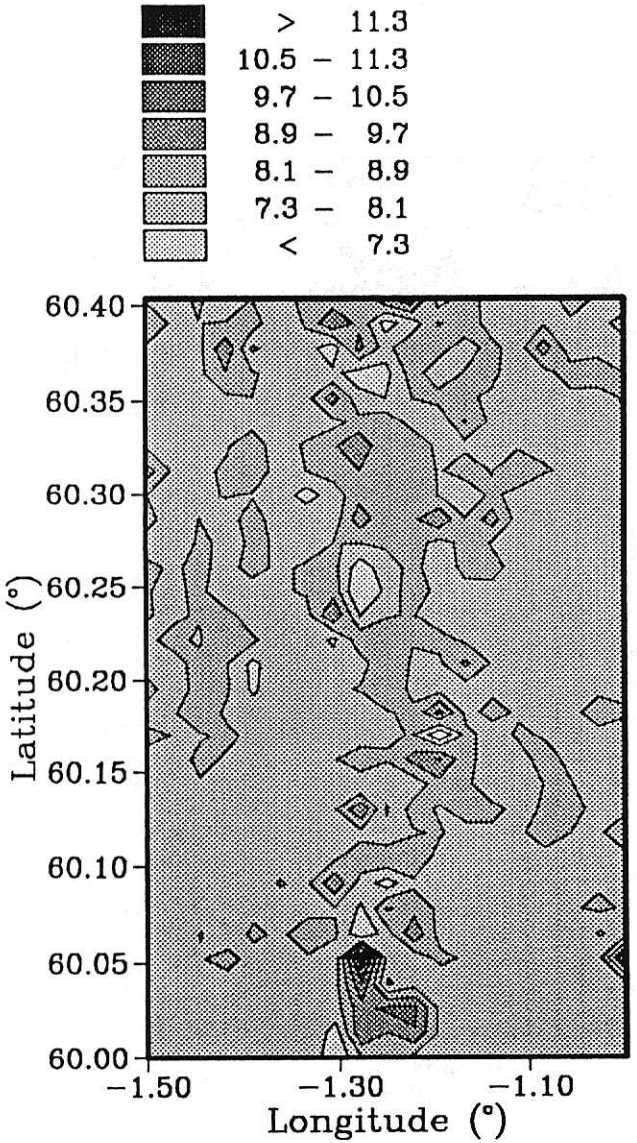

$2xCO_2$ summer mean wind speed (ms^{-1}) in Shetland for GFDL

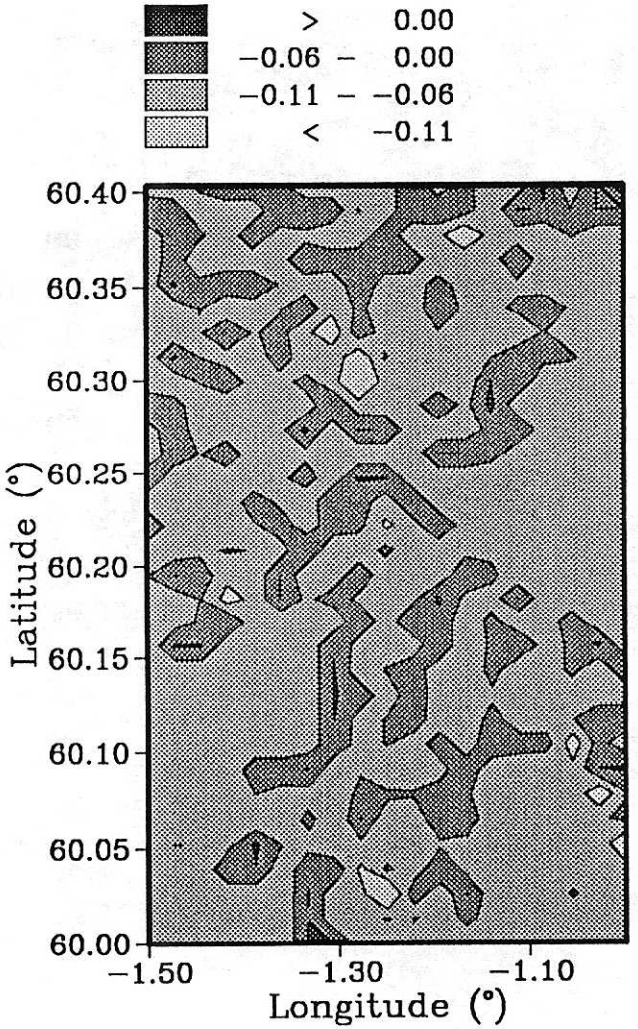

$2xCO_2 - 1xCO_2$ summer mean wind speed (ms^{-1}) in Shetland for GFDL

Fig. 1.75

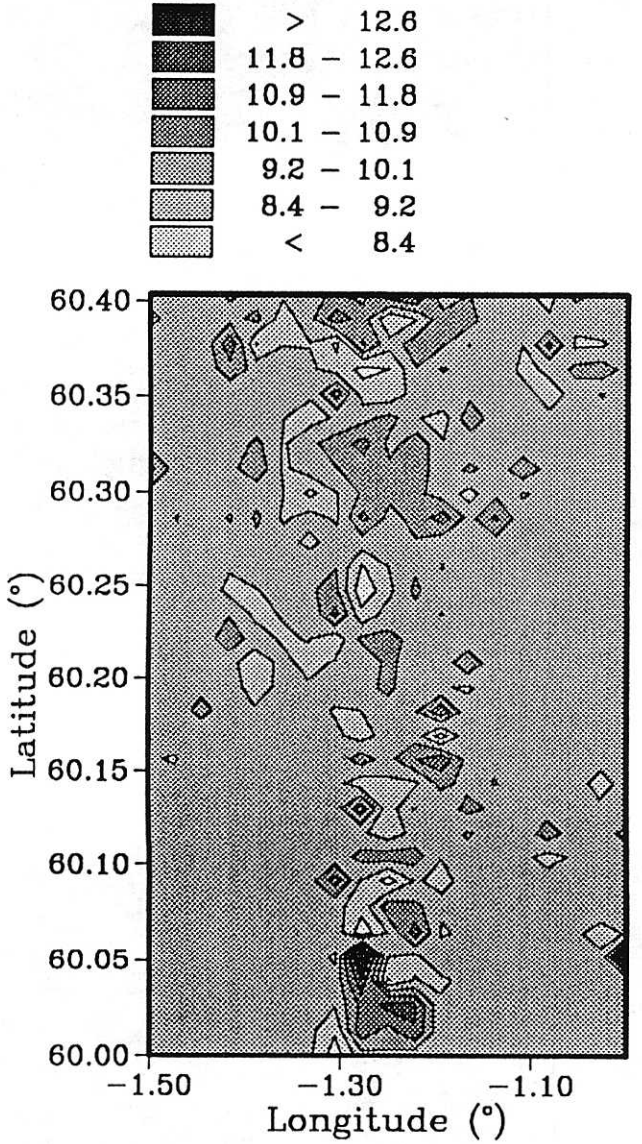

$2xCO_2$ autumn mean wind speed (ms^{-1}) in Shetland for GFDL

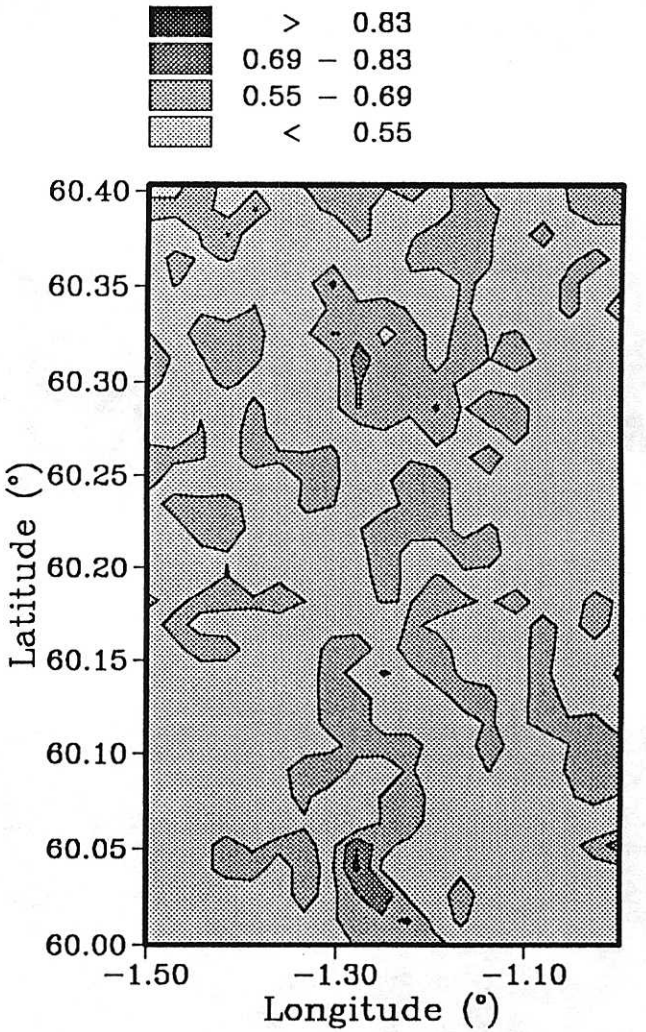

$2xCO_2 - 1xCO_2$ autumn mean wind speed (ms^{-1}) in Shetland for GFDL

Fig. 1.76

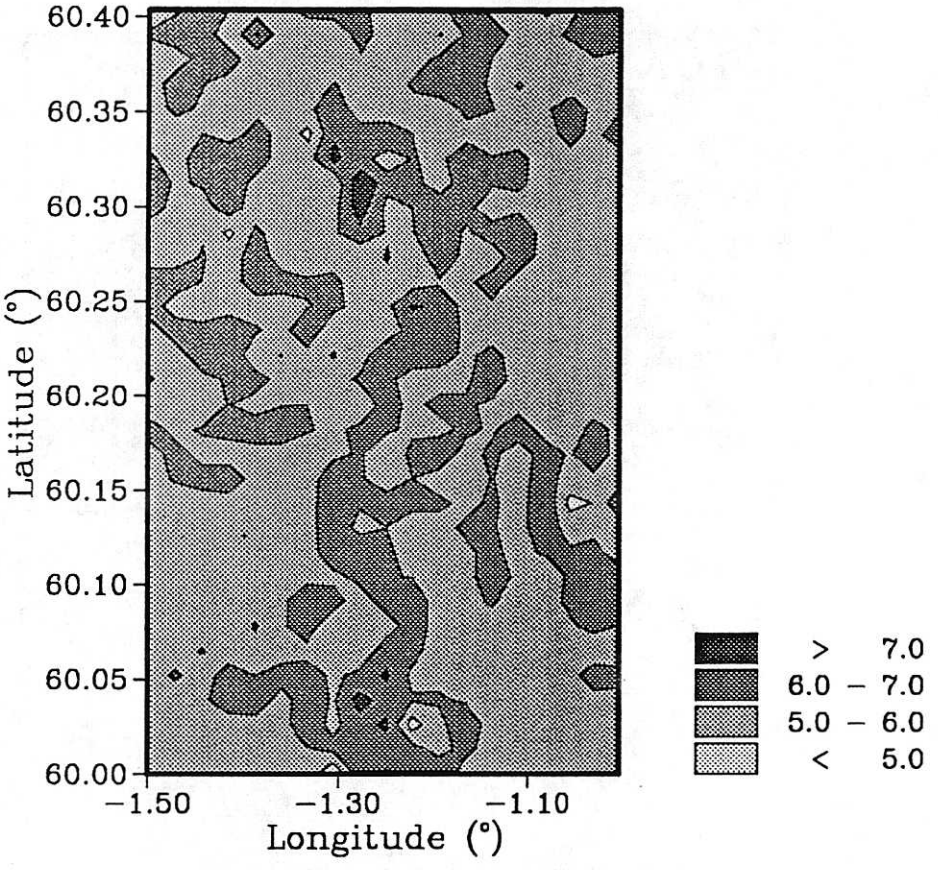

Fig. 1.77 $2xCO_2$-$1xCO_2$ percentage difference in autumn mean wind speed over the Shetland Main Island test region, as modelled by the GFDL GCM and CONFORM.

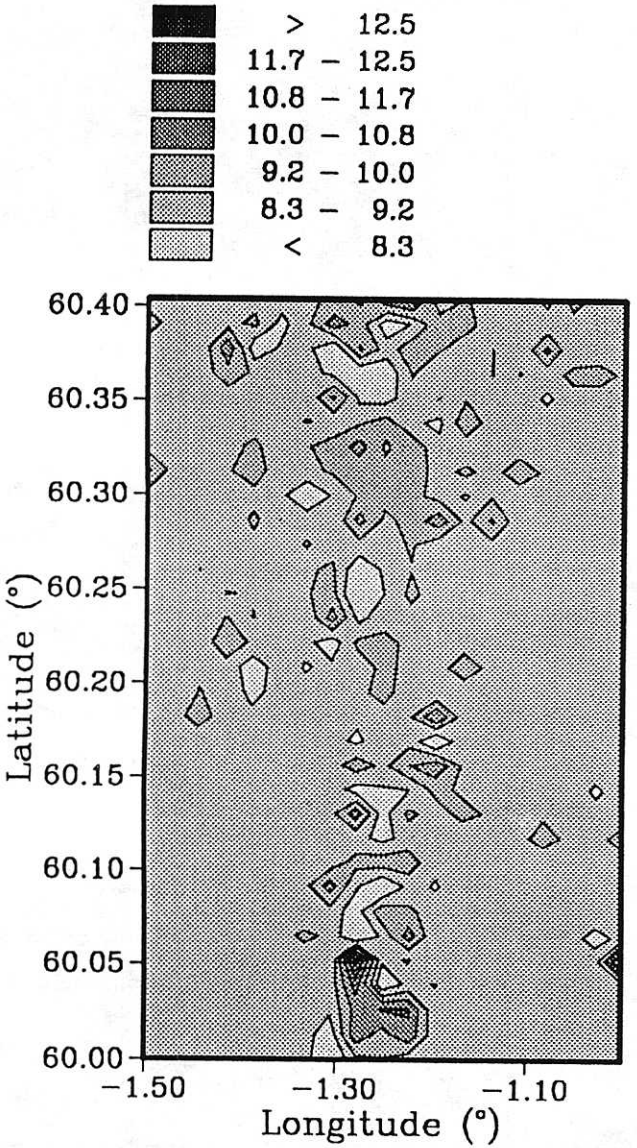

$2xCO_2$ annual mean wind speed (ms^{-1}) in Shetland for GISS

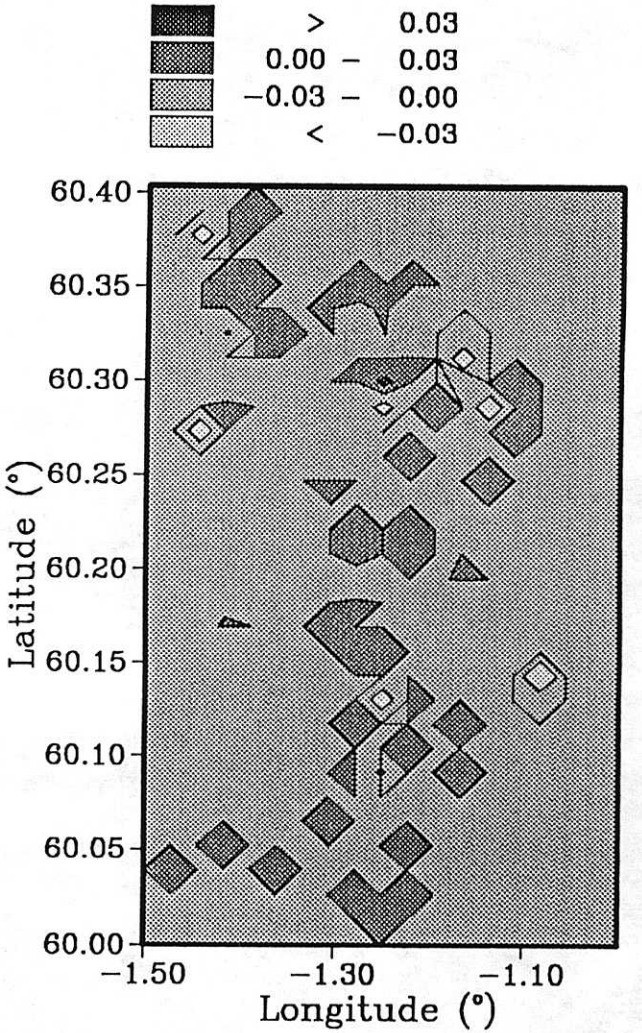

$2xCO_2 - 1xCO_2$ annual mean wind speed (ms^{-1}) in Shetland for GISS

Fig. 1.78

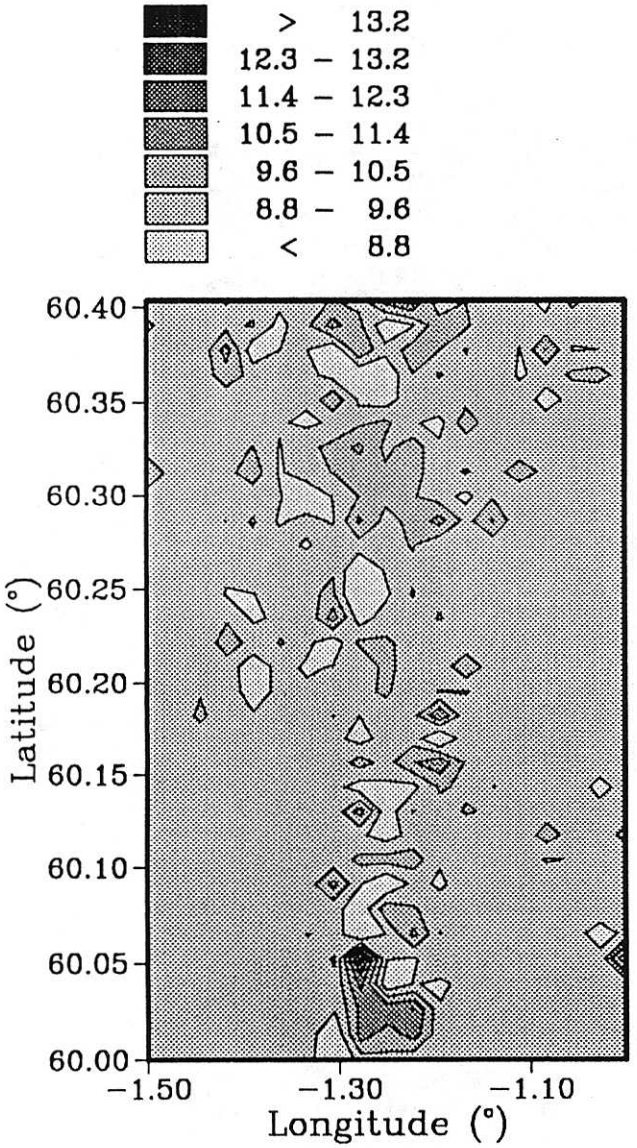

$2xCO_2$ winter mean wind speed (ms^{-1}) in Shetland for GISS

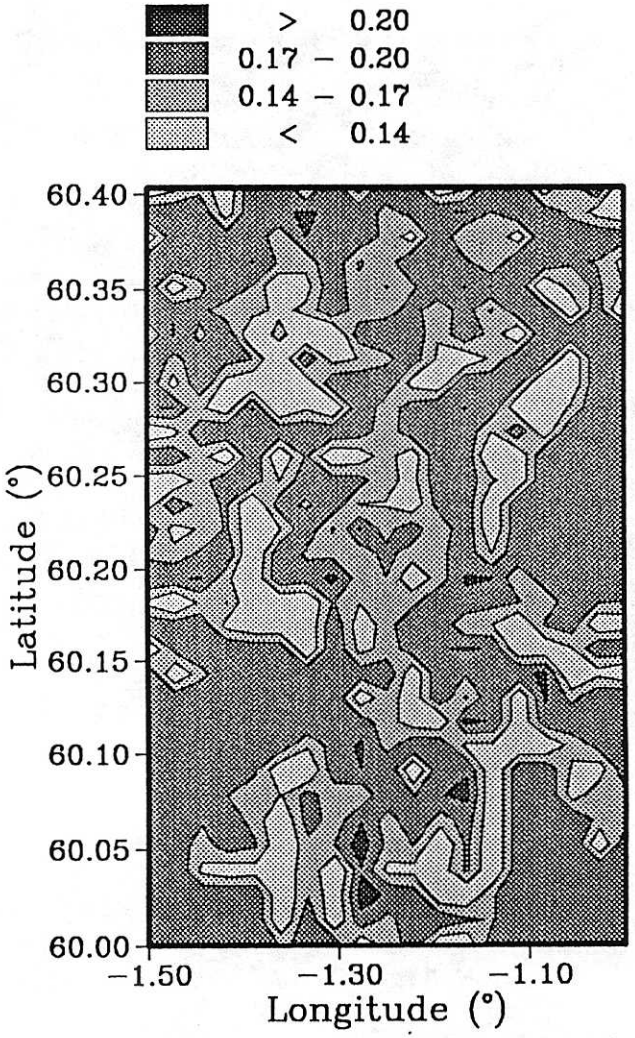

$2xCO_2 - 1xCO_2$ winter mean wind speed (ms^{-1}) in Shetland for GISS

Fig. 1.79

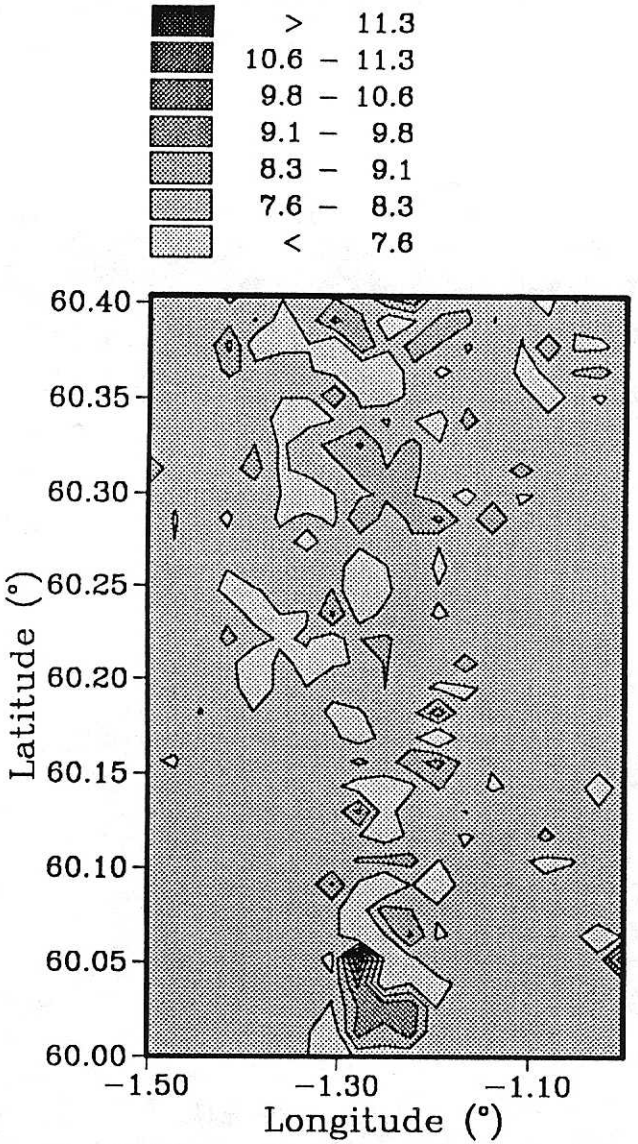

$2xCO_2$ spring mean wind speed (ms^{-1}) in Shetland for GISS

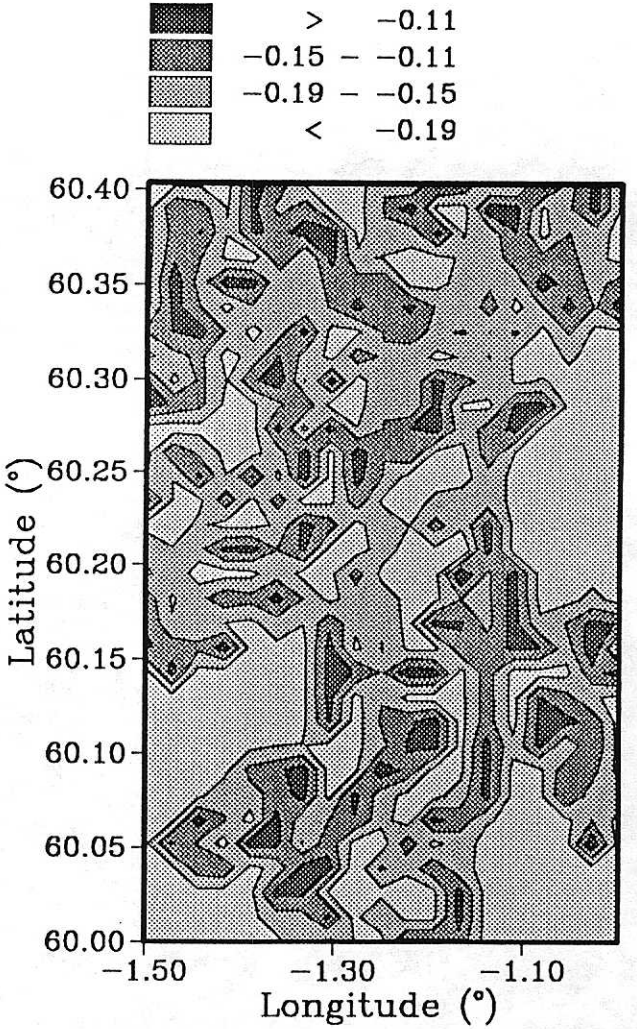

$2xCO_2 - 1xCO_2$ spring mean wind speed (ms^{-1}) in Shetland for GISS

Fig. 1.80

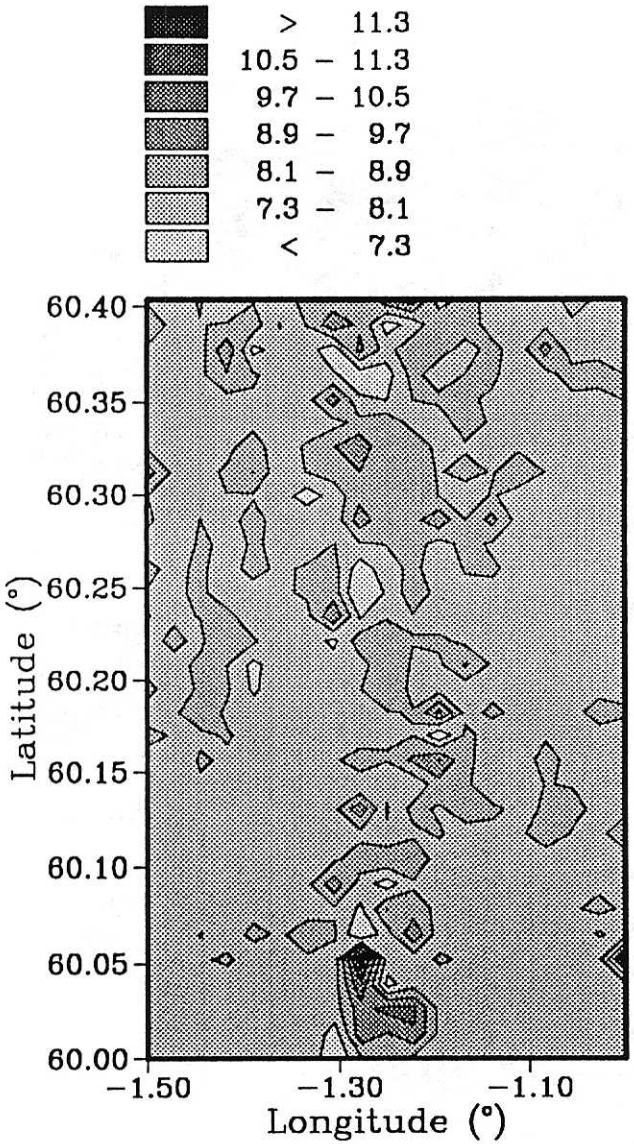

$2xCO_2$ summer mean wind speed (ms^{-1}) in Shetland for GISS

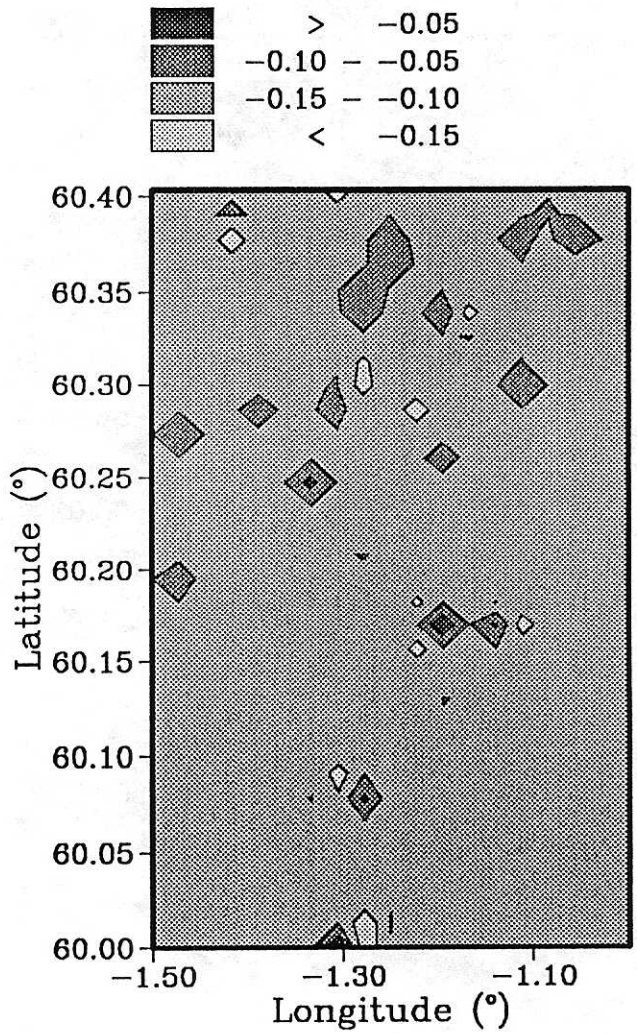

$2xCO_2 - 1xCO_2$ summer mean wind speed (ms^{-1}) in Shetland for GISS

Fig. 1.81

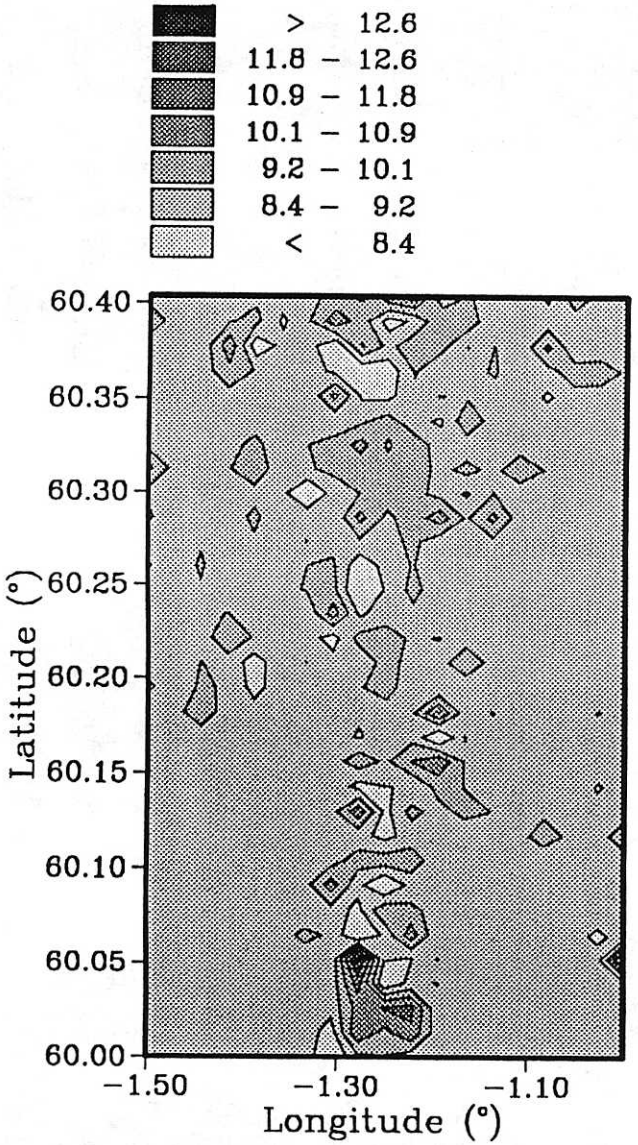

$2xCO_2$ autumn mean wind speed (ms^{-1}) in Shetland for GISS

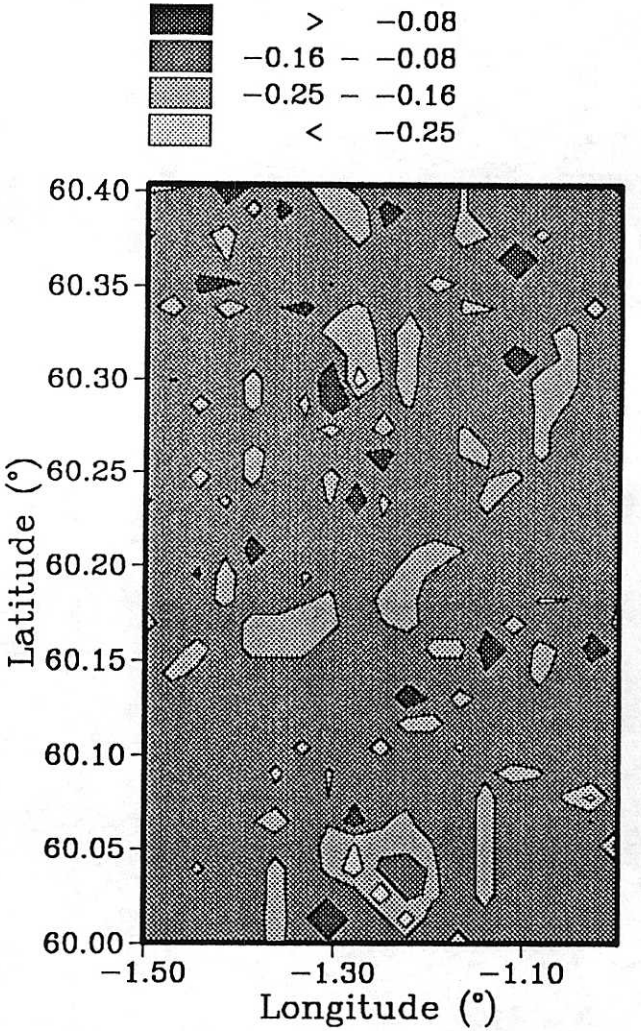

$2xCO_2 - 1xCO_2$ autumn mean wind speed (ms^{-1}) in Shetland for GISS

Fig. 1.82

4. THE GREENHOUSE EFFECT AND MAXIMUM GUST SPEEDS

A gust may be defined as a rapid increase in the strength of the wind relative to the mean strength obtaining at the time (McIntosh, 1972). Gust speeds are not modelled directly by GCMs. Yet for many applications it is more important to understand the implications of the greenhouse effect for gust speeds than it is to know the possible effects on mean wind speeds. The amount of damage to buildings, trees and electricity supply systems is determined by gust speeds, and if these speeds should increase in a high greenhouse gas world, then the amount of damage will also increase.

In order to investigate the effect of greenhouse warming on gust speeds, we have looked at the sensitivity of gust speeds to a change in the mean wind speed. If we examine the spectrum of the horizontal wind speed in temperate latitudes, we find two strong peaks. The first has a centre-frequency of 0.01 cycles/hour, corresponding to the typical 4-day transit time of major synoptic systems and termed the macrometeorological peak. The second peak contains higher frequencies corresponding to periods from about 10 minutes to less than 3 seconds and is associated with the turbulence in the boundary layer. This is called the micrometeorological peak. The hourly mean wind speed contains only fluctuations of the wind climate associated with the macrometeorological peak, whereas the gust speed contains also the turbulence of the micrometeorological peak. Thus the maximum gust speed for a particular hour can be expressed in terms of the mean wind speed of that hour and the inwind turbulence intensity. In turn, provided the terrain is flat and uniform, the ratio of the inwind turbulence intensity at a particular height above ground to the mean wind speed at the same height is a function only of the roughness length of the terrain, the zero-plane displacement and the gradient height. These relationships, taken from Cook (1985), form the basis of our analysis of the response of the maximum gust speed to a forcing of the mean wind speed.

4.1 The methodology

For these sensitivity studies, we took as our example the Dungeness wind record, using data from 1979. This anemometer, now closed, was sited on a shingle bank close to the sea at OS grid reference (61) 090171. The site therefore fulfills the criteria that it should be flat and that the incoming wind should not experience marked changes in the roughness length of the surface over which it passes. The relationship between the mean speed and the gust speed becomes more complex where these criteria are not fulfilled.

4.1.1. Treatment of the hourly mean wind speed data

The Dungeness hourly wind speed data were first standardized to a surface roughness length of 0.03m. We took the real roughness lengths, as computed from 1:25,000 topographic maps (see Palutikof et al., 1989). Then, assuming a logarithmic wind speed profile through the boundary layer, we computed the mean wind speed at each hour at 60m above the surface from the formula:

!!?
How can you get real surface roughness from 1:25000 map? Must be a modelled roughness of some sort.

$$v_m = v_h[\ln(z_m/z_0)/\ln(z_h/z_0)] \qquad ...1$$

where
v_m is the wind speed at 60m above the ground;
v_h is the observed wind speed;
z_0 is the roughness length in the 30° sector in which the wind speed observation occurs;
z_h is the anemometer height, here 10m above ground;
z_m is set equal to 60m.

The height of 60m is assumed to be the blending height, where the effect of the individual roughness length elements will have blended to an overall value (Wieringa, 1986). The wind at this height is termed by Wieringa the mesowind. If we therefore proceed to substitute a value of z_0 = 0.03m in an equation of the form of Equation 1, we can derive the 10m roughness-standardized wind speed from the mesowind speed.

We assumed, in common with many investigators, that the best-fit probability distribution for hourly mean wind speeds is the two-parameter Weibull distribution (see Conradsen et al., 1984 for a review). The Weibull probability density function may be expressed as follows:

$$P_w(V) = (k/c)(V/c)^{k-1}\exp[-(V/c)^k] \qquad ...2$$

where V is the wind speed;
c is the scale parameter (same units as V);
k is the shape parameter (dimensionless).

The two parameters of the distribution, c and k, can be calculated using the maximum likelihood method (Law and Kelton, 1982). When c and k are calculated for the actual and roughness-standardized hourly mean wind speeds at Dungeness we obtain:

	c(ms^{-1})	k
Observed	7.1158	2.0561
Roughness-standardized	7.1451	2.1039

Looking at the scale parameter, c, it can be seen that the standardization procedure has made little impact. This is because, as already noted, this is a flat open sea-side site, with few obstructions.

It was decided to investigate the sensitivity of gust speeds to an increase in the hourly mean wind speeds of 0.5ms^{-1}, 1.0ms^{-1} and 1.5ms^{-1}. Accordingly, three new data sets (F1, F2 and F3 respectively) were created from the standardized-roughness data set. This was done simply by adding the appropriate amount to each value in the initial, present-day, data set of hourly mean wind speeds. Taking the example of the +0.5ms^{-1} data set, the new c and k parameters are 7.6692ms^{-1} and 2.2225. It can be noted that the value for the shape parameter has changed. This is because the Weibull parameter commences at zero, and the shape parameter must therefore 'stretch' in order to accomodate the new distribution, rather than simply shift along. This is an important point, which will be returned to later.

4.1.2 Treatment of the maximum gust speeds

Using the method described by Cook (1985), the ratio of the maximum gust in any hour to the mean speed (the gust factor) can be computed. We obtained, by this method, a gust factor of 1.36 for 3-second gusts, and a gust factor of 1.41 for 1-second gusts. When these gust factors were compared with a set of actual gust speeds, they were found to be too low. It was assumed that the gust speeds would

Table 1.3 Gust speed data set scale and shape parameters.

Data set	c(ms^{-1})	k
G	11.4548	2.0832
GS	11.4654	2.1093
G1	12.3012	2.2236
G2	13.1207	2.3251
G3	13.9502	2.4372

also conform to a Weibull distribution (and visual inspection showed that this was a reasonable assumption). The scale parameter for the actual gust speeds was found to be 11.45ms^{-1}. When gust speeds were calculated from the roughness-standardized hourly mean wind speeds using the computed gust factors, we obtained a scale parameter of 10.11ms^{-1} for 1-second gusts and 9.71ms^{-1} for 3-second gusts. We therefore assigned a gust factor of 1.60, computed from the ratio of the gust speed scale parameter (11.45ms^{-1}) to the roughness-standardized hourly mean speed scale parameter (7.15ms^{-1}).

The three data sets of hourly mean wind speeds, F1, F2 and F3, were incremented at each hour using the gust factor of 1.60, to produce synthetic data sets of gust speeds, G1, G2 and G3. The scale and shape parameters of the Weibull distribution for each of the gust speed data sets were then calculated, and are listed in Table 1.3 along with c and k for the present-day observed gust speeds (G) and the gust speeds computed from the roughness-standardized wind speeds and a gust factor of 1.60 (GS).

4.2 Maximum gust speed scenarios

Using the c and k parameters and a random number generator, 100-year synthetic data series of the maximum gust speed in each hour were created for GS, G1, G2 and G3. The maximum value in each year was then extracted. The results are plotted in Fig. 1.83, and exceedance values are given in the upper part of Table 1.4.

Table 1.4 shows that at the present day we may expect the highest gust speed in a year to exceed 20ms^{-1} four times in a century. This frequency rises to 14

times per century when the mean hourly wind speeds are augmented by $0.5ms^{-1}$, and to 24 times per century for an augmentation of $1.5ms^{-1}$. For the four data sets, GS, G1, G2 and G3, the maximum gust speeds over the 100 years are:

GS	$22.97ms^{-1}$
G1	$26.89ms^{-1}$
G2	$29.83ms^{-1}$
G3	$28.58ms^{-1}$

It can be seen that the maximum gust speed actually decreases between G2 and G3 even though G2 is based on the mean hourly wind speed plus $1.0ms^{-1}$, whereas G3 is based on the mean hourly wind speed plus $1.5ms^{-1}$. The reason for this has already been referred to: as the scale parameter of the Weibull distribution changes, the shape parameter must also change in order to encompass the full range of values starting from zero. In Fig. 1.84 we show the percentage frequency distribution for GS and G3, along with the fitted Weibull curves. When the two Weibull curves are plotted together (Fig. 1.85a), it can be seen that the tail of the G3 curve extends by only a very small amount beyond the tail of the GS curve.

The impact of this effect has been investigated further, by constraining the shape parameter to the initial value for GS (2.11) while allowing the scale parameter to vary according to the imposed forcing. Fig. 1.85b shows the effect of prescribing the shape parameter. The tail of the G3 curve now extends well beyond that of the GS curve. In Fig. 1.86 the G3 frequency distribution is shown, with the Weibull curve for a free scale parameter and a shape parameter of 2.11 superimposed.

The effect of prescribing the shape parameter is shown in the lower part of Table 1.4. The number of occurrences greater than $20ms^{-1}$ for G1 (hourly mean wind speeds increased by $0.5ms^{-1}$) has risen from 14 to 15, and for G3 (hourly mean wind speeds increased by $1.5ms^{-1}$) from 24 to 30. For the four data sets the maximum gust speeds over the century are:

GS	$22.97ms^{-1}$
G1	$30.58ms^{-1}$

G2	31.92ms^{-1}
G3	32.93ms^{-1}

Thus the effect of prescribing the shape parameter is to increase the number of occurrences above the specified thresholds, and to increase the maximum gust speed over the century. The new time series of maximum annual gust speeds, based on prescribed shape parameters, are shown in Fig. 1.87.

4.3 Conclusions

Sensitivity studies have been performed to demonstrate the effect on maximum gusts of increases in hourly mean wind speeds of 0.5ms^{-1}, 1.0ms^{-1} and 1.5ms^{-1}. Wind data from Dungeness were taken as the example. In order to perform these analyses, it was assumed that the best-fit probability distribution for both mean wind and gust speeds is the two-parameter Weibull distribution. It was found that the imposition of the prescribed forcings led to a change in the scale parameter of the Weibull distribution, which in turn reduced the speed of the most extreme gusts. In order to solve this problem, the shape parameter was prescribed to the value obtained for present-day gusts.

Table 1.4 Number of times in 100 years stated thresholds exceeded

Free shape parameter

Threshold (ms^{-1})	GS	G1	G2	G3
20	4	14	20	24
22	2	8	15	15
24	0	4	7	5
26	0	2	4	3
28	0	0	4	1
30	0	0	0	0
32	0	0	0	0

Prescribed shape parameter

Threshold (ms^{-1})	GS	G1	G2	G3
20	4	15	25	30
22	2	9	12	19
24	0	5	9	15
26	0	3	4	8
28	0	2	2	3
30	0	1	1	3
32	0	0	0	1

Given the results from GCMs, and the scenarios developed from them in Section 3 of this report, it is clear that the most realistic forcing of hourly mean wind speeds is $0.5ms^{-1}$. The resulting expected maximum gust in 100 years would have a speed of $31ms^{-1}$, around $8ms^{-1}$ greater than the 100 year maximum calculated from present-day data. Whereas we would expect four occurrences in 100 years of gust speeds greater than $20ms^{-1}$ on the basis of current conditions, this figure rises to 15 for the realistic forcing scenario.

Mean wind and gust speeds for Dungeness are not particularly severe. This site was selected because it is flat and open, so that the effect of orography could be ignored in the initial development of the method. However, with some possible modifications, there should be no reason why the method could not be applied in any area of the British Isles, in particular those regions more vulnerable to the effects of damaging gusts.

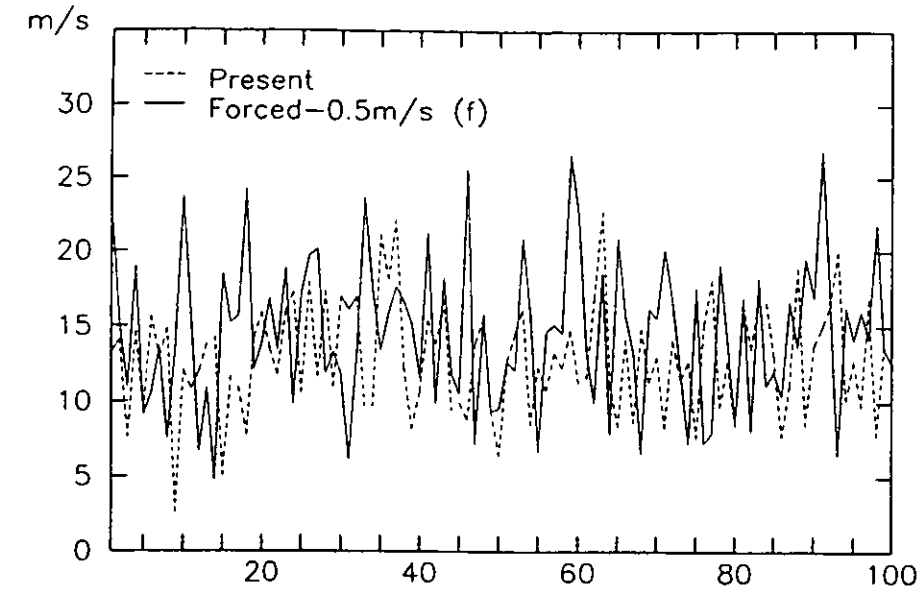

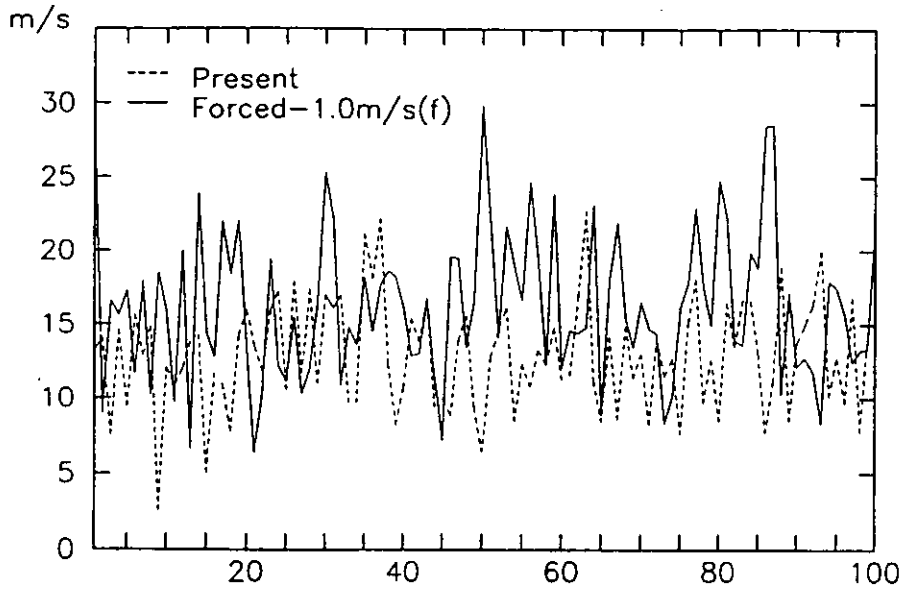

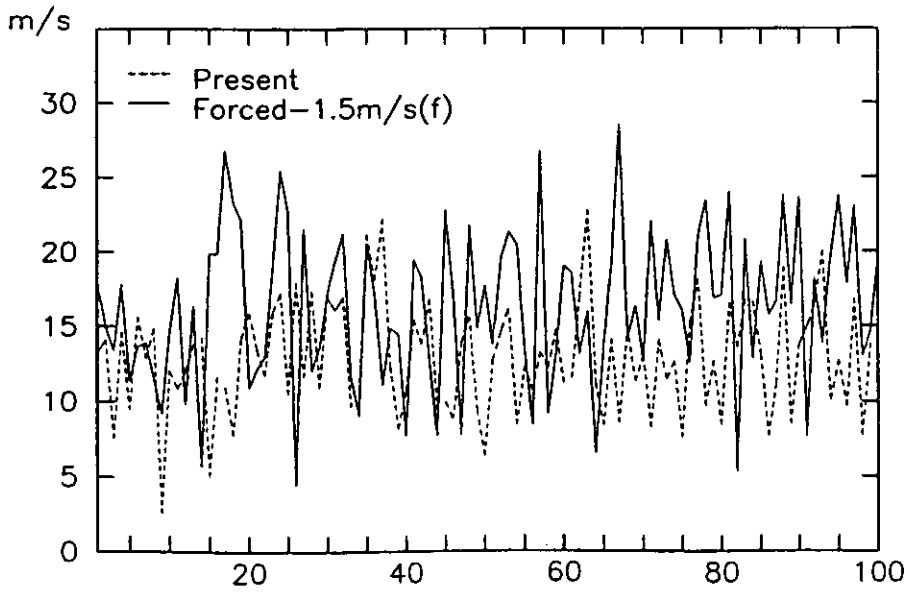

Fig. 1.83 Maximum gust speed in each year of 100 year synthetic gust speed time series computed for the present day and for forcings of 0.5ms^{-1}, 1.0ms^{-1} and 1.5ms^{-1} imposed on the hourly mean wind speeds.

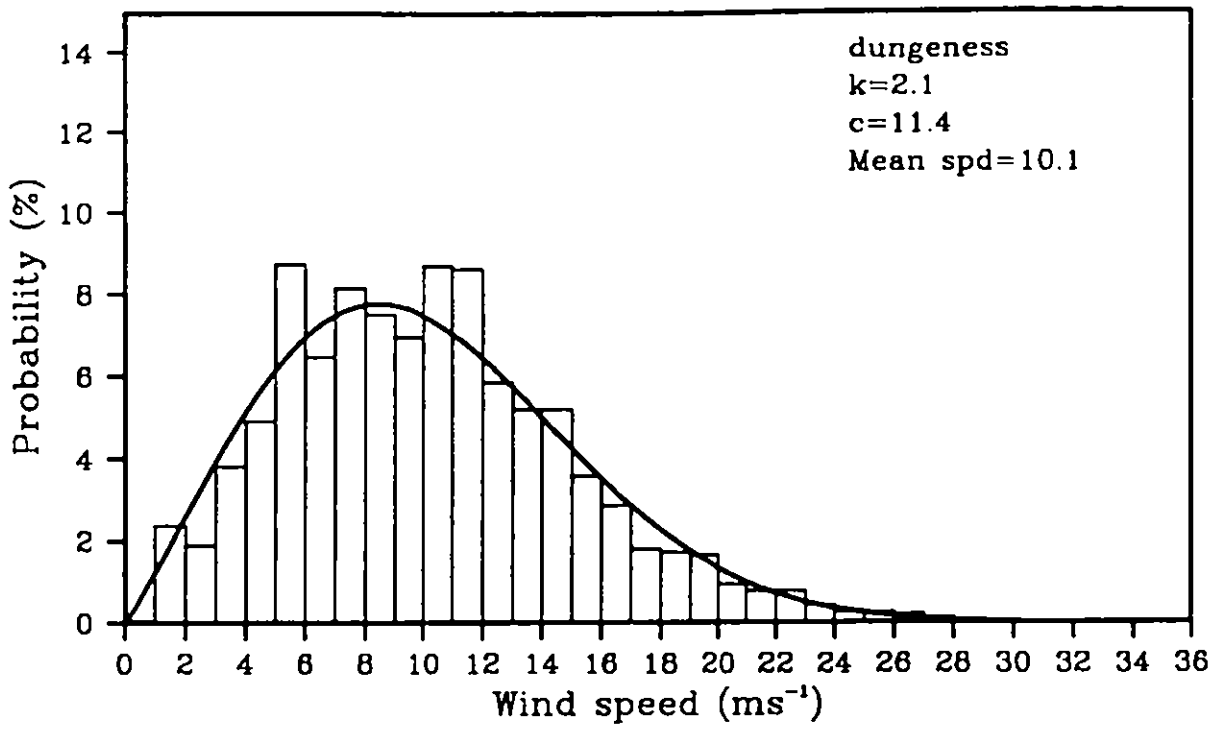

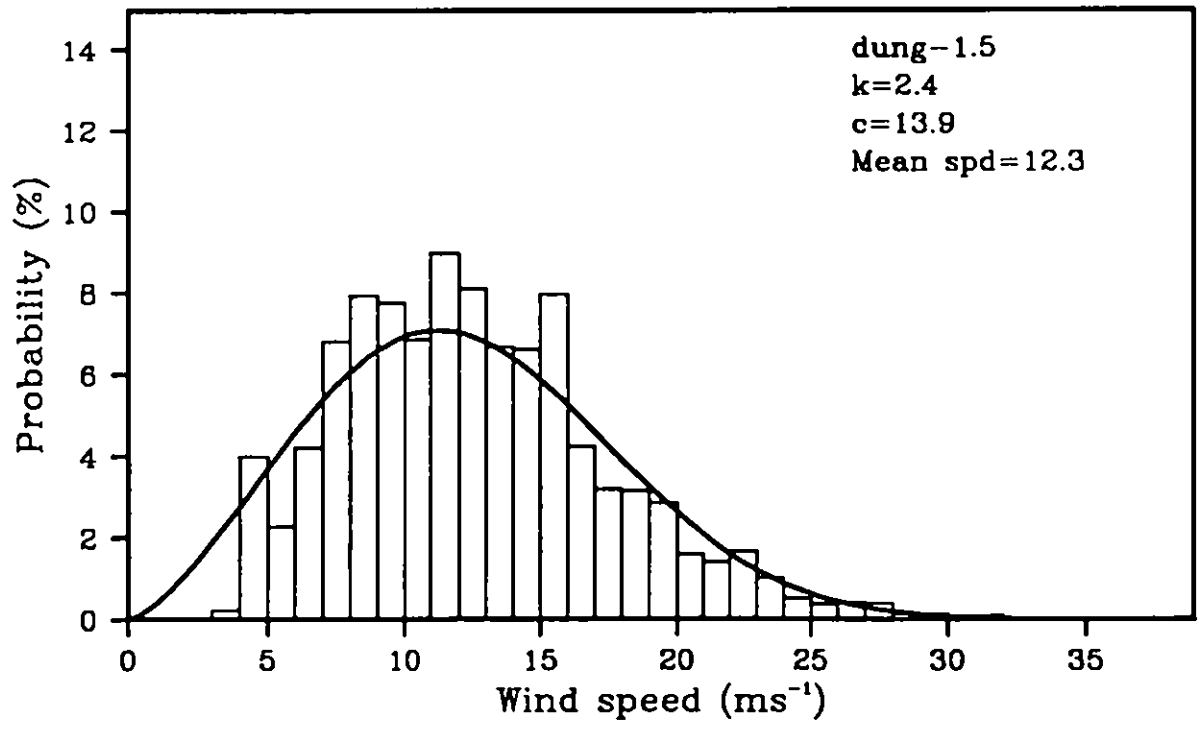

Fig. 1.84 Percentage frequency distributions and fitted Weibull curves for GS (upper diagram) and G3 (lower diagram).

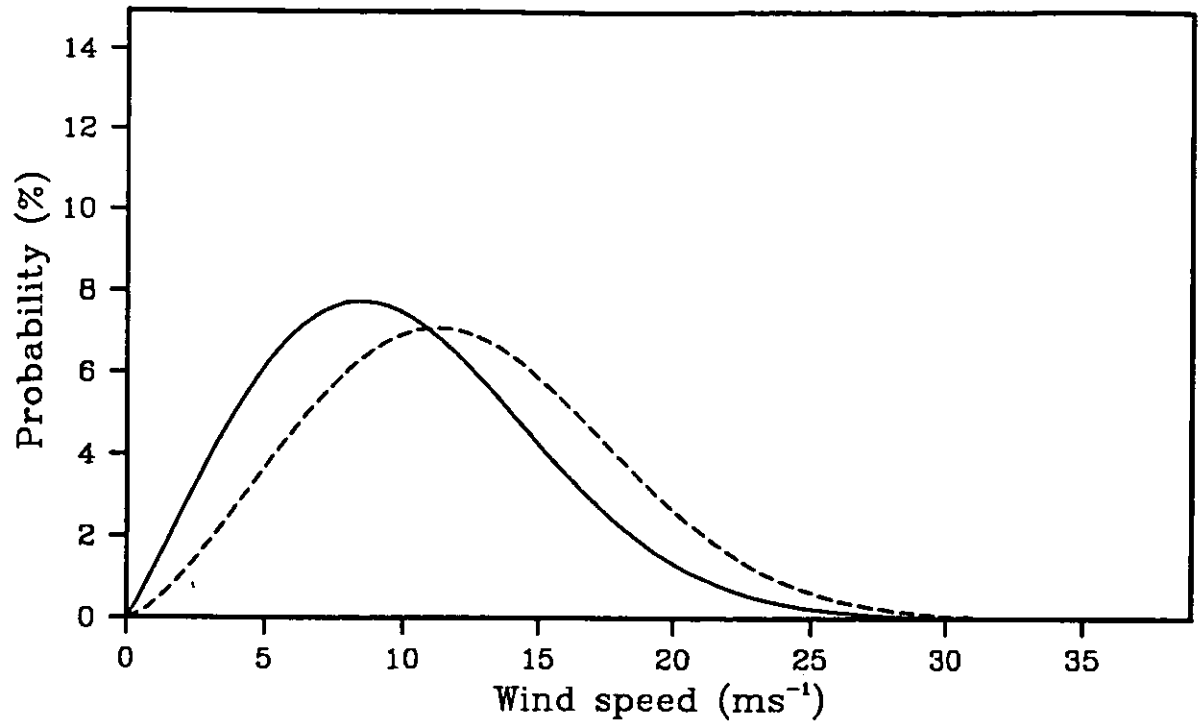

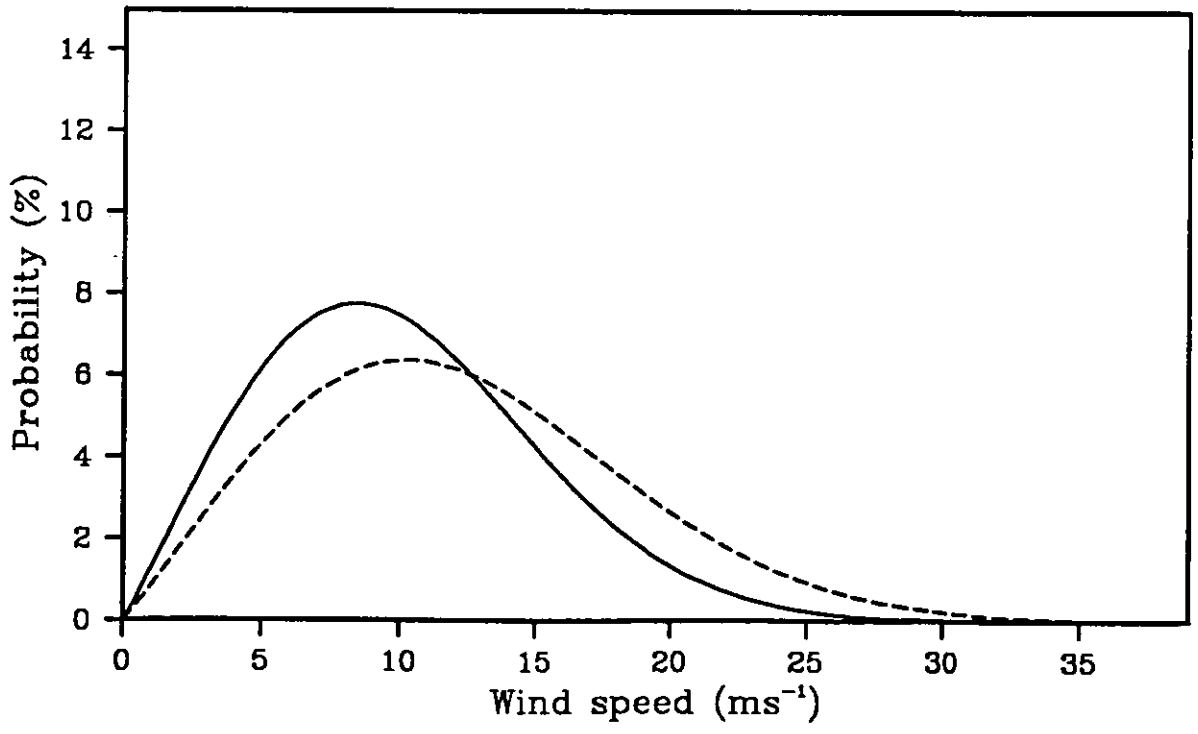

Fig. 1.85 Fitted Weibull curves for GS and G3 data sets. In the upper diagram (85a) the shape parameter k for G3 is free, in the lower diagram (85b) k is prescribed.

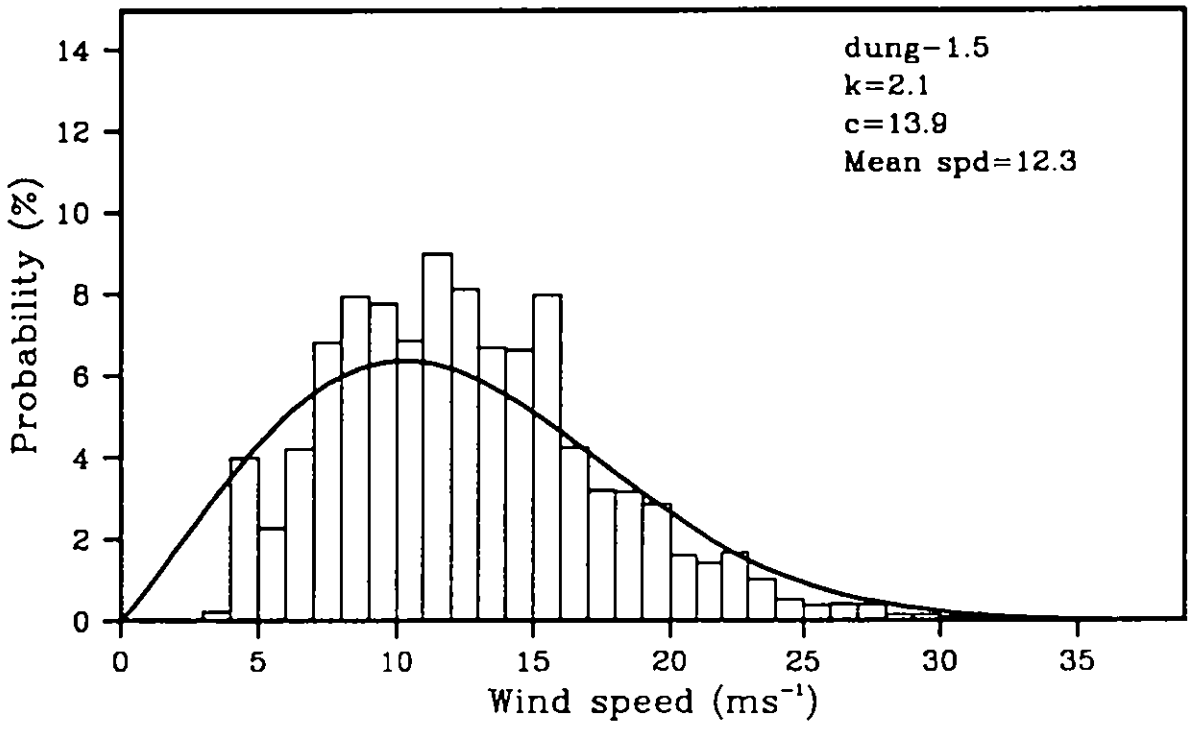

Fig. 1.86 Percentage frequency distribution and fitted Weibull curve for G3, shape parameter k set at 2.11.

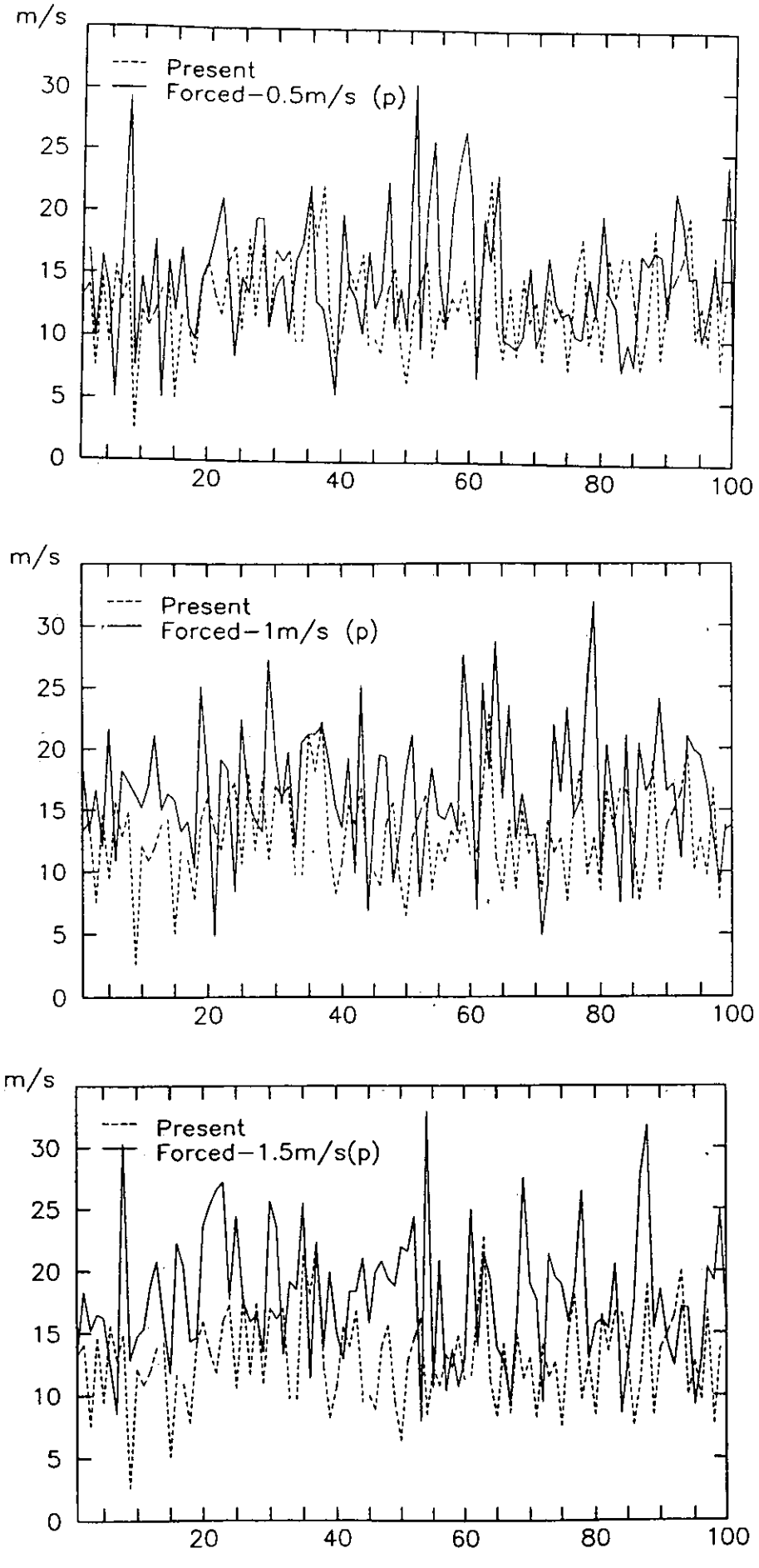

Fig. 1.87 Maximum gust speed in each year of 100 year synthetic gust speed time series computed for the present day and for forcings of 0.5ms^{-1}, 1.0ms^{-1} and 1.5ms^{-1} imposed on the hourly mean wind speeds. Based on Weibull distributions with the scale parameter k constrained to the present-day value.

5. CONCLUSIONS

In this section of the report we have produced scenarios of the change in mean wind speeds and maximum gusts over the British Isles due to the greenhouse effect. Three approaches have been taken to the problem of scenario construction. First, we have used the mean wind speeds from the UKMO GCM to look at broad-scale changes at the annual and seasonal level for the whole of the British Isles. However, because of the coarse model resolution, the results from this approach take little or no account of the factors which cause the near-surface wind to differ substantially from the wind above the boundary layer: topography, roughness length etc. For this reason, in the second approach we have linked GFDL and GISS GCM vector mean wind output to a boundary-layer flow model (CONFORM) in order to examine in detail the possible changes in three upland areas of Britain. Finally, the sensitivity of gust speeds to a change in mean wind speed has been examined by statistical analysis.

The UKMO GCM mean wind speed output suggests that annual wind speeds will increase slightly over central and northern Scotland in a high-CO_2 world, and decrease slightly (by not more than $0.3ms^{-1}$) over the remainder of the country. The greatest seasonal changes are seen in spring, ranging from an increase of 0.1-$0.2ms^{-1}$ over western Scotland, to a decrease of more than $0.2ms^{-1}$ in southern Ireland and southwest Britain.

By linking GCM results to a boundary-layer flow model, we can create fine-resolution scenarios which take into account the effects of orography, exposure and roughness length on wind speeds. Three test regions have been examined: the Northern Pennines, Devon and the Main Island of Shetland, using the GISS and GFDL GCMs. We consider the results from the GFDL GCM to have more validity.

The model results for two of the test regions demonstrate a substantial change in wind speeds due to the greenhouse effect. In both the Northern Pennines and Shetland, increases of between 5% and 8% are suggested in the

autumn season, the greatest changes occurring over hill tops and and just below the summits on slopes facing the prevailing wind.

Sensitivity studies have been performed to examine the effect on maximum gust speeds of increases in hourly mean wind speeds of $0.5ms^{-1}$, $1.0ms^{-1}$ and $1.5ms^{-1}$, taking data from Dungeness as the example. It was assumed that the best-fit probability distribution for both mean wind and gust speeds is the two-parameter Weibull distribution. The sensitivity experiments were performed with both a free and a prescribed (to the present-day value) shape parameter.

It was found that, for the most realistic forcing ($+0.5ms^{-1}$, given the results of the wind scenarios) the expected maximum gust in 100 years with a prescribed shape parameter would have a speed of $31ms^{-1}$. This is around $8ms^{-1}$ greater than the 100 year maximum calculated from present-day data. Whereas we would expect four occurrences in 100 years of gust speeds greater than $20ms^{-1}$ on the basis of current conditions, this figure rises to 15 for the realistic forcing scenario.

This section of the report has outlined a set of methods to investigate the possible implications of the greenhouse effect for mean wind and gust speeds over the British Isles. These methods have been applied to a limited number of locations, but this is only because of the limitations imposed by data availability and the time required for terrain digitization. Wind speeds vary strongly over relatively small distances, and it is not possible to extract a meaningful scenario from coarse resolution GCM output directly. However, we have shown here that it is possible to introduce interfaces which will allow the meaningful interpretation of GCM output in terms of specific locations.

REFERENCES

Barthelmie, R.J., Palutikof, J.P. and Davies, T.D., 1990: Prediction of offshore wind speeds - a comparison of methods. *Proc. 12th BWEA Energy Conference*, Mechanical Engineering Publications, London, in press.

Cook, N.J., 1985: *The Designer's Guide to Wind Loading of Building Structures Part 1: Background, Damage Survey, Wind Data and Structural Classification.* Building Research Establishment, Garston.

Conradsen, K., Nielsen, L.B. and Prahm, L.P., 1984: Review of Weibull statistics for estimation of wind speed distributions. *Journal of Climate and Applied Meteorology 23(8)*, 1173-1183.

Guo, X., 1989: *An Assessment of mesoscale Wind Modelling Techniques in Complex Terrain.* Ph.D. thesis, School of Environmental Sciences, University of East Anglia, Norwich.

Guo, X. and Palutikof, J.P., 1990: Perfromance of an ideal wind flow model over complex topography. Submitted to *Boundary-Layer Meteorology.*

Hansen, J., Lacis, A., Rind, D., Russell, G., Stone, P., Fund, I., Ruedy, R. and Lerner, J., 1984: Climate sensitivity: analysis of feedback mechanisms. In: *Climatic Effects of Increasing Carbon Dioxide, Geophysical Monograph Series 29*, (ed. J.E. Hansen and T. Takahashi), AGU, Washington, D.C., 130-163.

Law, A.M. and Kelton, W.D., 1982: *Simulation Modelling and Analysis.* McGraw-Hill, New York.

McIntosh, D.H., 1972: *Meteorological Glossary.* H.M.S.O., London.

Moore, D.J., 1982: 10 to 100m winds calculated from 900mb data. *Proc. 4th BWEA Wind Energy Conference*, Cranfield, 197-207.

Palutikof, J.P., Halliday, J.A., Davies, T.D., Bass, J.H., Holt, T., Watkins, C.P. and Kelly, P.M., 1987: Development of a site wind-regime prediction methodology for Britain: work in progress. *Wind Energy Conversion 1987*, (ed. J.M. Galt), Mechanical Engineering Publications, London, 271-278.

Petersen, E.L., Troen, I., Frandsen, S. and Hedegaard, K., 1981: *Windatlas for Denmark.* Riso National Laboratory, Denmark.

Physick, W.L., 1988: Review: mesoscale modelling in complex terrain. *Earth-Sciences Reviews 25*, 199-235.

Walmsley, J.L., Taylor, P.A. and Keith, T., 1986: A simple model of neutrally stratified boundary-layer flow over complex terrain with surface roughness modulations. *Boundary-Layer Meteorology 36*, 157-186.

Wieringa, J., 1986: Roughness-dependent geographical interpolation of surface wind speed averages. *Quarterly Journal of the Royal Meteorological Society 112*, 867-889.

Wilson, C.A. and Mitchell, J.F.B., 1987: A doubled CO_2 climate sensitivity experiment with a global climate model including a simple ocean. *Journal of Geophysical Research 92 (D11)*, 13315-13343.

PART 2

SCENARIOS OF DAILY WEATHER PATTERNS, GALE DAYS, RADIATION AND EVAPORATION IN A GREENHOUSE GAS WORLD.

P.D. Jones and D.Taylor

1 INTRODUCTION

This part of the report examines further the possible impacts of greenhouse gas induced changes on various aspects of British climate. Assessments are made of likely changes in daily weather patterns, the number of gales over the region and of possible changes in evaporation and radiation in the future. The coarse resolution of General Circulation Models (GCMs) means they are not appropriate for looking at changes in daily weather patterns and gale days. For these measures we assess possible changes by considering past variations.

First, we consider what changes in daily weather patterns may occur. The scenarios are developed from an analysis of past warm and cool periods over the Northern Hemisphere. The daily weather patterns during two hemispherically warm periods, 1934–53 and 1970–89 are contrasted and compared with patterns during the cool period of 1901–20. Possible changes in the future are indicated and their impact on changes in seasonal temperatures and precipitation totals is assessed.

Second, we investigate whether there has been a change in the number of gale days over the last 100 years in this region. We develop, for this purpose, a long (back to 1880), homogeneous index of the number of gales over the United Kingdom and the North Sea. Possible changes in the future are assessed by comparing seasonal gale counts during the above hemispheric warm and cool periods.

Third, we consider whether changes are likely in two other parameters of the climate system, the amount of solar radiation and evaporation totals. Both these parameters are produced as outputs from some GCMs. The models simulations of the present climate are intercompared. The lack of a real world climatology, however, means that it is not possible to say which model is better, if such a model exists. The implied changes from the models for the perturbed climate with $2\times CO_2$

concentrations are compared and major intermodel consistencies are highlighted.

GCMs and past climate variations are not the only methods that have been proposed for assessing what future changes in climate might be. The spatial analogue method has been proposed. This method seeks to find regions of the world where the present climate is similar to that which may occur in future Britain. The final part of the report concludes with some considerations for identifying candidate regions.

2 LAMB WEATHER TYPE AND GALE FREQUENCIES.

2.1 Lamb Weather Types

The Lamb Catalogue is a classification scheme which describes the daily weather patterns over the British Isles and the immediate surroundings (Lamb, 1972). This classification provides a means of quantitatively assessing the characteristics of the atmospheric circulation over monthly or seasonal periods without neglecting synoptic fluctuations on the daily time-scale.

The British Isles region has the world's longest series of daily weather charts, continuous from 1861. The Lamb classification is based on the character and general steering of the weather patterns in this region. Seven basic types are used : five types are directional (westerly, northerly, north-westerly, easterly, and southerly air flows) and two types are used when a synoptic system dominates the region (anticyclonic and cyclonic). The directional types relate to the steering of synoptic systems rather than the surface wind direction. These types are described in Table 2.1.

Each day is classified by the general circulation patterns throughout the whole day and not at a particular time during the day. Altogether, the classification has 27 possible types, including unclassifiable days and all compatible hybrids e.g. ASW. Although, by definition, the classification is subjective and may not be entirely reproducible, the catalogue is internally consistent since Lamb carried out the classification of the whole period himself.

Since its development, the Lamb catalogue has been used widely in studies of the climate of the British Isles. Barry and Perry (1973) present a useful discussion of a number of its applications. The catalogue contains a vast amount of information and a number of attempts have been made to condense the data, most popularly using indices. A Principal Components Analysis was carried out by Jones and Kelly (1982)

Table 2.1
The seven basic types of the Lamb daily weather classification scheme, after Lamb (1972).

Anticyclonic(A):	Anticyclones centred over, near, or extending over the British Isles.
Cyclonic(C):	Depressions passing frequently or stagnating over the British Isles. The central isobar of the depression should extend over the mainland of Britain or Ireland.
Westerly(W):	High pressure to the south and low pressure to the north, giving a sequence of depressions travelling eastwards across the Atlantic. This is the main, progressive zonal type.
North-westerly(NW):	Azores anticyclone displaced north-east or north towards the British Isles. Depressions forming near Iceland and travelling south-east into the North Sea.
Northerly(N):	High pressure to the west or north-west of Britain extending from Greenland southwards possibly as far as the Azores. Depressions travel southwards from the Norwegian Sea.
Easterly(E):	Anticyclones over Scandinavia extending towards Iceland across the Norwegian Sea. Depressions generally to the south of the region over south-west Europe and the western Atlantic.
Southerly(S):	High pressure over central and northern Europe. Depressions blocked to the west or travelling north or north-eastwards off western coasts.

and Briffa, Jones and Kelly (1990) which demonstrated that the basic types accounted for more than 70% of the total variance. In other words, hybrid Lamb Weather Types were not required to monitor climatic change.

2.2 Time-Series of Lamb Weather Types

The frequency of each of the seven basic Lamb Weather Type (LWT) classifications was examined on both seasonal and annual time-scales. The time-series of these frequencies were plotted for the period 1861–1989 along with the values when passed through a 10 year Gaussian Filter. The totals for each of the seven basic types takes

into account hybrids (i.e. AN would count half a day to both A and N while CSW would count one third of a day to the three types C, S and W).

The plots are presented in figures 2.1-2.7. The most important features of each classification are discussed below. The figures in brackets after each type show the average number of days per year (1861–1989) having that classification.

Anticyclonicity *(Annual Average Frequency = 91.5)*

This is clearly an important classification as it accounts for one quarter of the days in any year. The number of anticyclonic days are spread approximately evenly between the seasons, there being fewer on average in winter. Winter, spring and summer all show the same trend in the late 19th century; an increased frequency of anticyclonic days. These seasons also show the subsequent decline to the lowest totals which were recorded during the 1920s. Autumn shows comparatively little variation during these periods.

The 1940s and 50s show major variability only in spring with markedly higher frequencies than throughout the previous fifty years. The most notable trend in recent decades can be found in summer; since the mid 1960s, there has been a clear and abrupt shift towards a higher incidence of anticyclonic days.

Cyclonicity *(Annual Average Frequency = 64.8)*

A greater prevalence of cyclonic days is experienced in summer, the other seasons being evenly represented. The clearest changes in frequency have occurred within the last 30 years. Spring shows a marked increase from 1960 until the present while the summer total steadily declined from 1960 until the mid 70s but has since regained mean values. These variations are apparent in the annual plot; the mid 1970s show a drop which was formed by slight dips in all the seasons' totals. Since then, the annual total has increased, largely as a result of the spring changes noted above.

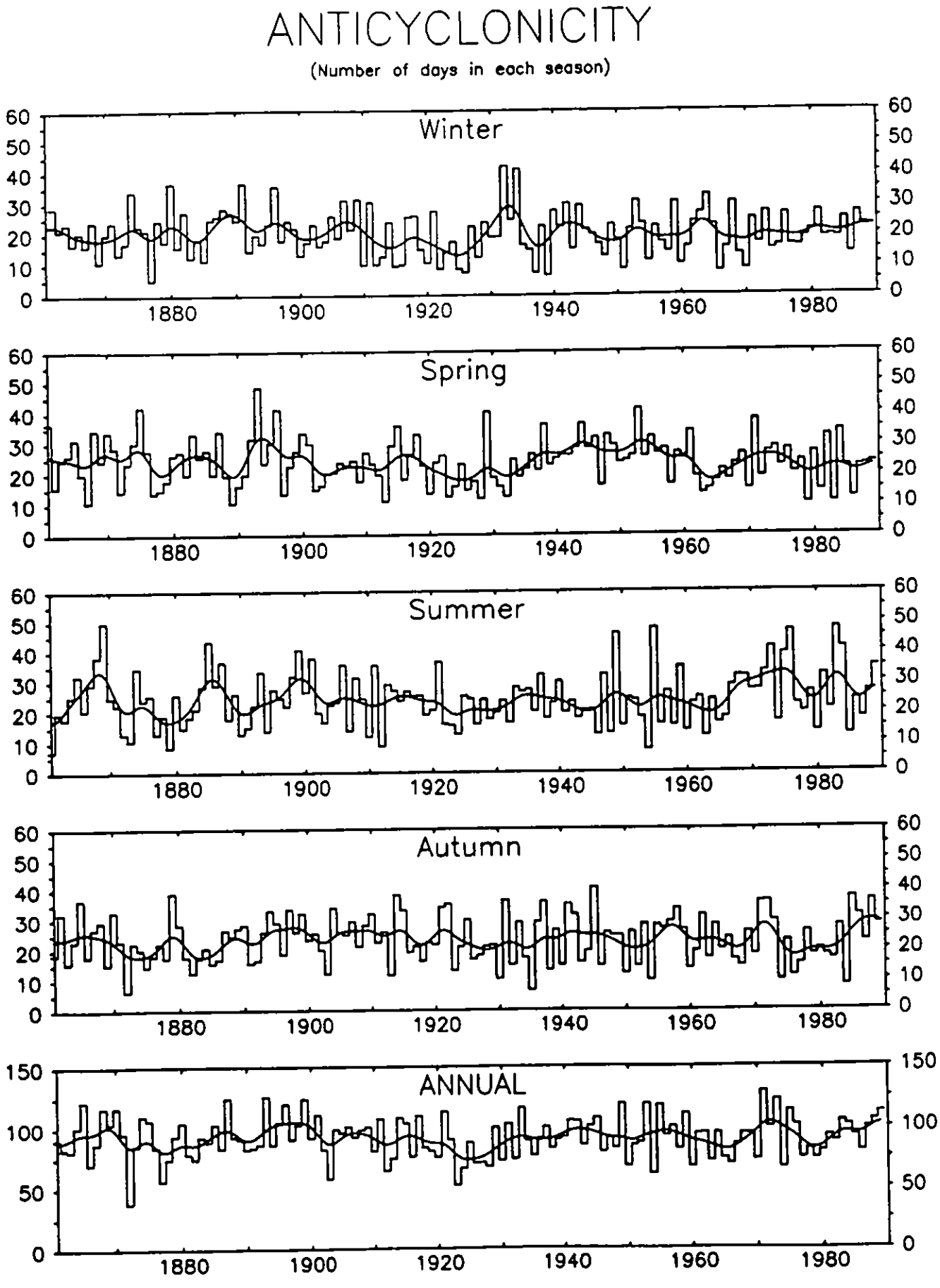

Fig. 2.1 Frequency of Anticyclonic days (1861–1989). Curved line represents values after being passed through a 10 year Gaussian filter.

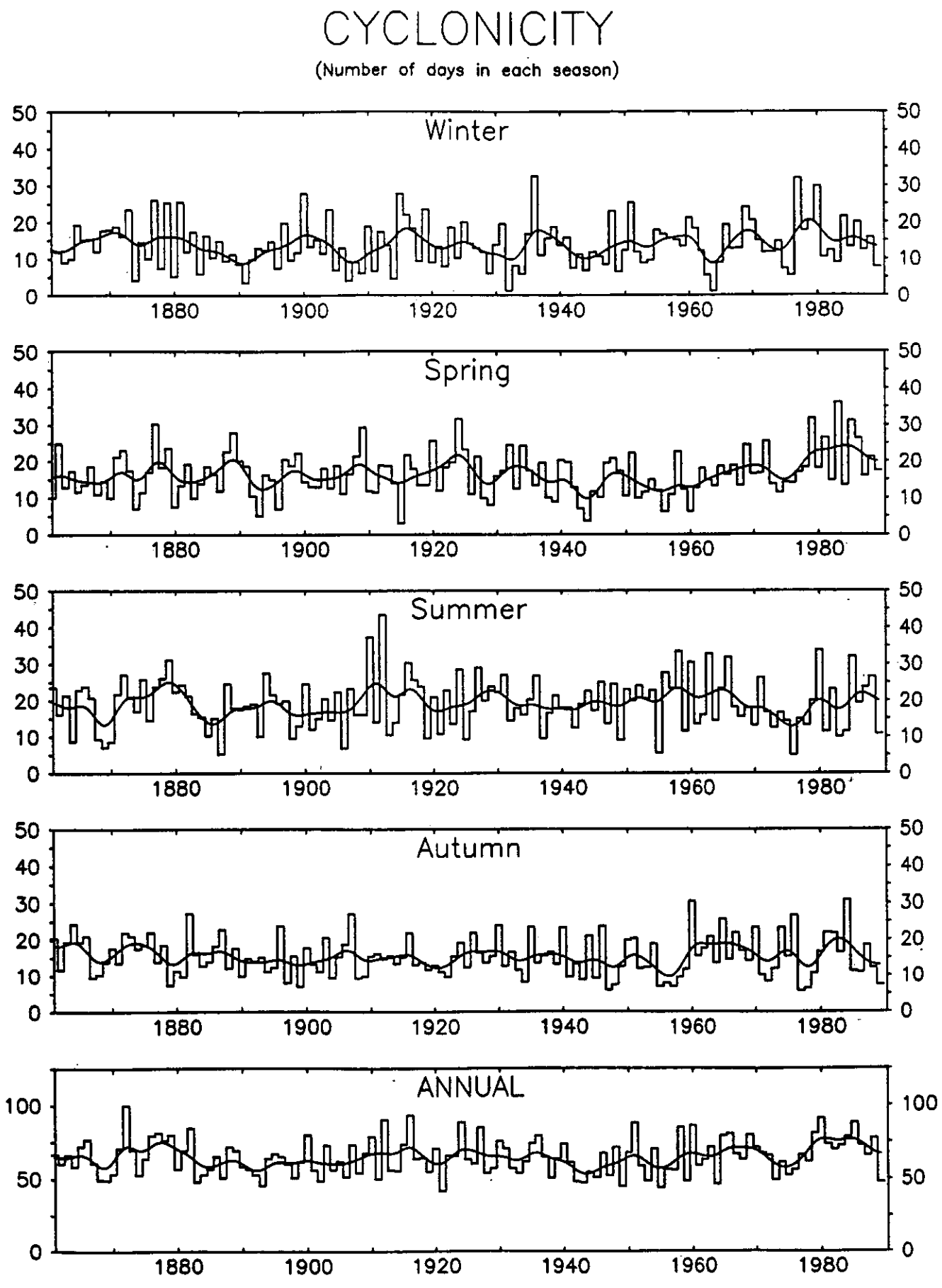

Fig. 2.2 Frequency of Cyclonic days (1861–1989). Curved line represents values after being passed through a 10 year Gaussian filter.

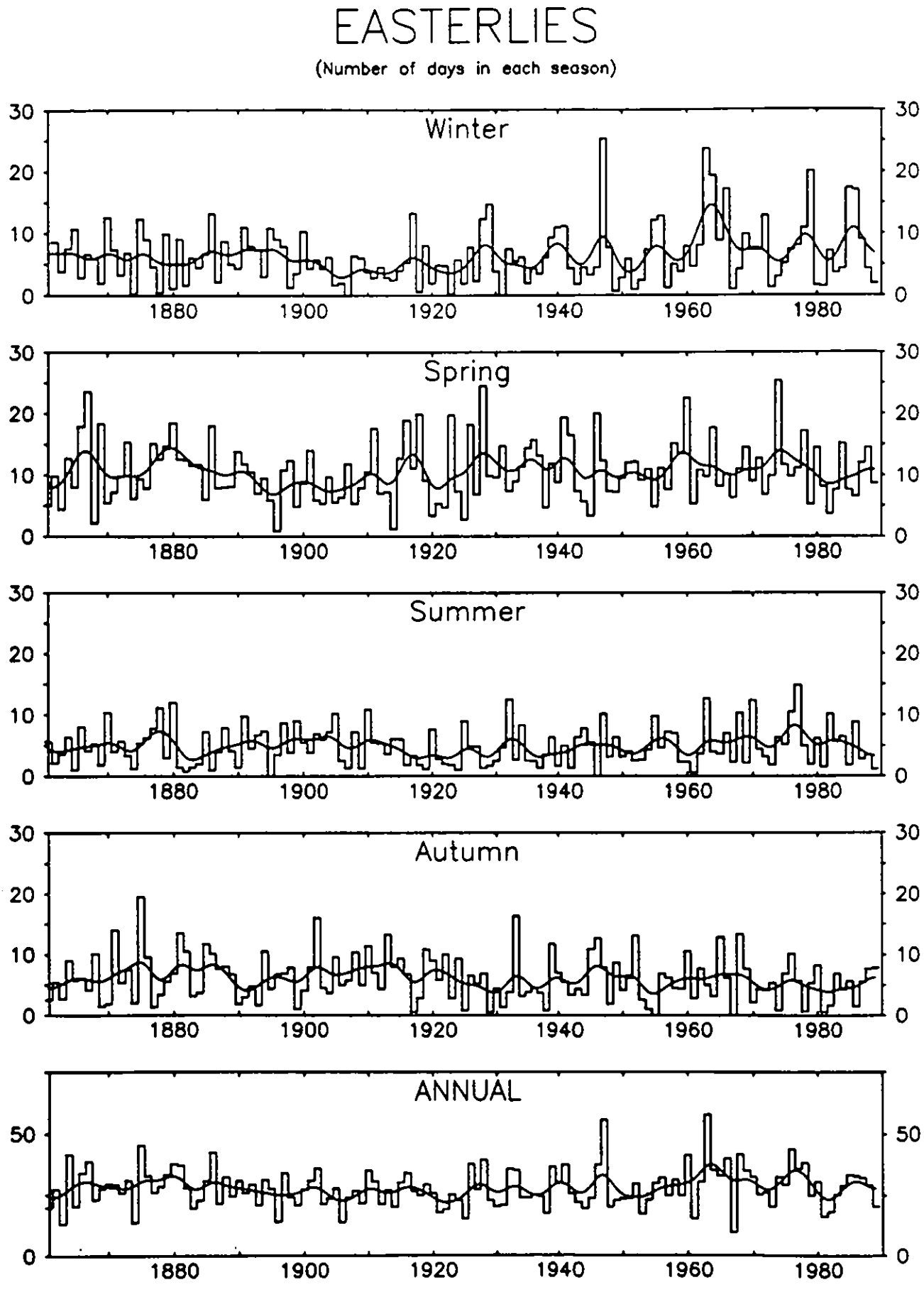

Fig. 2.3 Frequency of Easterly days (1861–1989). Curved line represents values after being passed through a 10 year Gaussian filter.

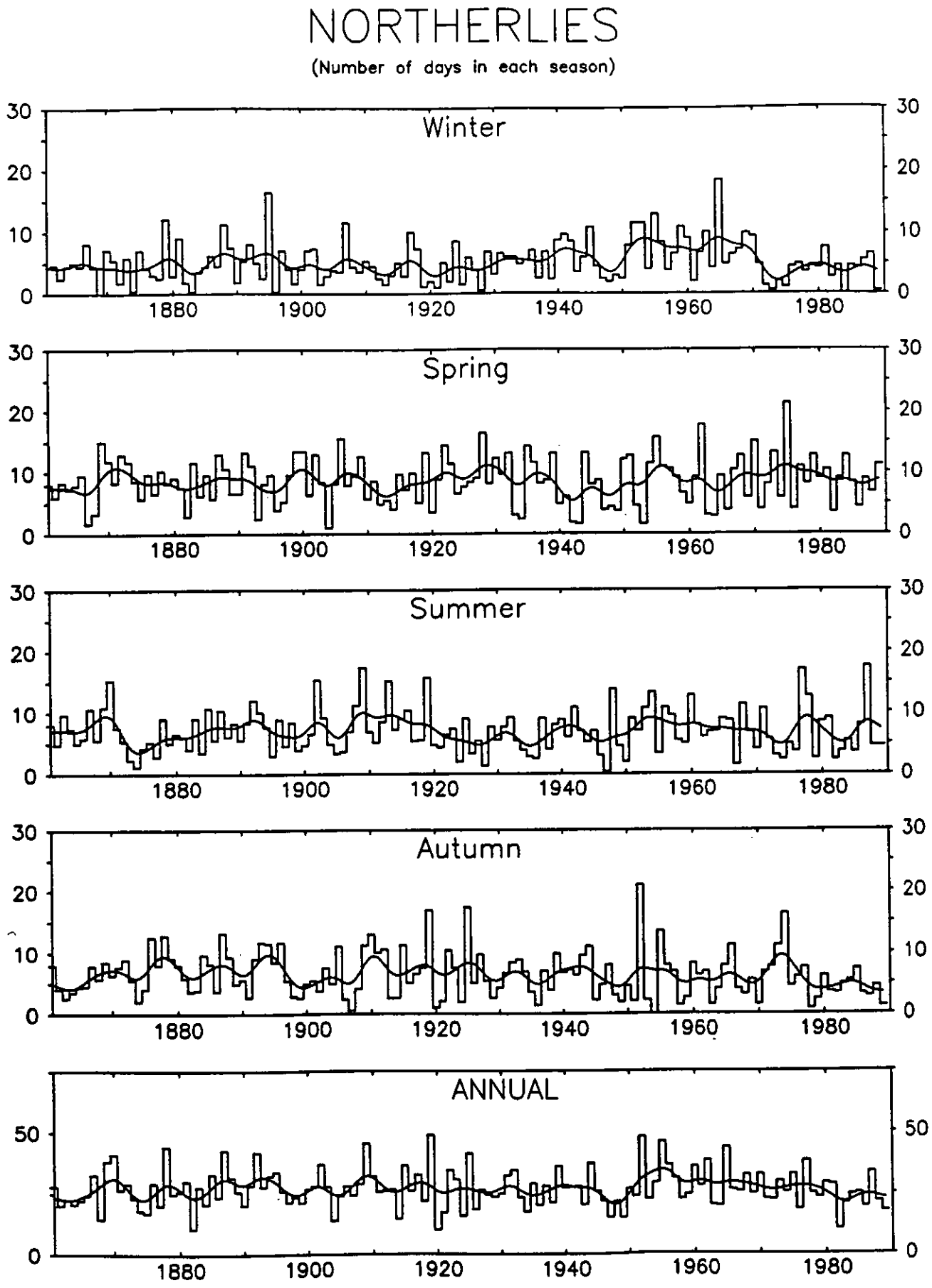

Fig. 2.4 Frequency of Northerly days (1861–1989). Curved line represents values after being passed through a 10 year Gaussian filter.

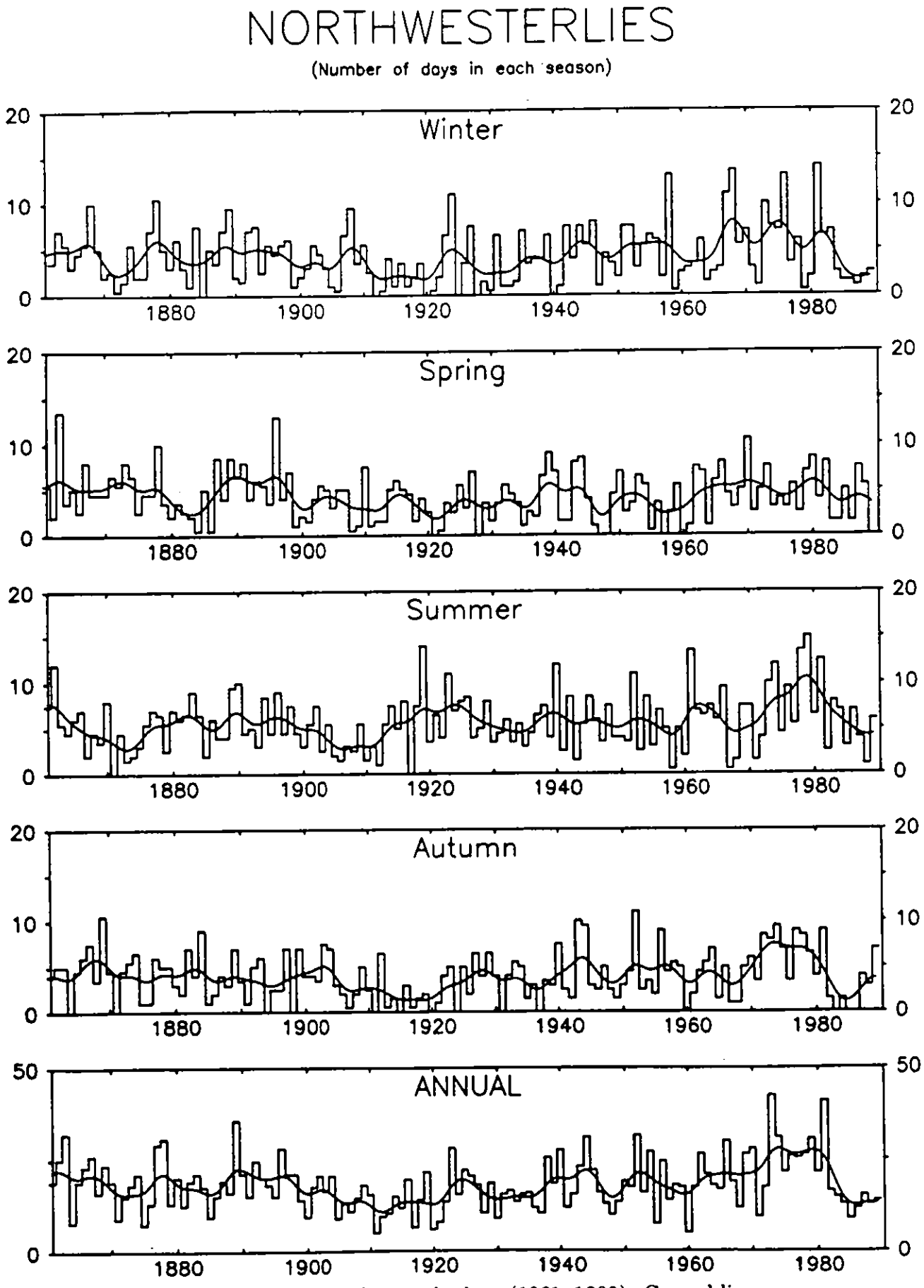

Fig. 2.5 Frequency of Northwesterly days (1861–1989). Curved line represents values after being passed through a 10 year Gaussian filter.

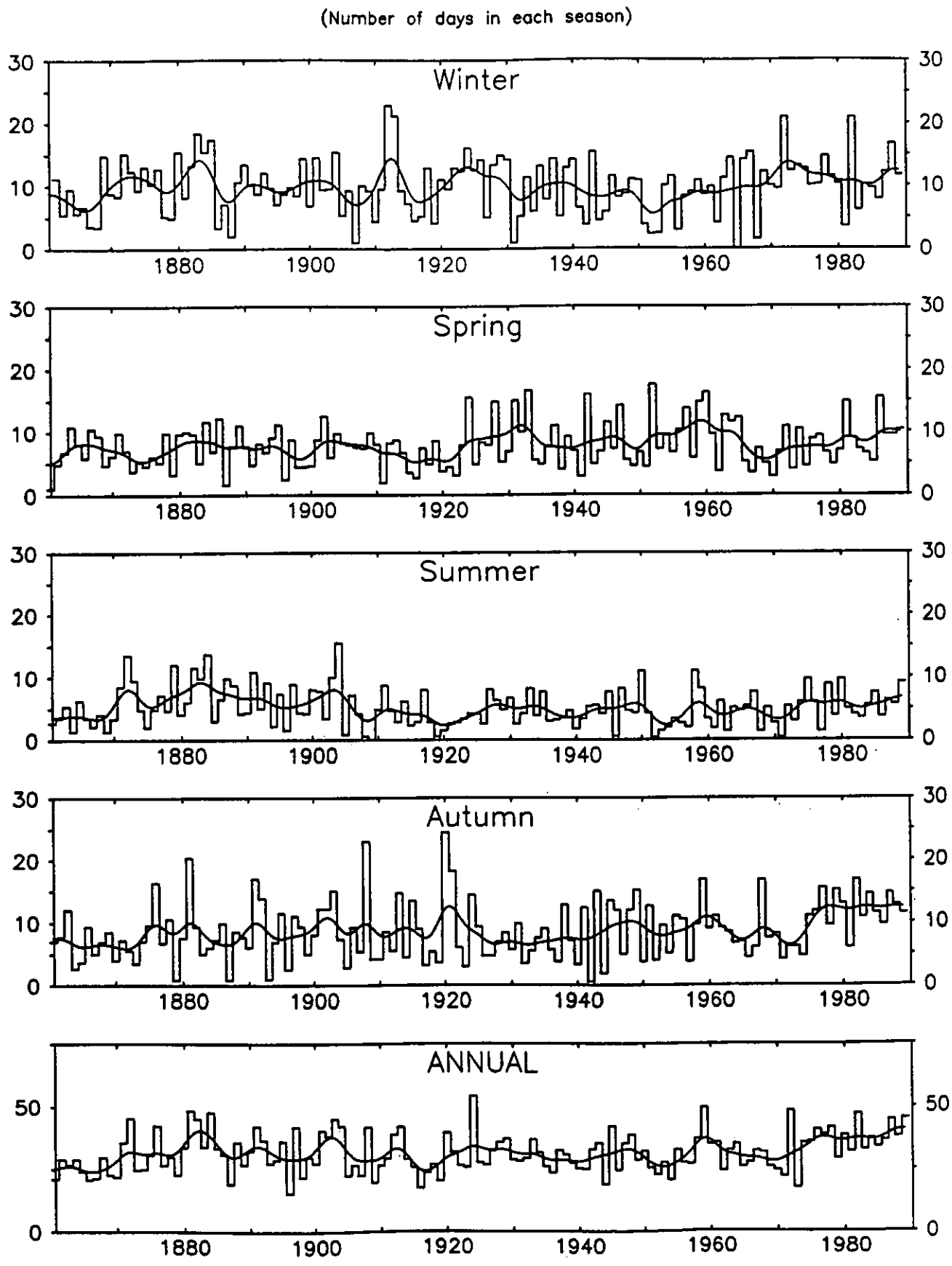

Fig. 2.6 Frequency of Southerly days (1861–1989). Curved line represents values after being passed through a 10 year Gaussian filter.

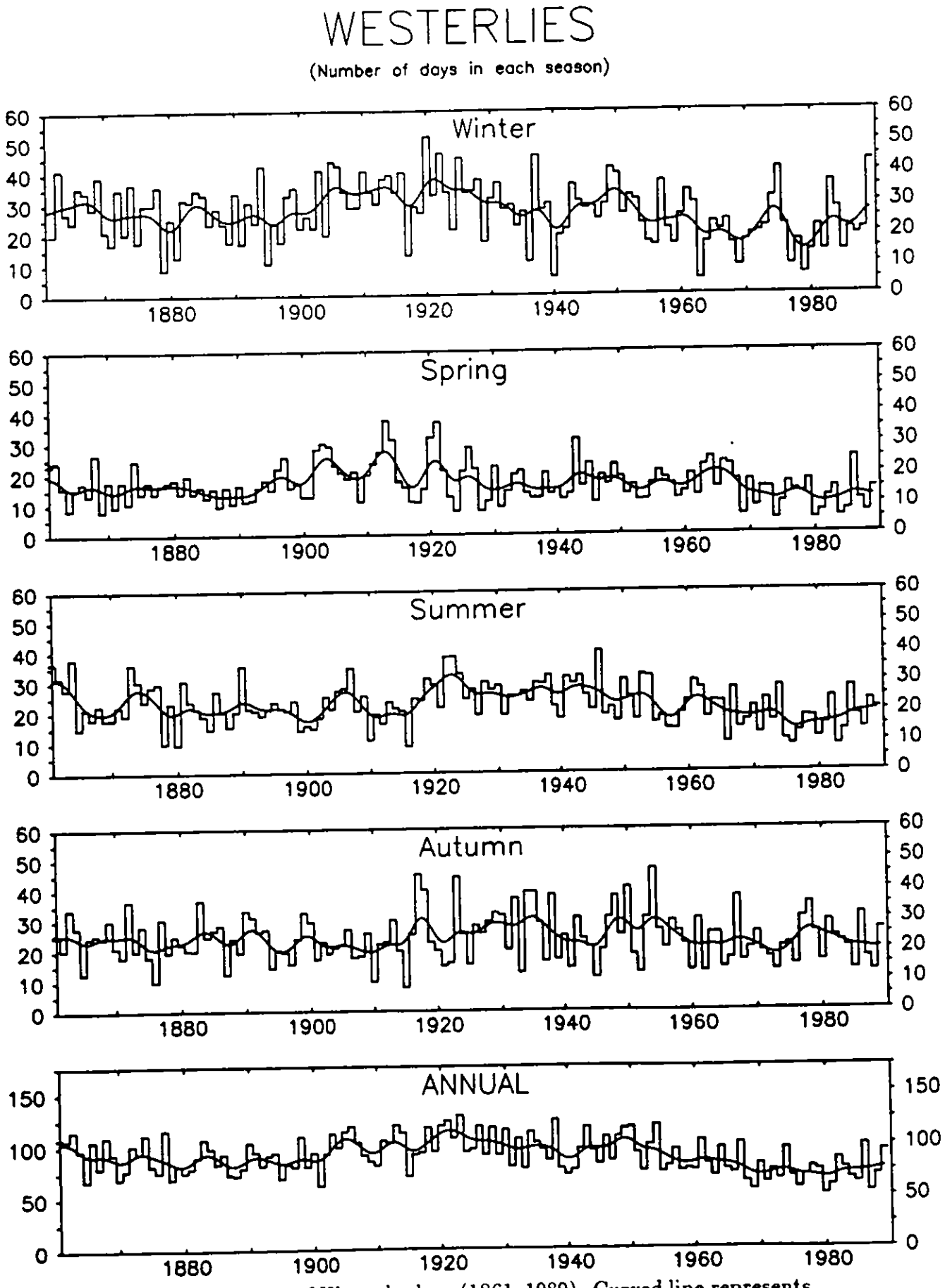

Fig. 2.7 Frequency of Westerly days (1861–1989). Curved line represents values after being passed through a 10 year Gaussian filter.

Easterlies *(Annual Average Frequency = 28.0)*

Summer and autumn usually have small easterly totals each year. Winter and spring experience more days on average and also more interannual variation. The most significant trend for this classification is apparent in winter; there is clearly an increase in the number of days classified as easterly from 1920 onwards, but equally importantly there is a discernible increase in the number of extreme high values — the seven highest winter totals all occurred during the last 45 years of the 130 year period. This variation is of such magnitude that its effects are clearly visible in the annual time-series.

Northerlies *(Annual Average Frequency = 27.0)*

The annual time-series shows the most interesting features. The period of interest begins with the late 1940s which experienced a low frequency of northerlies in all seasons. In years immediately following, there was a larger total of northerly days recorded, most clearly and abruptly during winter. Since 1955, however, the annual total has shown a steady decline which appears to be continuing. In particular, winter totals from 1970 onwards are about half their level of the previous 20 years.

North-westerlies *(Annual Average Frequency = 18.1)*

For this classification, all seasons show similar long-term trends and so the annual time-series can be considered representative. North-westerly totals were at average levels throughout the late 19th century but at the turn of the century began to decline until 1920 when frequencies returned to around the average. It was in the early 1960s that an upward trend began which lasted until 1980. A sharp decline was then experienced which has seen filtered totals during the '80s fall to half their level of the previous decade.

Southerlies *(Annual Average Frequency = 91.5)*

Autumn and winter show higher totals and variability than spring and summer. Autumn variability appears to have been greater in the period 1880 until 1930, although the average during these years was little different from that for the entire time-series.

In recent decades, frequencies have increased, particularly over the last 20 years. Winter totals have been rising since about 1960 but this was originally offset in the annual totals by a decline in autumn frequencies. This trend was reversed in 1970 and the annual values started to rise again.

Westerlies *(Annual Average Frequency = 90.0)*

The total number of westerly days remained stable both seasonally and annually until the 20th century. Increases then occurred most distinctly in winter and spring westerliness until the 1930s when a short decline was followed by a period of stable near-average values. However, from 1950 until the present there has been a gradual decrease in the total westerliness of all seasons. The aggregate effect upon the annual value is evident in the plot.

This decline is very important as its absolute magnitude is greater than all the other trends discussed above. Westerlies, along with anticyclonicity and cyclonicity form the three most important Lamb Weather Types, accounting for almost three-quarters of the days in any year between them. Thus this declining trend indicates a considerable shift in the atmospheric circulation patterns over the British Isles.

2.2.1 Summary

Figure 2.8 shows the annual time-series of all of the seven Lamb Classification types. By far the most significant feature is the marked decline in westerly totals since

1950. This drop in westerliness and, to a lesser extent northerliness, has been countered by increases in cyclonic and anticyclonic conditions. The number of southerly days has also increased during this period as had north-westerliness until 1980 when it dropped suddenly.

LWTs and England and Wales Precipitation

Tables 2.2 and 2.3 show the correlation coefficients between the seven main Lamb Weather Types and average rainfall over England and Wales (Wigley et al., 1984; Wigley and Jones, 1987) for both monthly and seasonal data. From these tables, it can be seen that there is a strong negative correlation between anticyclonicity and rainfall. As would be expected, there is a similar, physically reasonable, positive correlation between rainfall and cyclonicity. The other classifications produce relatively small correlation coefficients whose significance is negligible in comparison with anticyclonicity and cyclonicity.

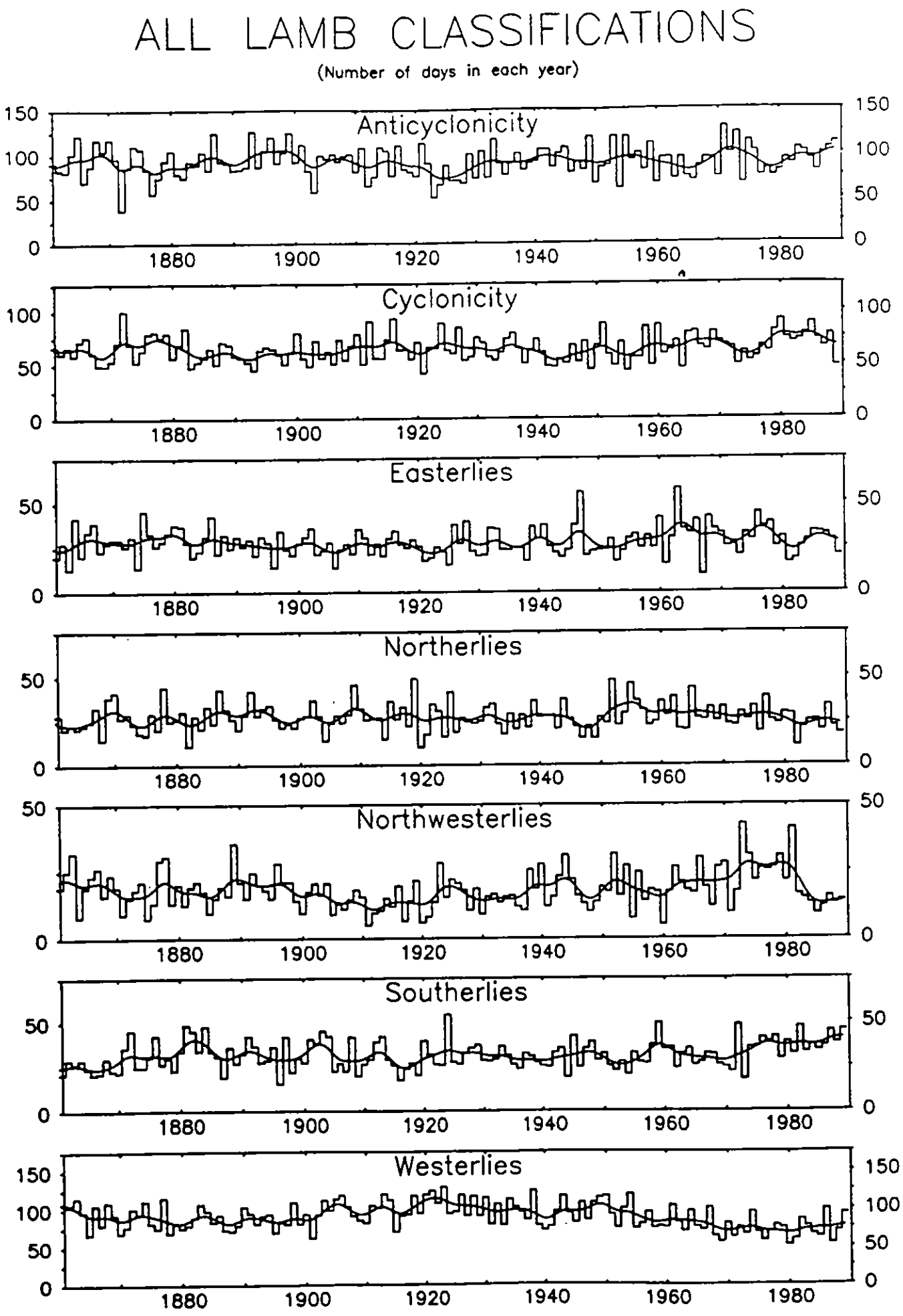

Fig. 2.8 Annual frequency of seven main LWTs (1861–1989). Curved line represents values after being passed through a 10 year Gaussian filter.

Table 2.2
Monthly Correlations between Lamb Weather Types and Rainfall in England and Wales for period 1861–1989

Matrix contains correlation coefficients.

Type	Jan	Feb	Mar	Apr	May	Jun	Jul	Aug	Sep	Oct	Nov	Dec
Anticyclonicity	−0.76	−0.76	−0.66	−0.72	−0.71	−0.67	−0.71	−0.74	−0.75	−0.66	−0.75	−0.68
Cyclonicity	+0.67	+0.76	+0.74	+0.74	+0.75	+0.75	+0.80	+0.81	+0.76	+0.72	+0.75	+0.72
Easterlies	−0.14	−0.26	−0.09	+0.01	−0.13	+0.11	−0.12	−0.15	+0.01	−0.05	−0.13	−0.13
Northerlies	−0.10	−0.17	−0.04	+0.07	−0.04	−0.06	+0.00	+0.03	+0.15	+0.06	−0.18	−0.13
North-westerlies	−0.23	−0.08	−0.16	−0.11	−0.18	−0.32	−0.15	−0.11	+0.03	−0.19	−0.10	−0.22
Southerlies	+0.15	+0.06	+0.12	+0.15	+0.26	+0.24	+0.16	−0.01	+0.04	−0.08	+0.06	+0.29
Westerlies	+0.24	+0.32	+0.07	+0.02	−0.05	+0.07	+0.08	+0.10	+0.14	+0.14	+0.29	+0.08

Table 2.4 shows the degree of success achieved by a Multiple Linear Regression analysis using the Lamb Weather Types to estimate the rainfall figures. The table shows the percentage of variance in the rainfall figures which can be explained by the Classification time-series.

The first point to note is that the Lamb classification can explain approximately 71% of the variance within the rainfall data. The figure is higher than this for summer and winter but lower for the transitional seasons, spring and autumn. The importance of anticyclonicity and cyclonicity is clear — they alone account for 69% of the variance within the rainfall.

LWTs and Central England Temperatures

Tables 2.5 and 2.6 show the correlation coefficients between the Central England temperature data set (Manley, 1974; Legg, 1989) and the Lamb classifications. The

Table 2.3
Seasonal Correlations between Lamb Weather Types and Rainfall in England and Wales for period 1861–1989

Matrix contains correlation coefficients.

Type	Winter	Spring	Summer	Autumn
Anticyclonicity	−0.82	−0.70	−0.75	−0.70
Cyclonicity	+0.73	+0.73	+0.82	+0.69
Easterlies	−0.10	−0.02	−0.01	+0.00
Northerlies	−0.22	−0.07	+0.01	−0.02
North-westerlies	−0.14	−0.10	−0.24	−0.07
Southerlies	+0.22	+0.18	+0.13	−0.04
Westerlies	+0.19	+0.07	+0.10	+0.21

Table 2.4
Variance in England and Wales rainfall data (1861–1989) accounted for by Lamb Weather Types.

	Jan	Feb	Mar	Apr	May	Jun	Jul	Aug	Sep	Oct	Nov	Dec
Variance (%)	72.3	78.6	66.5	69.5	65.7	69.5	74.0	71.4	70.6	65.3	74.4	71.6

	Winter	Spring	Summer	Autumn
Variance (%)	79.9	65.1	75.7	63.6

situation is more complicated than that for rainfall; the table of seasonal coefficients demonstrates this most clearly — no one classification is important in all seasons. As an illustrative example, look at anticyclonicity — a strong positive correlation in summer (+0.62) becomes small and negative in autumn (−0.05) with similarly disparate coefficients in winter and spring. For this reason, a reduced number of classifications cannot be relied upon — all 7 are equally important in the regression analysis.

Table 2.7 shows the variance values accounted for by LWTs. The relationship is stronger in Winter — accounting for 72% of the temperature variance and considerably weaker in the other seasons, explaining approximately 50%. It is clear then that temperature prediction from LWTs not only relies upon more variables than rainfall estimation but is ultimately less successful.

Table 2.5
Monthly Correlations between Lamb Weather Types and Central England Temperatures for period 1861–1989

Matrix contains correlation coefficients.

Type	Jan	Feb	Mar	Apr	May	Jun	Jul	Aug	Sep	Oct	Nov	Dec
Anticyclonicity	−0.33	−0.32	−0.05	+0.28	+0.23	+0.50	+0.56	+0.53	+0.17	+0.02	−0.33	−0.31
Cyclonicity	−0.03	+0.03	−0.18	−0.33	−0.18	−0.30	−0.46	−0.48	−0.18	−0.11	+0.08	−0.05
Easterlies	−0.55	−0.68	−0.37	−0.21	+0.04	+0.19	+0.21	+0.28	+0.05	−0.10	−0.23	−0.44
Northerlies	−0.55	−0.41	−0.58	−0.48	−0.61	−0.40	−0.37	−0.35	−0.61	−0.63	−0.59	−0.53
North-westerlies	+0.11	+0.12	−0.03	−0.01	−0.18	−0.17	−0.18	−0.16	−0.29	−0.17	−0.10	−0.02
Southerlies	+0.12	+0.22	+0.33	+0.33	+0.38	+0.06	+0.18	+0.24	+0.39	+0.49	+0.42	+0.31
Westerlies	+0.70	+0.74	+0.61	+0.31	+0.13	−0.13	−0.09	−0.13	+0.07	+0.16	+0.55	+0.56

Table 2.6
Seasonal Correlations
between Lamb Weather Types
and Central England Temperatures
for period 1861–1989

Matrix contains correlation coefficients.

Type	Winter	Spring	Summer	Autumn
Anticyclonicity	−0.28	+0.24	+0.62	−0.05
Cyclonicity	−0.07	−0.34	−0.45	−0.01
Easterlies	−0.63	−0.18	+0.21	−0.11
Northerlies	−0.57	−0.42	−0.33	−0.65
North-westerlies	+0.06	+0.01	−0.08	−0.10
Southerlies	+0.27	+0.34	+0.16	+0.47
Westerlies	+0.72	+0.28	−0.30	+0.15

Table 2.7
Variance in Central England temperature data (1861–1989)
accounted for by Lamb Weather Types.

	Jan	Feb	Mar	Apr	May	Jun	Jul	Aug	Sep	Oct	Nov	Dec
Variance (%)	72.2	73.9	62.3	47.0	52.8	42.9	55.7	54.9	49.8	52.4	55.4	64.0

	Winter	Spring	Summer	Autumn
Variance (%)	72.3	43.5	52.3	51.4

2.3 Gales

There are very few sites over the United Kingdom which have long records of daily wind strength. Both alterations to sites and changes in instrumentation mean that the maximum length of homogenous site records in the U.K. is only of the order of 30 years. In order to derive a daily objective catalogue giving numerical values of windflow and vorticity it is necessary to use the grid-point mean sea-level pressure data over the country. Here we follow the guidelines of Jenkinson and Collison (1977). They developed an objective definition of a gale day by calibration with the monthly frequency of gales over the sea areas around the British Isles for a ten year period.

The grid-point mean sea-level pressure data is available in daily form on a 5° latitude by 10° longitude grid extending back to the beginning of 1881.

The gridpoint pattern used for the British Isles region is :

	20°W	10°W	0°W	10°E
65°N		1	2	
60°N	3	4	5	6
55°N	7	8	9	10
50°N	11	12	13	14
45°N		15	16	

Windflow characteristics are computed as follows :

westerly flow :

$$W = \frac{1}{2}(12 + 13) - \frac{1}{2}(4 + 5)$$

southerly flow :

$$S = 1.74(\frac{1}{4}(5 + 2 \times 9 + 13) - \frac{1}{4}(4 + 2 \times 8 + 12))$$

resultant flow :

$$F = (S^2 + W^2)^{\frac{1}{2}}$$

westerly shear vorticity :

$$ZW = 1.07(\frac{1}{2}(15 + 16) - \frac{1}{2}(8 + 9) - 0.95(\frac{1}{2}(8 + 9) - \frac{1}{2}(1 + 2)))$$

southerly shear vorticity :

$$ZS = 1.52(\frac{1}{4}(6+2\times10+14)-\frac{1}{4}(5+2\times9+13)-(\frac{1}{4}(4+2\times8+12)-\frac{1}{4}(3+2\times7+11)))$$

total shear vorticity :

$$Z = ZW + ZS$$

The gale index G is then defined as

$$G = (F^2 + (0.5Z)^2)^{\frac{1}{2}}$$

The gale index for the North Sea region is compiled in the same way from a similar grid extending from 10°W to 20°E and 45°N to 65°N. Over the 10 year period a gale is recorded for G greater than 30, a severe gale for G greater than 40 and a very severe gale for G greater than 50.

The construction of the grid-point mean sea-level pressure data over time has not been consistent. Differences in the extraction of the grid-point data has led to some periods where the data are smoother (low and high pressures less intense) than other periods. Data for 1960–65 are particularly smooth. In order to allow for this the threshold definitions of gale days have been adjusted accordingly (Table 2.8).

The definition of the index based on grid-point mean sea-level pressure data has one particularly serious disadvantage. Gales which only affect a small region such as the October 16, 1987 event, will not be classified as severe as gales which affect a much larger part of the country (e.g. January 3, 1976).

Figures 2.9 – 2.10 show the gale counts for the U.K. and the North Sea from 1880 until the present day. Increasing totals are detectable in the U.K. series. In the 'gale' count this is apparent from 1970 onwards while the 'severe gale' category has shown a gradual rise since the mid 1940s. The 'very severe gale' plot shows the clearest but most recent rise — beginning in the late 1970s. For the first time since records began, one year (1982) contained 6 very severe gales.

The North Sea counts show much less clear trends; the 'gale' total once again shows an increasing value from 1970 onwards. The 'severe gale' plot shows no visible

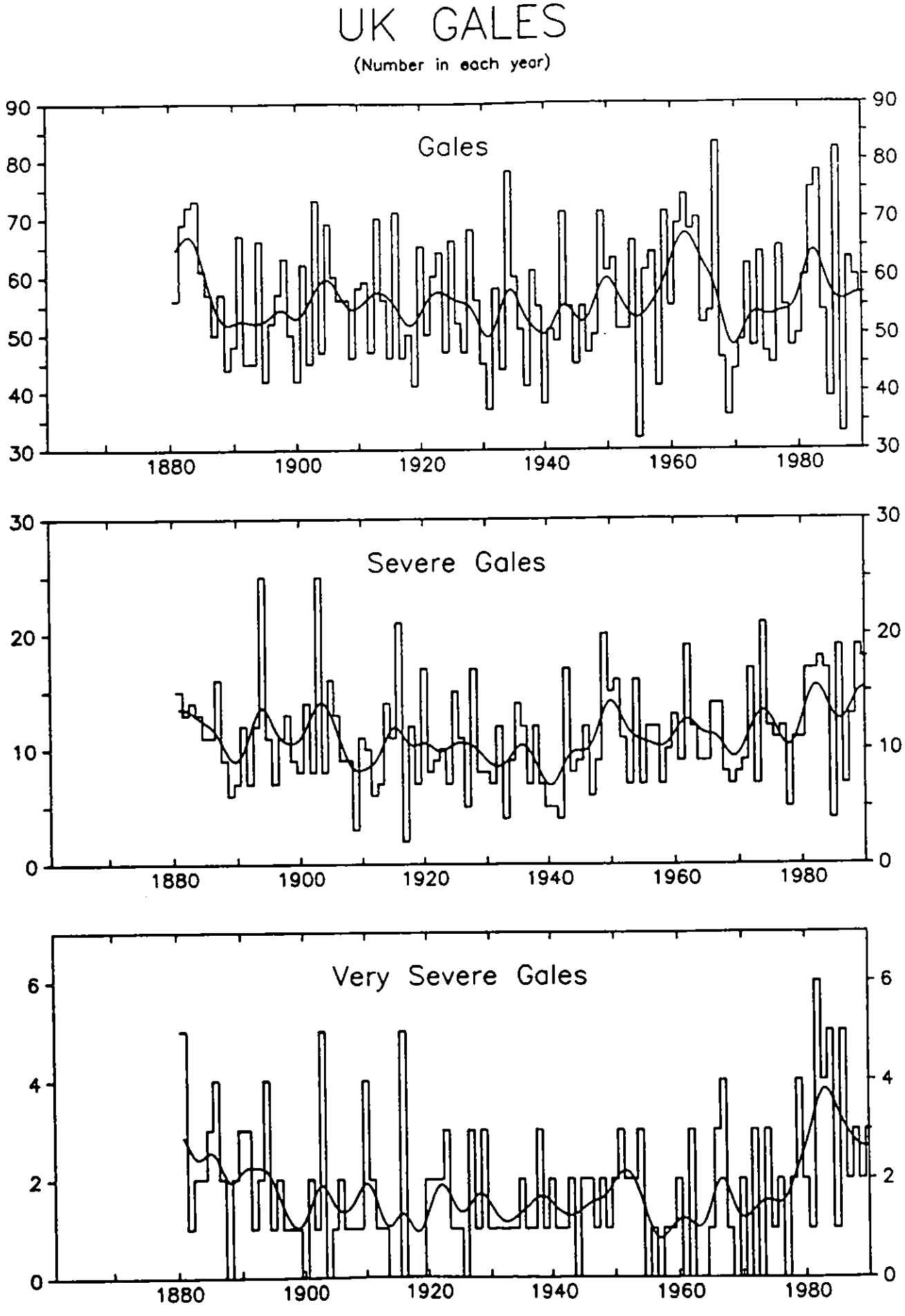

Fig. 2.9 Time-series of annual U.K. Gale counts (1880–1990). The 1990 value is the total for January, February and March only. Curved line represents values after being passed through a 10 year Gaussian filter.

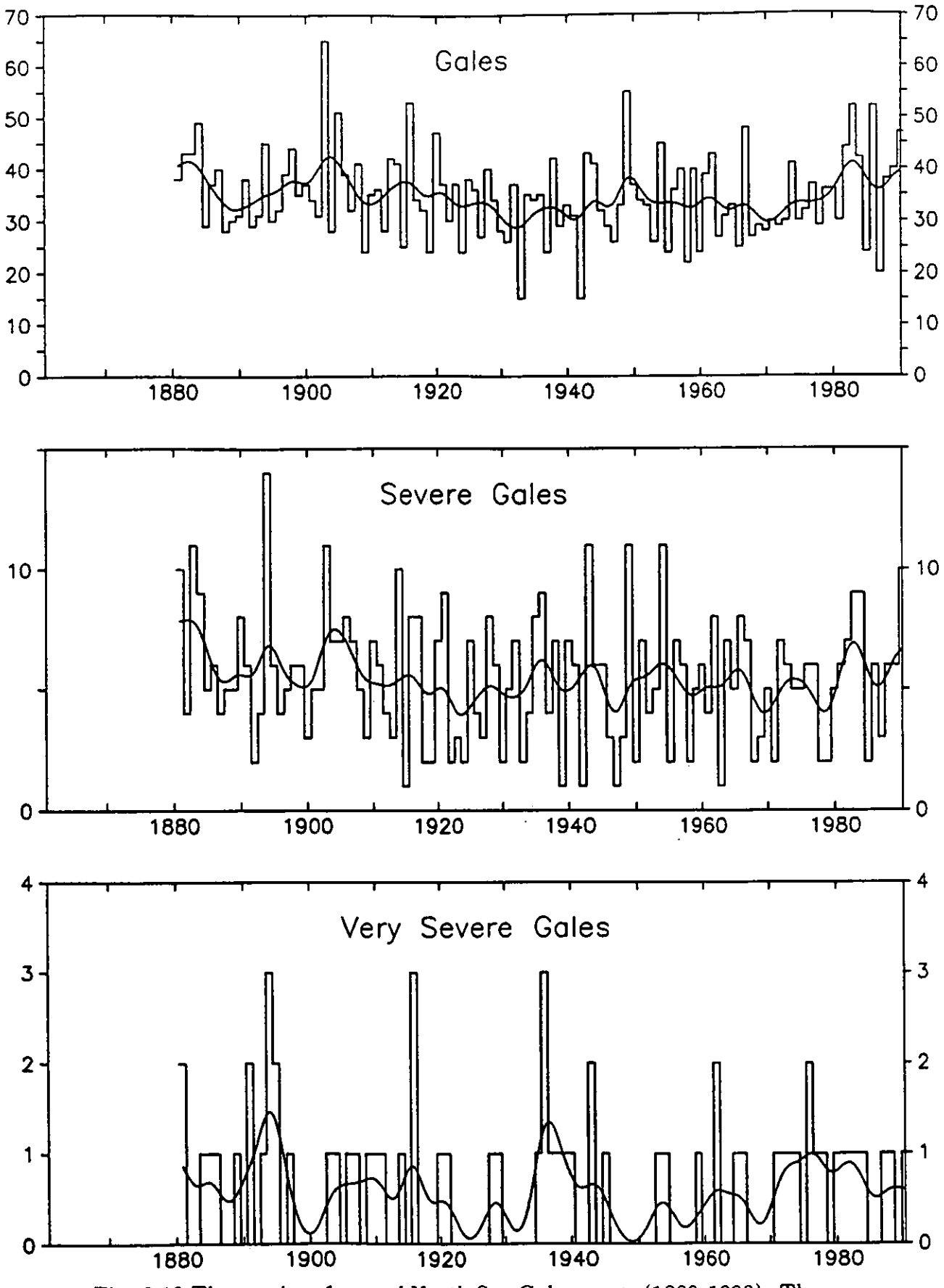

Fig. 2.10 Time-series of annual North Sea Gale counts (1880-1990). The 1990 value is the total for January, February and March only. Curved line represents values after being passed through a 10 year Gaussian filter.

Table 2.8
Threshold Value
of the gale index for different periods

	Threshold value, G		
Period	Gale	Severe Gale	Very Severe Gale
1880–1898	30	40	50
1899–1939	28	37	46
1940–1948	30	40	50
1949–1959	28	37	46
1960–1965	24	32	40
1966–	30	40	50

trend and the 'very severe gale' category shows only a slight rise over the last 30 years.

2.4 Climate Scenarios

As a result of Man's activities, the concentrations of a number of radiately-active trace gases in the atmosphere, in particular carbon dioxide, have increased substantially above their pre-industrial levels and are continuing to rise. It is predicted that the global climate will alter as a result of these changes (WMO, 1986). Not only will the world become warmer but the distribution of precipitation may alter drastically.

These are global changes — the models used to make estimations are still too crude to produce regional scale prediction of climate change. Two 'scenario' methods are often used to predict local effects. The first uses the output from General Circulation Models to produce the scenarios, the second makes use of instrumental analogues. The merits and drawbacks of the two approaches have been discussed

elsewhere. (Wigley et al., 1985; Wigley et al., 1986; WMO, 1988)

The instrumental analogue method was used in this case. Warm and cold periods were selected by examining the Northern Hemisphere Land Temperature records. The make-up of each period in terms of Lamb Weather Type frequencies could then be examined and differences between the periods highlighted.

The warmest and coldest 20 year periods were 1934–53 and 1901–20. Globally, the last 20 years (1970–89) have been the warmest although not in the Northern Hemisphere. This period was, therefore, also included in the analysis. The mean temperatures for the landmasses of the Northern Hemisphere (Jones et al., 1986a) and for the globe (Jones et al., 1986b) are listed in Table 2.9. The global average includes estimates from the land and marine areas. The global temperature difference between the two warm periods and the cold period is roughly the same, either 0.22°C or 0.30°C. Note, however, that for Northern Hemisphere temperatures the 1934–53 period is considerably warmer than the 1970–89 period. Note also that the later warm period has a possible disadvantage in that global mean temperature has changed markedly between its beginning and end (Jones et al., 1986b, updated).

2.4.1 Lamb Weather Types

The seasonal averages of each Lamb Weather Type were calculated for the three periods of interest. The plots of these are presented in figures 2.11 — 2.17. These graphs were examined to determine the differences in terms of Lamb Weather Types between past global warm and cool periods. The findings of this analysis are presented below:

Anticyclonicity

The two warm periods show departures from the cool period in spring and summer. Springs during the 1934–53 period had, on average, 3 more anticyclonic days

Table 2.9
Mean Northern Hemisphere and Global Temperatures (°C) for selected 20 year periods

Period	Northern Hemisphere	Global
(a) 1901–1920	−0.26	−0.23
(b) 1934–1953	+0.14	+0.01
(c) 1970–1989	+0.12	+0.13
(b) − (a)	+0.40	+0.22
(c) − (a)	+0.38	+0.36

than a 1901–20 spring. A summer of the 1970–89 time differed by a similar margin.

Thus, the implication is that during warm global periods in the future, the U.K. may experience increased anticyclonicity during spring and summer.

Cyclonicity

The two warm periods differ from the cold period in different directions during spring and so no consistent conclusions can be drawn for this season. In summer, both warm periods experienced slightly less cyclonicity than the 1901–20 period.

Easterlies

Both winter and spring experienced between one and three days more easterlies during the warm periods. During autumn, this situation was reversed with the warm periods having 2 fewer days on average than the 1901–20 season.

Northerlies

Winter and spring show no coherent differentiation. Two fewer days of Northerlies were recorded in the summer and autumn of the warmer periods.

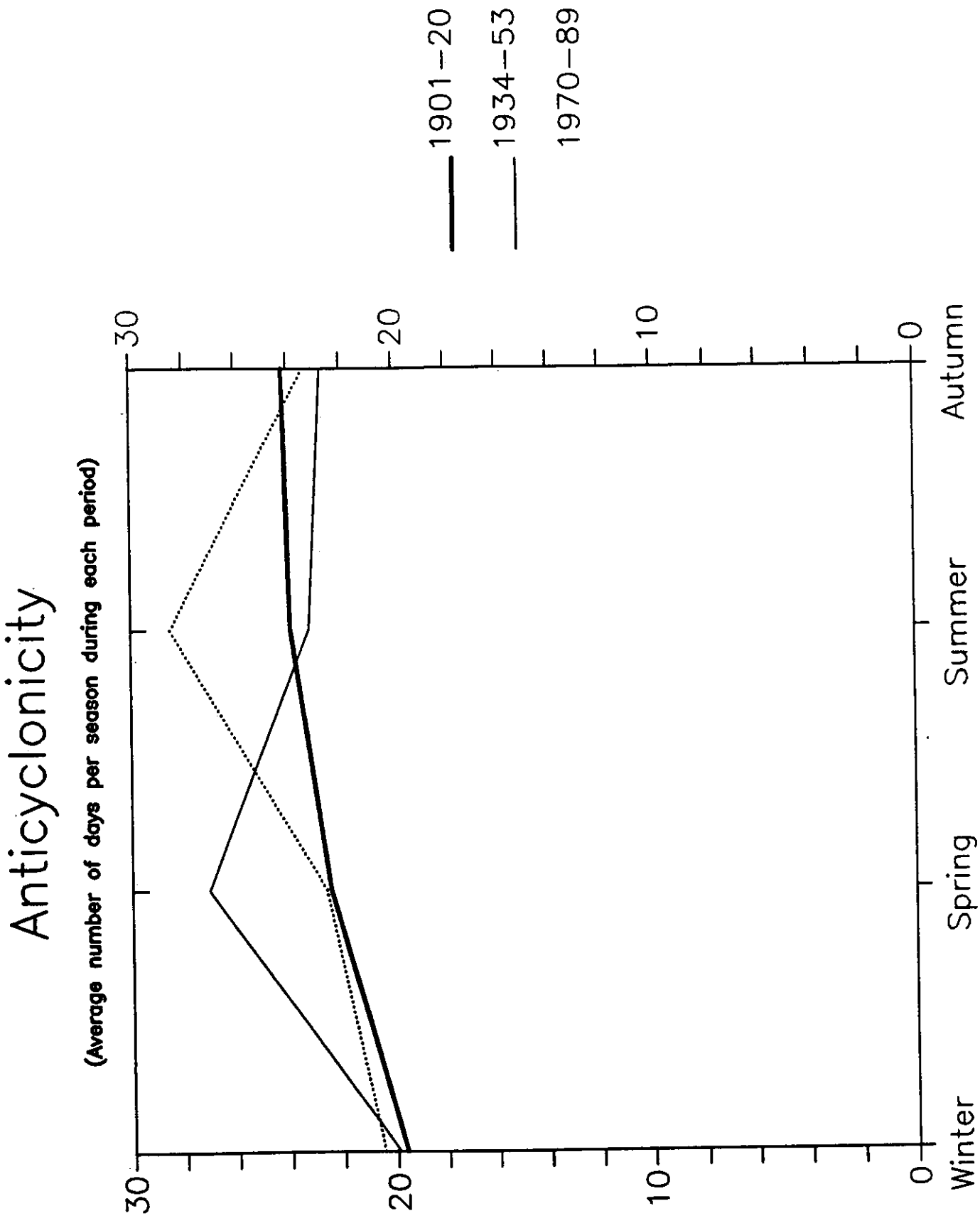

Fig. 2.11 Average seasonal frequencies of anticyclonic days for the periods 1901–20, 1934–53 and 1970–89.

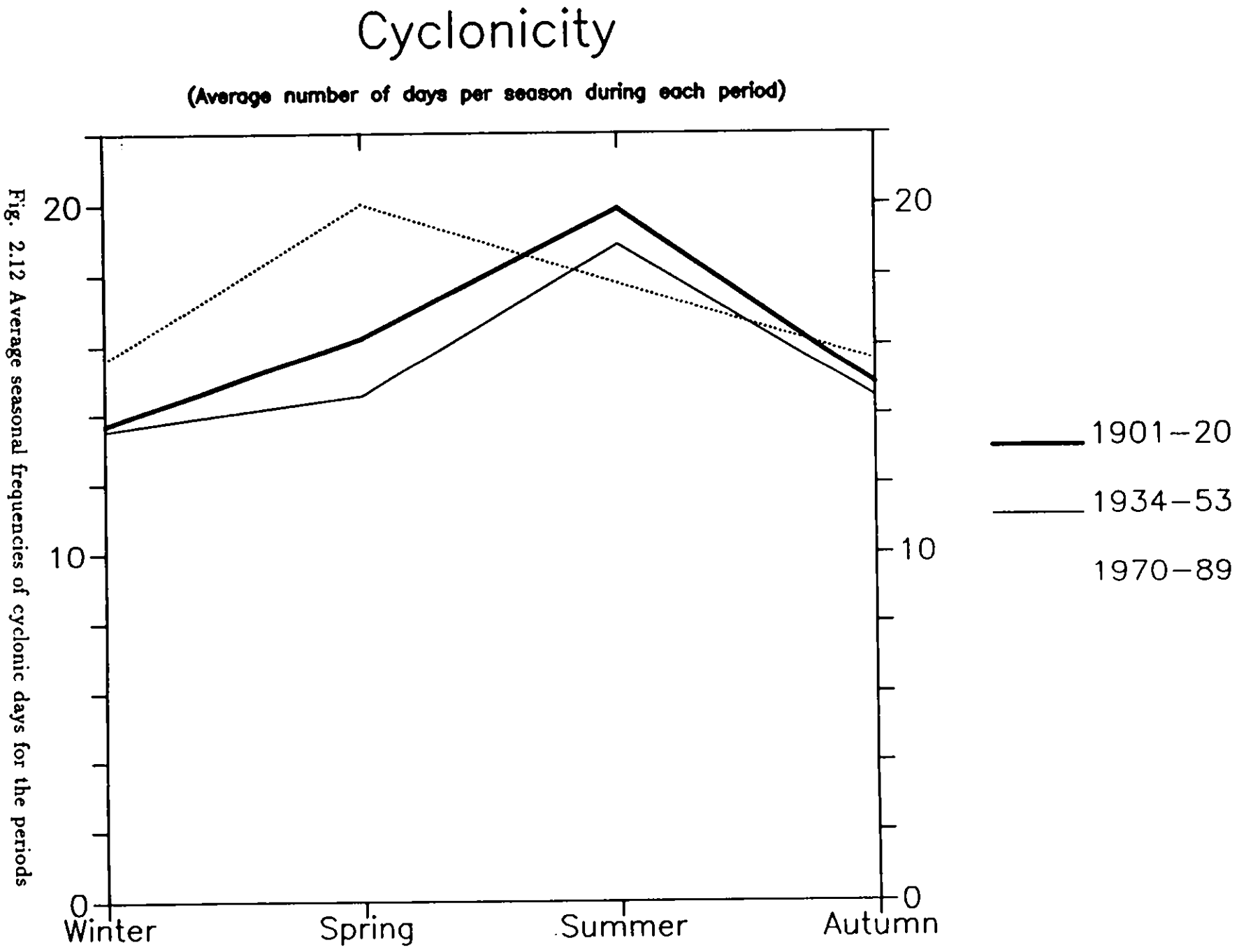

Fig. 2.12 Average seasonal frequencies of cyclonic days for the periods 1901–20, 1934–53 and 1970–89.

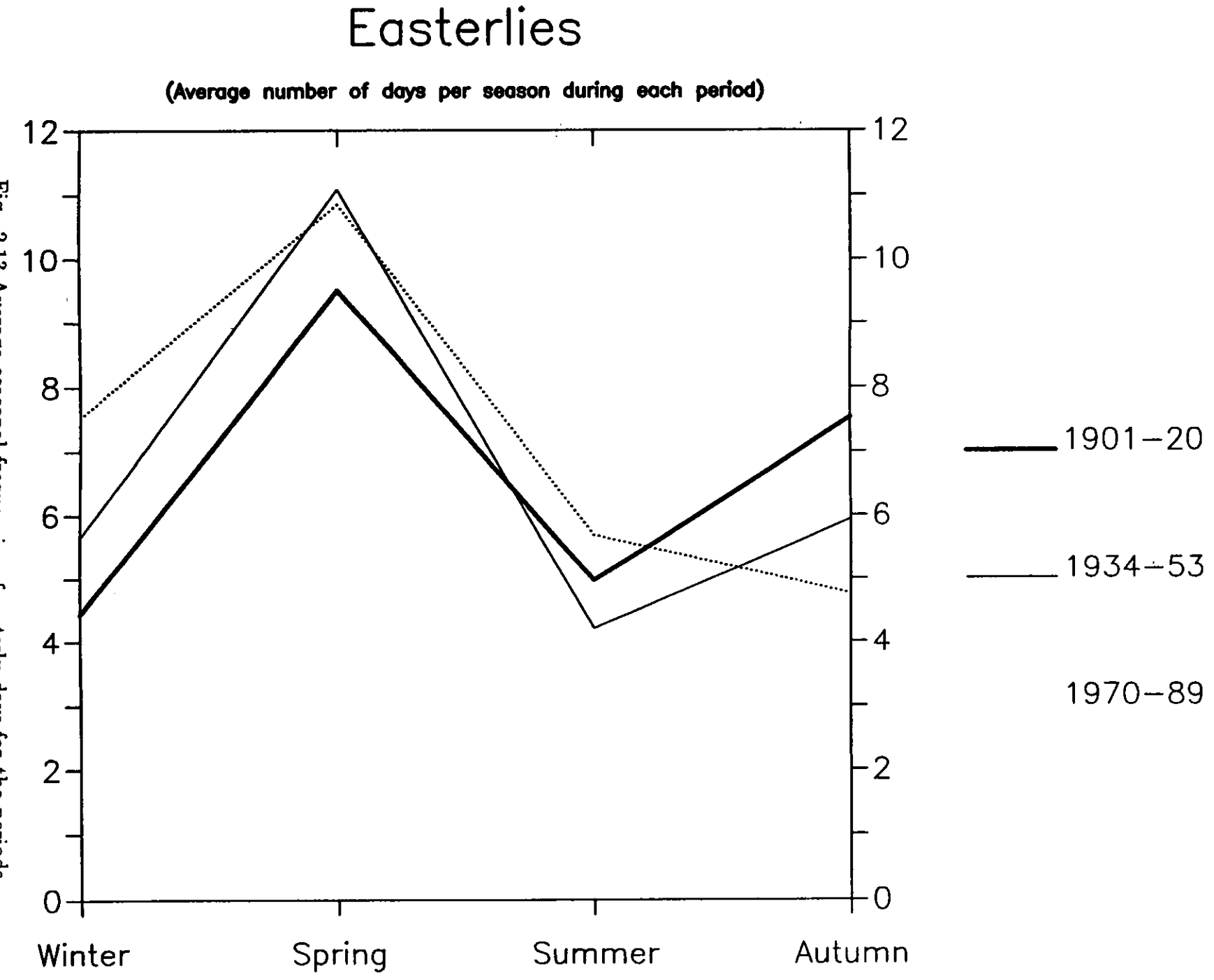

Fig. 2.13 Average seasonal frequencies of easterly days for the periods 1901–20, 1934–53 and 1970–89.

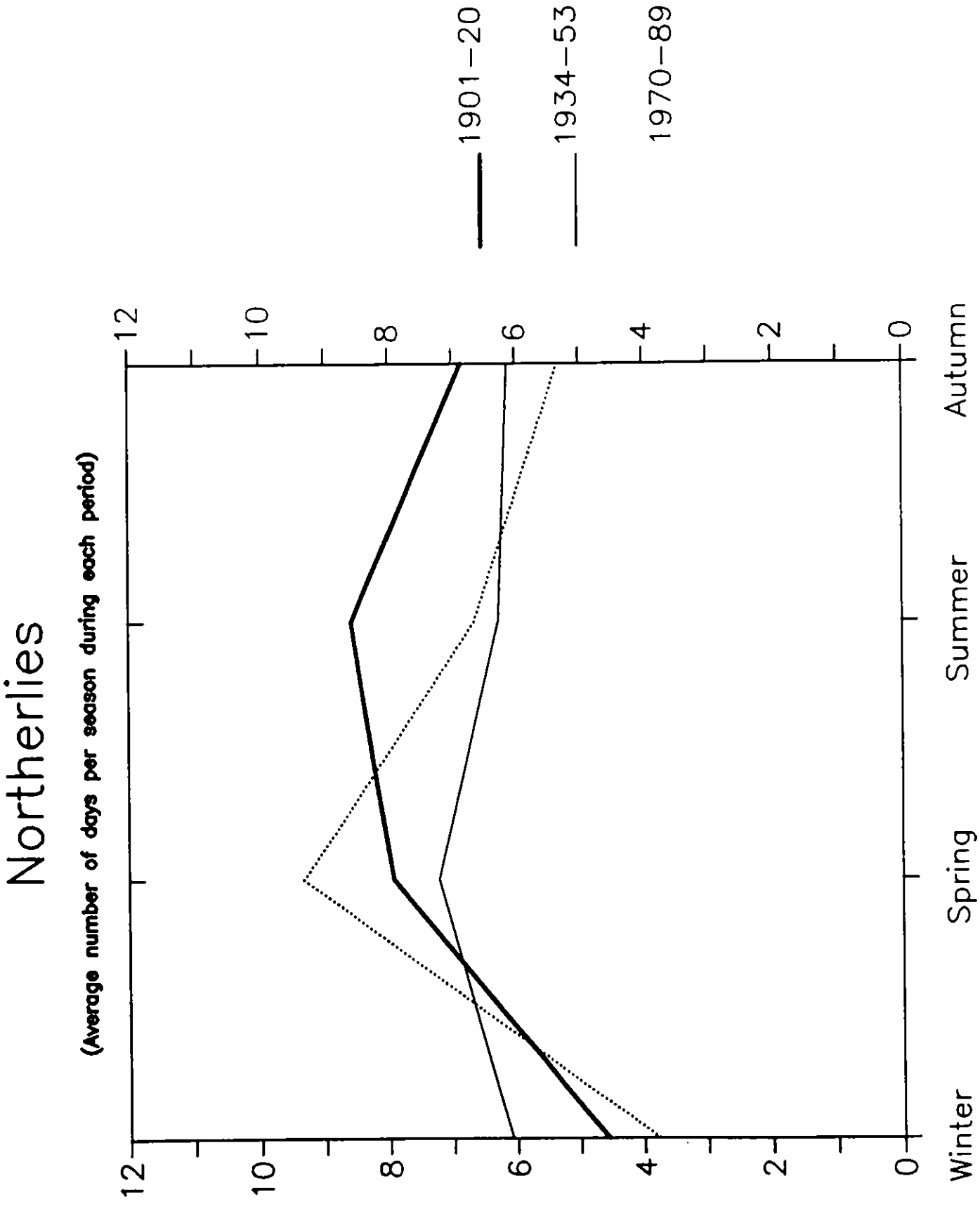

Fig. 2.14 Average seasonal frequencies of northerly days for the periods 1901–20, 1934–53 and 1970–89.

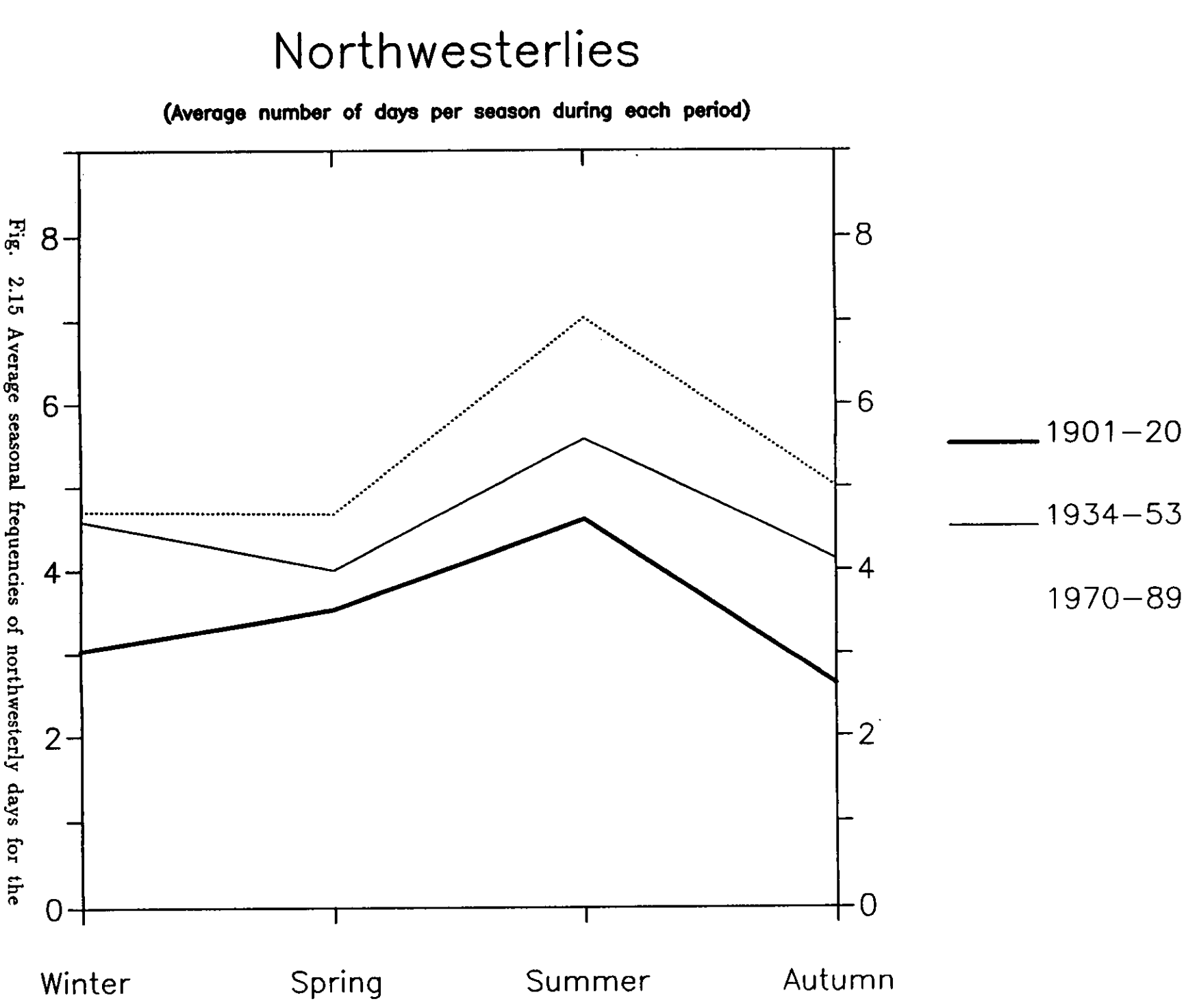

Fig. 2.15 Average seasonal frequencies of northwesterly days for the periods 1901–20, 1934–53 and 1970–89.

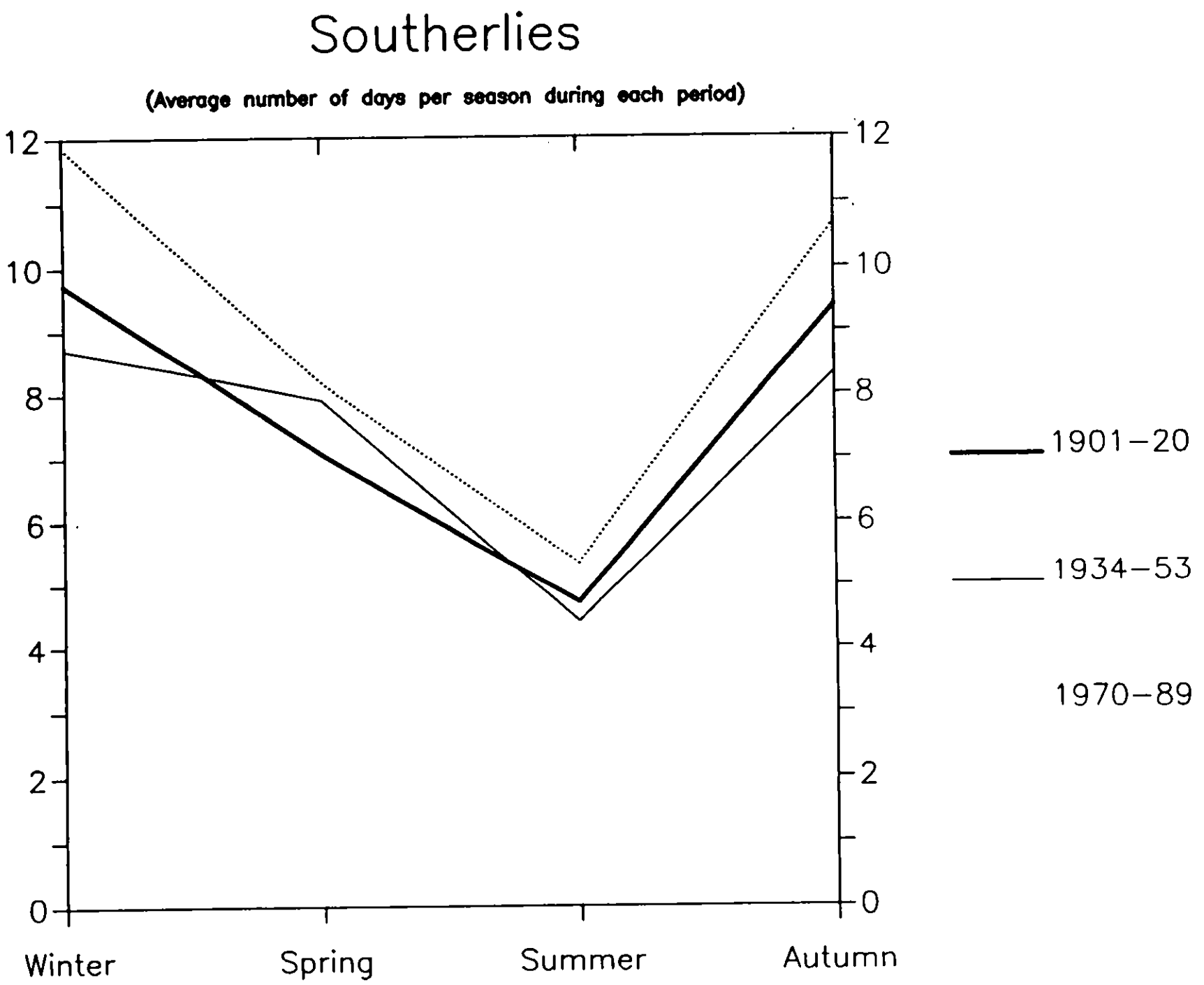

Fig. 2.16 Average seasonal frequencies of southerly days for the periods 1901–20, 1934–53 and 1970–89.

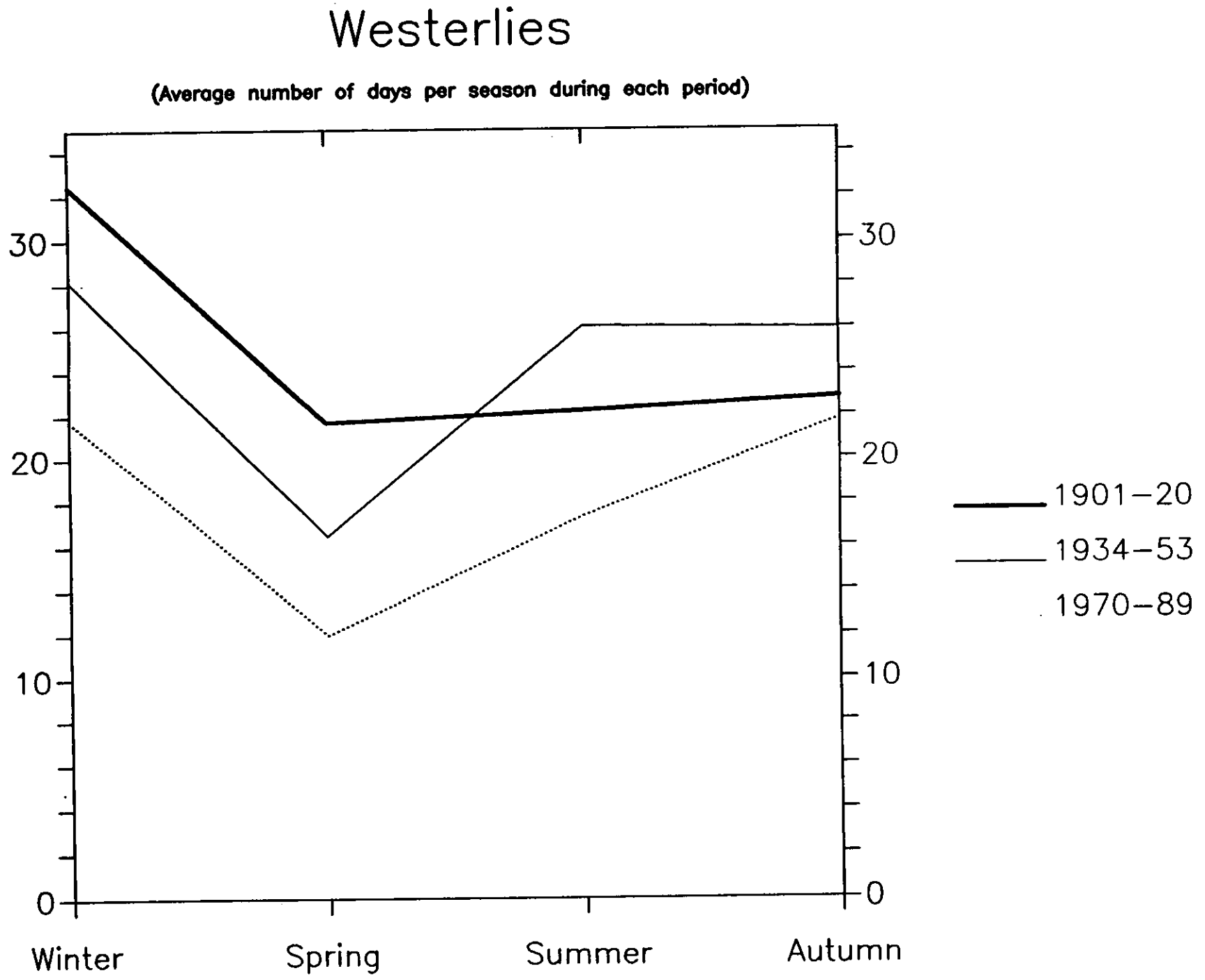

Fig. 2.17 Average seasonal frequencies of westerly days for the periods 1901–20, 1934–53 and 1970–89.

North-westerlies

This classification shows a consistent trend during all seasons. A difference is also maintained between the two warm periods themselves. The 1970–89 period has approximately 1 more day than the 1934–53 period which in turn has 1 more than 1901–20.

Southerlies

The earlier warmer period shows little significant difference from the cool period but the 1970–89 period exhibits on average 1 more southerly day in each season.

Westerlies

As would be consistent with the earlier discussed decline of the westerlies, a clear drop has occurred in winter and spring from 1901–20 to 1934–53 and then 1970–89. The difference between each of the periods is of the order of 2 or 3 days during all seasons.

2.4.2 Gales

The gale counts during the three periods were also examined. The plots of these are presented in figures 2.18 — 2.23.

U.K.

For all three severities of gale, the warm periods had markedly higher autumn counts. For both 'gale' and 'severe gale' categories, the cooler period had a larger winter total. Very severe gales however were more prevalent in the 1970–89 period during all seasons.

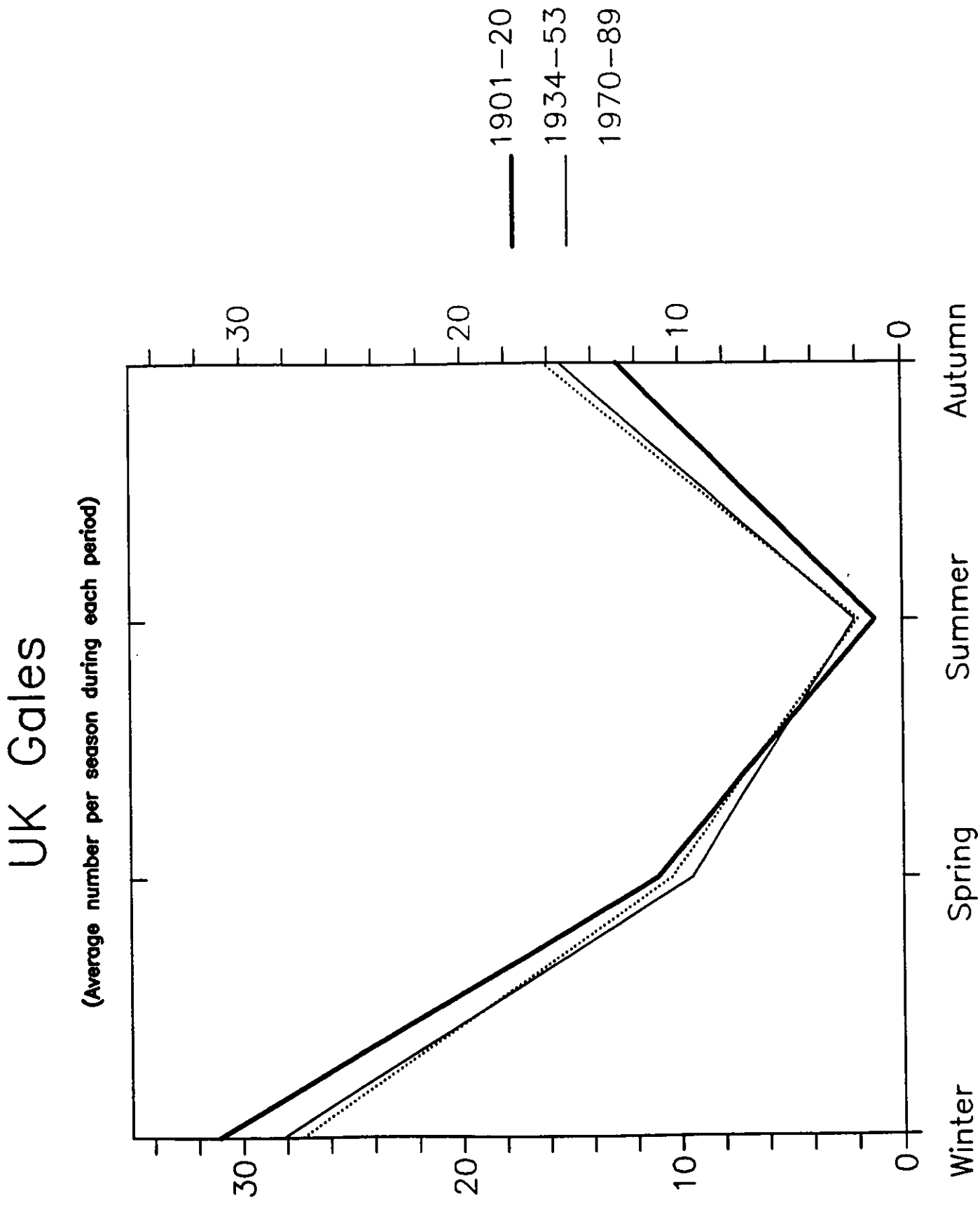

Fig. 2.18 Average seasonal frequencies of U.K. gales for the periods 1901–20, 1934–53 and 1970–89.

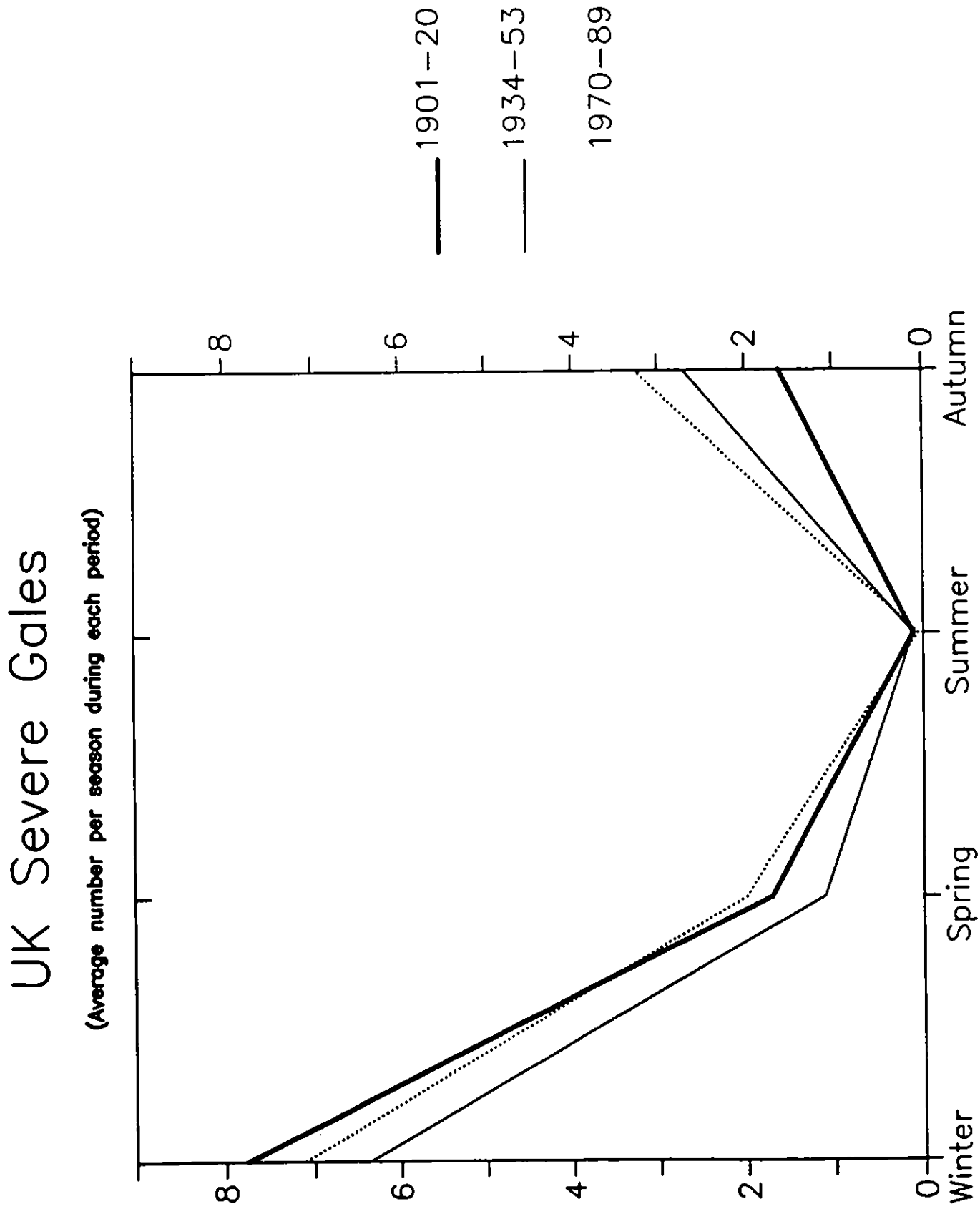

Fig. 2.19 Average seasonal frequencies of U.K. severe gales for the periods 1901–20, 1934–53 and 1970–89.

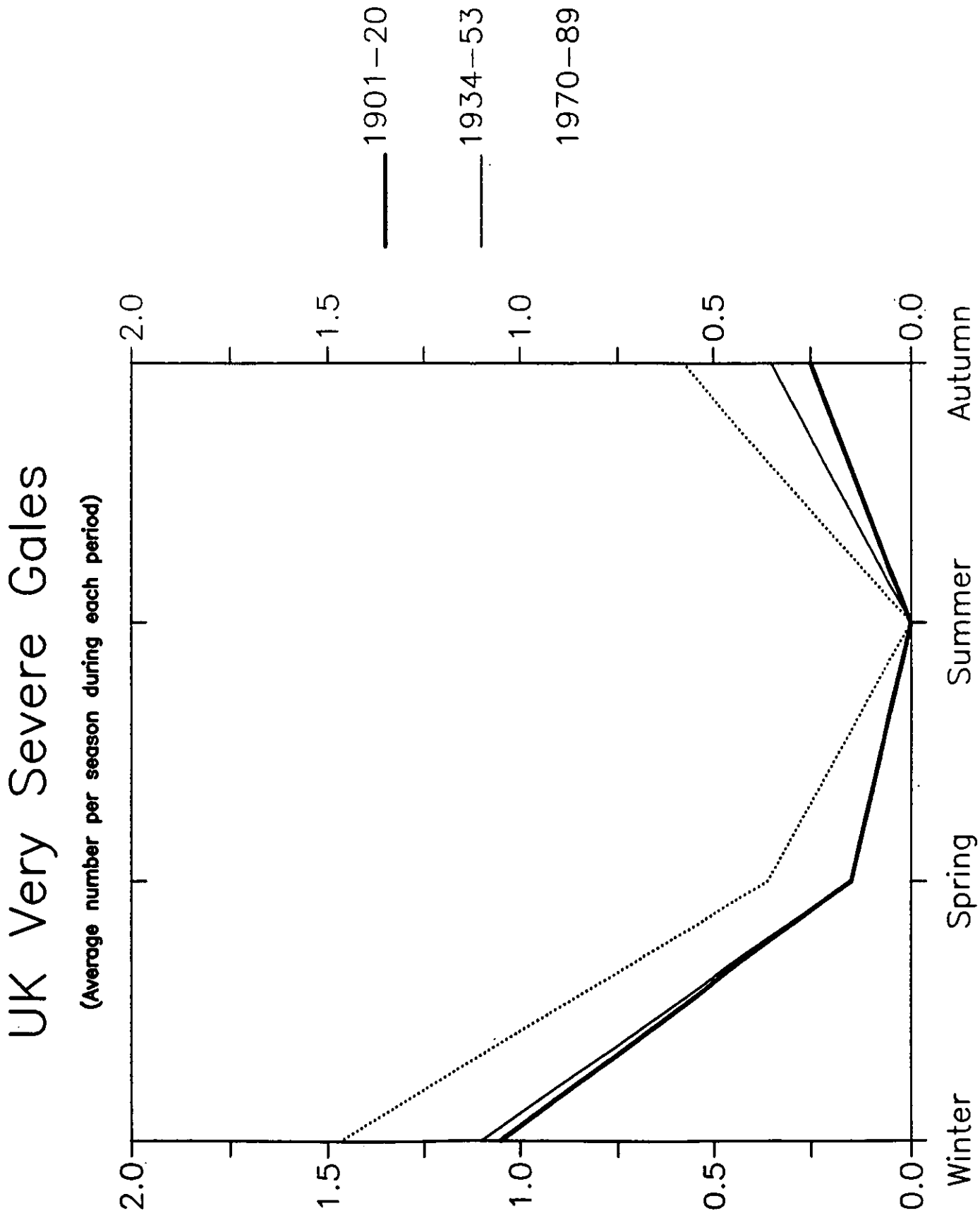

Fig. 2.20 Average seasonal frequencies of U.K. very severe gales for the periods 1901–20, 1934–53 and 1970–89.

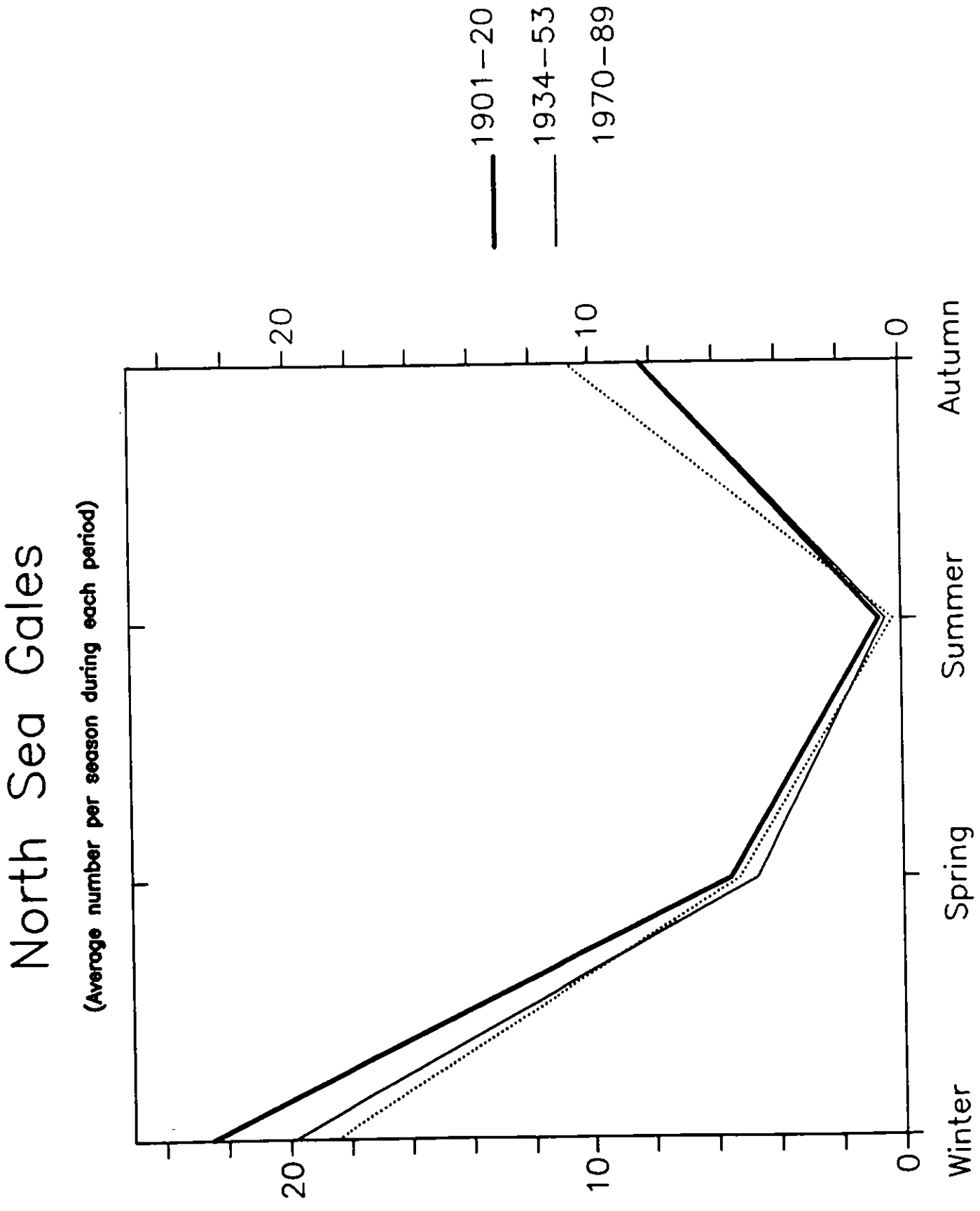

Fig. 2.21 Average seasonal frequencies of North Sea gales for the periods 1901–20, 1934–53 and 1970–89.

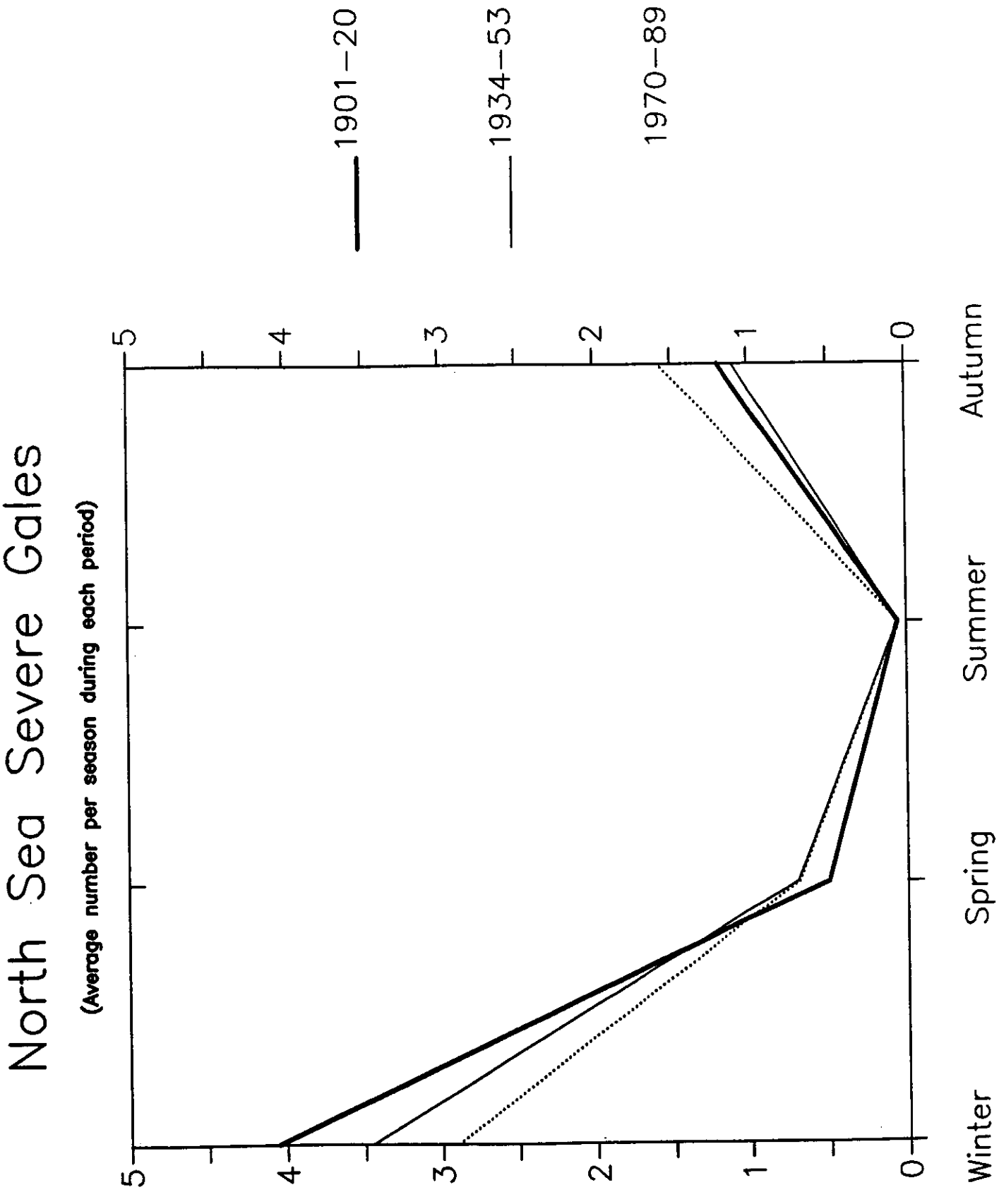

Fig. 2.22 Average seasonal frequencies of North Sea severe gales for the periods 1901–20, 1934–53 and 1970–89.

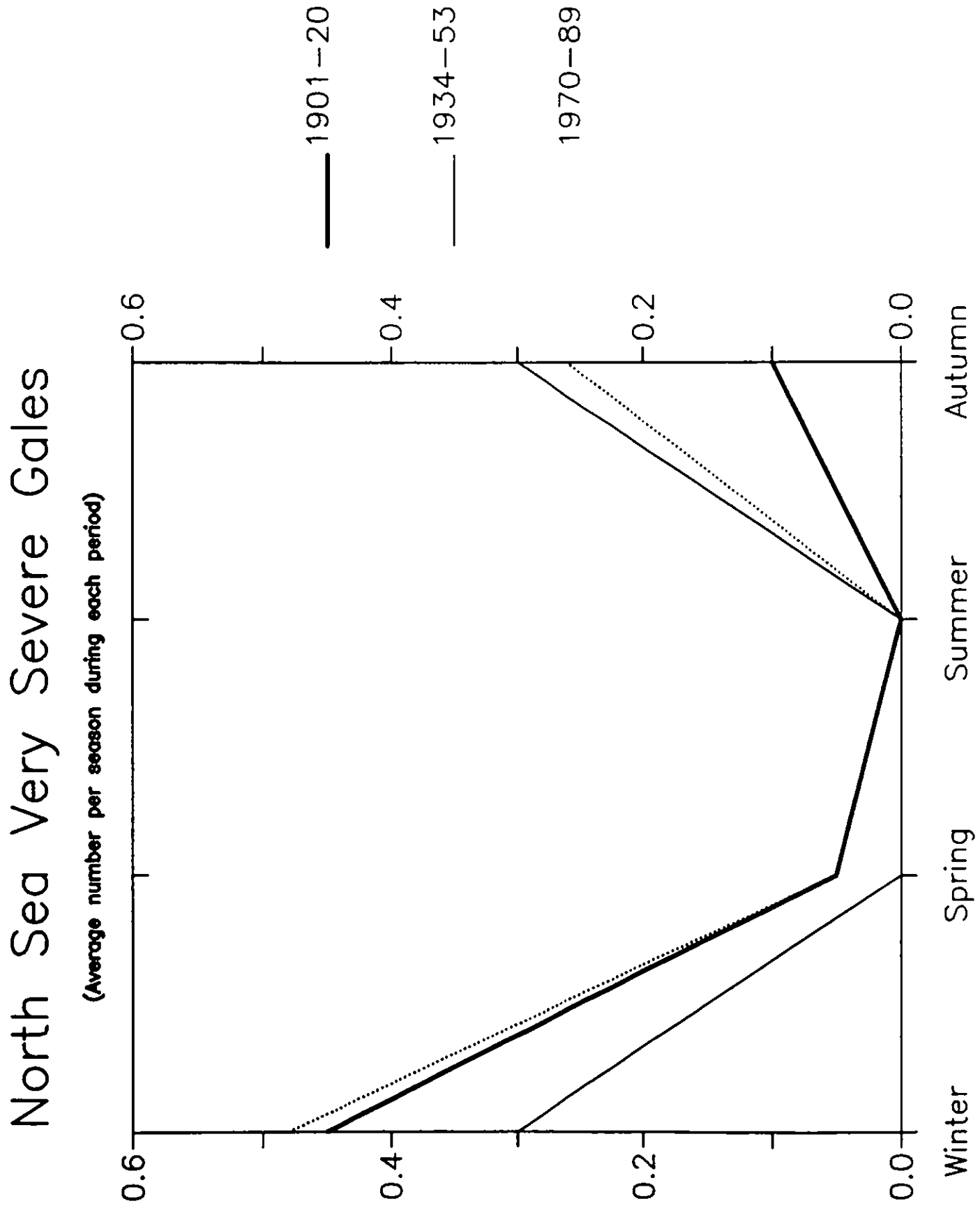

Fig. 2.23 Average seasonal frequencies of North Sea very severe gales for the periods 1901–20, 1934–53 and 1970–89.

North Sea

In the 'gale' count, the winters of the warmer periods contained 2 or 3 fewer gales than the cool period. Severe gales were also reduced in the warmer periods' winters. Very severe gales showed a less coherent pattern in winter but both warm periods had nearly 3 times the autumnal total of the colder period.

2.4.3 Summary

Once again, the westerly LWT shows the most important trait; considerably fewer westerly days were found in winter and spring of the warmer periods. Other significant findings are that more north-westerliness occurred in 1970–89 and 1934–53 than 1901–20. Although the two warmer periods were not consistent, increased anticyclonicity was found during their springs and summers. Also, less northerliness in summer and autumn was noted in the warmer periods.

A seasonal shift occurred in the timing of both U.K. and North Sea gales. Winter totals increased at the expense of the autumn frequency. Also, in the later warm period, a noticeably higher frequency of very severe gales was recorded.

2.4.4 Rainfall and Temperature Scenarios

By substituting the seasonal average frequencies of the Lamb Weather Types for the three periods back into the regression equations as discussed in 2.4, it was possible to determine the rainfall and temperature changes which may result in a warmer world. This could be done by making the assumption that changes in Lamb Weather Type frequencies from cool to warm periods would be reproduced and perhaps enlarged in any future warming of the world. The resulting estimations of rainfall in England and Wales and Central England temperatures for the three periods are plotted in figures 2.24—2.25. Since they are estimates based only upon Lamb Weather Type changes their accuracy as concerns the *actual* rainfall and temperatures is not

examined here. It is the differences between the periods which is under examination. The discussion below centres upon the predicted values from the regression equations *not* the actual data.

Rainfall in England and Wales

Essentially, the two warmer periods produced less estimated rainfall, particularly in winter and summer. In winter, this was largely the result of the decline in westerlies (which are associated with precipitation in winter) since the first 20 years of this century. Summers of 1970–89 particularly were judged drier because of increased anticyclonicity (associated with decreased rainfall) and slightly reduced cyclonicity.

Autumn helped reduce the precipitation deficit very slightly since the warmer periods were estimated as being some 4mm wetter than 1901–20. Spring produced an interesting result — the 1934–53 season was estimated at 15mm drier than 1901–20 and the 1970–89 time at 10mm wetter than the cool period. This perplexing result can be explained by examining the anticyclonicity and cyclonicity plots. The 1934–53 period had much increased anticyclonicity in spring which is linked with less rainfall. Conversely, cyclonic conditions are associated with increased rainfall, and these were more frequent during 1970–89 springs.

Less rainfall can be expected in Britain as a consequence of the greenhouse effect. This is as a result of increased anticyclonicity and decreased cyclonicity, the two LWTs strongly linked to rainfall.

Central England Temperatures

The temperature predictions were less accurate — it should also be remembered that only 50% of temperature variance was accounted for by the LWTs in the regression analysis. Summer and autumn produced warmer temperatures — the 1970–89 period to a much greater degree in both seasons (0.4°C) than the 1934–53

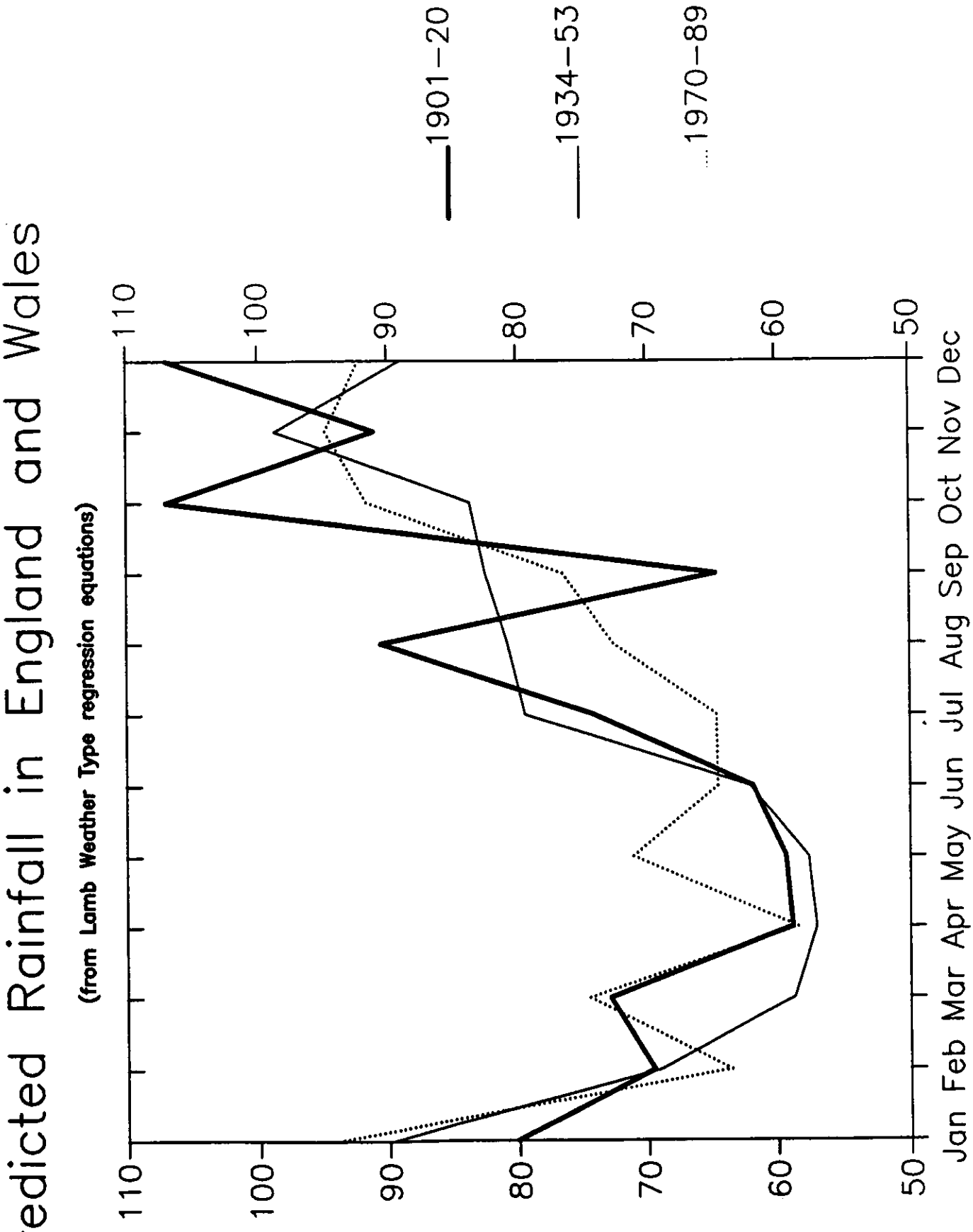

Fig. 2.24 Estimations of monthly average England and Wales rainfall totals for 1901–20, 1934–53 and 1970–89 using regression equations.

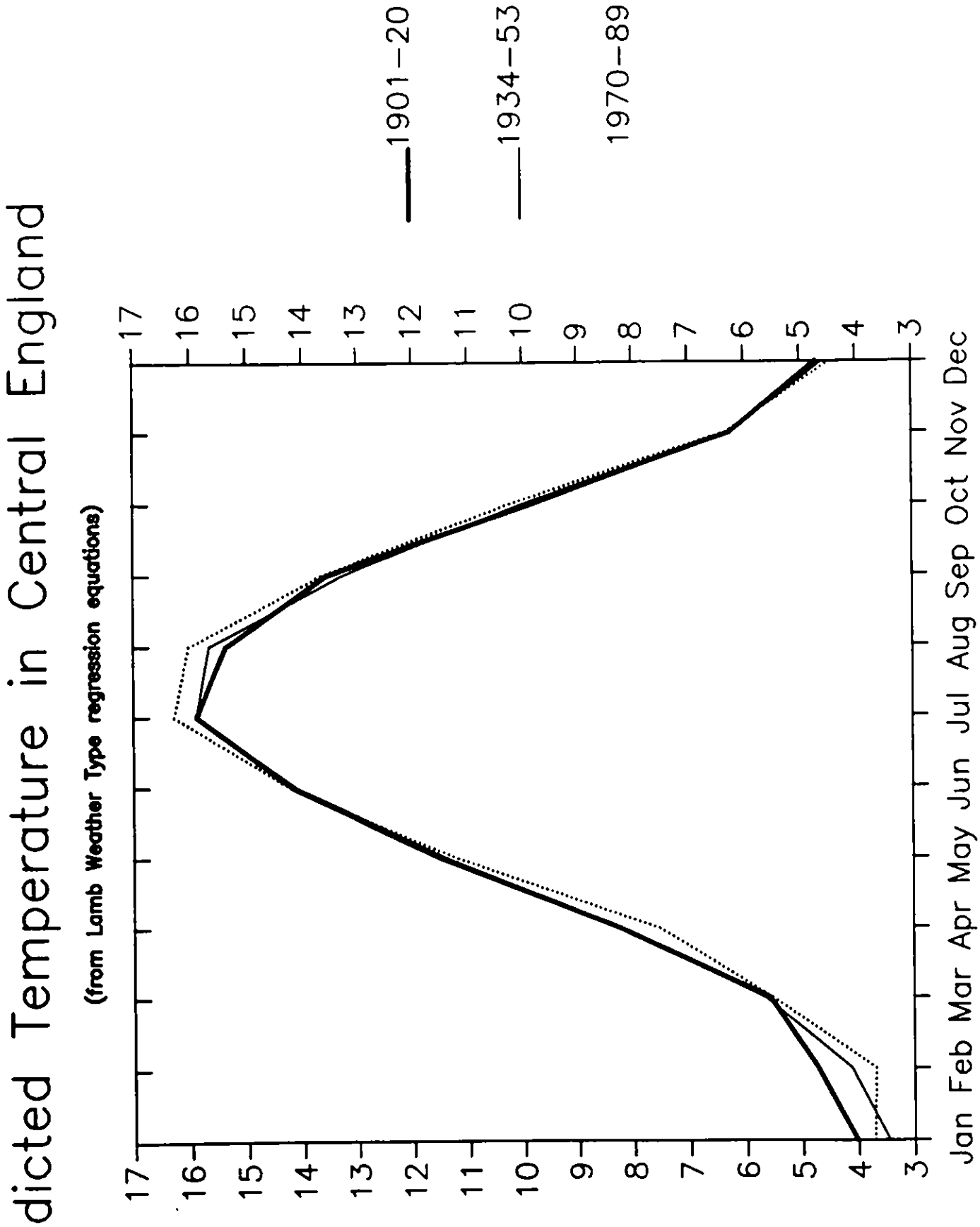

Fig. 2.25 Estimations of average Central England temperatures for 1901–20, 1934–53 and 1970–89 using regression equations.

period (0.1°C). In summer, both the warmer periods experienced increased Anticyclonicity but the extremity of 1970–89 is caused by the much reduced Westerliness during this period. The autumn differential was mostly due to the decreased frequency of easterlies and northerlies. Winter though produced estimates over 0.5°C cooler during the globally warm periods — this too was caused by the decline of the westerlies. As with the rainfall results, spring showed the two warm periods diverging; 1934–53 was 0.1°C warmer than 1901–20 and 1970–89 was 0.3°C cooler than the spring of the cool period. The 1934–53 spring had increased anticyclonicity which is associated with raised temperatures whereas the 1970–89 spring was cooler once again because of the decline in frequency of westerlies.

The decline of Westerly frequencies is the most important factor in the temperature predictions. If frequencies continue to fall, Britain is likely to experience cooler winters and warmer summers and autumns.

3 RADIATION AND EVAPORATION

Simulations from a number of GCMs are available. In this section we analyse the seasonal results from GCMs which have archived incident solar radiation and evaporation data. Some details about the models are given in Table 3.1. These models and others have been intercompared by a number of authors (see, for example, Schlesinger and Zhao, 1989). Most intercomparisons are made using model generated and real world temperature and precipitation data. The results indicate that while the models reproduce many features of the real world, models show deficiencies in any regions. Furthermore, there is great variability between the models.

Although no comparison between real world and model generated incident solar radiation and evaporation data are performed we would expect it to show similar deficiencies to the temperature and precipitation comparisons. Considerable intermodel variability can be expected for the variables analysed here as has been

Table 3.1
Characteristics of General Circulation Models

	UKMO	GISS	GFDL	OSU
Horisontal Resolution: Latitude	5°	7.83°	4.5°	4°
Longitude	7.5°	10°	7.5°	5°
°C change in global mean temp. for $2\times CO_2$	+5.2	+4.2	+4.0	+2.8
% change in global precip. for $2\times CO_2$	+15.0	+11.0	+8.7	+7.8
Reference	Wilson and Mitchell, 1987a	Hansen et al., 1984	Manabe (pers. comm.)	Schlesinger and Zhao, 1989

observed with temperature and precipitation.

Incident solar radiation information is available from the GISS, GFDL, OSU and UKMO models. Evaporation is also available only from the first three models.

3.1 Incident Solar Radiation

Winter

All four models predict small changes for winter. The GFDL and GISS both envisage small negative changes over most of Britain — in the order of -2 or -3 wm^{-2} ($\approx$5%). The OSU model, though, shows most of Britain experiencing slight increases in incident solar radiation. The UKMO model shows almost no change over the U.K..

Spring

The models show a much greater range of change for this season than winter. They all show positive changes over the majority of Britain. One feature of the GFDL model which recurs in many seasons is the large estimated changes at high latitudes — for instance, in this season, changes of more than 100 wm^{-2} (>50%) occur at around 66° latitude. These large fluctuations do not extend down as far as Britain but approach the Shetland region in some seasons. For spring, the scale is such that changes over Britain can only be labelled as being positive but less than 18 wm^{-2}. The UKMO concurs with this, showing an increase of 18 wm^{-2} ($\approx$10%) in Scotland. The OSU model disagrees strongly with the GFDL predictions for high latitudes — giving negative changes as large as -23 wm^{-2} ($\approx$14%) in these areas. Over Britain, though, small (near zero) positive changes are forecast by this model. The GISS model shows similar estimates.

Summer

Summer shows a broad agreement between the models. The largest positive

changes are forecast for this season. The UKMO shows the most extreme values — changes of +30 wm^{-2} (≈12%) are produced over northern Scotland, decreasing to around +10 (≈4%) in south-east England. GISS and OSU both show shifts of +10 (≈4%) in the south *decreasing* to +2 (≈1%) in northern Scotland i.e. the reverse of the regional pattern produced by UKMO. The GFDL model once again shows very large changes (over 150 wm^{-2}, >50%), in high latitudes and indicates positive change over Britain of the same order as the other models.

Autumn

Small changes were forecast by all the models. The GFDL model shows small negative changes over most of Britain with small positive changes in the south-west. The GISS and OSU models show similar patterns over Britain, both ranging from small negative fluctuations in Scotland to increases of around +4 wm^{-2} (≈5%) in southern England. The UKMO model shows the reverse pattern to this and also the largest changes for this season — increases of approximately +12 wm^{-2} (≈10%) in Scotland reducing to +3 (≈3%) over most of England.

3.1.1 Summary

Overall, significant increases are forecast for Britain particularly in summer and, to a lesser extent, spring. The changes are generally of the order of 10 wm^{-2} (≈4%). Some decreases were predicted but they were exceptions to the general increasing trend. Some degree of caution should be exercised, however, because of the great intermodel variability in the present climate simulations (1 $\times CO_2$ results).

The UKMO model predicts quite large increases in incident solar radiation for all seasons — particularly in Scotland where changes of 30 wm^{-2} (≈12%) are forecast during summer. The OSU model produces small positive changes for most seasons; the increases being larger in southern England with some negative shifts occurring in

Scotland. The GISS model shows marked similarities with the OSU model : again, small positive increases occur in most seasons with larger shifts in the south of England. During winter small negative fluctuations were forecast for the whole of Britain. The GFDL produced the most extreme maps of changes - summer in latitudes of around 65° is forecast to experience a doubling of incident solar radiation. Summer and spring will have large changes but winter and autumn will change little according to this model.

3.2 Evaporation

Winter

There was a large degree of agreement between the three models. Over all of Britain increases of around 0.2 mm/day (≈5–7%) were forecast. The extreme west and north show larger values. All the models also show much larger increases at higher latitudes (>65°N); of the order of 1 mm/day (≈20%).

Spring

Again, the models largely concur with larger increases being indicated in the north and west. The magnitude of the shifts show larger variance than for winter — OSU and GFDL show increases of around 0.2 mm/day (≈10%) but GISS estimates nearer 0.4 mm/day (≈20%) for the majority of the U.K..

Summer

This is the only season in which decreases in evaporation are predicted for Britain. OSU shows very small negative values (−0.03) in most of Britain with similarly small positive values in northern Scotland and south-west England. Both GISS and GFDL show small negative values in parts of southern Britain but positive values increasing as one travels northwards to values of +0.6 mm/day (≈8%) in Scotland (GISS) and

north-east England (GFDL).

Autumn

Autumn produces the greatest disagreement between all the models but also the largest rises over Britain. OSU estimates increases of between 0.4 (≈20%, Scotland) and 0.2 mm/day (≈8%, south-east England) for Britain. The GISS model shows a conflicting pattern with the largest increases (0.7 mm/day, ≈25%) in the south-west dropping to 0.2 mm/day (≈8%) in northern Scotland. Different again, the GFDL model shows changes of +0.6 mm/day (≈20%) in north-eastern England but only +0.1 (≈8%) in southern England.

3.2.1 Summary

Important increases are forecast in evaporation particularly for Scotland and northern England. All seasons except winter show similarly significant changes.

The OSU model shows the least predicted change of all the models. Only autumn shows fluctuations larger than 0.2 mm/day. GISS forecasts the largest shifts - spring, summer and autumn all having shifts of around 0.5 mm/day in areas of the British Isles. Autumn shows a unique feature — the greatest change on the map is found in the Atlantic Ocean level with France. This radiates outwards giving Wales and south-west England the greatest changes. Finally, the GFDL model shows positive change of around 0.2 mm/day during winter and spring. In summer and autumn there is a great deal of variation across the country with north-eastern England experiencing increases of 0.6 mm/day (summer and autumn) and the south-east decreases of 0.5 mm/day (summer only).

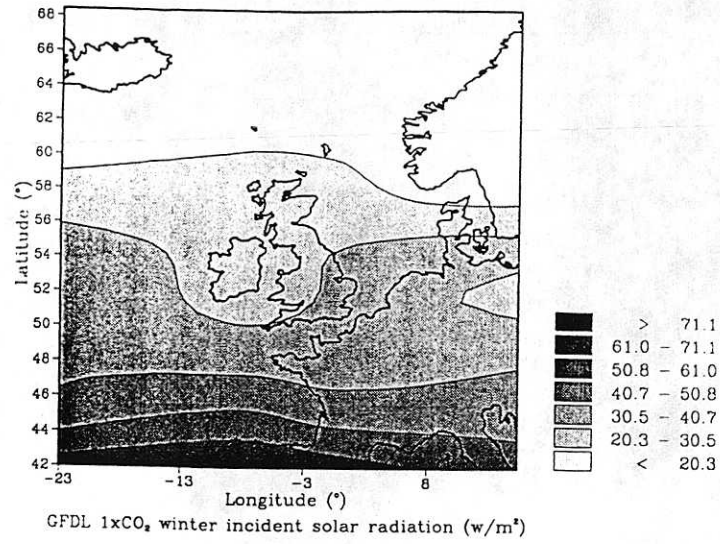

GFDL 1xCO$_2$ winter incident solar radiation (w/m^2)

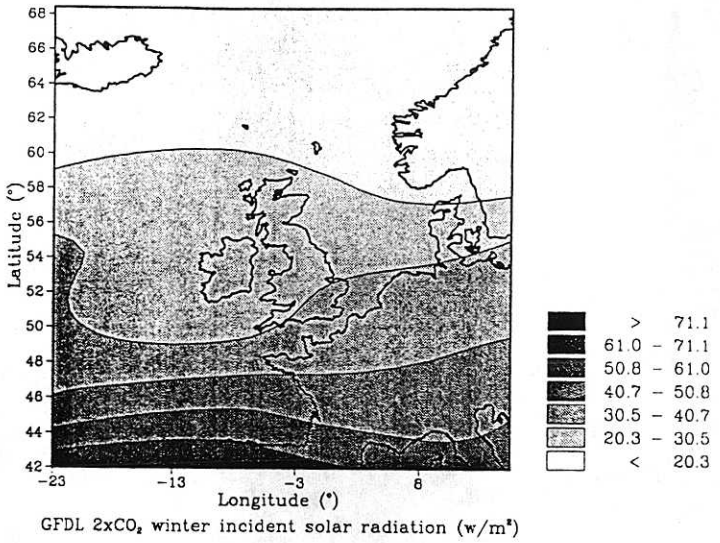

GFDL 2xCO$_2$ winter incident solar radiation (w/m^2)

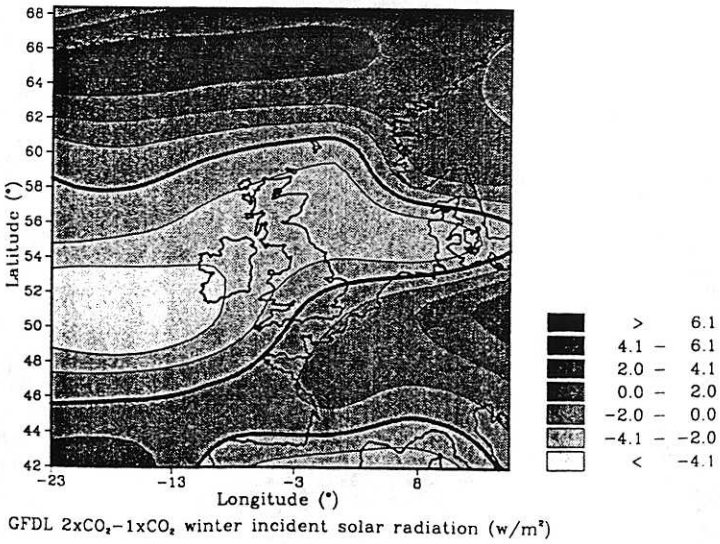

GFDL 2xCO$_2$−1xCO$_2$ winter incident solar radiation (w/m^2)

Fig 3.1 Incident Solar Radiation (Winter) from GFDL model for $1\times CO_2$, $2\times CO_2$ and $2\times CO_2-1\times CO_2$.

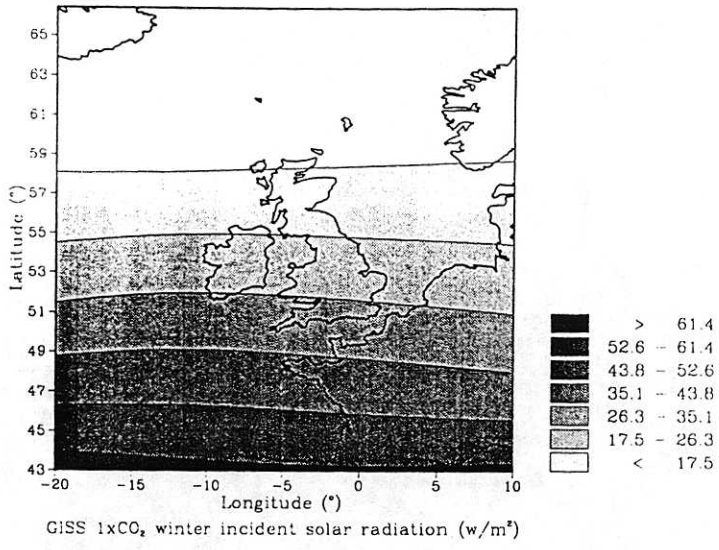

GISS $1xCO_2$ winter incident solar radiation (w/m^2)

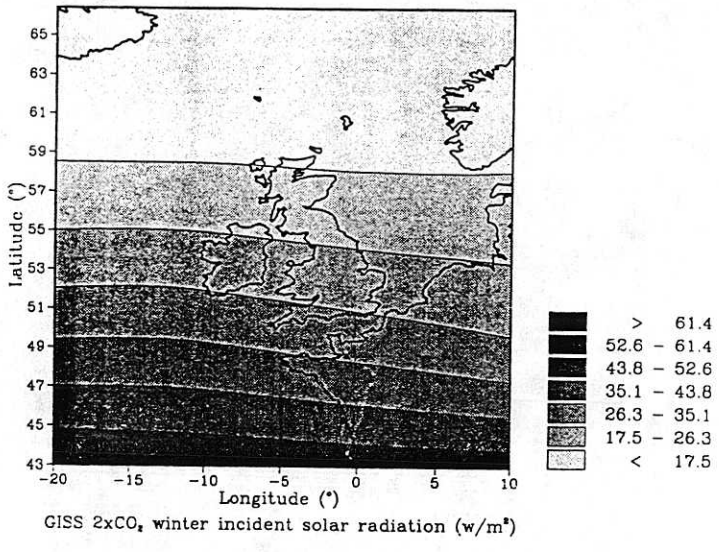

GISS $2xCO_2$ winter incident solar radiation (w/m^2)

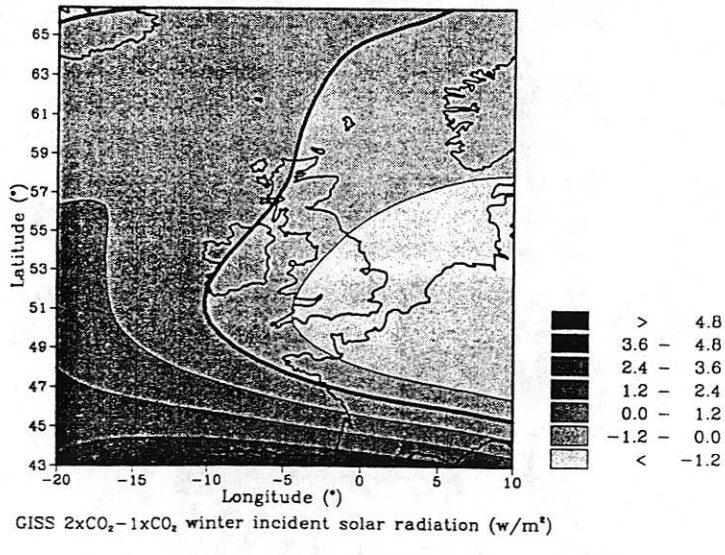

GISS $2xCO_2-1xCO_2$ winter incident solar radiation (w/m^2)

Fig 3.2 Incident Solar Radiation (Winter) from GISS model for $1\times CO_2$, $2\times CO_2$ and $2\times CO_2-1\times CO_2$.

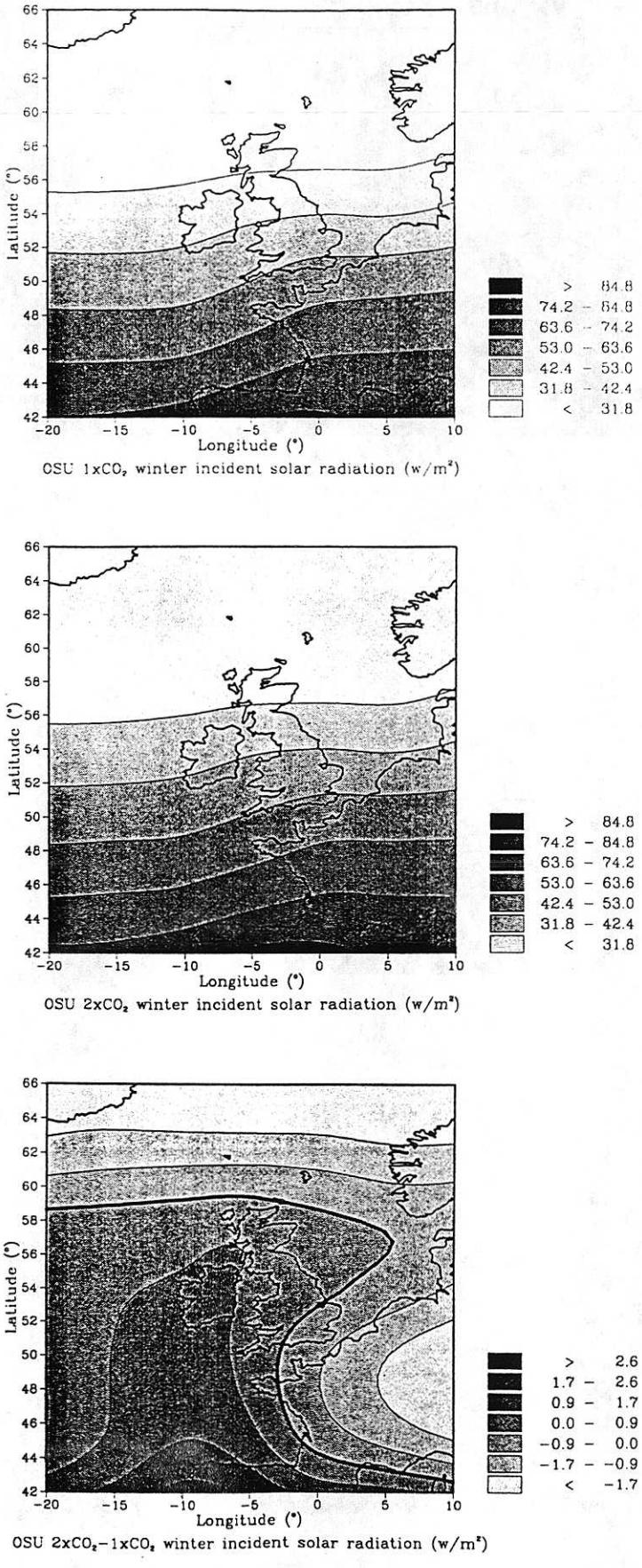

Fig 3.3 Incident Solar Radiation (Winter) from OSU model for $1\times CO_2$, $2\times CO_2$ and $2\times CO_2 - 1\times CO_2$.

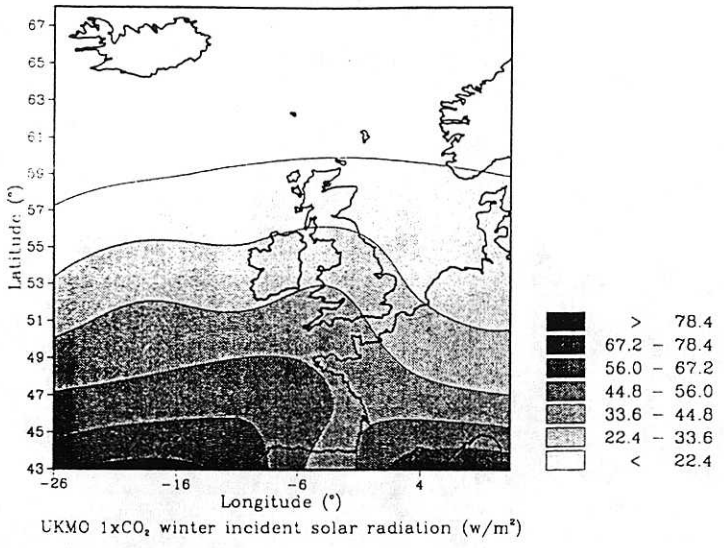

UKMO $1xCO_2$ winter incident solar radiation (w/m^2)

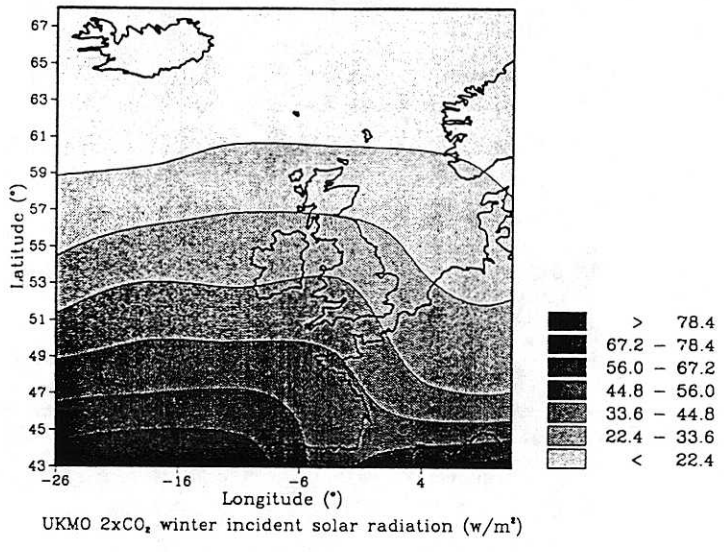

UKMO $2xCO_2$ winter incident solar radiation (w/m^2)

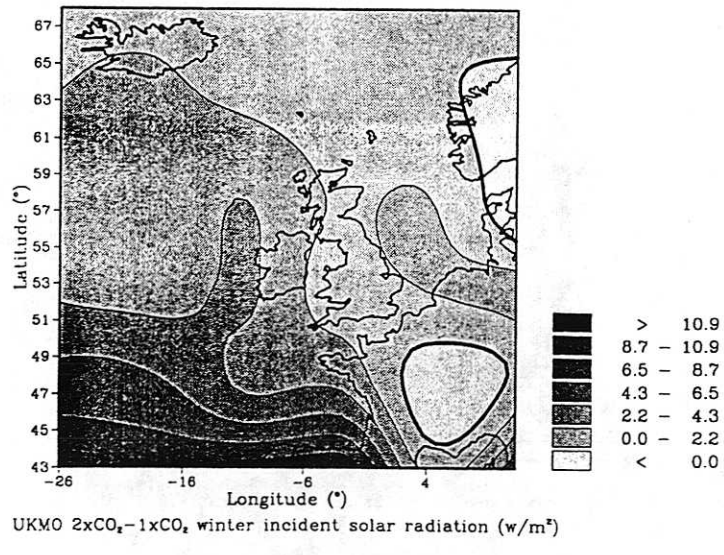

UKMO $2xCO_2-1xCO_2$ winter incident solar radiation (w/m^2)

Fig 3.4 Incident Solar Radiation (Winter) from UKMO model for $1\times CO_2$, $2\times CO_2$ and $2\times CO_2-1\times CO_2$.

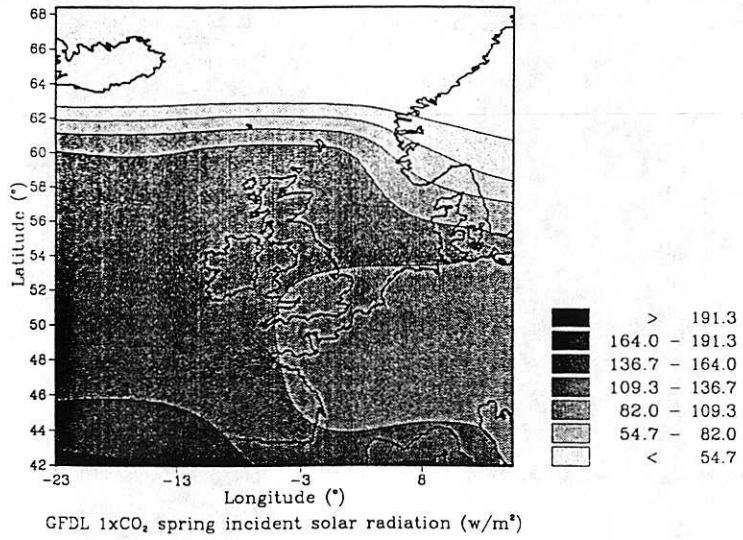

GFDL 1xCO$_2$ spring incident solar radiation (w/m^2)

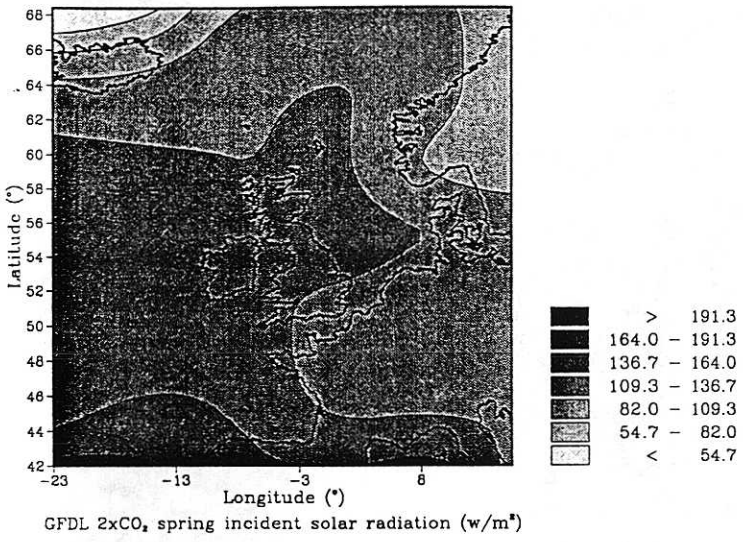

GFDL 2xCO$_2$ spring incident solar radiation (w/m^2)

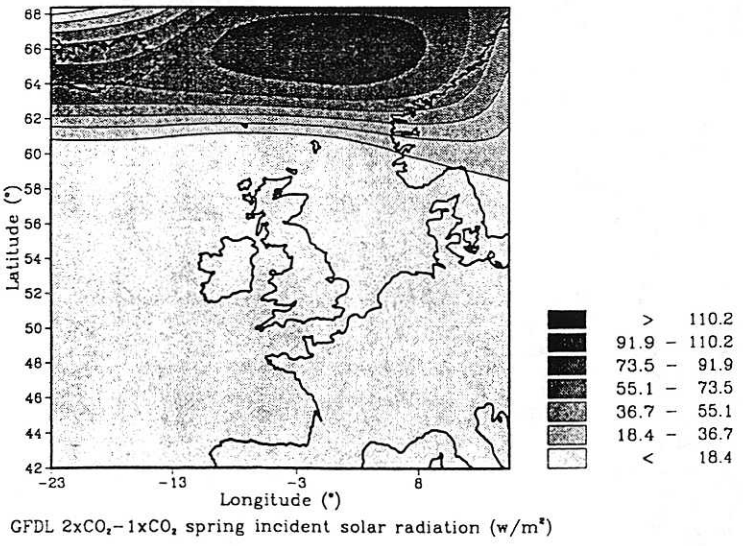

GFDL 2xCO$_2$-1xCO$_2$ spring incident solar radiation (w/m^2)

Fig 3.5 Incident Solar Radiation (Spring) from GFDL model for $1\times CO_2$, $2\times CO_2$ and $2\times CO_2 - 1\times CO_2$.

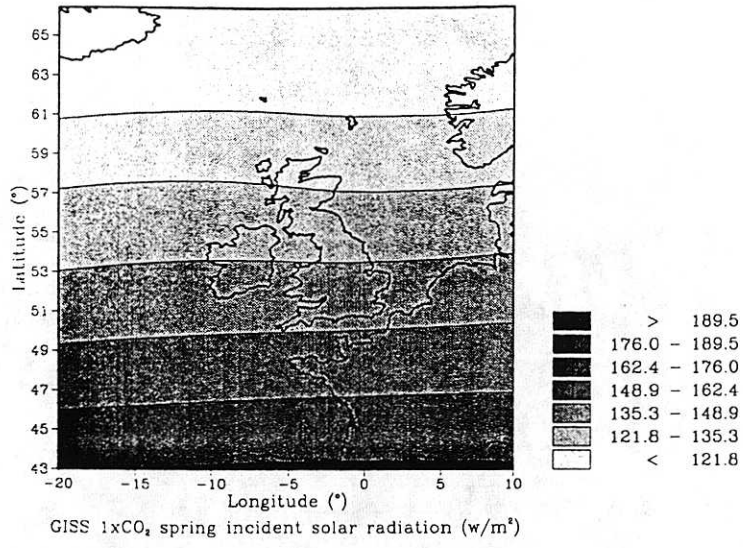

GISS $1xCO_2$ spring incident solar radiation (w/m^2)

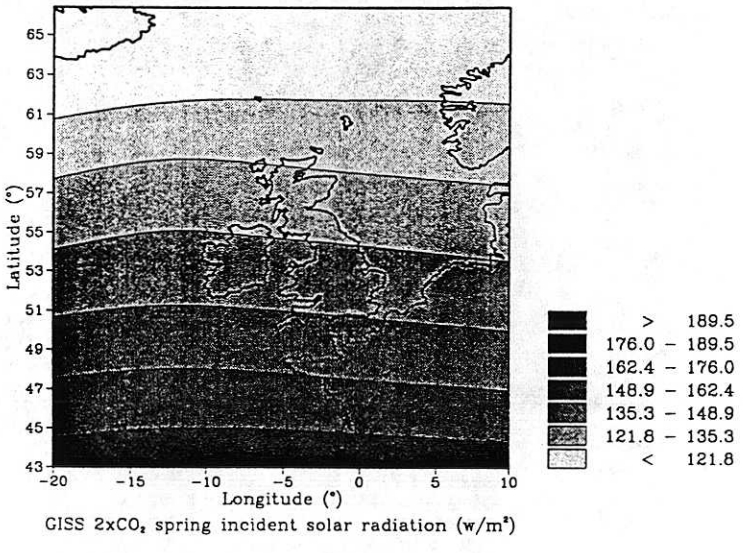

GISS $2xCO_2$ spring incident solar radiation (w/m^2)

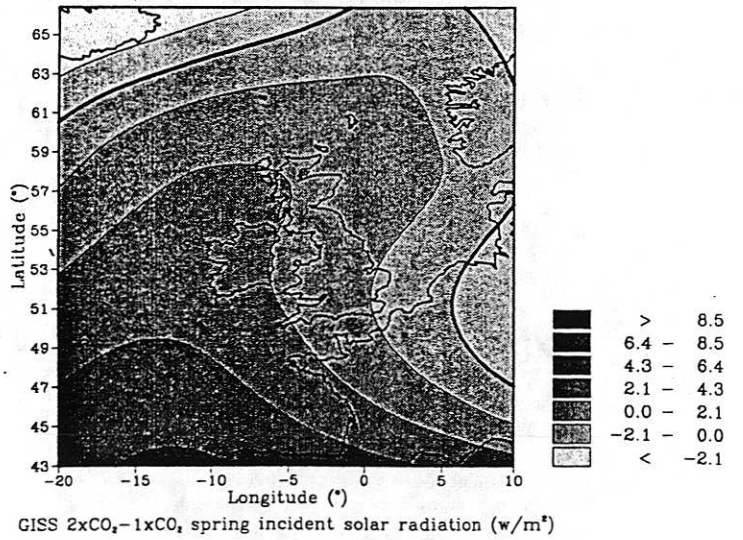

GISS $2xCO_2-1xCO_2$ spring incident solar radiation (w/m^2)

Fig 3.6 Incident Solar Radiation (Spring) from GISS model for $1\times CO_2$, $2\times CO_2$ and $2\times CO_2-1\times CO_2$.

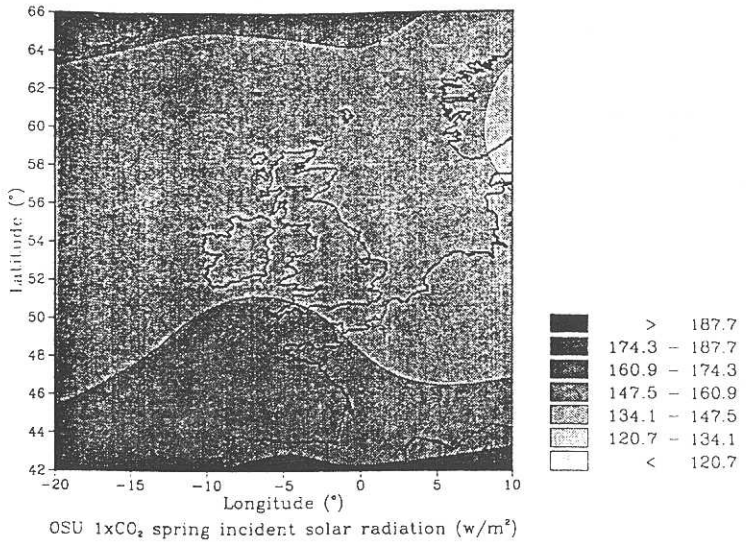

OSU $1xCO_2$ spring incident solar radiation (w/m^2)

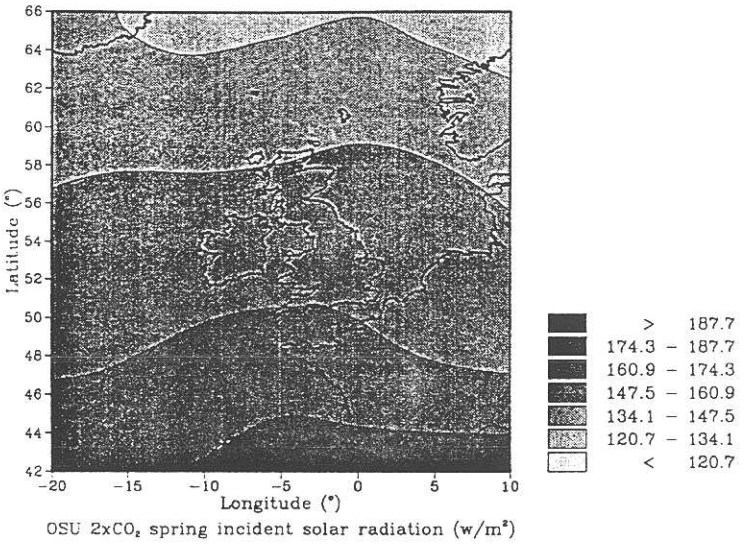

OSU $2xCO_2$ spring incident solar radiation (w/m^2)

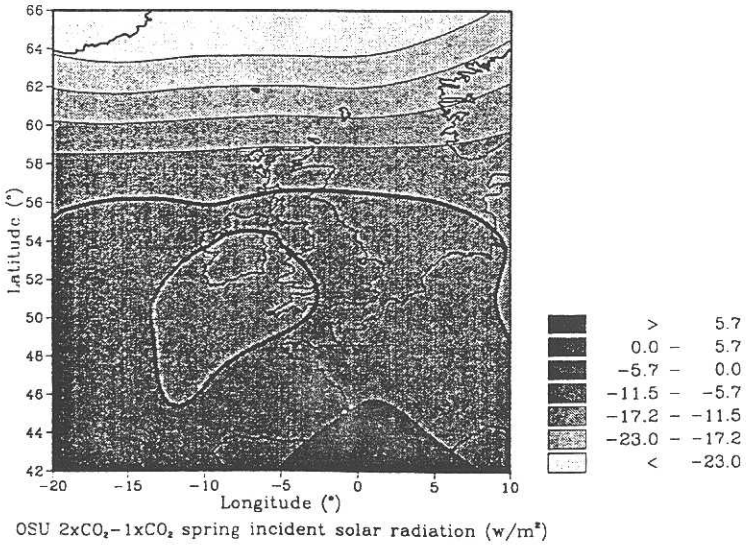

OSU $2xCO_2 - 1xCO_2$ spring incident solar radiation (w/m^2)

Fig 3.7 Incident Solar Radiation (Spring) from OSU model for $1\times CO_2$, $2\times CO_2$ and $2\times CO_2 - 1\times CO_2$.

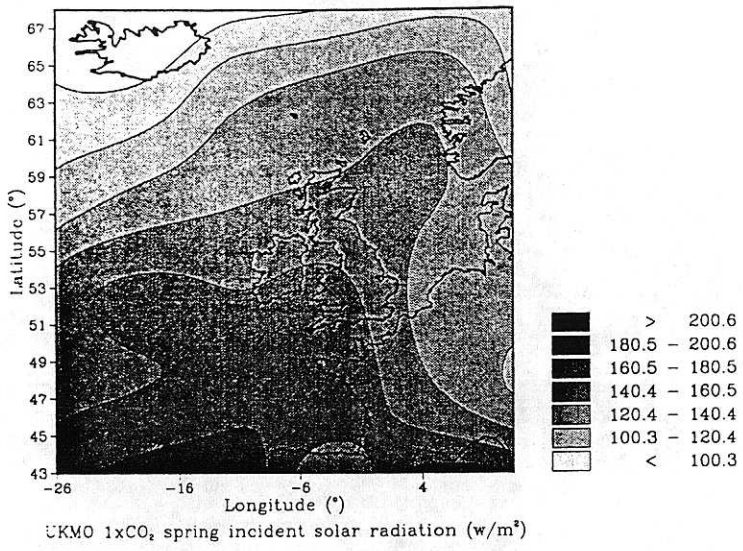

UKMO $1xCO_2$ spring incident solar radiation (w/m^2)

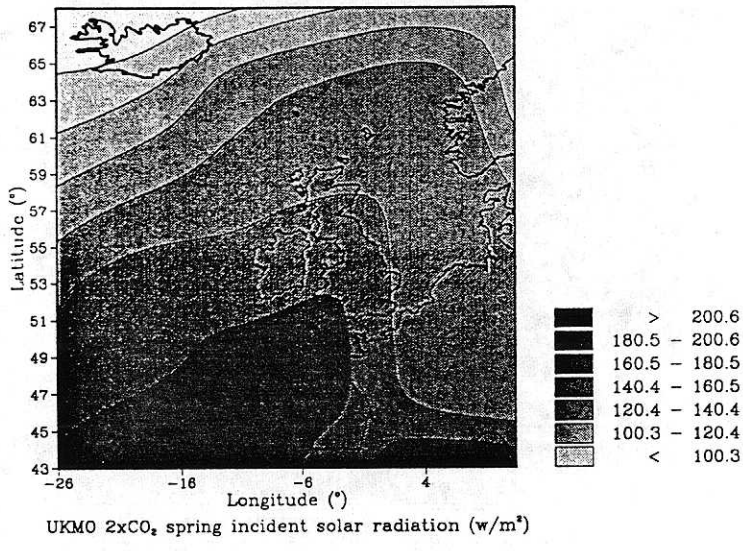

UKMO $2xCO_2$ spring incident solar radiation (w/m^2)

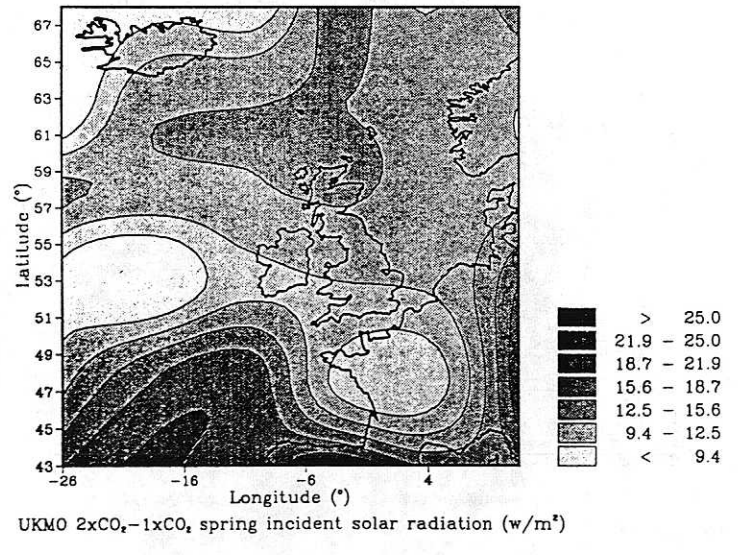

UKMO $2xCO_2-1xCO_2$ spring incident solar radiation (w/m^2)

Fig 3.8 Incident Solar Radiation (Spring) from UKMO model for $1\times CO_2$, $2\times CO_2$ and $2\times CO_2-1\times CO_2$.

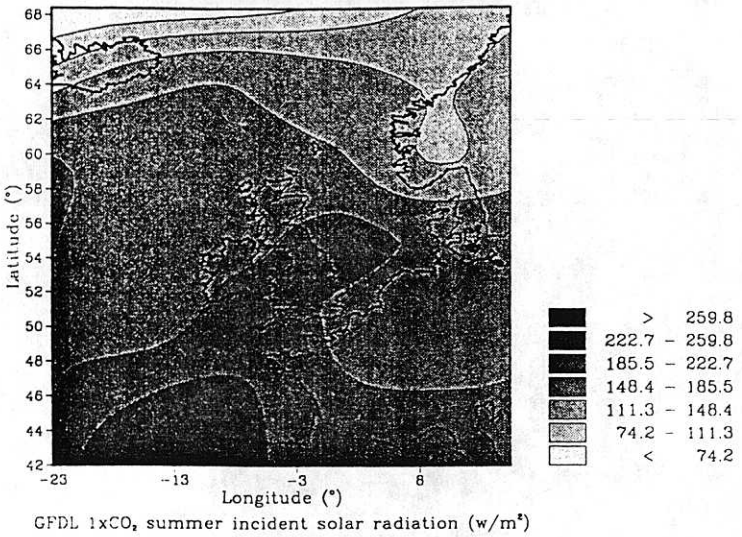

GFDL $1xCO_2$ summer incident solar radiation (w/m^2)

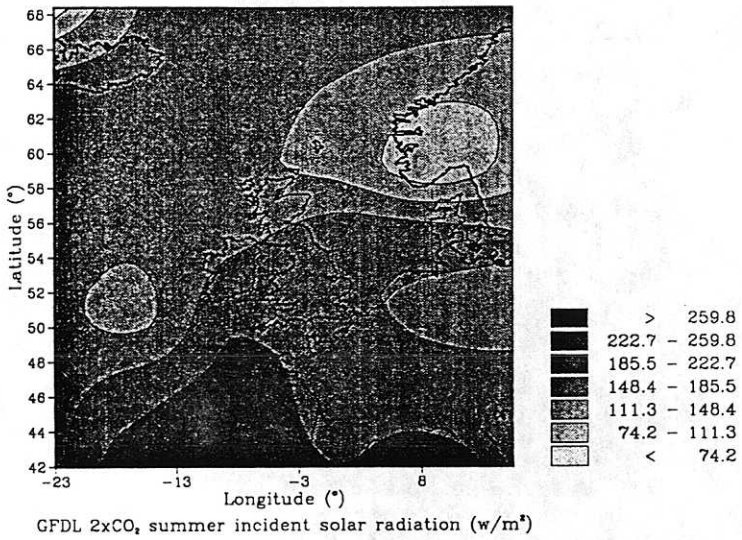

GFDL $2xCO_2$ summer incident solar radiation (w/m^2)

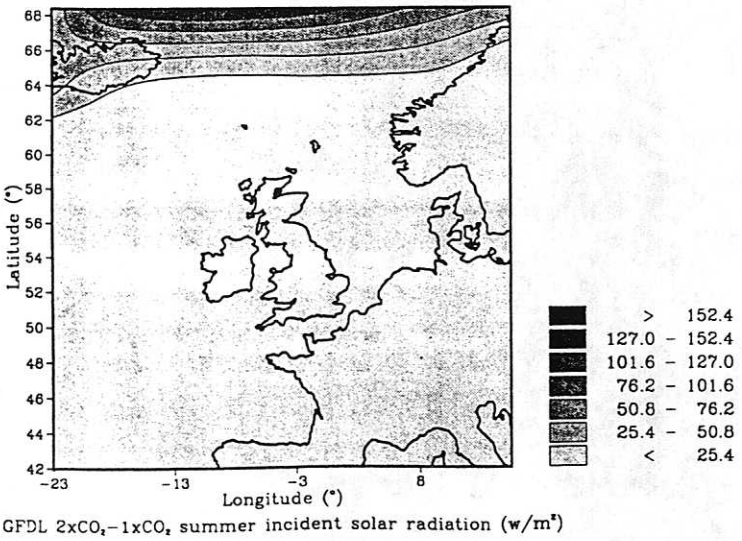

GFDL $2xCO_2-1xCO_2$ summer incident solar radiation (w/m^2)

Fig 3.9 Incident Solar Radiation (Summer) from GFDL model for $1\times CO_2$, $2\times CO_2$ and $2\times CO_2-1\times CO_2$.

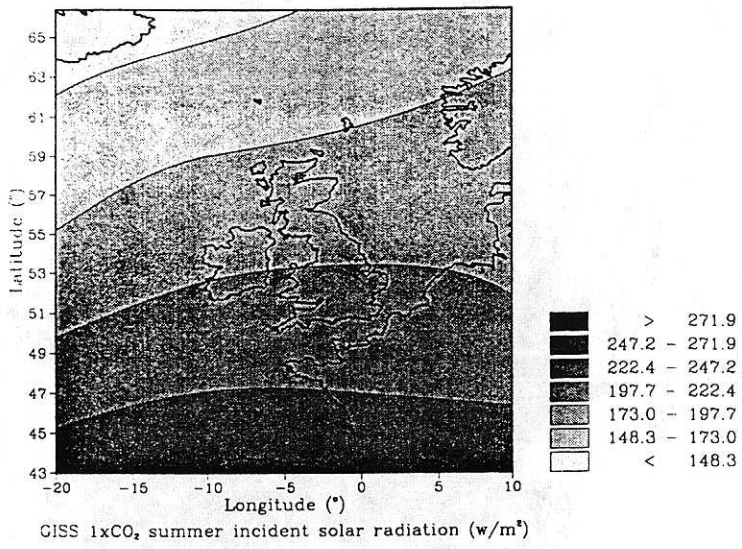

GISS $1xCO_2$ summer incident solar radiation (w/m^2)

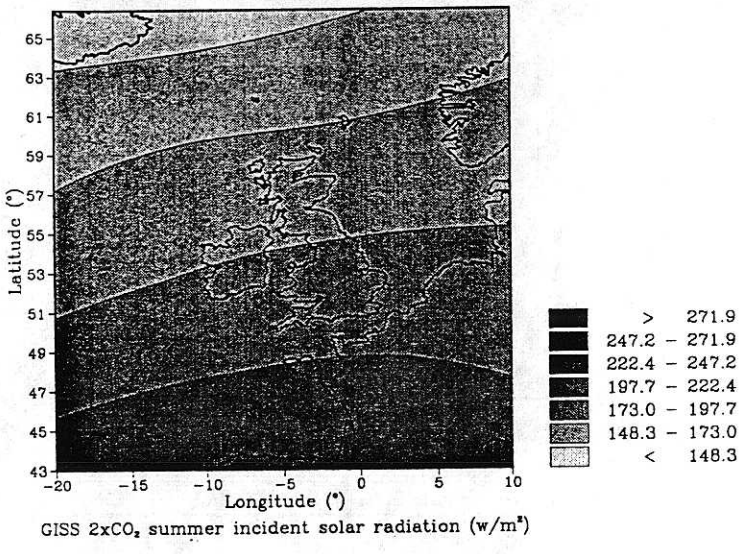

GISS $2xCO_2$ summer incident solar radiation (w/m^2)

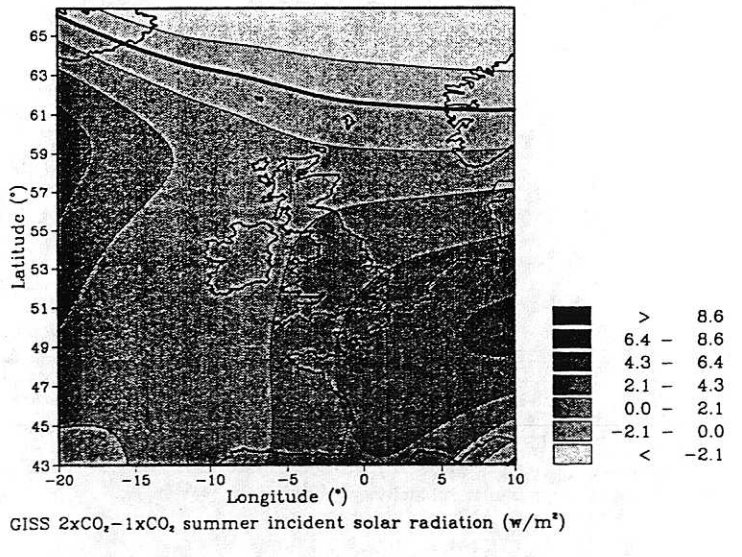

GISS $2xCO_2-1xCO_2$ summer incident solar radiation (w/m^2)

Fig 3.10 Incident Solar Radiation (Summer) from GISS model for $1\times CO_2$, $2\times CO_2$ and $2\times CO_2-1\times CO_2$.

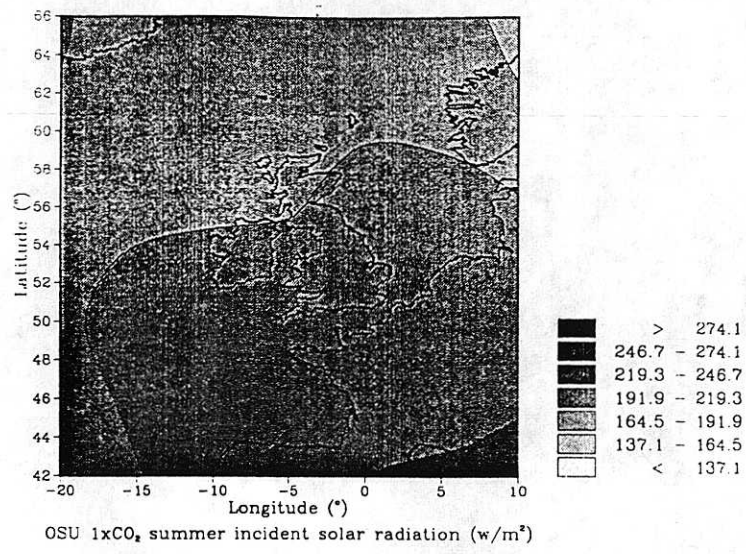

OSU $1xCO_2$ summer incident solar radiation (w/m^2)

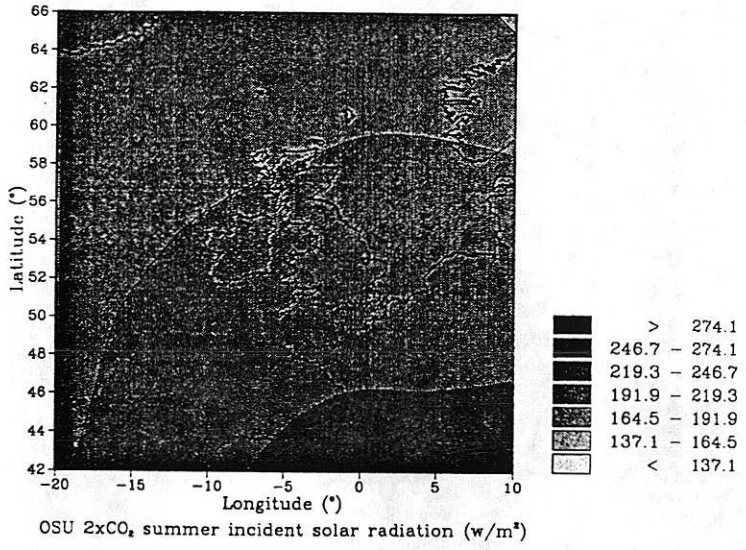

OSU $2xCO_2$ summer incident solar radiation (w/m^2)

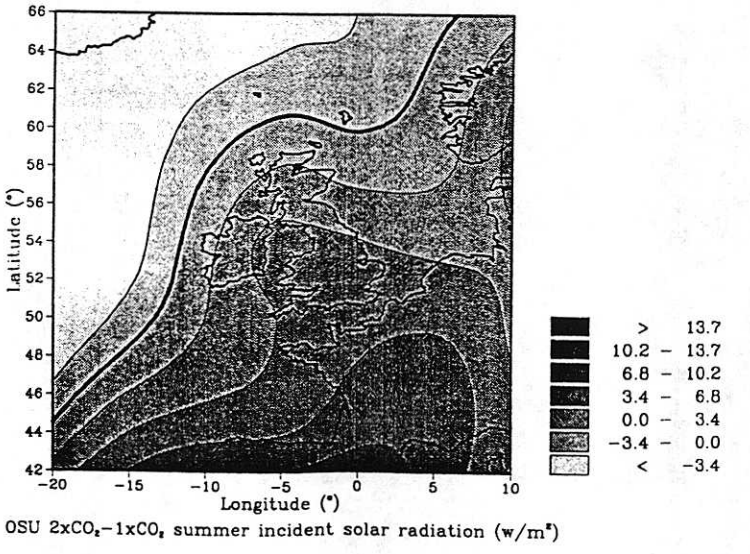

OSU $2xCO_2-1xCO_2$ summer incident solar radiation (w/m^2)

Fig 3.11 Incident Solar Radiation (Summer) from OSU model for $1\times CO_2$, $2\times CO_2$ and $2\times CO_2-1\times CO_2$.

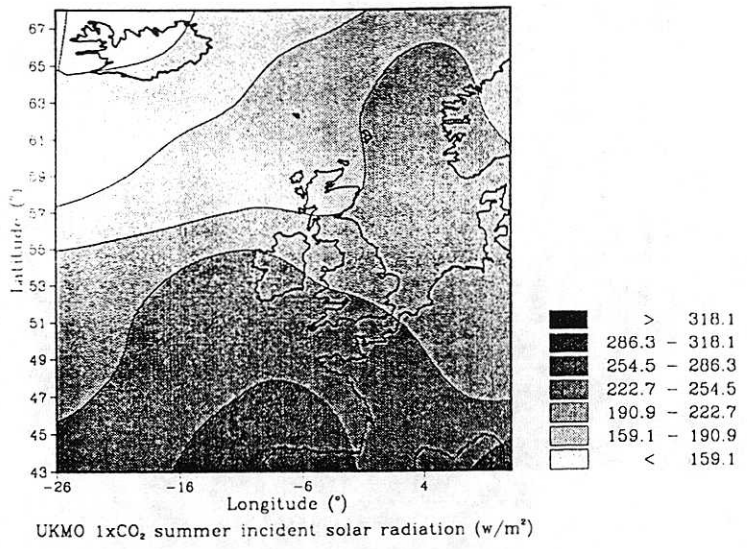

UKMO $1xCO_2$ summer incident solar radiation (w/m^2)

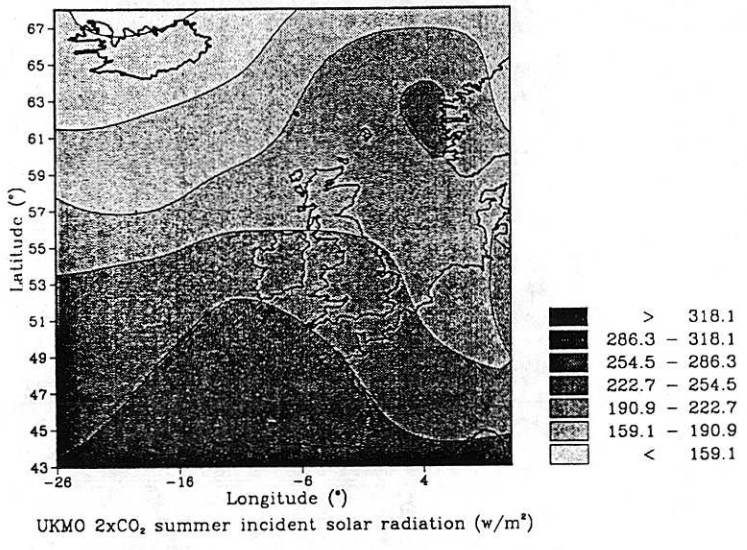

UKMO $2xCO_2$ summer incident solar radiation (w/m^2)

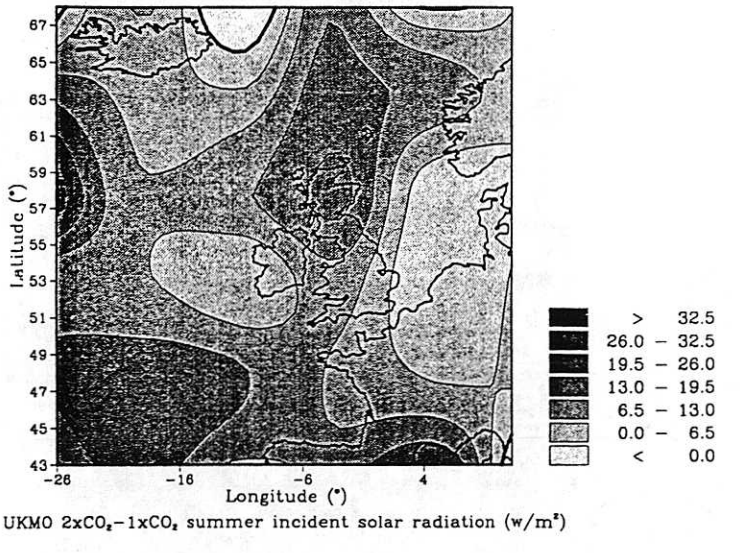

UKMO $2xCO_2-1xCO_2$ summer incident solar radiation (w/m^2)

Fig 3.12 Incident Solar Radiation (Summer) from UKMO model for $1\times CO_2$, $2\times CO_2$ and $2\times CO_2-1\times CO_2$.

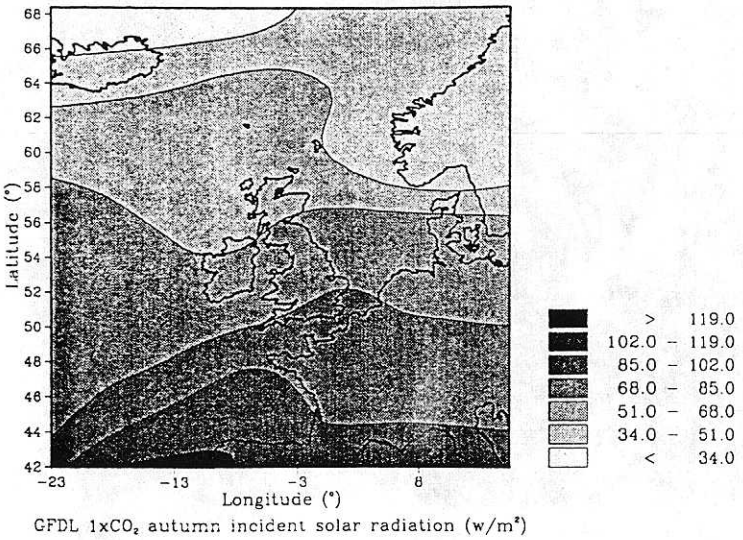

GFDL $1xCO_2$ autumn incident solar radiation (w/m^2)

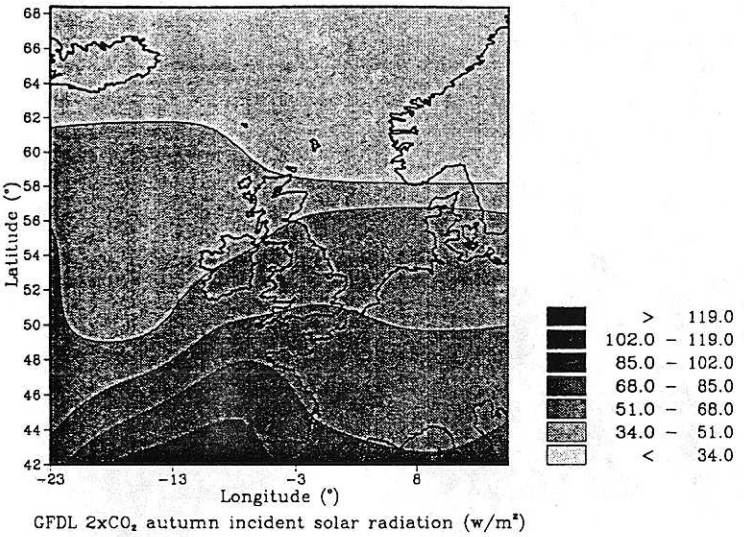

GFDL $2xCO_2$ autumn incident solar radiation (w/m^2)

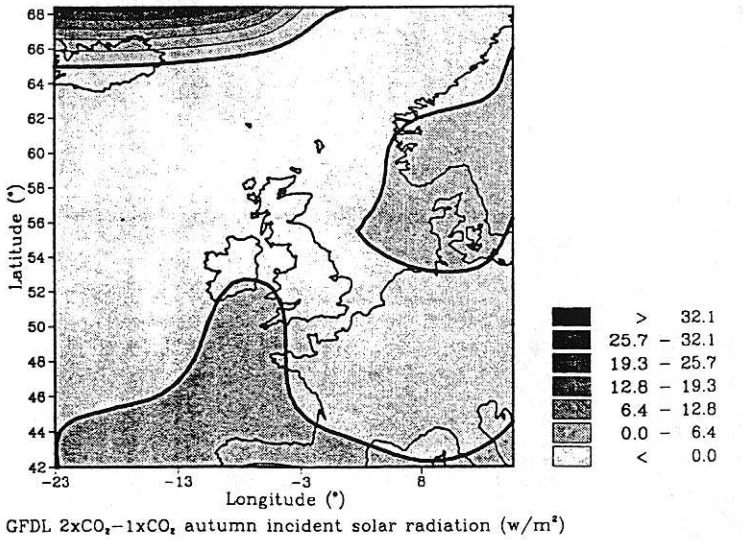

GFDL $2xCO_2-1xCO_2$ autumn incident solar radiation (w/m^2)

Fig 3.13 Incident Solar Radiation (Autumn) from GFDL model for $1\times CO_2$, $2\times CO_2$ and $2\times CO_2-1\times CO_2$.

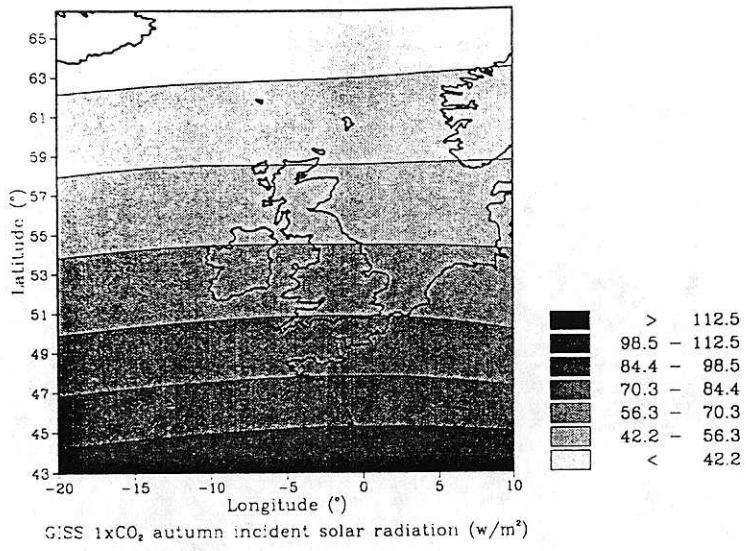

GISS $1xCO_2$ autumn incident solar radiation (w/m^2)

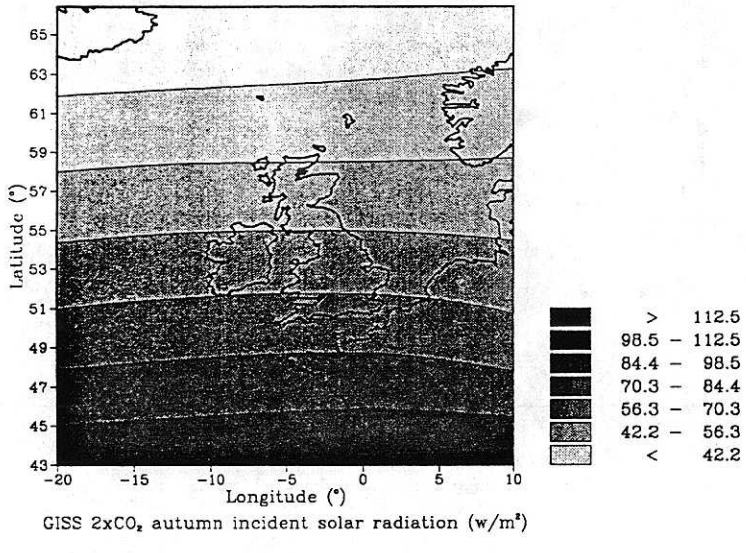

GISS $2xCO_2$ autumn incident solar radiation (w/m^2)

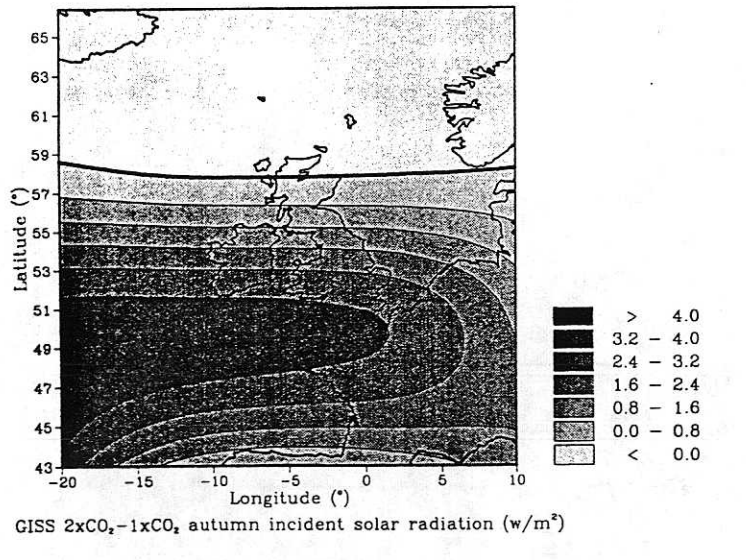

GISS $2xCO_2-1xCO_2$ autumn incident solar radiation (w/m^2)

Fig 3.14 Incident Solar Radiation (Autumn) from GISS model for $1\times CO_2$, $2\times CO_2$ and $2\times CO_2-1\times CO_2$.

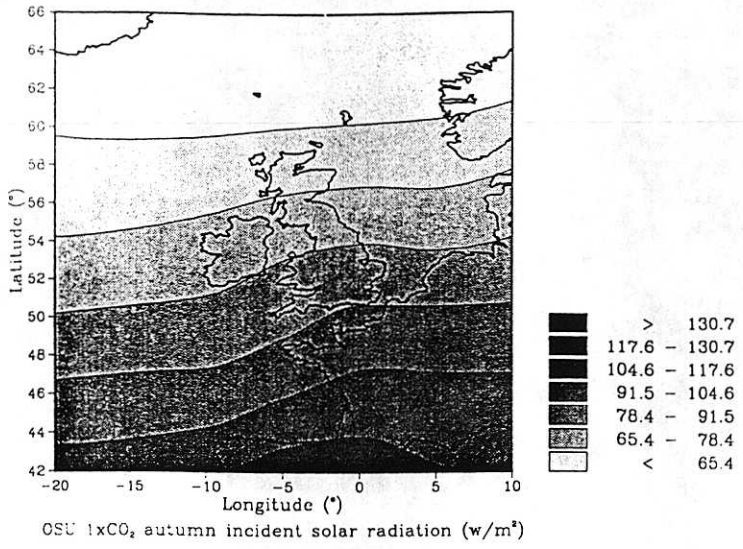

OSU $1xCO_2$ autumn incident solar radiation (w/m^2)

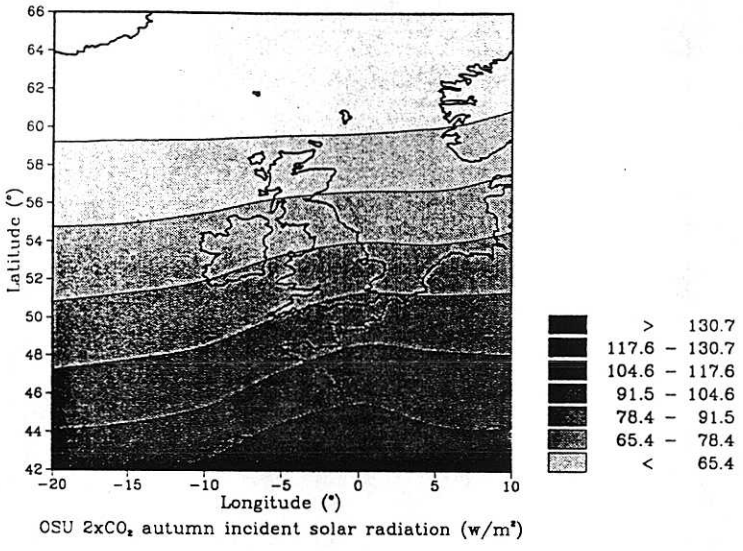

OSU $2xCO_2$ autumn incident solar radiation (w/m^2)

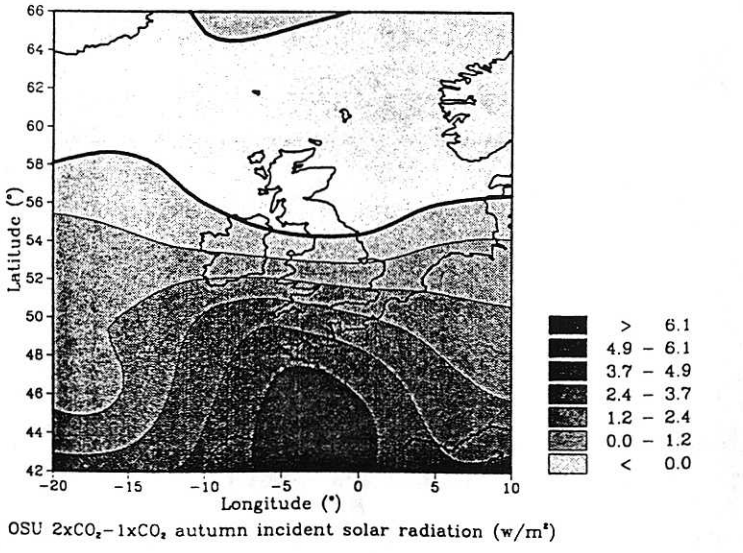

OSU $2xCO_2 - 1xCO_2$ autumn incident solar radiation (w/m^2)

Fig 3.15 Incident Solar Radiation (Autumn) from OSU model for $1\times CO_2$, $2\times CO_2$ and $2\times CO_2 - 1\times CO_2$.

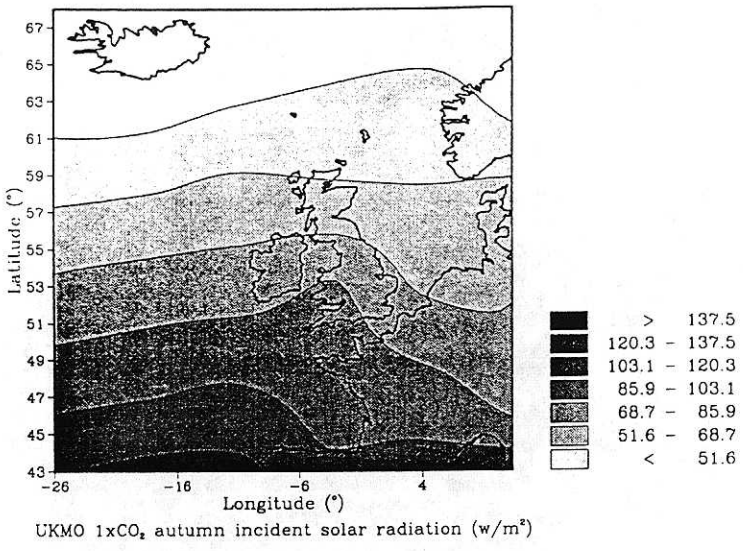

UKMO $1xCO_2$ autumn incident solar radiation (w/m^2)

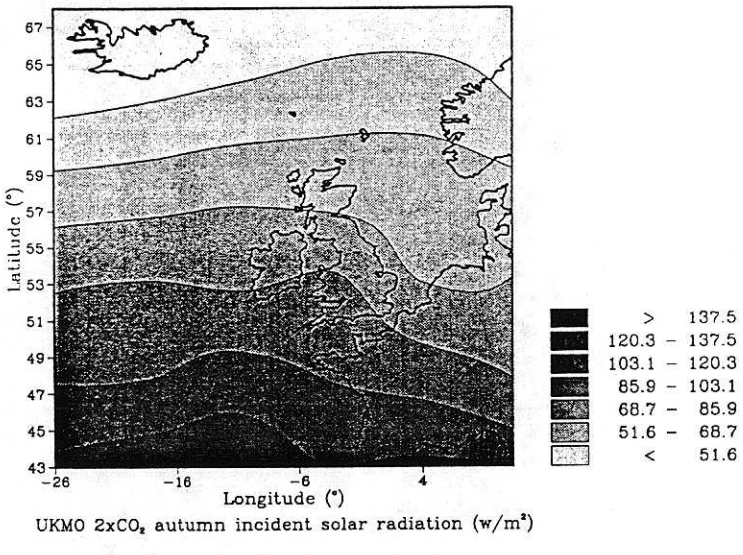

UKMO $2xCO_2$ autumn incident solar radiation (w/m^2)

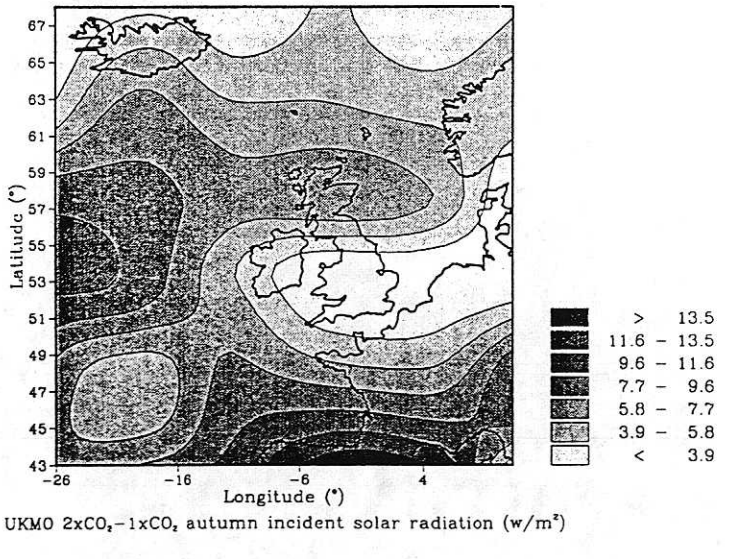

UKMO $2xCO_2-1xCO_2$ autumn incident solar radiation (w/m^2)

Fig 3.16 Incident Solar Radiation (Autumn) from UKMO model for $1\times CO_2$, $2\times CO_2$ and $2\times CO_2-1\times CO_2$.

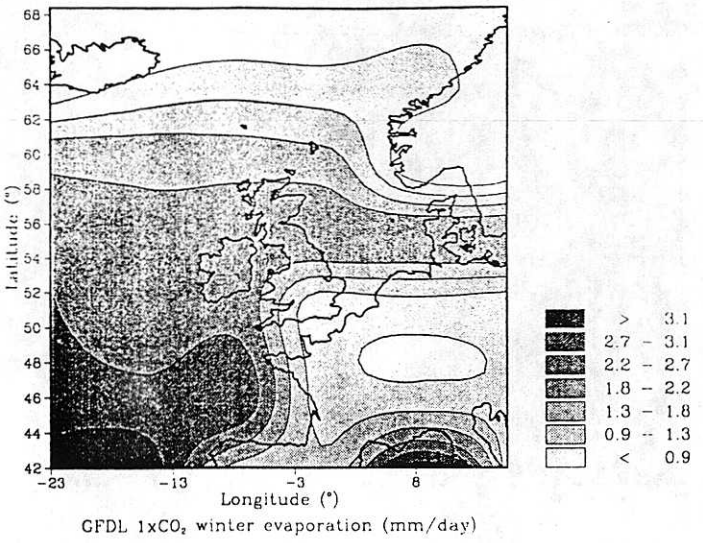

GFDL 1xCO$_2$ winter evaporation (mm/day)

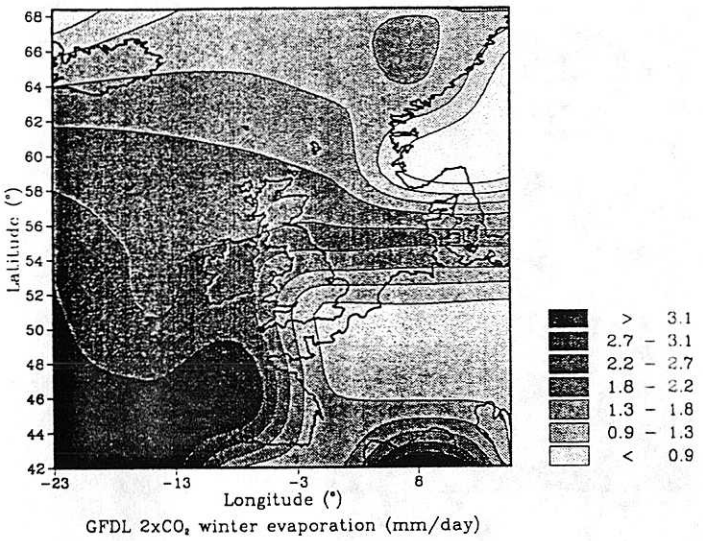

GFDL 2xCO$_2$ winter evaporation (mm/day)

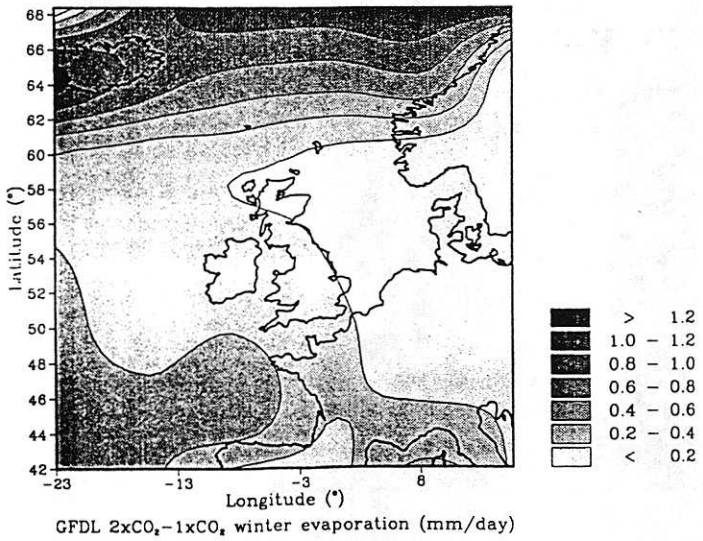

GFDL 2xCO$_2$−1xCO$_2$ winter evaporation (mm/day)

Fig 3.17 Evaporation (Winter) from GFDL model for $1\times CO_2$, $2\times CO_2$ and $2\times CO_2 - 1\times CO_2$.

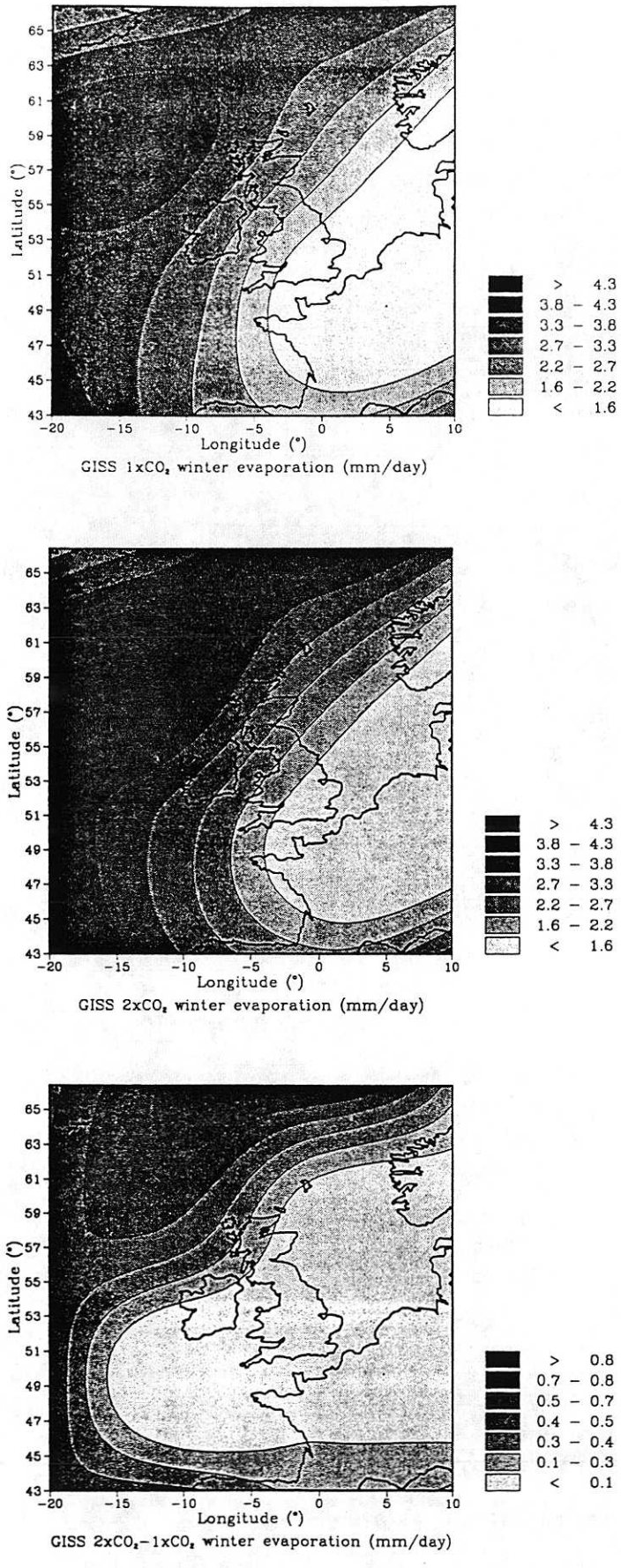

Fig 3.18 Evaporation (Winter) from GISS model for $1\times CO_2$, $2\times CO_2$ and $2\times CO_2 - 1\times CO_2$.

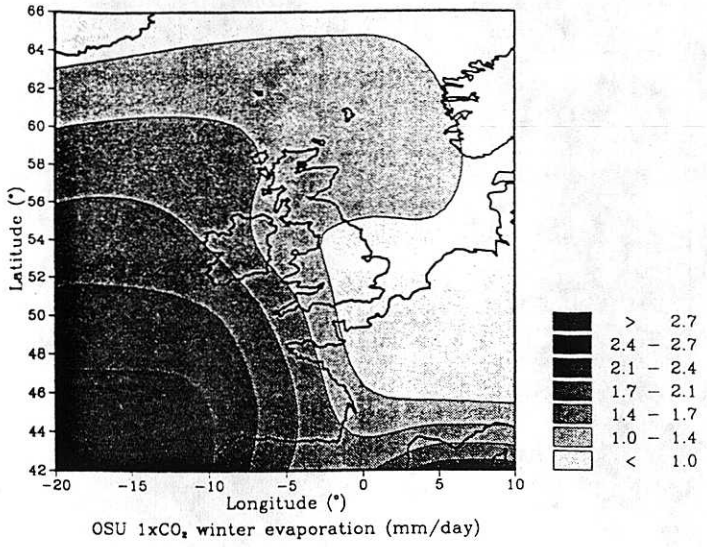

OSU 1xCO$_2$ winter evaporation (mm/day)

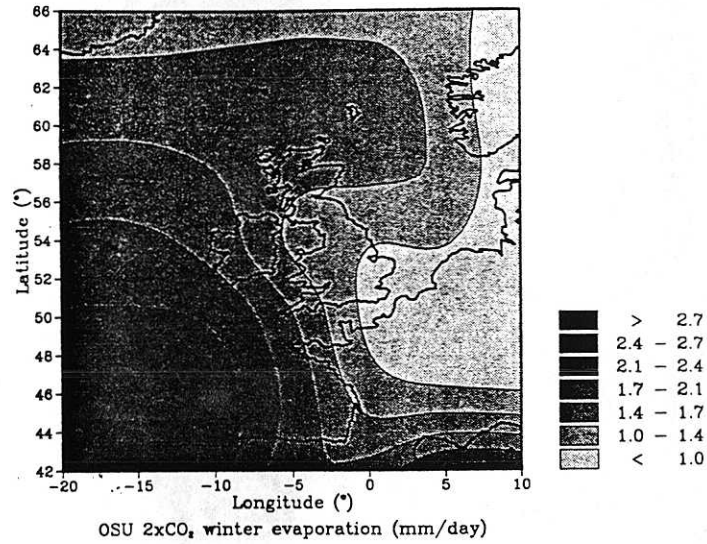

OSU 2xCO$_2$ winter evaporation (mm/day)

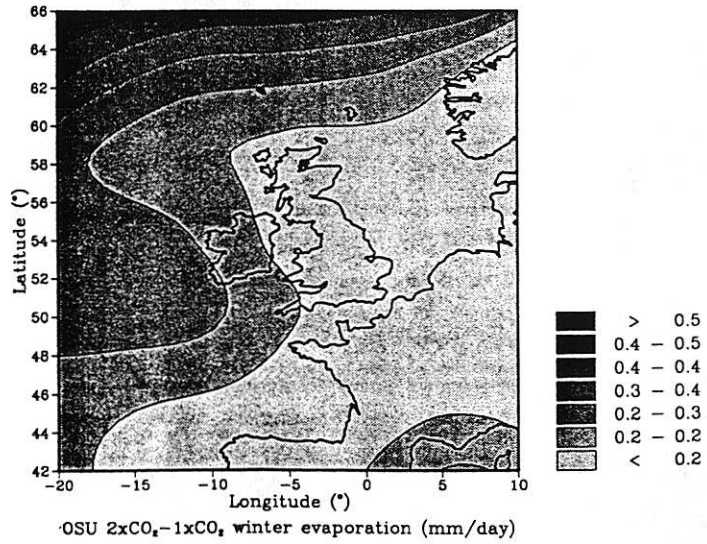

OSU 2xCO$_2$–1xCO$_2$ winter evaporation (mm/day)

Fig 3.19 Evaporation (Winter) from OSU model for $1\times CO_2$, $2\times CO_2$ and $2\times CO_2 - 1\times CO_2$.

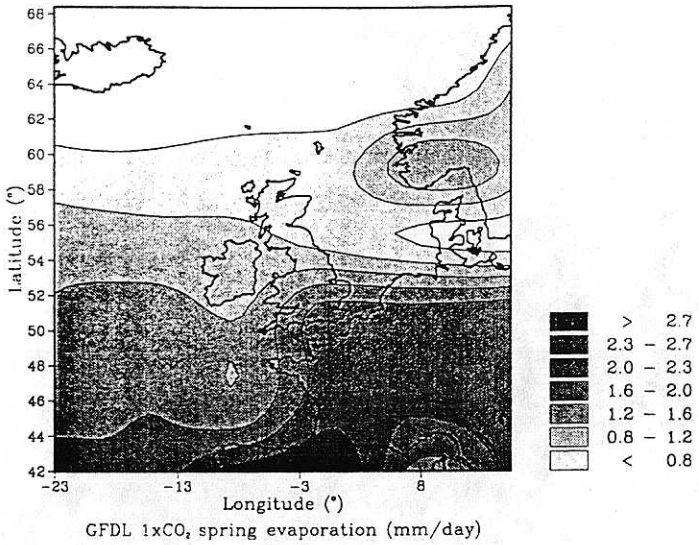

GFDL 1xCO$_2$ spring evaporation (mm/day)

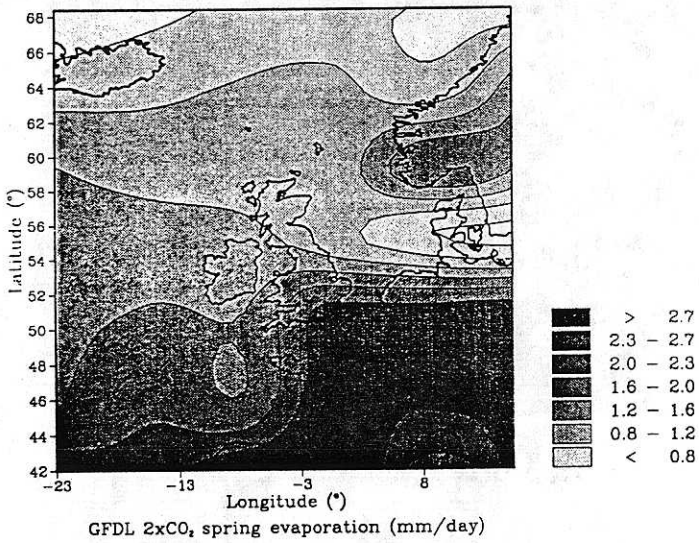

GFDL 2xCO$_2$ spring evaporation (mm/day)

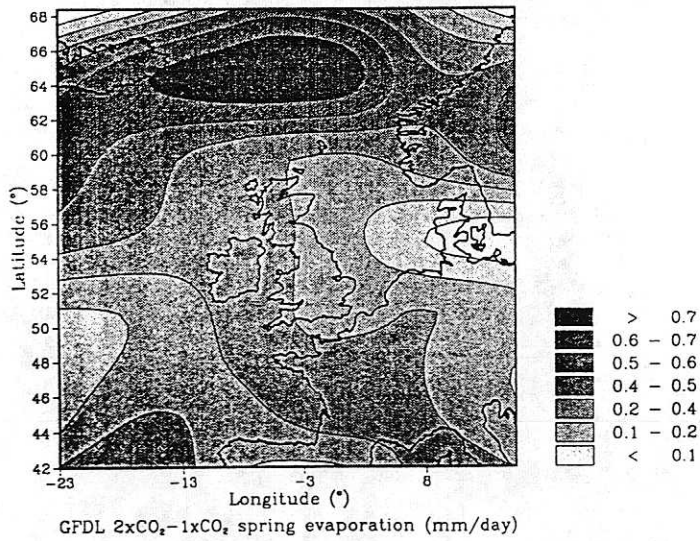

GFDL 2xCO$_2$–1xCO$_2$ spring evaporation (mm/day)

Fig 3.20 Evaporation (Spring) from GFDL model for $1\times CO_2$, $2\times CO_2$ and $2\times CO_2 - 1\times CO_2$.

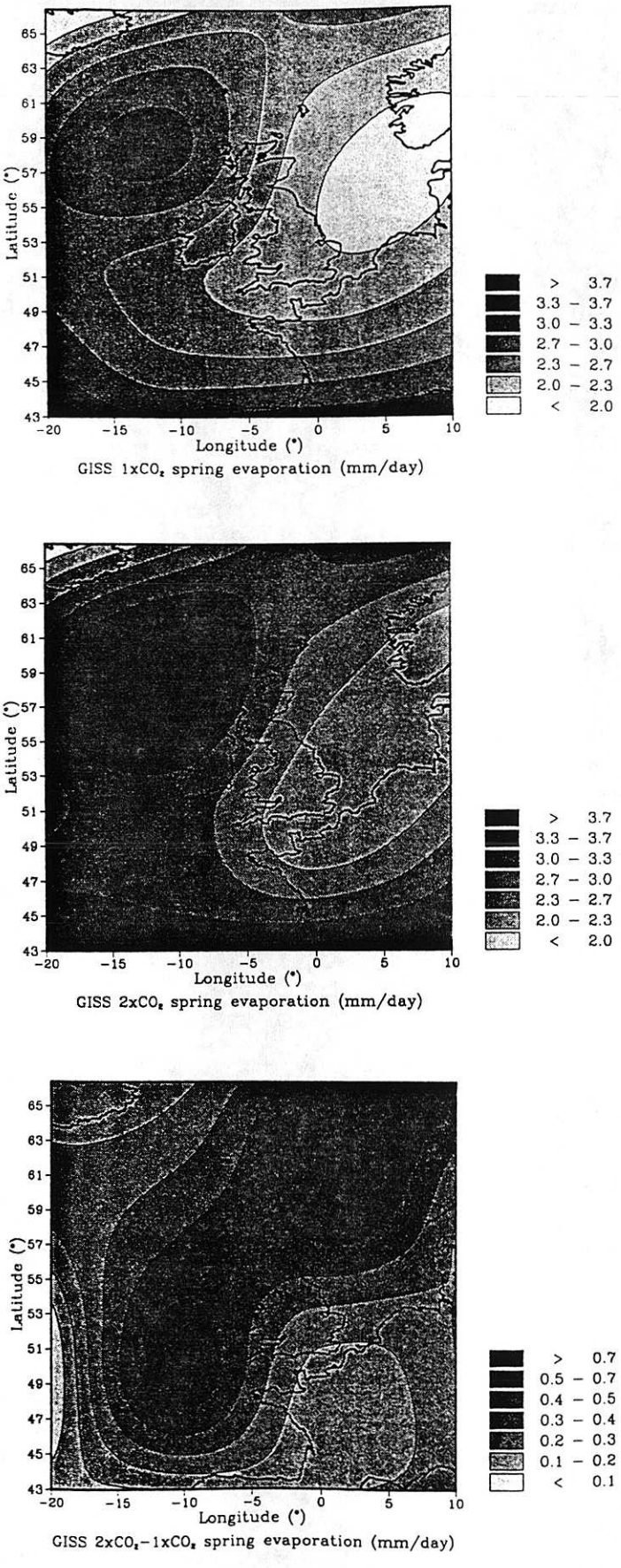

Fig 3.21 Evaporation (Spring) from GISS model for $1\times CO_2$, $2\times CO_2$ and $2\times CO_2 - 1\times CO_2$.

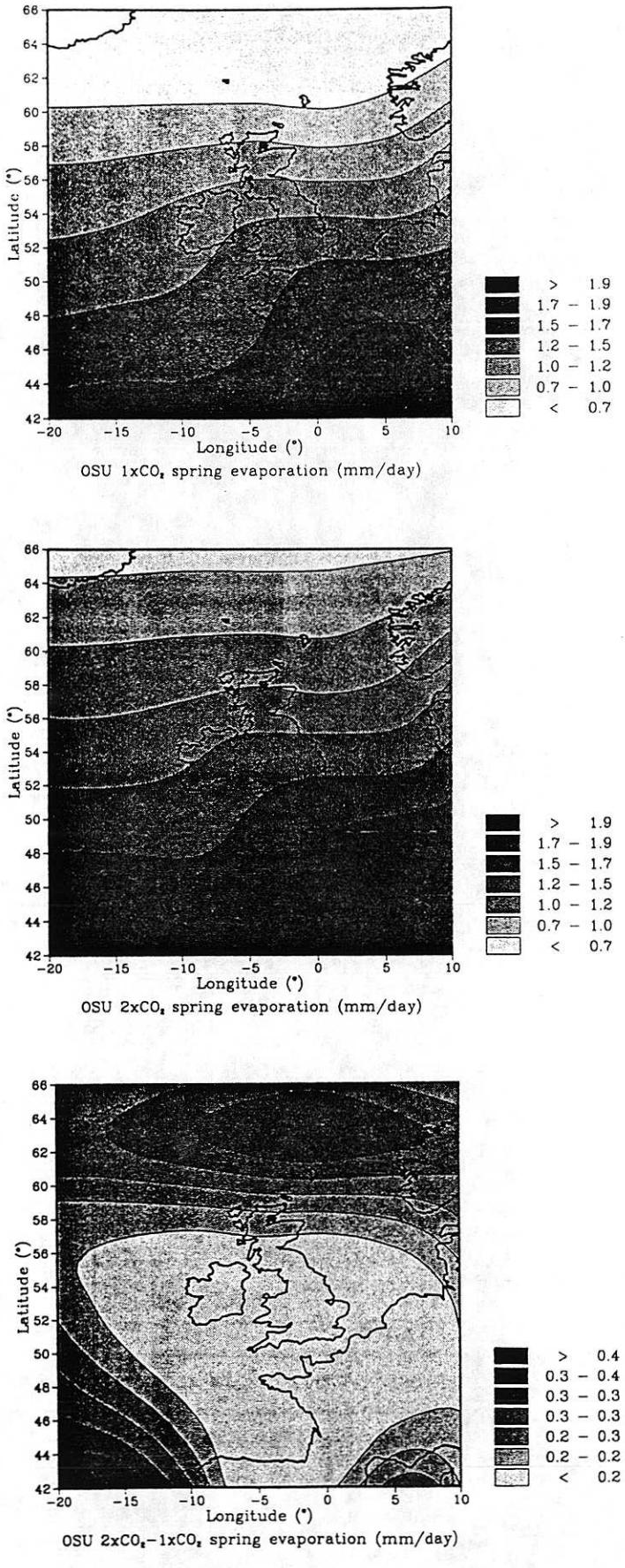

Fig 3.22 Evaporation (Spring) from OSU model for $1\times CO_2$, $2\times CO_2$ and $2\times CO_2 - 1\times CO_2$.

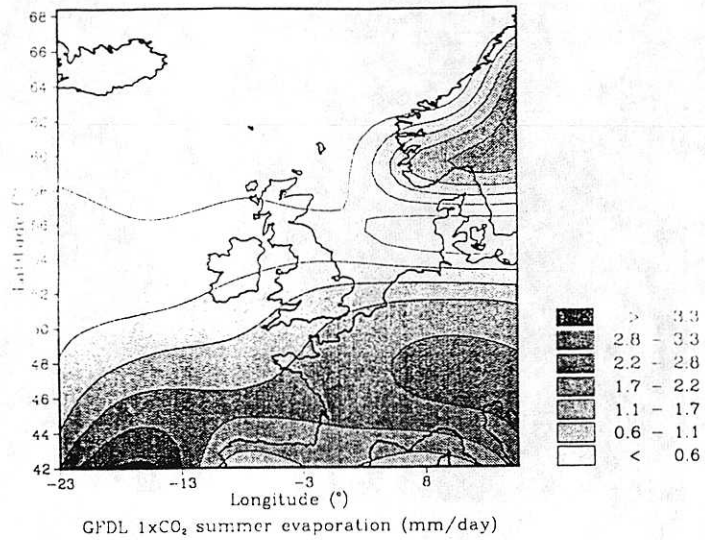

GFDL 1xCO$_2$ summer evaporation (mm/day)

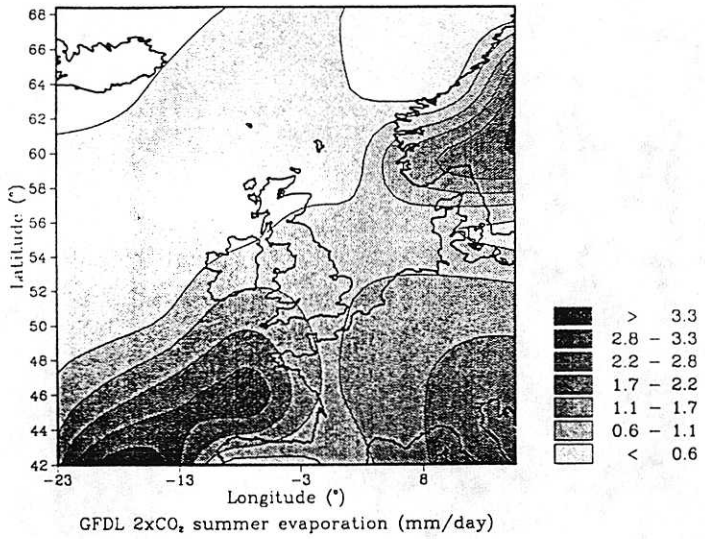

GFDL 2xCO$_2$ summer evaporation (mm/day)

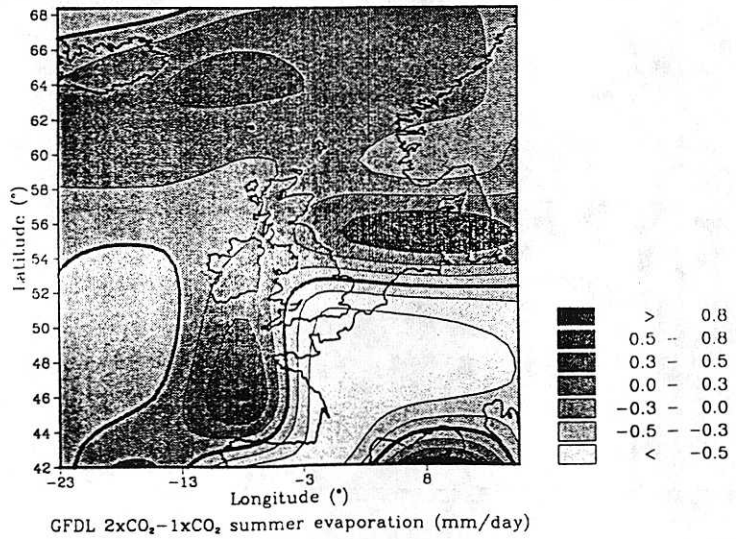

GFDL 2xCO$_2$−1xCO$_2$ summer evaporation (mm/day)

Fig 3.23 Evaporation (Summer) from GFDL model for $1\times CO_2$, $2\times CO_2$ and $2\times CO_2 - 1\times CO_2$.

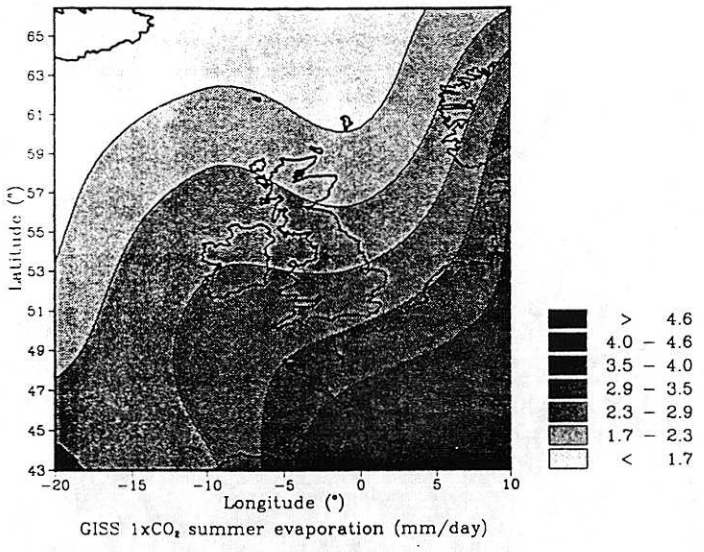

GISS $1xCO_2$ summer evaporation (mm/day)

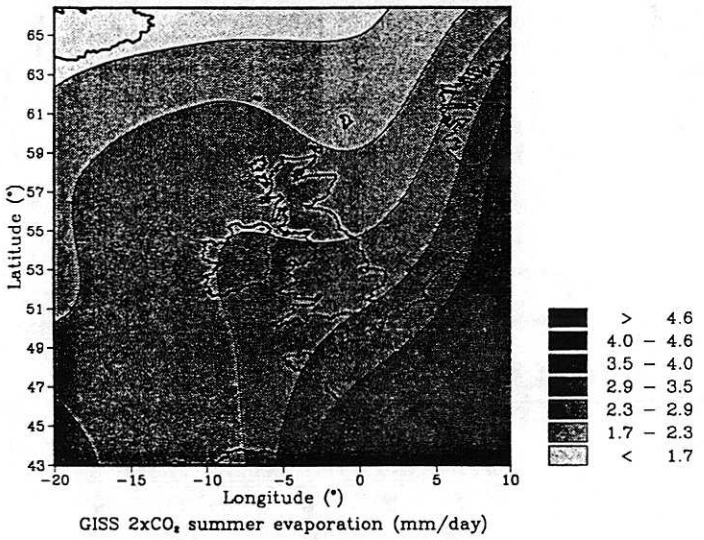

GISS $2xCO_2$ summer evaporation (mm/day)

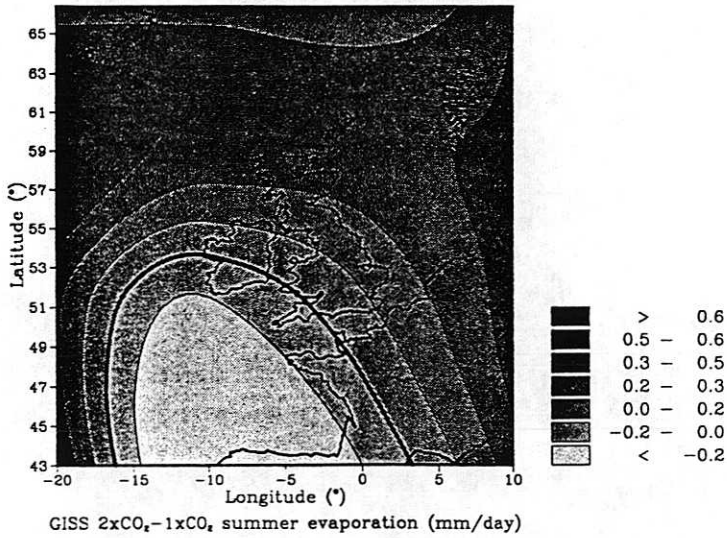

GISS $2xCO_2-1xCO_2$ summer evaporation (mm/day)

Fig 3.24 Evaporation (Summer) from GISS model for $1\times CO_2$, $2\times CO_2$ and $2\times CO_2 - 1\times CO_2$.

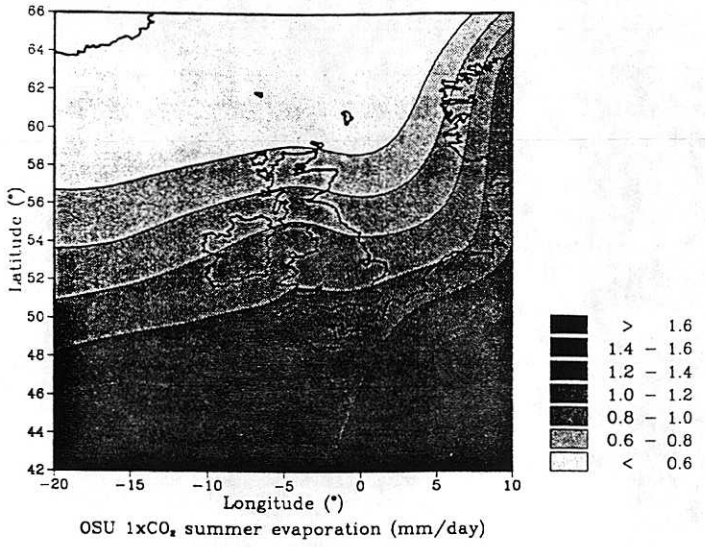

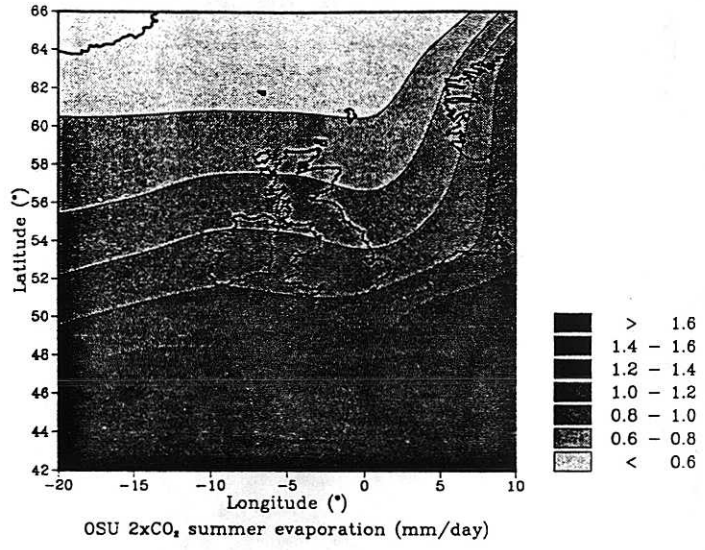

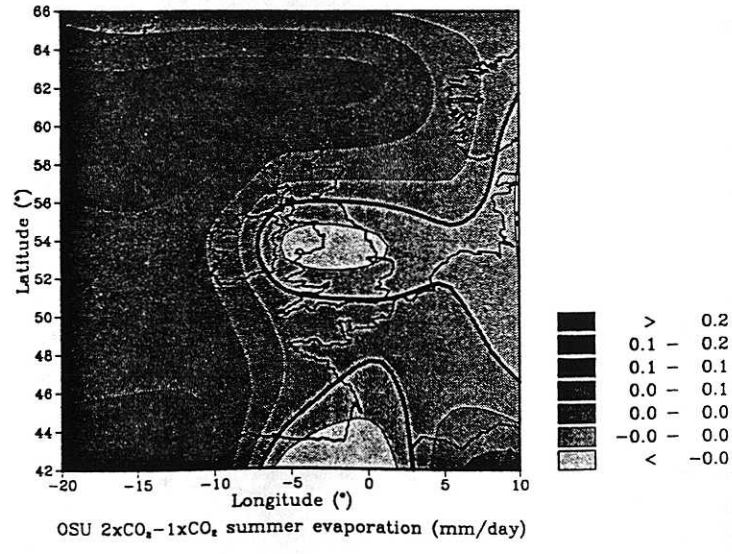

Fig 3.25 Evaporation (Summer) from OSU model for $1\times CO_2$, $2\times CO_2$ and $2\times CO_2 - 1\times CO_2$.

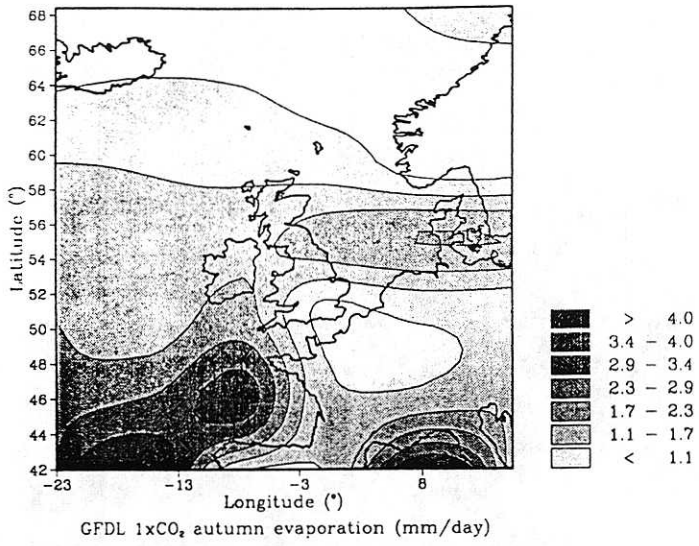

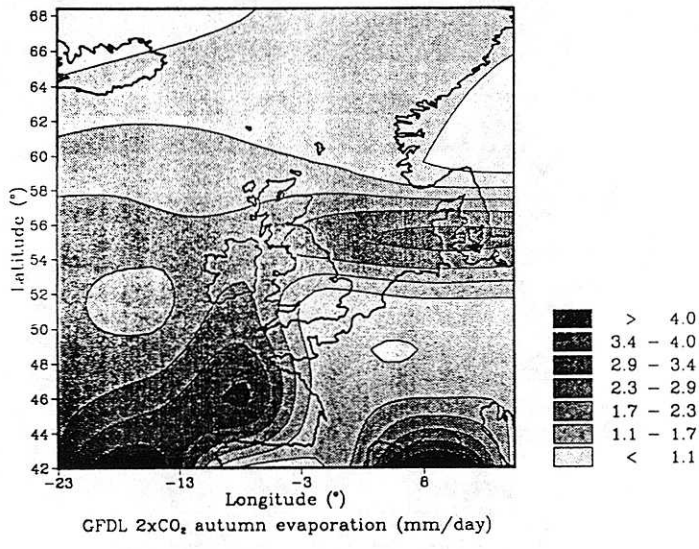

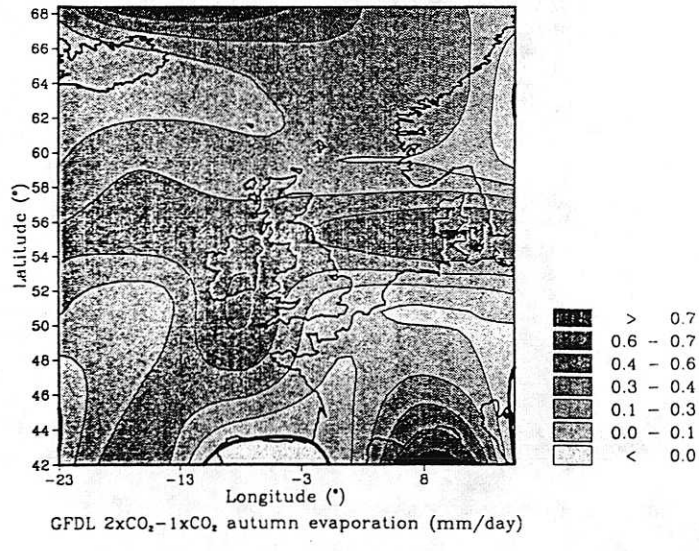

Fig 3.26 Evaporation (Autumn) from GFDL model for $1\times CO_2$, $2\times CO_2$ and $2\times CO_2 - 1\times CO_2$.

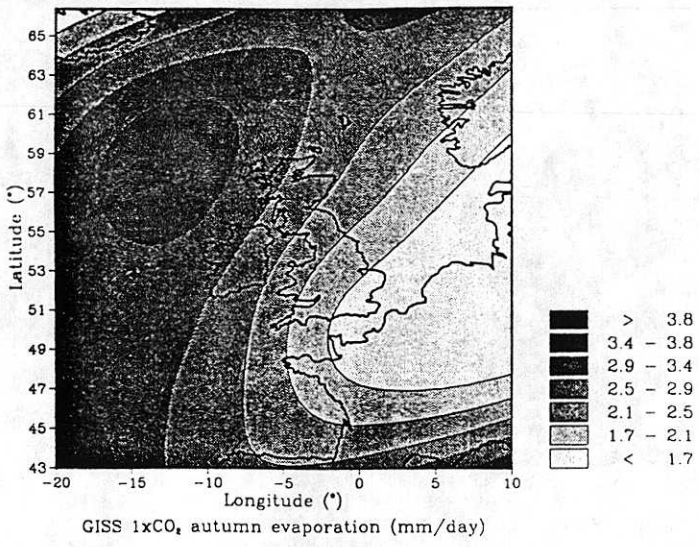

GISS $1xCO_2$ autumn evaporation (mm/day)

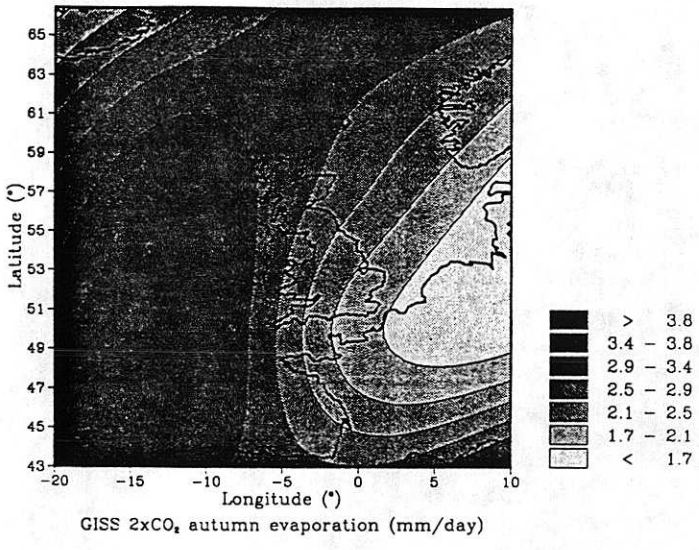

GISS $2xCO_2$ autumn evaporation (mm/day)

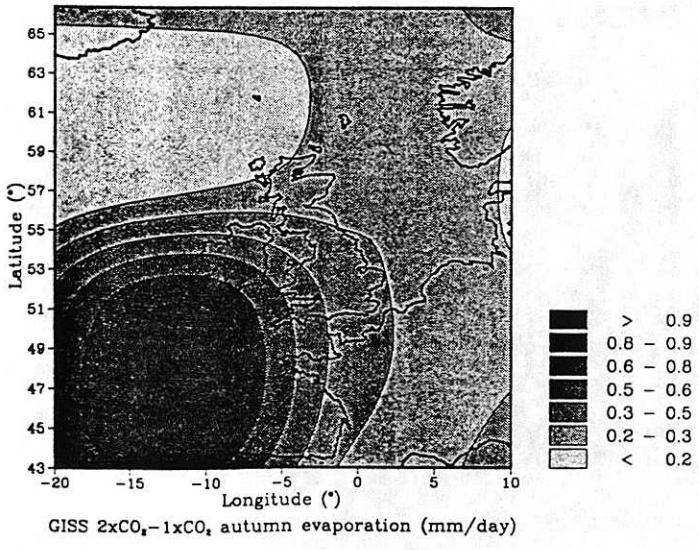

GISS $2xCO_2-1xCO_2$ autumn evaporation (mm/day)

Fig 3.27 Evaporation (Autumn) from GISS model for $1\times CO_2$, $2\times CO_2$ and $2\times CO_2-1\times CO_2$.

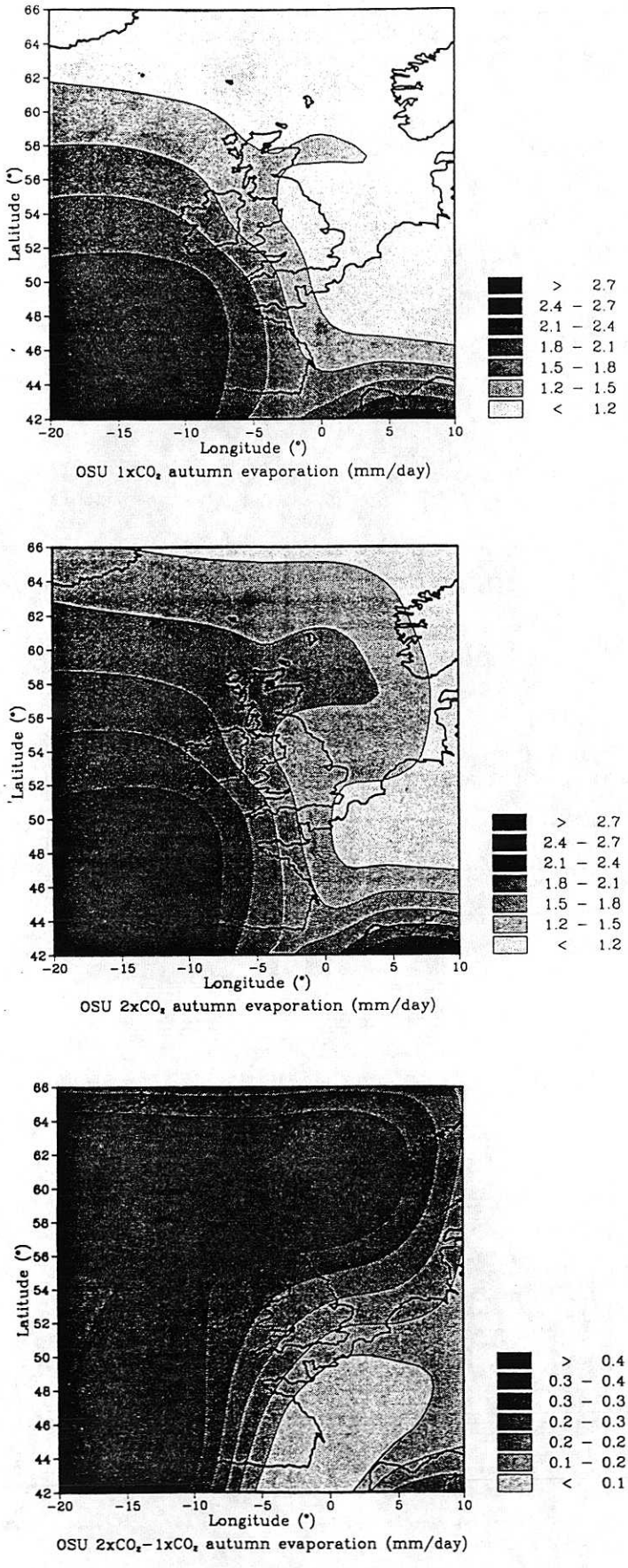

Fig 3.28 Evaporation (Autumn) from OSU model for $1\times CO_2$, $2\times CO_2$ and $2\times CO_2 - 1\times CO_2$.

4 SPATIAL ANALOGUES

Another approach to identifying what the future climate in the U.K. may be like, involves the use of present day instrumental data from different geographical regions. In this approach, instrumental data from meteorological stations in a warmer region of the world, such as the Mediterranean, is used as an analogue for the future. The main advantage of the approach is that the impacts of future change, on agriculture and hydrology, can be studied by considering present-day practices in the analogue region. The use of station time-series allows aspects of climate variability and extreme events to be studied.

There are, however, a number of potentially serious problems associated with the use of geographical or spatial analogues. These relate to differences in the location, particularly the latitude, height and aspect. Changes occur in the diurnal and seasonal cycle, for example, as one moves towards the tropics. Local topographic effects may rule out one region as a useful future analogue.

Selection of analogue sites should be undertaken using present day climatic normals based on the current climate of the U.K. region under study. An initial selection of useful stations could be identified based on annual mean temperature and total precipitation. This selection could then be refined by comparing seasonal data with the present-day seasonal cycle. In doing this a number of general principles should be followed. Analogue regions should generally be near the western coasts of a continent, away from continental interiors and they should not be stations which are subject to strong local climate or orographic influences.

An initial search would reveal many parts of the world on the eastern side of a major continent where mean temperature is greater than the U.K.. We can probably rule out regions where the annual precipitation is lower than that which currently

occurs in the U.K. as all the currently available GCM results indicate an increase in annual precipitation totals. Possible regions on the eastern coast of Australia, China and South America can be ruled out because of their location. Furthermore, the Rockies and Andes make analogues on the western coasts of North and South America inappropriate. Both regions exhibit a far greater influence on the regional climate than do the Pennines or the Scottish mountains. The best region would appear to be the Mediterranean area of southern Europe. This region has the advantage of being geographically close to the U.K. in terms of latitude and longitude, whilst also being a region which has had a long history of human development.

Selection of the analogue depends to a large extent on the degree of temperature increase expected. In other words how sensitive is the climate system to greenhouse-gas forcing and for what decade in the future is the analogue required. The oceanic influence on Britain's climate would tend to favour analogue regions in western France and northern and western parts of the Iberian peninsula. All such regions would indicate that increases in temperature and precipitation would be smallest during the summer. This is in accord with the GCM results which suggest a weakening of the seasonal cycle of temperature and, albeit with great intermodel variability, a tendency towards more winter and less summer precipitation.

Development of spatial analogue scenarios from regions in south-western Europe would appear to have considerable merit particularly for western parts of the U.K.. Even some of the geological features are similar in western France. Developing scenarios in this way for eastern England and Scotland would appear to be a bit more problematical. The European continent means that even in eastern France winters are generally colder than those experienced, even in eastern Scotland. The moderating influence of the North Sea on the climate of eastern England will not make the

temperatures cooler in the future. For south-east England the best analogue would appear to be south-western France as the full influence of the Atlantic Ocean is somewhat moderated by the Iberian peninsula.

For Scotland and even northern England the most appropriate analogue region is likely to be southern England, particularly if the climate sensitivity is low or if the desired scenario time is only up to about 50 years into the future. The advantage of the analogue being in the same country are that agricultural and hydrological practices are likely to be much more easily transferred.

5 CONCLUSIONS

In the first half of this part of the report we have considered past variations in daily weather patterns and gale day counts over the U.K.. The aim of this exercise was to develop scenarios which may result from the increasing concentrations of greenhouse gases in the atmosphere. The rationale for using past data is that the current generation of GCMs are incapable of reproducing realistic day to day weather variability.

The most important Lamb Weather Types (LWTs) are anticyclonic, cyclonic and westerly. Taken together these three weather types account for about 60% of all days. The most notable feature of the data set is a decline in the number of westerly days since the 1920s. Increases in anticyclonicity, cyclonicity and north-westerliness have to some extent made up for this deficit. To assess possible changes in the future we compared LWTs for two warm periods 1934–53 and 1970–89 with the cool period 1901–20. Although the two warm periods were not consistent in their features, both suggest increased anticyclonicity in springs and summers. Less northerliness in summer and autumn was evident in the warmer periods. Less westerliness occurred in both warm periods, but this may be related to the longer time-scale decline in the number of westerly days.

Also, using past climate data, we investigated changes in the number of gale days over the U.K. and North Sea regions. In order to do this over as long a period as possible we developed an objective index of the gale 'potential' for each day since December 1880. Increasing totals of the number of gales over the U.K. are apparent since 1970 with a greater increase in the numbers of severe and very severe gales. Changes over the North Sea region are less evident although slight rises are noticeable. Analysis of the past warm and cool periods suggests that the winter frequency of gales

over both regions are increasing at the expense of gales in autumn. No overall increase in annual frequency was noticed. The most recent warm period, 1970–89 has seen a higher frequency of very severe gales. The trend towards more gales in winter and more very severe gales in recent years would obviously be amplified by including data for the January to March 1990 period.

The second half of this part of the report considers what possible changes in incoming solar radiation and evaporation may occur as a result of increasing greenhouse gas concentrations. As both of these parameters are output by some GCMs, we have assessed the common features of their projections for a high-CO_2 world. Despite the great intermodel variability for both variables, the common features for incoming solar radiation would suggest increases over Britain during summer and, to a lesser extent, spring. Changes in the other seasons would be small. Overall the changes would be of the order 10 wm^{-2} or an increase of about 4%. For evaporation, increases are predicted, particularly for Scotland and northern England. Increases are expected in all seasons except for winter.

6 REFERENCES

Barry, R.G. and Perry, A.H., 1973 : Synoptic Climatology : Methods and Applications. Methuen, London, 555pp.

Briffa, K.R., Jones, P.D. and Kelly, P.M., 1990: Principal component analysis of the Lamb Catalogue of Daily Weather Types : Part 2, seasonal frequencies and update to 1987. *International Journal of Climatology*, in press.

Hansen, J., Lacis, A., Rind, D., Russell, G., Stone, P., Fung, I., Ruedy, R. and Lerner, J., 1984: Climate Sensitivity: Analysis of feedback mechanisms. In *Climate Processes and Climate Sensitivity*, Maurice Ewing Series, 5 (J.E. Hansen and T. Takahashi, Eds.), American Geophysical Union, Washington, D.C., 130–163.

Jenkinson, A.F. and Collison, F.P., 1977: An initial climatology of gales over the North Sea. *Synoptic Climatology Branch Memorandum No. 62*, U.K. Meteorological Office, Bracknell.

Jones, P.D. and Kelly, P.M., 1982: Principal component analysis of the Lamb Catalogue of Daily Weather Types : Part 1, annual frequencies. In *Journal of Climatology*, 2, 147–157.

Jones, P.D., Raper, S.C.B., Bradley, R.S., Diaz, H.F., Kelly, P.M. and Wigley, T.M.L., 1986a: Northern Hemisphere surface air temperature variations : 1851–1984. *Journal of Climate and Applied Meteorology*, 25, 161–179.

Jones, P.D., Wigley, T.M.L. and Wright, P.B., 1986b: Global temperature variations between 1861 and 1984. *Nature*, 322, 430–434.

Lamb, H.H., 1972: British Isles weather types and a register of the daily sequence of circulation patterns, 1861–1971. In *Geophysical Memoirs*, 116, HMSO London, 85pp.

Legg, T.P., 1989: Removal of urbanization from the Central England temperature data sets. *Long-range Forecasting and Climate Memorandum No. 33*, U.K. Meteorological Office, Bracknell.

Manley, G., 1974: Central England Temperatures: monthly means 1659 to 1973. *Quarterly Journal of the Royal Meteorological Society*, 100, 389–405.

Schlesinger, M.E., and Zhao, Z.C., 1989: Seasonal climatic changes induced by doubled CO_2 as simulated by the OSU atmospheric GCM/mixed-layer ocean model. *Journal of Climate*, 2, 459–495.

Wigley, T.M.L., Angell, J.K. and Jones, P.D., 1985: Analysis of the temperature record. In *Detecting the Climatic Effects of Increasing Carbon Dioxide*, DoE/ER-0235 (M.C. MacCracken and F.M. Luther, Eds.). U.S. Dept. of Energy, Carbon Dioxide Research Division, 55–90.

Wigley, T.M.L. and Jones, P.D., 1987: England and Wales precipitation: A discussion of recent changes in variability and an update to 1985. *Journal of Climatology*, 7, 231–246.

Wigley, T.M.L., Jones, P.D. and Kelly, P.M., 1986: Empirical Climate studies : warm world scenarios and the detection of climatic change induced by radiatively active gases. In *The Greenhouse Effect, Climatic Change, and Ecosystems* (B.Bolin, B.R. Dőős, J. Jäger and R.A. Warwick, Eds.) SCOPE 29, Wiley, 271–323.

Wigley, T.M.L., Lough, J.M. and Jones, P.D., 1984: Spatial patterns of precipitation in England and Wales and a revised homogeneous England and Wales precipitation series. *Journal of Climatology*, 4, 1–25.

Wilson, C.A. and Mitchell, J.F.B., 1987: A doubled CO_2 climate sensitivity experiment with a global climate model including a simple ocean. *Journal of Geophysical Research*, 92, 13315–13343.

World Meteorological Organisation, 1986: Report of the International Conference on the Assessment of the Role of Carbon Dioxide and of Other Greenhouse Gases in Climate Variations and Associated Impacts. Villach, Austria, 9–15 October, 1985. WMO No.661.

World Meteorological Organisation, 1988: Water resources and climatic change: Sensitivity of water-resource systems to climate change and variability. Report of a meeting of experts at Norwich, U.K., November 1987.